Foliation Boudinage Structures at the Mount Isa Cu Deposit, Australia

Benjamin J. Williams

Submitted in partial fulfilment of the requirements for the degree of

Doctor of Philosophy (PhD)

March 2023

The Mount Isa deposit was discovered by John Campbell Miles in 1923, it is fitting to reflect on the following report extract:

"The metal deposits in the Mount Isa field should last a century…"

- Mr B Dunstan,
Chief Government Geologist, 1925

"Much is expected of Mount Isa"

- Unknown, 1929

Acknowledgements

There are many people who have supported and assisted in some way during my PhD journey.

Firstly, I would like to extend my thanks to my supervisor, Tom Blenkinsop, who has always been on hand to answer questions on all aspects of geology. Tom has provided many hours of invaluable constructive criticism throughout my time at Cardiff. Richard Lilly, although from slightly further afield, has provided much assistance to all of my queries over the years. I would like to thank Richard for his support during my first, and ultimately, only fieldwork visit to Mount Isa.

Many thanks to all members of the Cardiff PhD community for your friendship and support over the years; it has been a pleasure to work alongside you all. Also, thanks to all members, past and present, of the 'Cracks and Copper' group for the many thoughtful discussions on new and unusual geology, as well as constructive comments on my own work. Likewise, a mention for those who have shared the journey from Bristol University and all others in the GW4+.

A special thanks to the laboratory staff at Cardiff, including Tony Oldroyd for the many thin sections he has produced, and hours of conversations enjoyed, and Duncan Muir for his expertise in all SEM analyses. Thanks to Julia Behnsen at the Royce Institute, University of Manchester for her help with CT scanning. I am grateful to everyone at Mount Isa Mines for their assistance during the fieldwork and particularly Pat Ila'ava.

To Mom and Dad, thanks for not discouraging me from picking up rocks and for your constant support throughout my time at university. James and the Luing crew who are a welcome break from work, where we have been able to rest and be thankful. Finally, I can't thank Erin enough for her countless cups of tea, her immeasurable generosity, hours of support and adventures over the last few years, thank you.

Abstract

Copper (Cu) is increasingly important as the global economy becomes more reliant on renewable energy sources. The Mount Isa Inlier, NW Queensland, is one of Australia's most important metallogenic provinces, hosting several deposits of Cu, Pb, Zn, Ag and U, including the famous world-class Mount Isa deposit. The Mount Isa Cu-Pb-Zn-Ag deposit is the second largest producer of Cu in Australia, yet the formation, geometry and timing of the mineralisation is still debated. One reason for this lack of consensus is that Mount Isa has undergone a long and complex deformation history with north-south shortening (D1), east-west shortening (D2), top to the east shear (D3), ENE-WSW shortening (D4a), WNW-ESE shortening (D4b), and east-west shortening (D5a and D5b). Recent studies at Mount Isa have suggested that Cu mineralisation initiated in D4a and proceeded through to the main Cu mineralisation in D4b, where the orebodies have a strong structural control on their geometries.

Foliation boudinage structures, which form in anisotropic and homogeneous rocks, have been identified in the Mount Isa Cu orebodies. Confusions in terminology that exist in the foliation boudinage literature have required a detailed review of the literature leading to a synthesis of current ideas. The formation and development of foliation boudinage structures have previously been modelled in 2-dimensions through analogue and computer techniques. However, no previous studies have investigated the formation and evolution of natural foliation boudinage structures in 3-dimensions. This study combines structural observations, kinematic analysis, petrography, and 3-dimensional modelling of foliation boudinage structures using computerised tomography (CT) and serial sectioning, to constrain their timing and importance in the mineralisation at Mount Isa and to infer the processes involved in their evolution.

Small scale foliation boudinage structures were sampled in drill core proximal to the Mount Isa Cu deposit and their orientations were recorded. Most drillholes analysed at Mount Isa were unoriented, however, foliation boudinage structures have been reoriented using new methods developed in this study. Desurveying methods were first compared to find the most precise method for plotting the drillhole pathway using examples from Mount Isa. New computer code was developed to determine the orientations and positions of drillholes along their entire length using the existing desurveying methods. The drillhole survey measurements given by the computer codes allow the original orientations of the foliation boudinage structures to be determined.

Foliation boudinage structures occur most commonly in the unaltered Urquhart Shale where the anisotropy and homogeneity provided by the shale layering is intact. Detailed petrographic analysis of the foliation boudinage structures has identified that an initial rim of quartz and dolomite was followed by infill and replacement by later sulphides. The dominant sulphides in the foliation boudinage structures are pyrrhotite and minor chalcopyrite, both associated with the Cu mineralisation at Mount Isa. The paragenesis of the foliation

boudinage structures is consistent with the established paragenesis of the main Cu mineralisation. The foliation boudinage structures plunge gently to the north and south as a result of approximately layer-normal shortening and layer-parallel extension of the steeply west-dipping Urquhart Shale. North-plunging structures formed by ENE-WSW dextral-reverse shortening during the D4a deformation event and the south-plunging structures formed by WNW-ESE sinistral-reverse shortening during the D4b deformation event.

Electron Backscatter Diffraction (EBSD), combined with 2-dimensional and 3-dimensional strain analyses show that the ore-related sulphide mineral infills of foliation boudinage structures at Mount Isa have undergone significant intracrystalline deformation. Pyrrhotite grains show well-developed grain shape and crystallographic preferred orientations, with *c*-axes normal to the shale layers. The strain ellipsoid shows a change from plane to flattening strain, indicating a progressive deformation during foliation boudinage. Previous studies have suggested that the foliation boudinage structures remain as fluid filled voids throughout their development. However, strain of the pyrrhotite infill, which has a low strength under the conditions of deformation, indicate that the voids were mostly filled during the final stages of foliation boudinage.

3-dimensional modelling of foliation boudinage structures suggest a model of propagation along their long-axes, with the oldest sections, greatest displacements, and most complex mineral phase boundaries in the central part of the structure, in a similar fashion to faults. Stages identified in the evolution of foliation boudinage structures at Mount Isa, are: 1) dolomite replacement of unaltered shale, 2) fracture and cleavage development, 3) exploitation of existing discontinuities by the developing structures during shortening, 4) silica-dolomite infill and 5) final infill with ore related sulphides. As the foliation boudinage structures at Mount Isa exploit existing discontinuities, fluid pressures during foliation boudinage are likely to be lower than during other types of foliation boudinage developed within undeformed host rocks.

This study, along with recent studies at Mount Isa, contrast to previous ideas about the Cu orebodies, and enable an improved explanation for their geometries, kinematics, and timing. This study supports the most recent ideas that the structural controls on the Mount Isa Cu orebodies resulted from epigenetic mineralisation at the time of ENE-WSW and WNW-ESE shortening of the Urquhart Shale during D4 deformation. This relatively late timing of foliation boudinage and Cu mineralisation in the deformation sequence is in contrast to the syngenetic and early timing of Cu mineralisation proposed by some previous authors. The strain and kinematics expected in both D4a and D4b are recorded in the formation and evolution of foliation boudinage structures at Mount Isa. The drill core scale structures proximal to the Cu orebodies may be used as a tool for vectoring towards mineralisation at the Mount Isa deposit. Foliation boudinage structures likely impart a structural control on the Cu mineralisation at the scale of the orebodies and may control the geometries of other deposits in similar rock types.

Contents

List of Figures

List of Tables

Abbreviations and Conventions

Ag	Silver
CPO	Crystallographic Preferred Orientation
CRSS	Critical Resolved Shear Stress
CT	Computerised Tomography
Cu	Copper
EBSD	Electron Backscatter Diffraction
ECV	Eastern Creek Volcanics
FBS	Foliation Boudinage Structures
FF	Flanking Fold
Fm	Formation
FS	Flanking Structure
GOS	Grain Orientation Spread
IB	Internal Boudinage
ISA	Instantaneous Stretching Axis
MAD	Mean Angular Deviation
MICO	Mount Isa Copper Operations
MIM	Mount Isa Mines
MUD	Multiples of Uniform Distribution
Pb	Lead
PPL	Plane Polarised Light
RD	Resource Development
RL	Reflected Light - microscopy
RL	Reduced Level (TVD elevation for drillhole collars) - elevation
SEM	Scanning Electron Microscope
SGR	Subgrain Rotation
SPO	Shape Preferred Orientation
TVD	True Vertical Depth
U	Uranium
XPL	Cross Polarised Light
XRD	X-Ray Diffraction
Zn	Zinc

- All planar data in this study are recorded in accordance with the right-hand rule, whereby the strike measurement is -90° in relation to the dip direction.
- Linear measurements are presented as plunge and azimuth (e.g., 25° plunge with an azimuth of 340° is shown as 25°→340°).
- Foliation boudinage structures are shown as linear measurements.

CHAPTER 1

Introduction

1.1 Background

Copper (Cu), along with other base metals such as zinc (Zn) and lead (Pb), are becoming increasingly important commodities as the global economy becomes more reliant on the use of electricity from renewable energy sources (Harmsen *et al.*, 2013; Allen, 2020; Riegel, 2020; Venditti, 2022). This so called 'transition to the green economy' (Pearce *et al.*, 1989) requires significant volumes of base metals for solar photovoltaics, wind turbines, electric vehicles and power storage systems (Kleijn *et al.*, 2011; Islam *et al.*, 2022). The demand for Cu is estimated to increase from 25 Mt in 2020 to 100-450 Mt per annum by 2100 (Schipper *et al.*, 2018; Garside, 2021; Watari *et al.*, 2021; Blackmon, 2022). Ciacci *et al.* (2020) showed that recycling scrap Cu can satisfy a portion of this future demand, however even with increased Cu recycling, increased production and reserves are still needed.

The long term security of Cu supply is also vital for the transition to renewable energy alternatives. It has been projected that Cu scarcity may pose a 'critical destabilising threat to international security' (Lazenby, 2022; S&P Global, 2022) and significant demand for Cu 'may cause a threat to energy security on a previously unknown scale' (Mróz, 2022). Australia is one of the UK's most trusted trading partners, with the top commodity in the first half of 2020 being non-ferrous metals, accounting for 15.9% of all UK imports from Australia (Department for Foreign Affairs and Trade, 2020; Office for National Statistics, 2020). In 2021, Australia was the fifth largest producer of Cu (~4% of global copper). As such, Australia has a small but significant role in the global Cu supply chain.

Much of Australia's mineral wealth is hosted within deposits from the Proterozoic (~2.5-0.5 Ga), including 90% of Australia's uranium (U) and lead, 85% of zinc and 70% of copper. Most of Australia's world-class deposits such as Broken Hill, Hilton, Mount Isa, McArthur River

(HYC), Century and Olympic Dam formed between 1870 Ma and 1550 Ma. Australia's Cu resources are dominated by two Proterozoic deposits, the Olympic Dam and the Mount Isa deposits (Jaques *et al.*, 2002). The importance of Australia's Proterozoic rocks for hosting significant Cu and other base metal resources should not be underestimated.

The Proterozoic Mount Isa Inlier comprises a significant Proterozoic base metal province that covers an area of 50,000 km^2 **[Figure 1.1]** (Williams, 1998b; Ford and Blenkinsop, 2008). Base and precious metals of the inlier include copper, gold, uranium, lead and zinc **[Table 1.1]** (Williams, 1998b; Ford and Blenkinsop, 2008). The Mount Isa Inlier is host to four supergiant ore deposits as defined by Singer (1995): Century (Zn-Pb-Ag), Hilton (Zn-Pb-Ag), George Fisher (Zn-Pb-Ag), and Mount Isa (Cu-Pb-Zn-Ag) (Large *et al.*, 2002, 2005). The neighbouring Proterozoic McArthur Basin is host to the McArthur River (HYC) Zn-Pb supergiant (Large *et al.*, 2002, 2005).
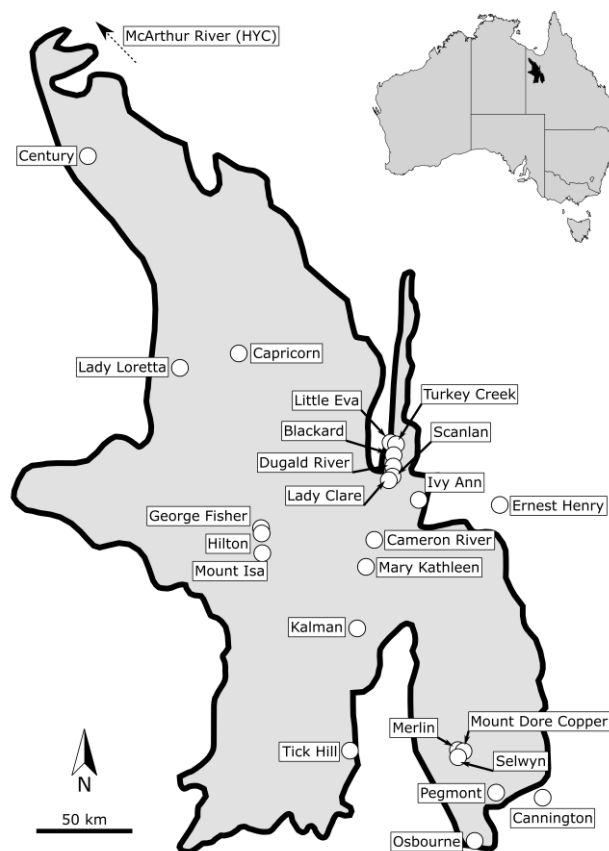
Figure 1.1: The Proterozoic Mount Isa Inlier is a significant base metal province of NW Queensland, Australia. Some of the major deposits of the inlier are shown.

Mine	Metals	References
Mount Isa (Cu-Zn-Pb-Ag)	225 Mt @ 3.3% **Cu** 150 Mt @ 7% **Zn**, 6% **Pb**, 150 g/t **Ag**	(Forrestal, 1990; McGoldrick and Large, 1998; Waring *et al.*, 1998; Davis, 2004; Geological Survey of Queensland, 2011)
George Fisher (Zn-Pb-Ag)	108 Mt @ 11.5% **Zn**, 5.4% **Pb**, 93 g/t **Ag**	(McGoldrick and Large, 1998)
Hilton (Zn-Pb-Ag)	120 Mt @ 10.2% **Zn**, 5.5% **Pb**, 100 g/t **Ag**	(Forrestal, 1990; McGoldrick and Large, 1998)
Cannington (Pb-Zn-Ag)	43.8 Mt @ 11.6% **Pb**, 4.4% **Zn**, 538g/t **Ag**	(Walters and Bailey, 1998; Williams, 1998b)
Century (Zn-Pb-Ag)	167 Mt @ 8.2% **Zn**, 1.2% **Pb**, 33 g/t **Ag**	(McGoldrick and Large, 1998; Kelso *et al.*, 2001)
McArthur River (HYC) (Zn-Pb)	227 Mt @ 9.2% **Zn**, 4.1% **Pb**,	(Logan *et al.*, 1990; McGoldrick and Large, 1998)
Lady Loretta (Zn-Pb-Ag)	8.3 Mt @ 18.4% **Zn**, 8.5% **Pb**, 125 g/t **Ag**	(Cox and Curtis, 1977; Hancock and Purvis, 1990; McGoldrick and Large, 1998)
Dugald River (Zn-Pb-Ag)	38 Mt @ 13.2% **Zn**, 2.1% **Pb**, 42 g/t **Ag**	(Connor *et al.*, 1990; Newbery *et al.*, 1993; McGoldrick and Large, 1998)

Table 1.1: Table of important base and precious metal deposits in the Mount Isa Inlier.

The Mount Isa orebodies occur within the Urquhart Shale, a thinly laminated, highly anisotropic and homogeneous unit of the Mount Isa Group. The Urquhart Shale appears to have a specific disposition for metal endowment, as although many kilometres apart, the Mount Isa, Hilton, and George Fisher deposits are all hosted within this unit. Other deposits in the inlier such as Century, McArthur River (HYC), Lady Loretta, and Dugald River are situated in similar rock types and have likely undergone similar deformation histories.

Mount Isa Mine is the second largest Cu producer in Australia. Pre-mining estimates for the Mount Isa deposit comprise 405 Mt of ore, with 150 Mt at 7% Zn and 6% Pb, and 255 Mt at 3.3% Cu (Forrestal, 1990; McGoldrick and Large, 1998; Waring *et al.*, 1998; Geological Survey of Queensland, 2011). Mount Isa processes around 6.5 Mt of ore per year at grades up to

3.3% Cu (Potgieter, 2015; Glencore, 2022). Due to the size and economic significance of the Mount Isa deposit, the metallogenic model is frequently used to guide regional exploration (Cave *et al.*, 2022). Despite this, controversy still remains over the origin, formation, and geometry of the Mount Isa orebodies, hindering exploration for new resources both within the mine and regionally.

Unusual structural patterns and geometries of Cu mineralisation have recently been documented by Mount Isa mine geologists in both drill core and orebody block models. Such structures resemble foliation boudinage structures that are described in the literature and from those observed at other deposits (Hambrey and Milnes, 1975; Platt and Vissers, 1980; Mandal and Karmakar, 1989; Aerden, 1991; Swanson, 1992; Arslan *et al.*, 2008, 2012). Foliation boudinage structures are vein-like boudins that can open into voids that contain large volumes (10-100s cubic metres) of infill. The Pb-Zn orebodies at the Rosebery Mine, Tasmania, are located within large scale (up to 100s of metres) foliation boudinage structures, which control the formation, distribution, and orientation of the orebodies (Aerden, 1991). The foliation boudinage structures at Rosebery are also hosted within lithologies similar to those at Mount Isa.

Mine geologists at Mount Isa consider that these foliation boudinage structures could exert some structural control on the Cu orebodies. However, the role of foliation boudinage structures in the Mount Isa mineralisation is unknown. In order to investigate the relation between foliation boudinage structures and mineralisation at Mount Isa, as well as their potential implications for exploration, their geometries, scale, distribution, and ore hosting potential must be described. These descriptions enable the formation, evolution, and timing of the foliation boudinage structures to be inferred. Investigating the hypothesis that foliation

boudinage structures control the Cu orebodies may have important consequences for mine and near mine exploration for new Cu orebodies and in extending the life of mine of the Mount Isa deposit to help satisfy future Cu demands. The results and conclusions made at Mount Isa may also have implications for other deposits in the Mount Isa Inlier and deposits in similar structural settings worldwide.

Previous modelling of foliation boudinage structures focused on their formation mechanisms in 2-dimensions, such as the cross sectional models of Arslan et al. (2008, 2012) and Mandal and Karmakar (1989). These studies have modelled the theoretical formation of foliation boudinage structures using analogue and computer methods. Yet, despite this previous work, the geometry of the foliation boudinage structure in the 3rd dimension (long-axis) is almost always ignored, meaning that the complete 3-dimensional geometry, evolution, and mineral hosting potential of real foliation boudinage structures are still not understood. Therefore, this study will model the geometries of real foliation boudinage structures from the Mount Isa Cu deposit to infer the processes involved in their formation and evolution.

1.2 Research Objectives

The aim of this thesis is to characterise the distribution, geometry, and timing of foliation boudinage structures at the Mount Isa Cu deposit, in order to understand their evolution and relation to Cu mineralisation. This will be achieved by bringing together existing and new data through structural drill core logging, petrographic analysis, electron backscatter diffraction (EBSD) techniques and 3-dimensional modelling to achieve the following objectives:

(1) Develop a method to calculate 3-dimensional coordinates and orientations of foliation boudinage structures by combining measurements on oriented and unoriented core with drillhole surveys. (1.1) 'Desurveying' methods will be investigated to find the optimum procedure for determining the location and orientation of drill core samples. (1.2) A method to orient the foliation boudinage structures in unoriented core relative to an assumed orientation of bedding will be developed.

(2) Describe the orientation and distribution of foliation boudinage structures and their importance in mineralisation at Mount Isa.

(3) Describe the geometry of the mineral infill in foliation boudinage structures to determine their relative timing of formation and subsequent deformation history of ore-related sulphides at Mount Isa.

(4) Ascertain the 3-dimensional geometries and evolution of foliation boudinage structures using examples from Mount Isa.

1.3 Thesis Outline

This thesis is subdivided into nine chapters, comprising: an introduction, background geology, literature review, methodology, four chapters of original research and final conclusions. Eight appendices contain detailed petrographic descriptions, methods, tables, and results.

CHAPTER 1: Introduction. This chapter is a broad introduction to the project, comprising background material on global copper production and future demand, the Mount Isa Inlier as a significant Proterozoic base metal province, the potential significance of foliation boudinage structures in the formation of the Mount Isa copper deposit, the lack of knowledge about the

3-dimensional geometry and evolution of foliation boudinage structures, and an outline of the project aims.

CHAPTER 2: Mount Isa Geological Background. This chapter reviews the current understanding of the Mount Isa copper ore system.

CHAPTER 3: Foliation Boudinage Structure Literature Review. This chapter is a literature review of foliation boudinage structures, with comparisons to the geometrically similar structures of internal boudins and flanking folds. This chapter arrives at a new synthesis of the subject.

CHAPTER 4: Methodology. This chapter outlines the main methods of data collection and sample preparation that apply to all aspects of this study.

CHAPTER 5: A Comparison of Drillhole Desurveying Methods. This chapter compares the accuracy and reliability of drillhole desurveying techniques for varied drillhole lengths, at multiple angles to the anisotropy. The chapter also presents multiple desurveying methods in easy-to-use Python and R computer codes to calculate the 3-dimensional position, azimuth and plunge at any point along the drillhole. This chapter is a modified version of the manuscript that has been submitted to Computers and Geosciences:

- Williams, B.J. and Blenkinsop, T.G., The Impact of Anisotropy and Drillhole Length on the Existing Desurveying Methods: Examples from Mount Isa. *Computers and Geosciences*

Modifications have been made to add further context in relation to this thesis. Benjamin J. Williams is the lead author of the manuscript, contributing the computer code, analyses and

writing of the manuscript. Professor Thomas Blenkinsop gave guidance and comments throughout the manuscript.

CHAPTER 6: Foliation Boudinage Structures in the Mount Isa Cu System. In this chapter, the petrography, geometry, orientation, distribution, and timing of foliation boudinage structures are investigated. Copper grades and lithologies where foliation boudinage structures occur are assessed. This chapter is a modified version of the paper:

- Williams, B. J., Blenkinsop, T. G., Lilly, R., Thompson, M. P., & Ila'ava, P. (2023). Foliation boudinage structures in the Mount Isa Cu system. *Australian Journal of Earth Sciences (spec. ed.)*, 1–18. https://doi.org/10.1080/08120099.2022.2153384

Modifications have been made to remove the material from the manuscript that is presented in chapters 2, 3 and 4 to avoid repetition. Benjamin J. Williams is the lead author of the manuscript, contributing the fieldwork, analyses and writing of the manuscript. Professor Thomas Blenkinsop gave guidance and comments throughout the manuscript. Dr Richard Lilly helped with the initial fieldwork setup and gave minor comments on the manuscript. Michael Thompson initiated the project and gave detailed comments on the manuscript. Patricia Ila'ava helped facilitate the fieldwork. Julian Vearncombe and Nick Hayward gave constructive reviews on the submitted manuscript.

CHAPTER 7: Strain in Sulphide Filled Foliation Boudinage Structures at Mount Isa. This chapter investigates the strain present within the foliation boudinage structures at Mount Isa. The chapter is a modified version of the manuscript currently in review:

- Williams, B.J. and Blenkinsop, T.G., Strain in Foliation Boudinage Structures at Mount Isa. *Journal of Structural Geology*

Modifications have been made to remove material from the manuscript that is now included in chapters 2, 3 and 4 to avoid repetition. Benjamin J. Williams is the lead author of the manuscript, contributing the fieldwork, analyses and writing of the manuscript. Professor Thomas Blenkinsop gave guidance and comments throughout the manuscript.

CHAPTER 8: 3-Dimensional Modelling of Foliation Boudinage Structures. This chapter compares different models for the closure of foliation boudinage structures using 3-dimensional models from serial sections; investigates and analyses the geometries of foliation boudinage structures and their mineral hosting potential during their evolution; and shows how the foliation boudinage structures at Mount Isa evolved over time from undeformed shale to sulphide filled structures. This chapter will be submitted to a peer reviewed journal.

CHAPTER 9: Conclusions. The results are synthesised, and the main overarching conclusions of the research objectives are presented in this chapter.

Appendices: Eight appendices have been added, that include: background work on foliation boudinage structures and sample descriptions from Mount Isa; detailed methodologies; detailed results that complement those in the main thesis; an electronic appendix that includes drillhole computer codes and virtual models of foliation boudinage structures that are not available in hard copy format.

1.4 Contributions to this study

All fieldwork in this study, including the surface outcrop mapping, structural logging of drill core and sample collection was conducted by Benjamin J. Williams. Lithological and assay logs were provided by Mount Isa Mines for use in this study. Professor Thomas Blenkinsop provided field support for 3 days and Dr Richard Lilly for 10 days during the March-April 2019 field season.

All samples in this study were collected by Benjamin J. Williams in March-April 2019. Preparation of samples for polished thin sections were carried out by Benjamin J. Williams and all polished thin sections were made by Anthony Oldroyd at Cardiff University. Petrographic analysis was carried out by Benjamin J. Williams. Scanning electron microscope (SEM) and electron backscatter diffraction (EBSD) analyses were carried out by Benjamin J. Williams and Dr Duncan Muir at Cardiff University.

Computerised tomography (CT) scanning was carried out by Julia Behnsen and processed by Benjamin J. Williams. CT scanning was generously provided by the Henry Royce Institute for Benjamin J. Williams through the Royce PhD Equipment Access Scheme at the University of Manchester (EPSRC Grant Number EP/R00661X/1).

CHAPTER 2

Mount Isa Geological Background

2.1 Introduction

This chapter gives a detailed overview of the geology of the Mount Isa Inlier, Mount Isa deposit, and the orebodies. The deformation sequence in section 2.3 is used throughout the thesis, with specific detail in Chapter 6 and Chapter 7. The details of the deposit geology in section 2.4 are used in Chapter 5, Chapter 6, Chapter 7, and Chapter 8.

2.2 Regional Geology

Mount Isa is located within the late Paleo- to early Meso-Proterozoic Mount Isa Inlier **[Figure 2.1]**. The Mount Isa Inlier can be subdivided into broad tectonic divisions as the Western Fold Belt, the Kalkadoon-Leichhardt Belt and the Eastern Fold Belt (Day *et al.*, 1983; Blake, 1987). The Mount Isa mine lies within the Leichhardt River Fault Trough of the Western Fold Belt **[Figure 2.1]**. The Western Fold Belt is composed of a succession of volcanic and sedimentary rocks and is separated from the generally higher metamorphic grade and more deformed Eastern Fold Belt by the Kalkadoon-Leichhardt Belt (O'Dea *et al.*, 1997a, 1997b). The central Kalkadoon-Leichhardt Belt exposes crystalline basement rocks deformed and metamorphosed during the 1900-1870 Ma Barramundi Orogeny (Page and Williams, 1988; O'Dea *et al.*, 1997b).

The post-basement stratigraphy of the Mount Isa Inlier is characterised by periods of intracontinental rifting, resulting in sediment accumulation in basin settings. It has been suggested that, rather than a continuous series of rift-sag phases, the evolution of the Mount Isa Inlier was characterised by oscillatory extensional-contractional tectonics (Brown *et al.*, 2023). Nonetheless, there are two ways of categorising this post-basement stratigraphy in the

present literature, one in terms of cover sequences and the other as superbasins.
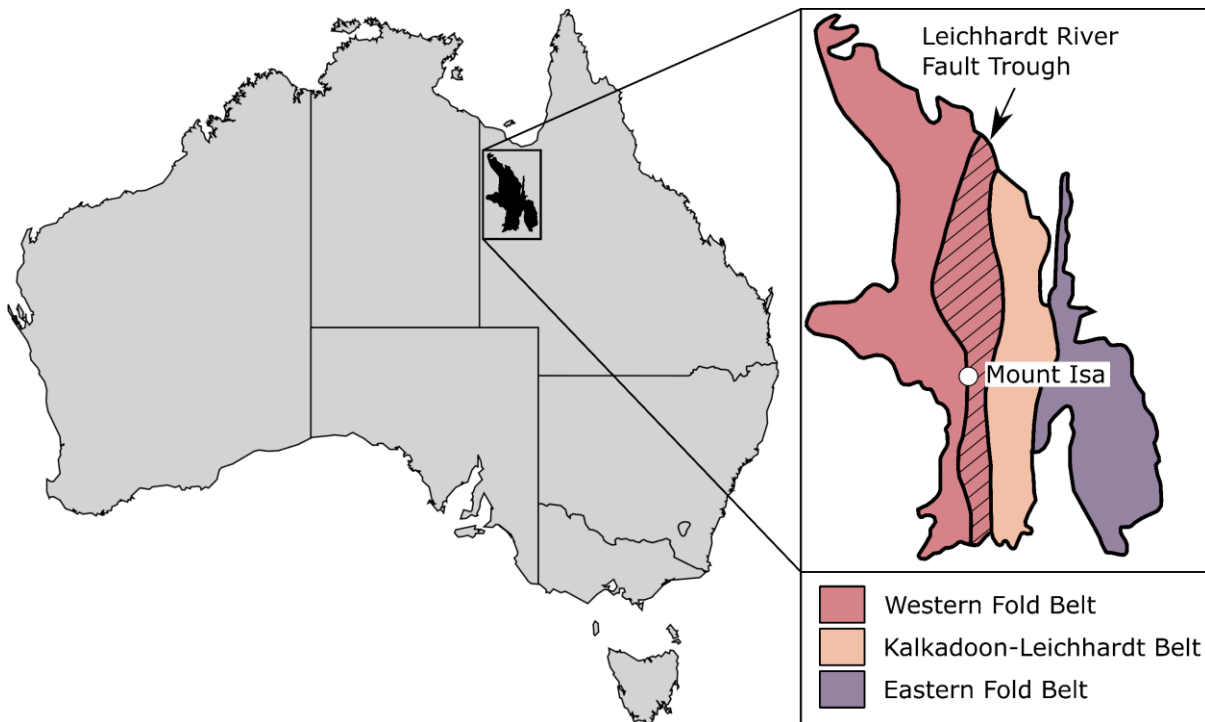
Figure 2.1: The location of Mount Isa and the main tectonic divisions of the Proterozoic Mount Isa Inlier of northwest Queensland, Australia, after Blake and Stewart (1992) and Davis (2004).

The post-basement stratigraphy of the whole Mount Isa Inlier can be split into three younger cover sequences, which did not undergo significant regional deformation prior to the 1590-1500 Ma Isan Orogeny (Blake, 1987; O'Dea *et al.*, 1997a; Betts *et al.*, 2006; Giles *et al.*, 2006). The first rifting event, post-Barramundi Orogeny, resulted in the deposition of cover sequence 1 at 1870-1850 Ma (Blake, 1987). There is some ambiguity over the dates of cover sequence 2 and 3, probably as a result of differential deposition within the inlier. The age of cover sequence 2 has been published as 1800-1740 (O'Dea *et al.*, 1997a; Williams, 1998a; Potma and Betts, 2007; Austin and Blenkinsop, 2010), 1790-1760 (Blake, 1987) and 1790-1720 (O'Dea *et al.*, 1997a; Ford and Blenkinsop, 2008a, 2008b). The age of cover sequence 3 is determined as 1740-1670 (Derrick, 1982), 1680-1670 or younger (Blake, 1987) or 1680-1600

(Blake and Stewart, 1992; Ford and Blenkinsop, 2008a, 2008b). It is worth noting that some studies have included a fourth cover sequence (O'Dea *et al.*, 1997b, 1997a; Davis, 2004), which broadly aligns with the youngest units of cover sequence 3.

More commonly in the later literature, the post-basement stratigraphy of the Mount Isa Inlier is separated into the Eastern and Western Successions (Blake, 1987; Blake and Stewart, 1992). The Western Succession broadly occurs in the Western and Kalkadoon-Leichhardt Fold Belts. The regional stratigraphy of the Western Succession constitutes basement metamorphics overlain by three stacked "superbasins" **[Figure 2.2]**; the Leichhardt (1800-1750 Ma), Calvert (1735-1690 Ma) and Isa (1670-1575 Ma) superbasins (Jackson *et al.*, 2000; Page *et al.*, 2000; Scott *et al.*, 2000; Southgate *et al.*, 2000). The three superbasins did not experience significant large strain regional contraction prior to the onset of the Isan Orogeny (1610-~1500 Ma) (O'Dea *et al.*, 1997b). The Leichhardt Superbasin may be contemporaneous with cover sequence 2 of the overall Mount Isa Inlier, and the Calvert and Isa Superbasins may align with cover sequence 3 (Neumann *et al.*, 2006; Austin and Blenkinsop, 2010).

The Leichhardt Superbasin comprises deep marine sediments of the 1790±9 Ma Bottletree Formation (Page, 1983; Page and Sun, 1998) to later fluvial and shallow marine deposits of the 1773±16 Ma Mount Guide Quartzite (Neumann *et al.*, 2006). The early Leichhardt sediments are succeeded by vast iron-rich continental flood basalts of the ca. 1780 Ma Eastern Creek Volcanics, including the 1779±4 Ma Lena Quartzite (Neumann *et al.*, 2006). The overlying Myally Subgroup (1773±2 Ma Bortala Formation and 1768±8 Ma Whitworth Quartzite; Neumann *et al.*, 2006) consists of clastic sedimentary successions, largely controlled by extensional faulting (O'Dea *et al.*, 1997a; Betts *et al.*, 2006) and is overlain by shallow marine quartzites and carbonates of the 1763±8 Ma Quilalar Formation (Jackson *et*

al., 2000; Betts *et al.*, 2006; Neumann *et al.*, 2006). Post-rift thermal subsidence is believed

to initiate in either the upper Myally Subgroup or the overlying Quilalar Formation.
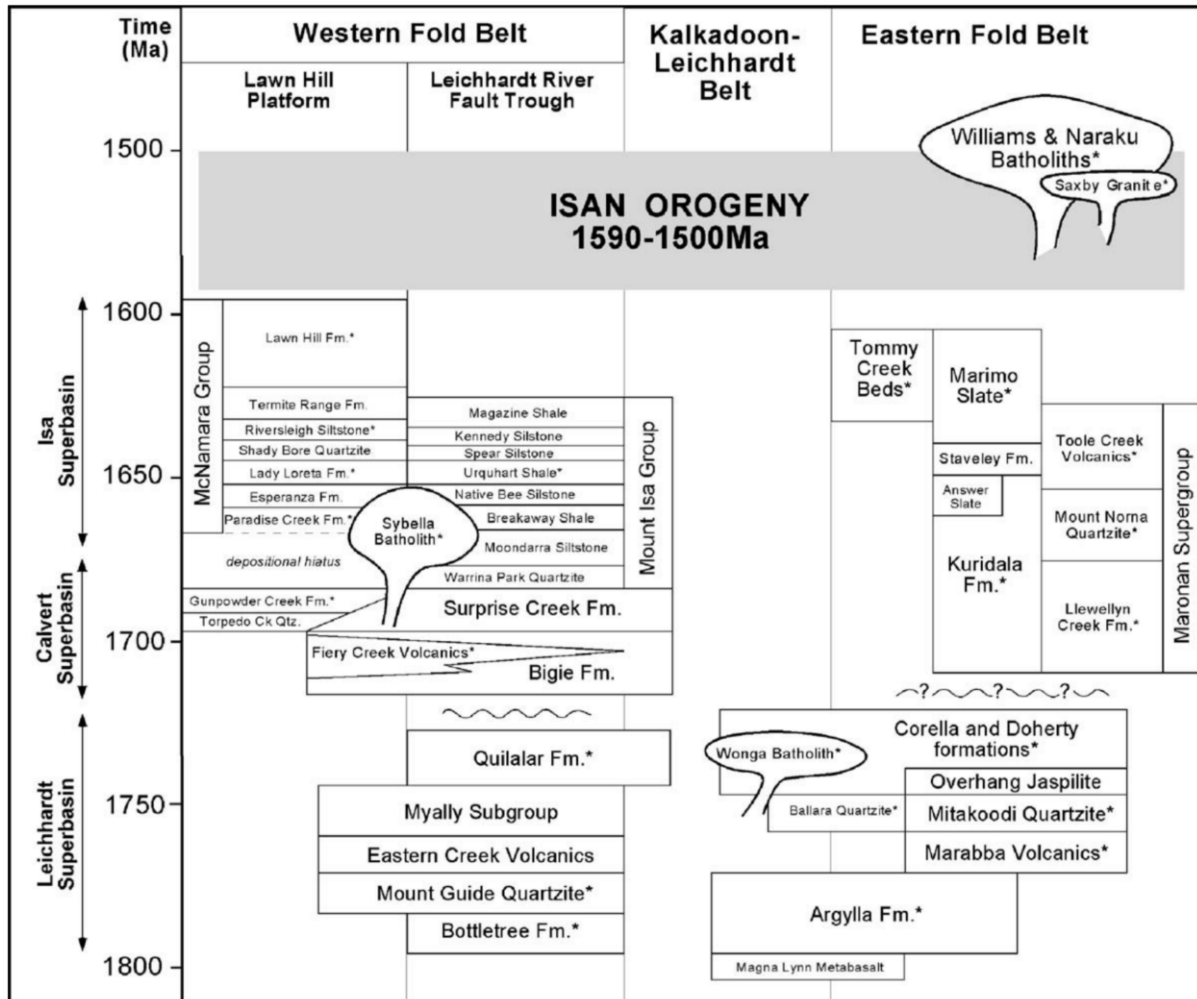
Figure 2.2: Chronostratigraphy-space diagram showing the major stratigraphic subdivisions and magmatic rocks of the Mount Isa Inlier. From Giles *et al.* (2006).

The Calvert Superbasin is separated from the Leichhardt Superbasin by a compressional

tectonic event (Jackson *et al.*, 2000). The Calvert Superbasin is largely composed of clastic

fluvial and shallow marine sediments, with interbedded bimodal volcanic rocks deposited in

a half graben during NW-SE extension (O'Dea *et al.*, 1997a; Betts *et al.*, 1998, 1999). The

1762±18 Ma Bigie Formation (Neumann *et al.*, 2006) unconformably and paraconformably

overlies the Quilalar Formation and Myally Subgroup (Betts *et al.*, 1999) and is overlain by the 1709±3 Ma Fiery Creek Volcanics (Page and Sweet, 1998) and Surprise Creek Formation.

Emplacement of the 1670±3 Ma Sybella Granite (Neumann *et al.*, 2006) marks the boundary between the Calvert Superbasin and overlying Isa Superbasin, the latter being made up of the Gun, Loretta, River, Term, Lawn, Wide and Doom supersequences (Domagala *et al.*, 2000; Page *et al.*, 2000). In the Mount Isa region, the basal Gun and Loretta supersequences are dominated by carbonaceous shale, stromatolitic dolostone, and turbiditic sandstone and siltstone of the Mount Isa Group **[Figure 2.3]** (Domagala *et al.*, 2000; Page *et al.*, 2000; Southgate *et al.*, 2000). The lithostratigraphy of the Mount Isa Group includes the 1668±8 Ma Moondarra Siltstone (Southgate *et al.*, 2000), 1663±3 Ma Breakaway Shale (Page *et al.*, 2000; Southgate *et al.*, 2000), Native Bee Siltstone, 1652±7 Ma Urquhart Shale (Page and Sweet, 1998; Page *et al.*, 2000), Spear Siltstone, 1648±3 Ma Kennedy Siltstone (Page *et al.*, 2000), and 1648±3 Ma Magazine Shale (Page *et al.*, 2000). The Mount Isa Cu-Pb-Zn(Ag) deposit is hosted within the Urquhart Shale unit.

A series of short-lived shallow marine incursions have also been identified in the Isa Superbasin (Southgate *et al.*, 2000). Crustal extension was interrupted prior to the formation of oceanic crust by episodes of shortening and regional low-pressure high-temperature metamorphism during the Isan Orogeny (Betts *et al.*, 2006; Foster and Rubenach, 2006).
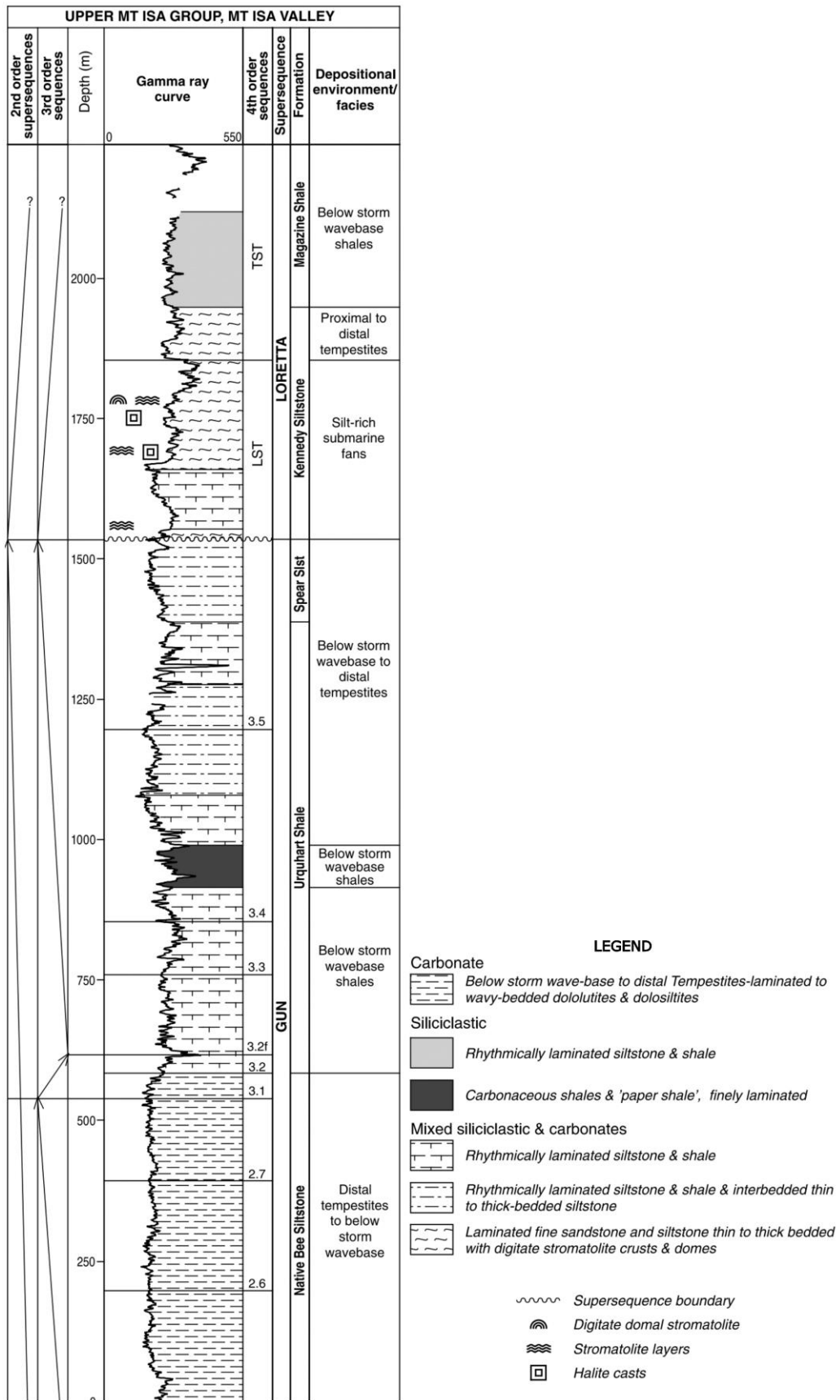
Figure 2.3: Composite chart of sequence, formation, and depositional environment in the Mount Isa Valley. From Domagala *et al.* (2000).

2.3 Deformation

The Western Succession of the Mount Isa Inlier has undergone a long and complex deformation history. Multiphase deformation during the Isan Orogeny is recorded in the western Mount Isa Inlier as a minimum of five deformation events (D1-D5) **[Figure 2.4]**.

2.3.1   D1

The 1610±13 Ma (Rb-Sr dating; Page and Bell, 1986) D1 event was initially interpreted as a large-scale north to south directed thrust complex, producing local east-west oriented faults and an S1 axial planar cleavage (Bell, 1983, 1991; Perkins, 1984; Swager, 1985; Winsor, 1986; Page and Bell, 1986; Blake, 1987; Bell *et al.*, 1988; Bell and Hickey, 1998; Perkins *et al.*, 1999; Davis, 2004; Wilde, 2011). The tectonic transport in the Leichhardt River Fault Trough was interpreted to be over distances greater than 200 km (Bell, 1983; Blake, 1987). However, O'Dea and Lister (1995) and O'Dea *et al.* (1997a, 1997b) dismissed the thrust duplex theory and have instead shown D1 produced east-west oriented reverse faults as a result of north-south shortening of previous syn-rift normal faults.

Near vertical foliation, parallel to bedding (Winsor, 1986) is recorded, with a north-south trending mineral elongation lineation (Bell, 1991). Swager (1985) identified S1 seams in the Urquhart Shale which are sub-perpendicular to bedding. D1 extension veins are also observed in the Urquhart Shale, with two possible sets, one at a small angle to bedding and a second at a high angle (Swager, 1985). Regional metamorphism during this phase of deformation is recorded up to amphibolite facies in the inlier (Blake, 1987).
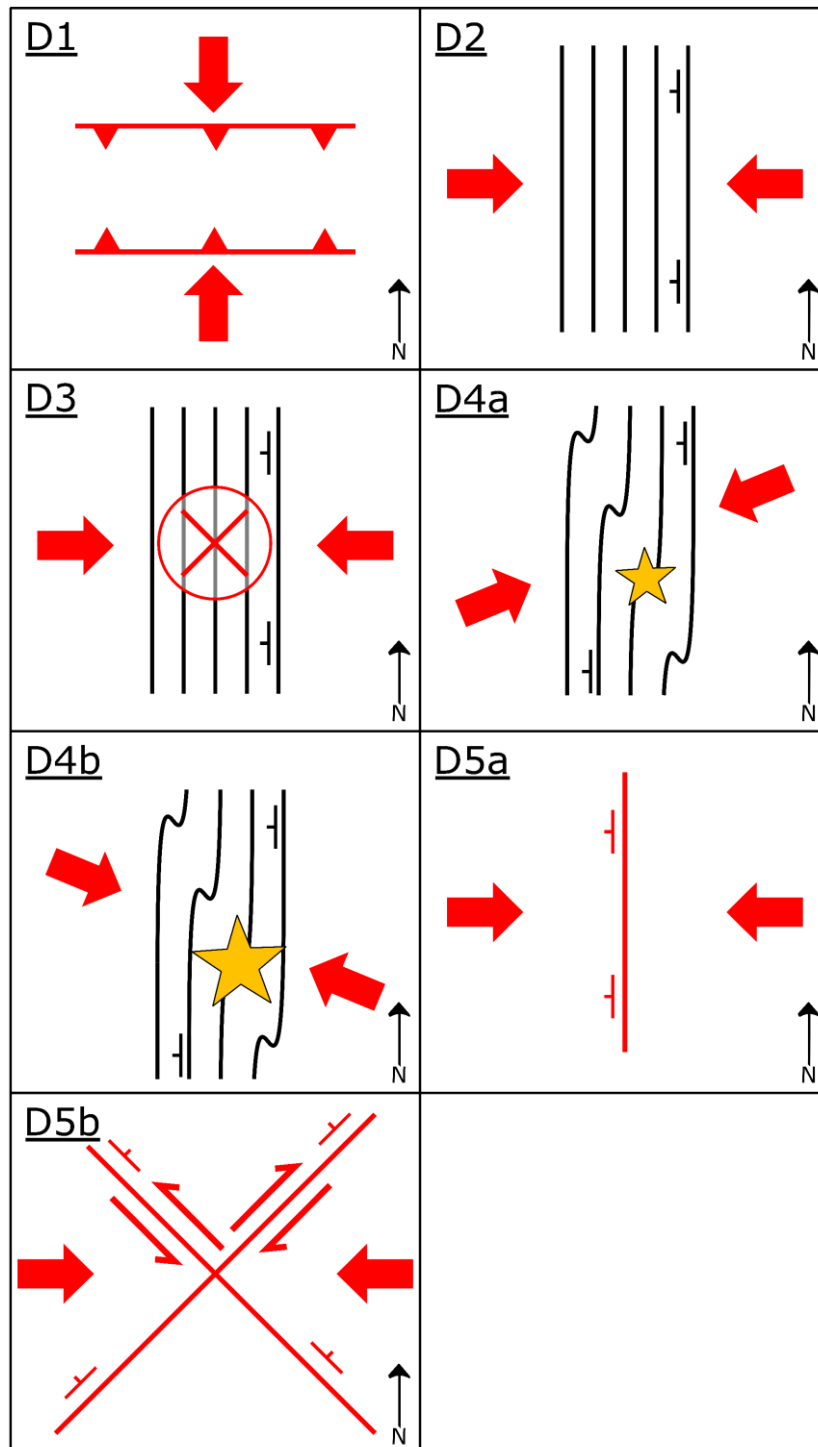
Figure 2.4: Summary of deformation events from the previous literature, shown in map view (Perkins, 1984; Swager, 1985; Bell *et al.*, 1988; O'Dea and Lister, 1995; O'Dea *et al.*, 1997a, 1997b; Davis, 2004; Miller, 2007; Wilde, 2011). **D1** – localised reverse reactivation of normal faults as a result of north-south shortening; **D2** – east-west shortening and peak metamorphism; **D3** – top to the east shear, weakly developed at Mount Isa Mine; **D4a** – ENE-WSW shortening and mineralisation at Mount Isa; **D4b** – WNW-ESE shortening and mineralisation at Mount Isa as introduced and described by Miller (2007); **D5a** – top to the east transport direction on west-dipping reverse faults; **D5b** – conjugate sinistral-reverse and dextral-reverse faults with top to the east or west transport directions consistent with continued east-west shortening.

2.3.2   D2

D2 involved east-west shortening, creating macroscopic north-south striking upright folds with gently plunging regional anticlines and synclines (Bell, 1983; Perkins, 1984; Swager, 1985; Page and Bell, 1986; Blake, 1987; Bell *et al.*, 1988; Bell and Hickey, 1998; Perkins *et al.*, 1999; Davis, 2004; Wilde, 2011). At Mount Isa Mine, a subvertical S2 axial planar foliation is generally bedding parallel within the Mount Isa Group (Swager, 1985; Wilde, 2011). Dolomite filled D2 extension veins formed at high angles to bedding and are truncated against bedding planes and contain fibres that are sub-parallel to S2 (Swager, 1985; Wilde, 2011). The S2 cleavage rarely crenulated S1 (Bell, 1983) and is variably developed in the mine (Perkins, 1984). A steeply south pitching stretching lineation (L2) is observed in the region (Bell and Hickey, 1998). The D2 event is responsible for the steep (~65°) westerly dip seen in the mine area (Wilde, 2011) and refolds D1 folds (Bell, 1983). Peak metamorphism is recorded during D2 prograde metamorphism up to amphibolite facies in the inlier.

Early dating of D2 yielded ages of 1532±7 Ma from biotite formed during large-scale fracture-controlled calcite-Fe oxide alteration of metabasalts and locally associated U mineralisation east of Mount Isa (Page, 1993a, 1993b; Connors and Page, 1995). Other ages of D2 in the west of the inlier have been calculated as 1550 Ma (Blake, 1987) and 1544 ± 12 Ma (Page and Bell, 1986). An age of 1534 Ma (^{40}Ar/^{39}Ar dating; Perkins *et al.*, 1999) approximates prograde metamorphism and D2 deformation in the Mount Isa area. More recent studies have produced ages of ca. 1575 Ma which are consistent with D2 ages from the Eastern Fold Belt (Duncan *et al.*, 2006).

2.3.3   D3

D3 of Davis (2004; D2.5 of Bell and Hickey, 1998) is observed as sub-horizontal axial planes with reactivation and intensification of the existing S2 fabric by top to the east shear and rotation of S2 into more gently dipping orientations (Bell and Hickey, 1998). Sub-horizontal crenulations on a microscopic scale occur within cordierite porphyroblasts west of the Mount Isa Fault and against zones of silicification and dolomitisation within the Mount Isa mine (Perkins, 1997; Bell and Hickey, 1998). This event is generally weak and spatially localised, being poorly developed at Mount Isa Mine (Perkins, 1997; Bell and Hickey, 1998).

2.3.4   D4a

D4a (Davis, 2004; Miller, 2007; Wilde, 2011 and previously D3) locally formed NNW-SSE striking fold zones with sub-vertical axial planes as a result of ENE-WSW shortening (Perkins, 1984; Swager, 1985; Bell *et al.*, 1988; Bell and Hickey, 1998; Davis, 2004; Wilde, 2011). The axial planes rotate to a northwest strike in the north of the mine (Davis, 2004). This event is confined to narrow zones, as opposed to the D2 deformation event (Wilde, 2011). Deformation is typically confined to 10-20 m wide fold zones in the Urquhart Shale, which are locally as much as 100 m wide. The Mount Isa Fold found at the north end of the mine is the largest of these F4 fold zone (Davis, 2004). Most folds in the mine belong to this event, which has been dated to 1510±13 Ma (Page and Bell, 1986).

An S4 fabric sub-parallel to S2 is observed as a slaty cleavage in dolomitic shale and as a crenulation cleavage in black shale lithologies (Bell, 1983; Swager, 1985). Due to the relative sub-parallelism between the S2 and S4, reactivation and intensification of the existing S2 allowed some strain to be accommodated during D4a (Bell and Hickey, 1998). Axial plane

foliation S4 also developed in areas where D3 has significantly reoriented the S2 fabric (Bell and Hickey, 1998). Where S4 is present, it forms a pervasive fabric containing a steeply south pitching stretching lineation (Bell and Hickey, 1998). Wilde (2011) noted that D4a resulted in reactivation of favourably oriented faults with a sinistral strike-slip movement. $^{40}Ar/^{39}Ar$ dating of Perkins *et al.* (1999) indicate a transition from regional metamorphism and ductile D2 folding to a major event of regional scale flow of NaCl-rich brines associated with transitional ductile to brittle D4a deformation.

No evidence exists for Cu ore prior to D3 (Wilde, 2011), with mineralisation at some point post-D3 and probably post-dating the peak of metamorphism (Perkins *et al.*, 1999). Most authors associate the D4a deformation with the brecciation and Cu mineralisation event (e.g. Smith *et al.*, 1978; Perkins, 1984, 1997; Swager, 1985; Bell and Hickey, 1998; Davis, 2004; Wilde, 2011). Swager (1985) associated dolomite breccia veins with D4a, which are polygonal, crosscutting and/or parallel to S0 veins. Swager (1985) also showed that D4a dolomite and quartz extension veins have fibres that parallel the S4 fabric. S4 cleavages are present in the brecciated shale clasts but are not observed within the breccia itself (Perkins, 1984) and indicates a post-S4 age for the breccias (Perkins, 1984; Swager, 1985; Swager *et al.*, 1987; Bell *et al.*, 1988; Davis, 2004; Miller, 2007; Wilde, 2011).

Davis (2004) argued that fluid flow was facilitated by brecciation caused by differential shearing on opposite sides of the Paroo Fault during D4a. Miller (2007) proposed that linkage of S4 cleavage provided additional permeability for the Cu bearing fluids. The S4 fabric provided a pre-existing anisotropy that facilitated brittle failure, which along with F4 folds, had a strong structural control on the development of breccias (Perkins, 1984; Swager, 1985; Bell *et al.*, 1988; Miller, 2007). Miller (2007) showed that where there was a strong S4

cleavage, the Cu breccia developed by fragmenting the rock by failure along the bedding planes, development of extension veins orthogonal to the slip direction and by failure of the pre-existing S4 cleavages. The three fracture directions rapidly fragmented the rock, resulting in a spatial link between the F4 fold plunge (L_4^0 intersection lineation) and ore shoot plunge (Miller, 2007).

2.3.5 D4b

Although most studies have attributed the Cu mineralisation to the D4a event, Miller (2007) proposed that the majority of the Cu mineralisation occurred during a post-D4a, pre-D5a sinistral-reverse strike-slip event, with a stress field distinct from D4a. This event was left unnamed by Miller (2007), however for ease and clarity has been termed D4b in this thesis and in Williams *et al.* (2023). The D4b event involved a sinistral-reverse slip direction attributed to WNW-ESE shortening.

During a detailed study of the Mount Isa deposit using underground and Leapfrog mapping, Miller (2007) noted the presence of NW-trending structures that were dilated and hosted Cu mineralisation. Miller (2007) proposed that reactivation of these NW-trending D4a structures during D4b resulted in the dilation and fluid focussing at this time. The dilation of these favourably oriented and Cu mineralised structures would occur during sinistral-reverse slip and a D4b event was included in the updated deformation sequence (Miller, 2007).

2.3.6 D5a and D5b

S4 is overprinted by a weak NW-striking crenulation cleavage (Swager, 1985; Bell *et al.*, 1988; Bell and Hickey, 1998), with localised folds (Perkins, 1984; Swager, 1985). Post-D4b

crenulation is restricted to domains in the greenschist basement contact, with kinking of S4 in post-D4b shear zones at higher structural levels.

Some studies have documented post-mineralisation events D5a and D5b (which Miller, 2007 termed D4a and D4b), that overprint the Cu orebodies (Mathias and Clark, 1975; Miller, 2007). The D5a reverse faults and D5b conjugate reverse faults were interpreted to result from continued east-west shortening (Miller, 2007). The D5a faults are described as typically steeply west-dipping structures that parallel the Mount Isa Fault Zone, with most D5a faults showing slip along bedding, with a top to the east transport direction (Miller, 2007). The Buck Quartz Fault is an example of a gently dipping D5a fault (Miller, 2007), which intersects the Paroo Fault beneath the Mount Isa deposit.

The D5a faults are overprinted by later conjugate northwest-trending sinistral-reverse and northeast-trending dextral-reverse strike-slip faults (Miller, 2007). The D5b faults have top to the east and top to the west hangingwall transport directions for the northeast-trending and northwest-trending faults, respectively, consistent with east-west shortening (Miller, 2007). The S48 fault is an example of a NE-trending D5b fault that overprints the Cu mineralisation.

2.4 Deposit Geology

2.4.1 Spatial Distribution

The Cu and Pb-Zn-Ag orebodies are hosted within the Urquhart Shale unit of the Mount Isa Group and are situated on the steeply (~65°) west-dipping limb of a regional D2 anticline **[Figure 2.5]** (Bell *et al.*, 1988). The Pb-Zn-Ag orebodies are generally close to the surface **[Figure 2.5b** and **Figure 2.5c]**, where stratiform galena and sphalerite are hosted within

dolomitic layers (Bell *et al.*, 1988; Cave *et al.*, 2020). The breccia-dominated Cu orebodies are located within a silica-dolomite alteration halo and occupy a deeper level in the Mount Isa system (Perkins, 1984; Swager, 1985; Bell *et al.*, 1988). The Cu orebodies are typically discordant to bedding and interdigitate with the Pb-Zn-Ag orebodies (Perkins, 1984; Swager, 1985; Swager *et al.*, 1987; Bell *et al.*, 1988; Cave *et al.*, 2020). The Cu is separated into two distinct orebody regions, the Enterprise Mine, comprising mainly the 3000 and 3500 orebodies and the X41 Mine with the 1100 and the 1900 orebodies **[Figure 2.5c]**. The largest Cu orebodies (1100, 1900, 3000 and 3500) are adjacent to the Paroo Fault (Davis, 2004). The smaller 200, 500 and 650 are perched orebodies that are distal to the Paroo Fault and have a close association with the Pb-Zn-Ag ore (Davis, 2004; McLellan *et al.*, 2014). This has been used as evidence for a zoned Cu-Pb-Zn-Ag system (Perkins, 1997).
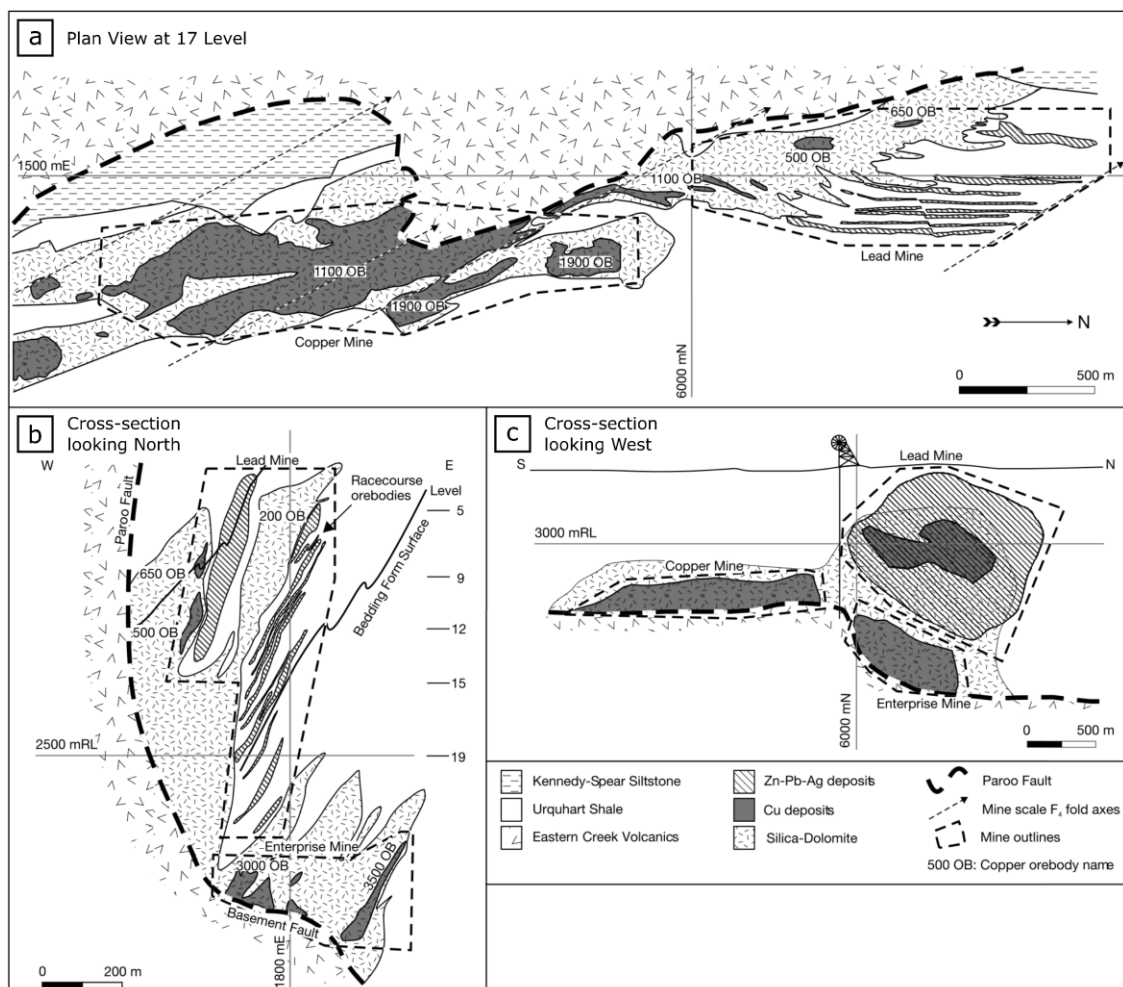
Figure 2.5: (Previous page) Map and cross-sections through the Mount Isa orebodies. **a)** Plan view at Level 17 showing horizontal positions of the silica-dolomite mineralisation and Cu and Pb-Zn-Ag orebodies. **b)** Cross-section viewed looking north at 6510 mN, showing the vertical positions of the silica-dolomite mineralisation and Cu and Pb-Zn-Ag orebodies. The sigmoidal geometry of the Paroo Fault (Basement Contact) and sub-horizontal ramp beneath the Cu mineralisation can be seen. **c)** Cross-section viewed looking West showing the relative positions of the Enterprise and X41 Cu mines and the Pb-Zn-Ag mine. From Davis (2004).

2.4.2 Urquhart Shale

The Urquhart Shale comprises a sequence of finely laminated interbedded dolomitic shales, siltstones, and mudstones that produces a strong west-dipping structural anisotropy (Neudert, 1983; Davis, 2004). The Urquhart Shale is a fine-grained (5-80 µm) dolomitic rock, that can be divided into lithologies based on the ratio of dolomite to mica and carbonaceous material (Swager, 1985; Bell *et al.*, 1988). These lithologies are black shale (<25% dolomite), dolomitic shale (25-75% dolomite) and dolomitic siltstone (>75% dolomite).

Neudert (1983) described a number of facies in the Urquhart Shale and subdivided it into upper and lower units. The lower unit was interpreted as a sabkha or playa depositional environment, whilst the upper unit developed from a distal basin slope to a proximal carbonate slope, eventually progressing to a semi-emergent environment (Neudert, 1983).

Pyrite is present as minor phases in the Urquhart Shale, but also occurs as massive beds of pyritic shales (Swager, 1985; Bell *et al.*, 1988). Thin but laterally extensive tuffaceous beds are used as marker horizons and known as tuff marker beds (Mathias and Clark, 1975; Swager, 1985).

2.4.3 Paroo Fault (Basement Contact)

East of the Mount Isa Fault in the mine vicinity, Eastern Creek Volcanics are separated from the overlying Urquhart Shale by the sigmoidal-shaped Paroo Fault **[Figure 2.5** and **Figure 2.6]** (Davis, 2004; Long, 2010). To the west and east of the deposit the Paroo Fault is sub-vertical, but has an undulating geometry and gentler dip beneath the Cu orebodies where it has also been termed the Paroo Fault ramp and the basement contact (Bell *et al.*, 1988; Davis, 2004). The flat dipping zones of the Paroo Fault are thought to be zones of structural weakness at high angles to the extension direction during the Cu mineralisation, resulting in fluid focussing and brecciation (Bell *et al.*, 1988).

Most studies agree that the Paroo Fault has played some role in the localisation of the Mount Isa orebodies, owing to the position and geometry of the orebodies seemingly emanating from the ramp in the Paroo Fault. Perkins (1997) argued that the sub-horizontal ramp in the Paroo Fault is the fundamental control on the zonal pattern of mineralisation at Mount Isa. It has been proposed that mineralising fluids were transported up and along the Paroo Fault (Long, 2010), however, the Paroo Fault is relatively unmineralised. A more widely accepted argument is that the fluids originated from the Eastern Creek Volcanics and migrated across the Paroo Fault into the Urquhart Shale (Bell *et al.*, 1988), where geochemical and structural controls focused fluids (Heinrich *et al.*, 1993, 1995; Perkins *et al.*, 1999).

In places along the Paroo Fault a graphitic 'mylonite' zone has developed, containing both S2 and S4 cleavages and D4a folds that transect the Paroo Fault (Bell *et al.*, 1988; Miller, 2007). Owing to this, the Paroo Fault is interpreted to be either a syn-basin rift normal fault or a D1 extension fault, both scenarios involving later D2 folding and D4a deformation into the present day geometry (Bell *et al.*, 1988; O'Dea *et al.*, 1997a).
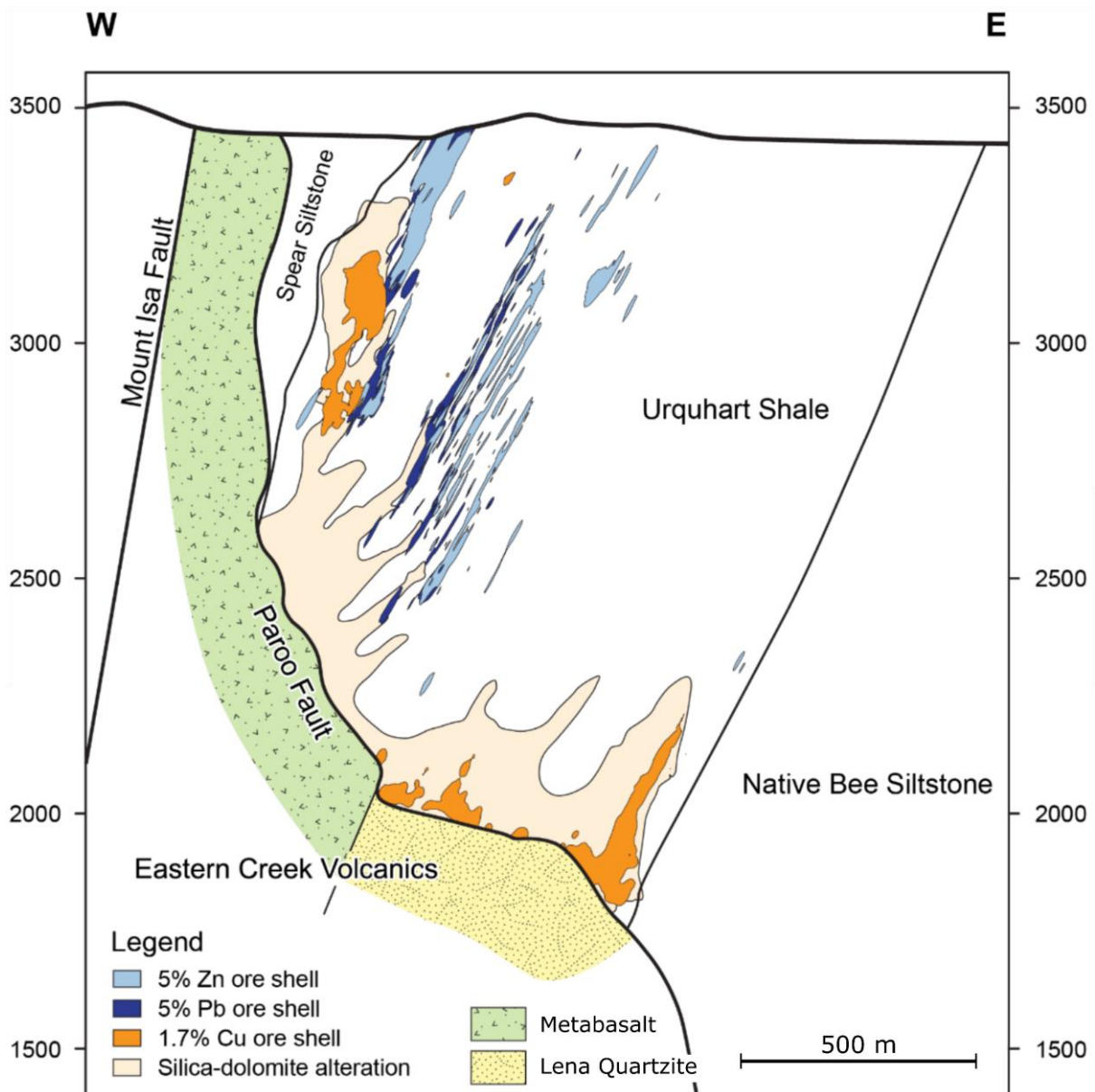
Figure 2.6: Typical cross-section through the south of the mine, showing the silica-dolomite, Cu, Pb and Zn halos. The Eastern Creek Volcanics are depicted below the Paroo Fault with the Lena Quartzite member shown beneath the sub-horizontal section. From Andrew (2020).

2.4.4 Eastern Creek Volcanics

The Palaeoproterozoic Eastern Creek Volcanics (ECV) are a series of continental tholeiitic basalts that were erupted in a continental rift setting (Wilson *et al.*, 1985). This rift system is now expressed as the Leichhardt River Fault Trough (Gregory *et al.*, 2008). The Eastern Creek Volcanics are ~7 km thick and cover an area of approximately 150x40 km (Blake and Stewart,

1992; Gregory, 2006). The Eastern Creek Volcanics are divided into the lower Cromwell Member and upper Pickwick Member, separated by the Lena Quartzite (Blake and Stewart, 1992; Gregory *et al.*, 2008). Both basalt members are made up of 20-50 metre thick dolerite sills and basalt flows that have a massive medium- to coarse-grained base that fines upwards into an amygdaloidal zone capped by flow top breccias (Wilson *et al.*, 1985; Blake and Stewart, 1992; Hannan *et al.*, 1993; Gregory, 2006). Basalt flows are intercalated with sedimentary rocks (Hannan *et al.*, 1993; Gregory *et al.*, 2008).

2.4.4.1 Lena Quartzite

Cessation of the Cromwell basalt eruption led to the deposition of the Lena Quartzite in a period of volcanic quiescence. It is proposed that during this time of reduced volcanic activity, the crustal magma chamber refilled with unfractionated magma, which quickly fractionated resulting in the eruption of the less-evolved Pickwick Member above (Wilson *et al.*, 1985).

The Lena Quartzite is 200-1000 metres thick and is composed of a feldspathic quartzite and orthoquartzite with rare pebbles. At the Mount Isa deposit, the Lena Quartzite dips steeply to the west where it is located beneath the sub-horizontal section of the Paroo Fault **[Figure 2.6]**. The Lena Quartzite has been proposed as a significant fluid flow pathway (Matthäi *et al.*, 2004; Miller, 2007; Andrew, 2020). It has also been tentatively suggested that the Lena Quartzite may in fact be a silicified leached metabasalt.

2.4.4.2 Role of the Eastern Creek Volcanics in Cu Mineralisation

The Eastern Creek Volcanics have long been suggested as the Cu source for the Mount Isa deposit (Wilson *et al.*, 1985; Wyborn, 1987; Hannan *et al.*, 1993; Heinrich *et al.*, 1995; Gregory, 2006; Gregory *et al.*, 2008). This is based on the high Cu content of the Eastern Creek Volcanics (Gregory *et al.*, 2008). The Eastern Creek Volcanics beneath the Cu deposit are

highly sheared and altered, with variable silicification. They are depleted in Ca and Cu, and have extremely low Fe^{3+}/Fe^{2+} ratios (Wyborn, 1987; Hannan *et al.*, 1993), but are rich in Mg chlorite and rutile, with some biotite (Perkins *et al.*, 1999).

Wilson *et al.* (1985) showed that where alteration had taken place, the Eastern Creek Volcanics were significantly depleted in Cu. They suggest that widespread alteration probably liberated vast quantities of Cu from the Eastern Creek Volcanics, which were transported and deposited in reactive carbonate and sulphide lithologies of the Urquhart Shale. Hannan *et al.* (1993) showed that altered mafic rocks of the Eastern Creek Volcanics below the sub-horizontal portion of the Paroo Fault interacted with hydrothermal fluids. Gregory (2006) showed that epidote alteration zones were refractured due to post-metamorphic deformation which allowed oxidised potassium-rich fluids to remobilise copper from the Eastern Creek Volcanics. This lead to deposition of Cu in the overlying reduced sedimentary rocks of the Urquhart Shale (Gregory, 2006). Gregory *et al.* (2008) used Os-isotope signatures to show the Mount Isa Cu ore may have been derived from a fluid mixing through both the Cromwell and Pickwick Members.

2.4.5 Mount Isa Fault

The Mount Isa orebodies are situated in the footwall to the east of the N-S oriented Mount Isa Fault **[Figure 2.6** and **Figure 2.7]**. The Mount Isa Fault is a steeply west-dipping regionally significant feature, as it juxtaposes higher grade amphibolite facies rocks to the west with lower grade greenschist facies rocks to the east (Bell, 1991; Rubenach, 1992; Bell and Hickey, 1998; Perkins *et al.*, 1999; Davis, 2004). Long (2010) argued that the Mount Isa Fault could have been an original basin bounding fault. Alternatively, it has been suggested that the

Mount Isa Fault Zone was active during and after the D2 deformation event (Perkins *et al.*, 1999), with the Mount Isa Fault truncating a D2 anticline south of the mine (Bell, 1991). However, Bell *et al.* (1988) state that the Mount Isa Fault truncates the Mount Isa Fold and Miller (2007) suggests that the Mount Isa Fault zone could be a late post-ore D5a thrust that overprints the earlier architecture associated with Cu.
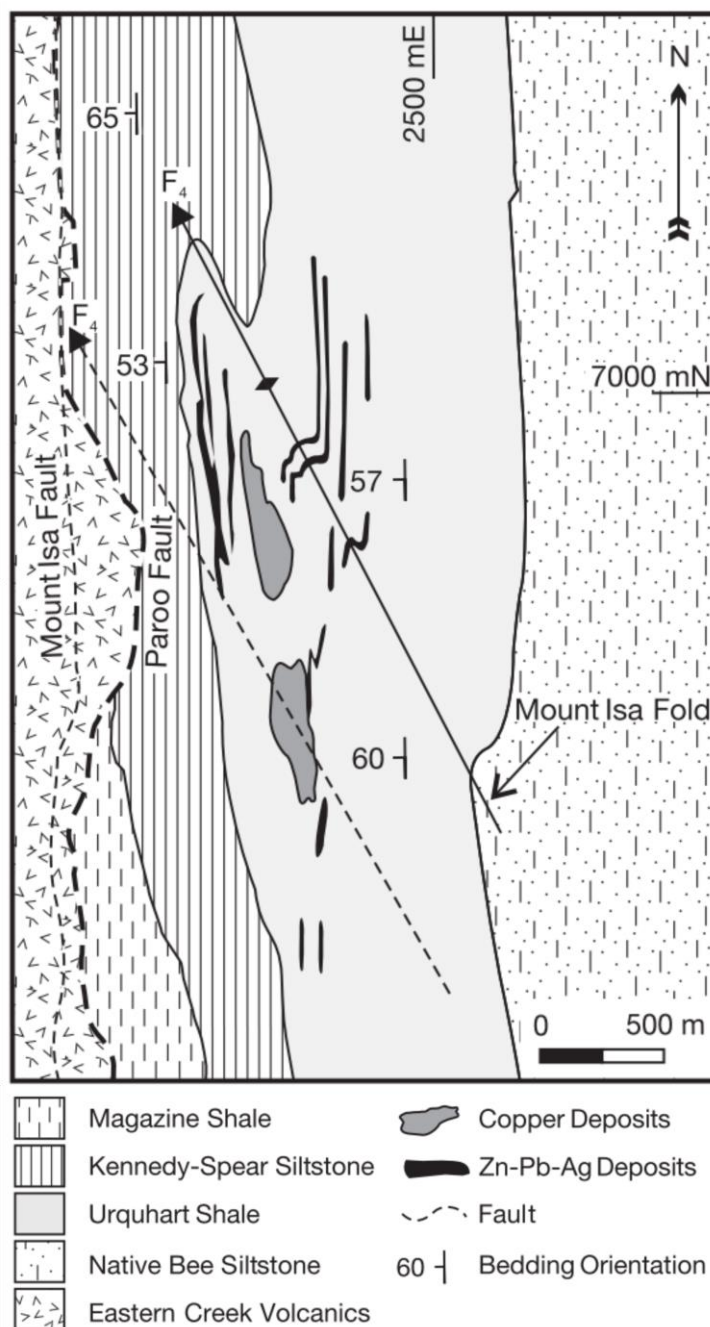
Figure 2.7: Map view of Mount Isa showing the Mount Isa Fault and Mount Isa Fold, with relative positions of the Cu and Pb-Zn-Ag orebodies. From Davis (2004).

2.4.6 Mount Isa Fold

The Mount Isa Fold is the largest fold in the mine and is thought to be D4a in age **[Figure 2.7]** (Perkins, 1984; Page and Bell, 1986; Bell *et al.*, 1988). In the north of the mine, the Mount Isa Fold is a large asymmetrical fold, verging to the east, that can be traced through all levels of the mine (Davis, 2004). The Mount Isa Fold has a wavelength of 200-400 metres and amplitude of 130 metres (Perkins, 1997). The fold has a near vertical short limb and axial plane and trends approximately NW-SE, plunging to the NW (Davis, 2004). The wider zone of folding in the mine, the Mount Isa fold zone, contains both north-south and NW-SE trending axes. Along with the sub-horizontal section of the Paroo Fault, Perkins (1997) considered the western long limb of the Mount Isa Fold as the other major structural control on ore formation.

2.4.7 Alteration and Brecciation

2.4.7.1 Fluid Origin

The Urquhart Shale has been progressively altered and brecciated where it is bounded by the Paroo Fault (basement contact) below. Alteration at Mount Isa is complex and in many cases, the paragenetic relationships between each phase remains unclear (Andrew, 2020). However, an estimated addition of 22.5 Mt of Cu, 43 Mt of S and 200 Mt of SiO_2 to the Mount Isa area during the late metamorphism is associated with the alteration and mineralisation event (Waring, 1990; Waring *et al.*, 1998b). Sparse dolomite ± chalcopyrite veins are the first visible indication of the periphery of the silica-dolomite Cu alteration system (Waring *et al.*, 1998b).

The dolomite associated with the Cu ore in the Mount Isa system is ^{18}O-depleted compared to the background dolomitic shales (Waring *et al.*, 1998a, 1998b). A halo of $\delta^{18}O$-depletion in

visibly unaltered dolomitic shale extends greater than 2 km surrounding visible silica-dolomite alteration and the Cu ore (Waring *et al.*, 1998b). This halo of ^{18}O-depletion extends much further than the visible vein network (Waring *et al.*, 1998b). Waring (1990) noted that the areas of high Cu ore-grades and structures related to the ore forming fluids all coincide with the maximum ^{18}O-depletion.

Saline fluids responsible for the syn- to post-metamorphic Cu mineralisation in the silica-dolomite altered metasediments have unusually high Br/Cl ratios (Heinrich *et al.*, 1993). This ratio is similar to the fluids associated with the fracture controlled carbonate-magnetite alteration of metabasalts up to tens of kilometres away from the mine (Heinrich *et al.*, 1993), implying a common origin for the fluids and a possible link between the regional and deposit scale fluid flow and fluid rock interactions (Heinrich *et al.*, 1993).

It is suggested that after being subjected to greenschist facies temperatures within the underlying Eastern Creek Volcanics, fluids were focused upwards, and south to north, into an extensional site along the Mount Isa fault zone **[Figure 2.8]** (Heinrich *et al.*, 1993, 1995). Interaction with pyrite and carbonaceous meta-dolomites promoted the deposition of the chalcopyrite ore predominantly within the Urquhart Shale (Heinrich *et al.*, 1993, 1995). Waring *et al.* (1998b) showed that a temperature decrease from around 330 °C to 250-300 °C during retrograde metamorphism could cause a transition from a $CaCl_2$ rich brine to a NaCl rich fluid. This change in fluid composition could also facilitate the introduction of Cu into the fluids (Waring *et al.*, 1998b). A simple pH change upon reaction with carbonates may have been sufficient to induce chalcopyrite precipitation (Waring *et al.*, 1998b).
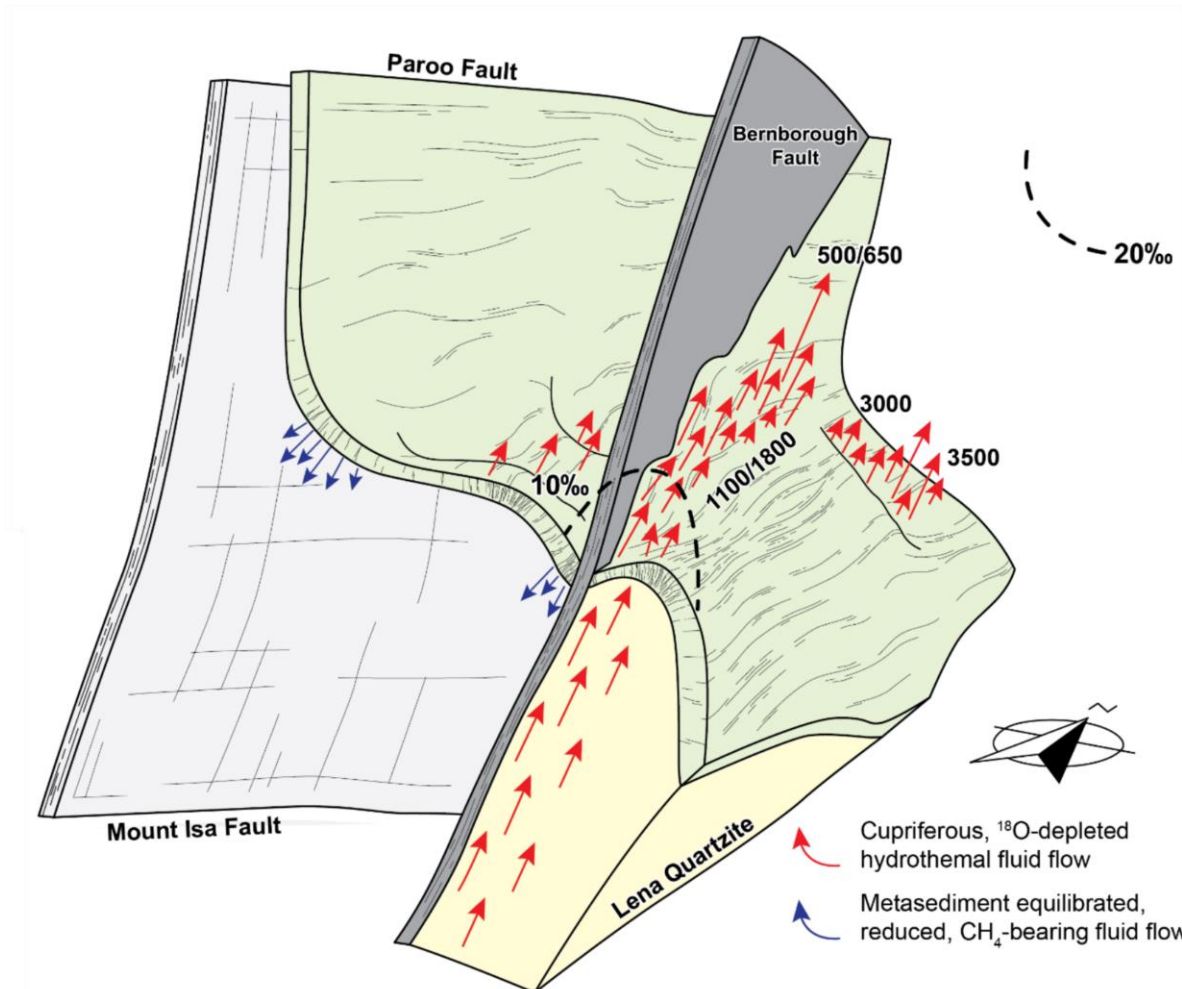
Figure 2.8: Diagram showing the south to north fluid flow pathway for Cu-rich fluids and the Bernborough Fault as the potential deep feeder structure. It has been proposed that the Bernborough Fault focused fluid flow from the underlying Eastern Creek Volcanics to the sites of mineralisation. Bold numbers refer to orebodies. The zone of greatest silica-dolomite alteration is indicated by intense oxygen depletion (10‰). From Andrew (2020).

Waring *et al.* (1998b) noted that the pre-mineralisation pyrite in the Urquhart Shale could have been a source of sulphur which helped localise precipitation. However, they also noted that the Cu ore is found surrounding or adjacent to pyrite rich stratigraphy rather than replacing it. Through detailed mass-balance measurements Waring (1990) indicated that approximately twice the amount of sulphur contained in chalcopyrite was added to the Cu system to form chalcopyrite and additional pyrite. Mixing of pre-existing light sulphur ($\delta^{34}S$ =

2-30‰) with new heavy sulphur ($\delta^{34}S$ = ~20‰) would give the range seen in chalcopyrite (10-16‰) at Mount Isa (Andrew *et al.*, 1989; Waring, 1990; Waring *et al.*, 1998b). This suggests a large amount of sulphur from the diagenetic pyrite was supplied to the Cu ore, but also sulphur availability was not a limiting and critical factor in the precipitation of chalcopyrite (Waring *et al.*, 1998b).

2.4.7.2 Breccia

Copper mineralisation is contained within a zone of mineral alteration, brecciation and veining, known as silica-dolomite **[Figure 2.5** and **Figure 2.6]**. The brecciation occurred in zones of structural weakness where the flat dipping zones of the basement contact are at a high angle to the extension direction (Bell *et al.*, 1988). It has been proposed by Bell *et al.* (1988) that the combined impact of the competency contrast across the basement contact, the stretching direction perpendicular to it and the antithetic shearing above it, resulted in a zone of weakness. In addition, the development of asymmetric folds during D4a generated tensional forces across the subhorizontal section of the Paroo Fault, causing differential movement and dilation within the Urquhart Shale and within F4 fold hinges and short limbs (Bell *et al.*, 1988). It has been suggested that this event caused a large drop in fluid pressure, resulting in the explosive fracturing and local brecciation of the Urquhart Shale, allowing the ingress of fluids to form the silica-dolomite alteration and Cu mineralisation (Perkins, 1984; Bell *et al.*, 1988; Cave *et al.*, 2020).

Breccia veins commonly crosscut bedding at a high angle, with some bedding parallel branches (Bell *et al.*, 1988). The breccia veins also show evidence of D4a effects including strong S4 development against their margins, with pinch and swell structures and dissolution of the vein walls (Swager, 1985; Bell *et al.*, 1988). These breccia veins locally contain variably

rotated shale clasts in a coarse dolomite matrix (Bell *et al.*, 1988). Perkins (1984), however, noted that the rotated shale fragments are exceptional occurrences, with the majority of clasts being relatively unrotated. Despite the shale clasts commonly containing fine-grained pyrite, Cave *et al.* (2020) noted that there are no examples of stratabound sphalerite and galena being brecciated and overprinted by silica-dolomite. This provides evidence for a coeval chalcopyrite, galena, and sphalerite timing.

Swager (1985) identified prominent breccia veins consisting of coarse dolomite (± quartz) with concentrations of chalcopyrite ± pyrrhotite and/or pyrite along one or both vein walls. Swager (1985) used the presence of breccia veins in the Urquhart Shale around the silica-dolomite to suggest that channelling of fluids through selected veins occurred over large distances and there may have been several fluid pulses.

2.4.7.3 Silica-Dolomite

Variably brecciated silica-dolomite produces four main rock types that reflect silicification ('siliceous shale' and 'brecciated and fractured siliceous shale') and dolomitisation ('recrystallised shale' and 'irregularly brecciated and recrystallised shale') of the host rock (Clark, 1968; Mathias and Clark, 1975; Knights, 1976; Perkins, 1984; Miller, 2007). Perkins (1984) and Swager (1985) showed that silicification and dolomitisation were coincident with D4a.

The siliceous alteration is found within the core of the deposit **[Figure 2.5** and **Figure 2.6]**, known as the siliceous inner core, and whose location is associated with the majority of Cu mineralisation **[Figure 2.5]** (Perkins, 1984). Mineralisation also occurs outside of the siliceous inner core, within the dolomitic breccias (Miller, 2007). The silica-dolomite alteration and brecciation are generally understood to lay the groundwork for the subsequent Cu

mineralisation (Perkins, 1984; Swager, 1985; Bell *et al.*, 1988; Miller, 2007; Cave *et al.*, 2020).

Dolomite overprints quartz, with both quartz and dolomite dissolution interpreted to have occurred during chalcopyrite mineralisation (Wilde *et al.*, 2006; Wilde, 2011). Fine-grained pyrite, silica-dolomite, calcite, quartz, and coarse-grained pyrite all pre-date chalcopyrite (Gulson *et al.*, 1983; Perkins, 1984; Cave *et al.*, 2020).

2.4.7.4 Pyrrhotite and Chalcopyrite

The sulphides that are predominantly associated with the silica-dolomite are chalcopyrite, pyrite, cobaltite and pyrrhotite (Mathias and Clark, 1975). Swager (1985) identified chalcopyrite extensively replacing the coarse dolomite in the early syn-D4a breccia veins. Similarly, Swager (1985) also identified chalcopyrite ± quartz replacing both the D2 vein dolomite and D3 overgrowths.

Chalcopyrite accompanies pyrrhotite, with the pyrrhotite forming a halo zone around and within the silica-dolomite (Perkins, 1984; Swager, 1985). Chalcopyrite is the most prevalent Cu ore mineral found at Mount Isa and is commonly considered to be coeval with pyrrhotite (e.g. Swager, 1985; Cave *et al.*, 2020), forming replacive growths across all generations of veins and microstructures (Perkins, 1984; Miller, 2007). The pyrrhotite is most prevalent in the zone between the Pb-Zn orebodies and Cu mineralisation (Perkins, 1984), with only minor chalcopyrite occurring in pyrrhotite dominated lithologies (Cave *et al.*, 2020).

2.4.7.5 Pb-Zn-Ag

The dominant Pb and Zn minerals are galena and sphalerite, respectively, which occur as stratiform bands that replace stratabound fine-grained pyrite-rich and dolomitised shale layers or occur as infill around highly-deformed carbonaceous shales (Grondijs and Schouten,

1937; Perkins, 1997; Cave *et al.*, 2020). At the periphery of the Pb-Zn-Ag system, galena and sphalerite replace discordant pre-mineralisation silica-dolomite alteration (Cave *et al.*, 2020).

Davis (2004) showed that the highest Pb/Zn values are proximal to the Cu orebodies. However, when grade contours are plotted, Zn mineralisation is situated further from the Cu ores than the Pb, with Ag correlating with the Pb (Davis, 2004). This may suggest a temperature gradient control on the deposition of Cu$\rightarrow$Pb(+Ag)$\rightarrow$Zn (e.g. Cave *et al.*, 2020).

2.4.7.6 Paragenesis

Fine grained pyrite is the earliest mineralisation **[Figure 2.9]** and is possibly diagenetic (Painter *et al.*, 1999) or replacive (Perkins, 1998). S2 cleavages are truncated and overgrown by early dolomite porphyroblasts, which are truncated themselves by some of the S4 cleavages (Perkins, 1984). In other cases, the S4 cleavages are truncated by the dolomite porphyroblasts and are perceived to be consistent with a syn-D4a timing of the dolomite (Miller, 2007). Phyllosilicate minerals grew at the silicification stage during early syn-D4 and are believed to be coeval with the silica-dolomite alteration and introduction of Cu during D4 (Swager *et al.*, 1987). Multiple phases of quartz veins occur throughout the deposit (Miller, 2007), however some quartz fibres are axial planar to D4a fold hinges, implying a phase of quartz growth which was syn-D4a (Perkins, 1984). Although S4 cleavages have been observed in the previously mentioned rotated shale clasts, the S4 cleavages are not seen in the silica-dolomite and chalcopyrite matrix (Perkins, 1984). Miller (2007) used this as evidence to state that the timing of brecciation was in fact post-S4.

Cave *et al.* (2020) showed that silica-dolomite predates minor calcite veining and siderite. Coarse-grained pyrite has been found in calcite veins, silica-dolomite and siderite dominant lithologies (Cave *et al.*, 2020). However, the coarse-grained pyrite commonly includes silica-

dolomite pressure shadows and has evidently experienced some strain. Arsenopyrite commonly rims and forms around the coarse-grained pyrite (Cave *et al.*, 2020). Chalcopyrite and pyrrhotite envelopes and infills cracks in the coarse-grained pyrite and arsenopyrite (Cave *et al.*, 2020). Cave *et al.* (2020) showed that sphalerite and galena occur replacing silica-dolomite and calcite, as inclusions in pyrrhotite and infill in coarse-grained pyrite and arsenopyrite. This has been used as evidence to suggest that the timing of sphalerite and galena is similar to the chalcopyrite and pyrrhotite mineralisation (Perkins, 1997). Other gangue minerals associated with the Cu mineralisation include biotite, chlorite, K-feldspar, apatite and cobaltite (Cave *et al.*, 2020).

Mineral	Pre-Mineralisation	Mineralisation
Pyrite (F.G)	▬	
Dolomite	▬	
Silica-Dolomite	▬	
Calcite	▬	
Siderite	▬	
Pyrite (C.G)	▬	
Arsenopyrite	▬	
Sphalerite		▬
Galena		▬
Apatite		▬
Chlorite		▬
K-Feldspar		▬
Freibergite		▬
Tetrahedrite		▬
Pyrrhotite		▬
Chalcopryite		▬
Biotite		▬
Cobaltite		▬

Figure 2.9: Summary paragenetic chart based on the observations of Cave *et al.* (2020).

As chalcopyrite dissolves and replaces earlier phases, the timing of chalcopyrite post-dates both the dolomite and quartz. Chalcopyrite forms replacive growths across all generations of veins and microstructures, implying a very late D4a precipitation (Perkins, 1984; Miller, 2007).

In some areas, dolomite veins which truncate and sometimes displace D4a folds are replaced by chalcopyrite (Perkins, 1984). Perkins (1984) observed that, once precipitated, chalcopyrite does not redissolve and reprecipitate, implying no remobilisation of the Cu occurs.

2.4.8 Cu Orebodies

The Cu orebodies occur as large bodies (10's to 100's metres) of chalcopyrite-rich breccia which are hosted within silica-dolomite alteration halos **[Figure 2.5]** (Perkins, 1984). The Cu orebodies were interpreted to be associated with NNW-plunging F4 fold hinges which appear to control their geometry, orientation and development **[Table 2.1]** (Perkins, 1984; Bell *et al.*, 1988; Davis, 2004; Miller, 2007). The Cu orebodies are located in the short limbs and hinges of asymmetrical folds (Davis, 2004). Some of the orebodies have developed within the axial plane of F4 folds, paralleling the S4 cleavage, and transecting the west-dipping bedding surfaces (Bell *et al.*, 1988; Miller, 2007). In general Cu grade-contours parallel the F4 fold hinges and silica-dolomite boundaries (Davis, 2004).

Davis (2004) argued that strain localisation within less competent units played an important role in the formation of the deposits, as they allowed fluids to access only specific parts of the rock, producing stratiform ores at low grades. However, structural heterogeneities within those same units concentrated metals into high-grade shoots (Davis, 2004). Recent investigations have potentially shown the presence of a deep feeder structure relating to the NNW-trending Bernborough Fault **[Figure 2.8]** (Andrew, 2020). A south to north directed hydrothermal fluid flow pathway has been determined through mineralogical and geochemical alteration patterns (Waring, 1990; Andrew, 2020), resulting in the multiple Cu orebodies that are detailed below.

Orebody	Length (m)	Width (m)	Vertical Extent (m)	Plunge (°)	Azimuth (°)
200	300	50	250	-	~000
500	1300	230	500	25	000
650	320	30	450-500	40	340
1100	2330	530	700	~0	~000
1900N	440	80	250	~0	~000
1900S	470	160	300	~0	~000
3000	1200	290	250	32	324
3500	1340	260	500	35	339

Table 2.1: Table of Cu orebodies showing their dimensions and orientations.

2.4.8.1 200, 500 and 650 Orebodies

The 500 and 650 orebodies are found in the western part of the Pb-Zn mine in the structural hanging wall of the Pb-Zn-Ag deposit (Davis, 2004). Davis (2004) suggested that the 500 and 650 orebodies are bifurcated branches of the same orebody based on the distribution of Cu ore in level plans. The highest Cu grades and greatest combined widths are found where the 500 and 650 orebodies intersect (Davis, 2004). The 500 orebody is a vertically dipping flattened cigar shape, plunging 25° north, whilst the 650 orebody plunges 40° towards 340°, extending 500 metres down plunge (Davis, 2004). The 200 Cu orebody is lower grade and situated within the centre of the Pb-Zn-Ag mine and is found along the WSW enveloping surface of the Racecourse Pb-Zn-Ag domain (Davis, 2004). Davis (2004) noted that the 200, 500 and 650 orebodies have similar geometries to the Pb-Zn-Ag ores.

2.4.8.2 1100 and 1900 Orebodies

In the south, the mine is dominated by the 1100 and 1900 Cu orebodies (Davis, 2004). First noted by Perkins (1984), the 1100 orebody is located on the synclinal hinge and short limb of a large fold at the contact between the Mount Isa Group units and the Eastern Creek Volcanics. These D4a folds seemingly control the overall geometry of the 1100 and 1900 orebodies (Bell *et al.*, 1988; Davis, 2004).

The Paroo Fault (basement contact) forms an almost flat to very gently dipping structure beneath the 1100 and 1900 orebodies. Both orebodies show local plunge variations that broadly parallel the intersection between the shale bedding and the underlying Eastern Creek Volcanics. As a result, these orebodies have a sub-horizontal plunge, with a long-axis that extends roughly north-south. The 1100 and 1900 orebodies dip moderately to the WSW, an approximate 15° sinistral rotation from the orientation of bedding (Miller, 2007). The 1100 orebody narrows to the north where the adjacent 1900 orebody has developed (Law, 1999). The 1900 orebody developed adjacent to where the northern part of the 1100 orebody narrows (Law, 1999). In some studies the 1900 orebody is further separated into north and south arms (Long, 2010; Valenta, 2018).

2.4.8.3 3000 and 3500 Orebodies

The 3000 orebody is North-South striking with high grade shoots in an en echelon array (Davis, 2004). The enveloping surface is NNW-SSE striking, with an overall plunge of the orebody of 32° towards 324° and is located on the southern long limb of the Mount Isa fold (Davis, 2004). Individual shoots extend up-dip of bedding 220 metres from the Paroo Fault and are up to 80 metres wide (Davis, 2004). Where the shoots are close to the Paroo Fault they are generally gently dipping to the west and become steeper up-dip (Davis, 2004).

The 3500 orebody is found on the northern long limb of the Mount Isa fold and located to the east of the 3000 orebody, where it is around 500 metres long and North-South striking (Davis, 2004). The overall plunge of the 3500 orebody is 35° towards 339° and dips steeply to the west, extending up-dip of bedding around 320 metres (Davis, 2004). It has been suggested that the similar distances (~200 m) between the 1100 and 1900 orebodies and the 3000 and 3500 orebodies may be related to the wavelength of folds in the mine (Law, 1999).

2.4.9 Pb-Zn-Ag Orebodies

At the northern end of the Mount Isa system, above the Cu orebodies, the Pb-Zn-Ag mineralisation occurs in over 30 stratiform lenses **[Figure 2.5, Figure 2.6** and **Figure 2.7]** (Valenta, 2018), resulting in approximately 10 orebodies (Cave *et al.*, 2020). The Pb-Zn-Ag orebodies are located at least 100 metres up-dip from the Paroo Fault (Cave *et al.*, 2020), with the highest grades of mineralisation coinciding with the hinges and short limbs of D4a folds (Davis, 2004).

Individual Pb-Zn-Ag orebodies are sheetlike bodies with long-axes up to 1200 metres long and plunging between 23°-60° towards 323°-348° (Davis, 2004). The ores typically comprise massive sheetlike conformable sulphide bands and breccias up to 40 cm thick and interlayered with unmineralised Urquhart Shale (Davis, 2004). Bedding in the mineralised layers can be intensely folded (Davis, 2004).

The Pb-Zn-Ag orebodies are separated into two groups, the Black Star and Racecourse domains (Davis, 2004). The Racecourse domain comprises NNE-SSW to north-south striking Pb-Zn-Ag orebodies, each of which are typically 30 metres across strike and 600 metres along strike (Davis, 2004). The orebodies are arranged in an en echelon array with NNW-SSE striking enveloping surfaces. The Black Star domain strikes north-south, with a maximum across strike width of 200 metres, extending for more than 1200 metres along strike (Davis, 2004). High-grade mineralisation terminates in the short limb of the 650 fold in the south and near the Mount Isa anticline to the north (Davis, 2004).

2.4.10 Buck Quartz Fault

Miller (2007) recorded two sets of post-ore faults which he termed D4a and D4b [now D5a and D5b; **Figure 2.4**]. The D5a faults are typically west-dipping, whilst the later D5b faults are NW and NE trending sinistral-reverse and dextral-reverse faults, respectively (Miller, 2007). Miller (2007) interpreted the Buck Quartz Fault to be a major example of the west-dipping D5a faults.

The Buck Quartz Fault follows the sub-horizontal contact between the Cu ore and the underlying greenschists (Eastern Creek Volcanics) over a large area within the southern part of the mine (Bell *et al.*, 1988). The Buck Quartz Fault is composed of a relatively thick quartz filling (up to 10's metres), but loses the thick quartz filling where it cuts down into the underlying Eastern Creek Volcanics (Bell *et al.*, 1988). The Buck Quartz Fault has produced drag of the S4 cleavage by late eastward directed movement (Miller, 2007). At least the last stages of movement on the Buck Quartz Fault deformed some of the Cu ore (Perkins, 1997). Some transverse faults such as the northeast-striking S48 dextral reverse fault are observed truncating and offsetting the Buck Quartz Fault (Miller, 2007).

2.4.11 Other Post-Ore Faults

According to Miller (2007) the NW- and NE-trending D5b faults are post-Buck Quartz in age. These faults are observed mainly in the region of the Enterprise mine, but some (e.g. O52 Fault) are also mapped in the X41 mine (Miller, 2007). Miller (2007) associated the NW-trending faults with extensive quartz veining in some areas and that these faults also control the geometry of the lower basement contact beneath the 3500 orebody. The late-stage NE-

trending faults are associated with reverse and dextral offsets and include the S48, T45 and M44 faults **[Figure 2.10]**.

The S48 fault has a strike of 020°-040°, with a net horizontal shift of the northern block of 200 metres to the northeast (Bell *et al.*, 1988). Plans of the 19 Level in Perkins (1984) show the S48 fault dextrally offsetting the 1100 orebody by approximately 200 metres. North of the S48 fault, the Buck Quartz Fault has been described as having a displacement of only 70 metres and a tear fault relationship has been used to account for this change (Bell *et al.*, 1988). Bell *et al.* (1988) described these fault relationships as postdating the ore.
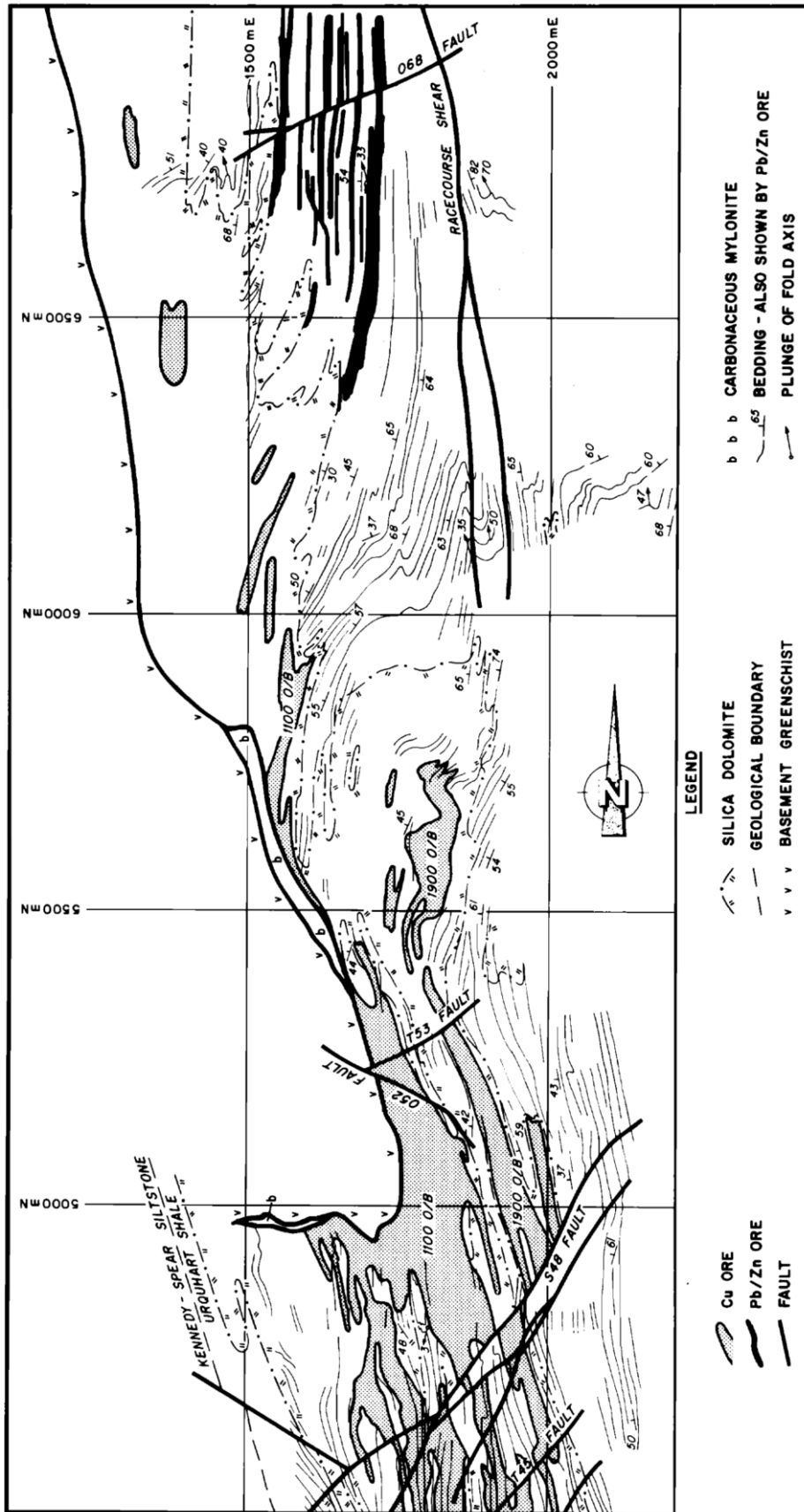
Figure 2.10: Plan of the 17 Level showing the Pb-Zn-Ag orebodies predominantly in the north and the Cu orebodies in the south. Post-mineralisation faults crosscut and offset some orebodies. From Perkins (1984).

2.5. Syngenetic vs Epigenetic Origin – Previous Genetic Models

As shown in previous sections, there is a close spatial association between the Mount Isa Cu and Pb-Zn-Ag mineralisation (Cave *et al.*, 2020) and the origins of both have been much debated, with many studies being published (Grondijs and Schouten, 1937; Murray, 1961; Stanton, 1962, 1963; Kelly, 1967; Smith and Walker, 1971; Mathias and Clark, 1975; Finlow-Bates and Stumpfl, 1979; Perkins, 1984). The ore genesis and relative timings of both the Pb-Zn-Ag and Cu mineralisation have been attributed to either a syngenetic or an epigenetic origin, with at least three different metallogenic models **[Figure 2.11]**: (1) syn-sedimentary Pb-Zn-Ag and Cu mineralisation **[Figure 2.11b]** (Stanton, 1962, 1963; Mathias and Clark, 1975; Finlow-Bates and Stumpfl, 1979; Robertson, 1982; McGoldrick and Keays, 1990); (2) syn-sedimentary Pb-Zn-Ag overprinted by epigenetic Cu mineralisation **[Figure 2.11a]** (Murray, 1961; Kelly, 1967; Smith and Walker, 1971; Gulson *et al.*, 1983; Perkins, 1984); (3) epigenetic Cu-Pb-Zn-Ag mineralisation **[Figure 2.11c]** (Grondijs and Schouten, 1937; Perkins, 1997; Davis, 2004; Cave *et al.*, 2020). The most recent study on this topic, by Cave *et al.* (2020), showed convincing evidence that the Mount Isa deposit formed by epigenetic and coeval Cu-Pb-Zn-Ag mineralisation.
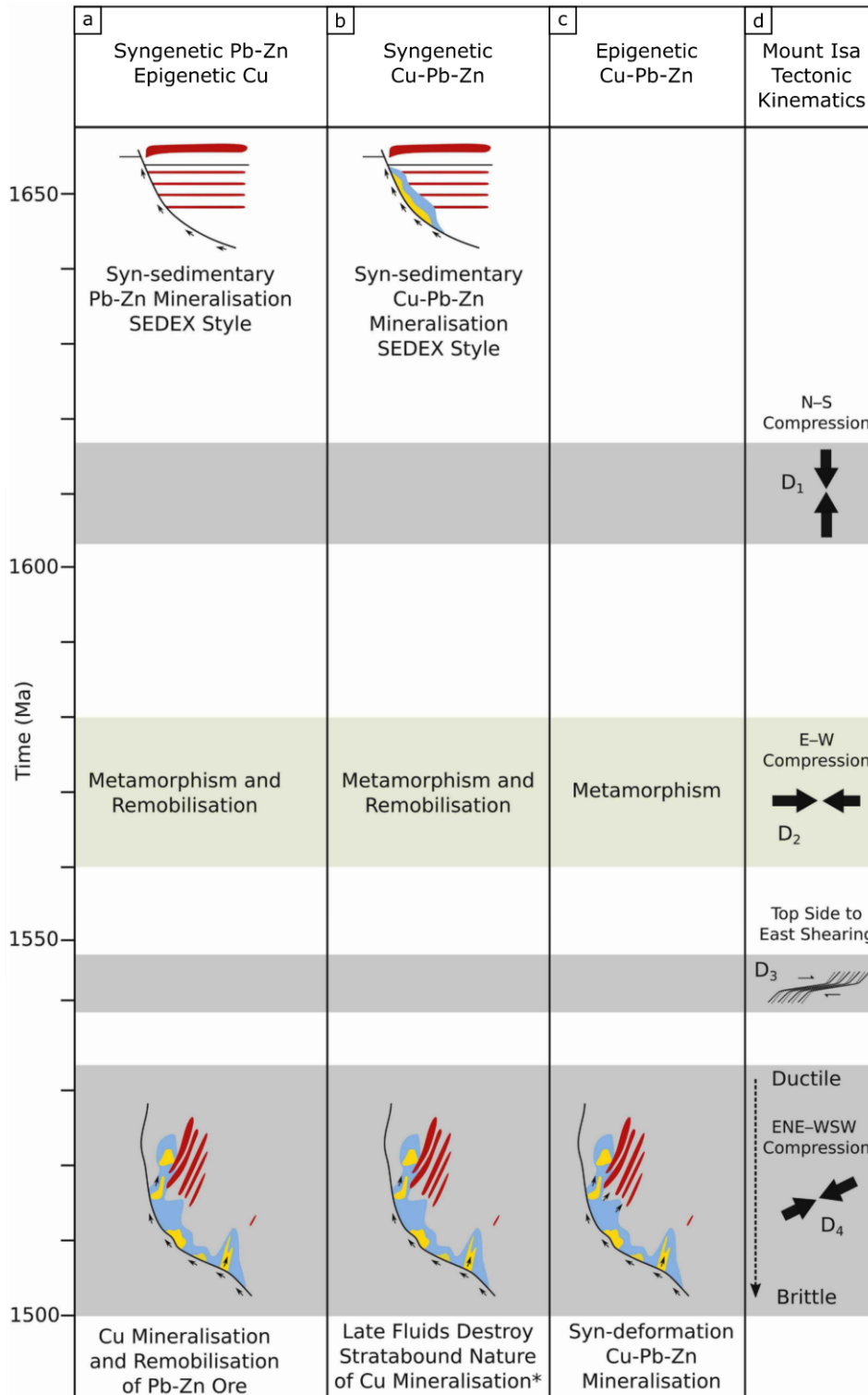
Figure 2.11: Schematic diagrams showing the metallogenic models described in this section. From Cave *et al.* (2020).

2.6 Final remarks

A synthesis of the literature on the deformation history of Mount Isa has been presented in this chapter. The existing deformation scheme for the Mount Isa deposit has been altered to accommodate the addition of D4b, the unnamed deformation event of Miller (2007). A new paragenetic chart has been included that has been developed from the observations in the previous literature.

Despite the proximity of two world class deposits situated adjacently, and the likely linked origins, the main aim of this study will be on the formation of the Cu deposit at Mount Isa. The origin of the Pb-Zn-Ag deposit will not be detailed here, with previous studies focusing on this topic (e.g. McGoldrick and Keays, 1990; Perkins, 1997; Davis, 2004; Cave *et al.*, 2020).

CHAPTER 3

Foliation Boudinage Structures: Literature Review and Synthesis

3.1 Introduction

This chapter constitutes a literature review of foliation boudinage structures and associated geological structures, including some data synthesis and descriptions. A synthesis of the structures found at Mount Isa, including images, is available in **Appendix A** and **Appendix B**.

The distinctive structures that form during extension of anisotropic rocks along foliation or strong layering have been the focus of experimental, field and theoretical research (Coe, 1959; Milnes, 1964; Cobbold *et al.*, 1971; Hambrey and Milnes, 1975; Platt and Vissers, 1980; Mandal and Karmakar, 1989; Aerden, 1991; Grasemann and Stüwe, 2001; Passchier, 2001; Arslan *et al.*, 2008, 2012). A plethora of terminology has arisen to describe these structures **[Figure 3.1]**, including foliation boudinage structures, internal boudinage, extensional crenulation cleavage, shear bands and kink bands (Cobbold *et al.*, 1971; Hambrey and Milnes, 1975; Platt and Vissers, 1980; Kidan and Cosgrove, 1996). The latest additions to this list are flanking folds and flanking structures (Grasemann and Stüwe, 2001; Passchier, 2001). There are significant geometric and kinematic similarities between all these structures, leading to confusion about their definitions. The distinction between some are often not clear since different terms have been used for the same or very similar structures. As there were notable confusions in the literature, it was apparent a complete review and synthesis was needed to allow the thesis aims to be achieved. This literature review will focus on the terms: foliation boudinage, internal boudinage and flanking structures, which can be particularly difficult to distinguish.
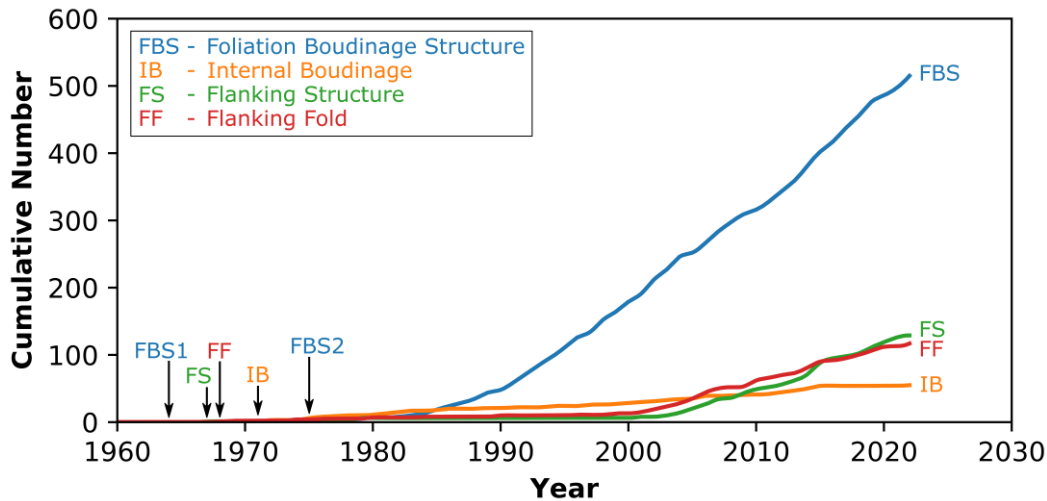
Figure 3.1: Google Scholar search results (Feb 2023) for the terms 'Foliation Boudinage', 'Internal Boudinage', 'Flanking Structure' and 'Flanking Fold' by year. Cumulative occurrences year on year, with the year of their first recorded use shown by arrows. FBS1 refers to the first reference to the foliation boudinage structures in Milnes (1964) unpublished thesis. FBS2 refers to the first published article in Hambrey and Milnes (1975).

3.2 Review

3.2.1 Foliation Boudinage Structures

3.2.1.1 Review of Foliation Boudinage Structures

Foliation boudinage structures were first described by Coe (1959) in siltstones in West Cork, Ireland, but were left unnamed, instead being termed 'special features'. No obvious lithological variations were observed in the siltstones and consequently no apparent change in competence between layers existed, which Ramberg (1955) considered to be vital for 'regular boudins' to form. Coe (1959) observed that lens shaped boudins were separated by segregations of quartz, with complete recrystallisation of the central part of the band and a strong flow of material into the zones of thinning **[Figure 3.2a]**. Coe (1959) associated the origin of the 'special features' with a set of shear joints. This was based on the similar (within

3°) strike orientations of the shears with the elongation of the knot of quartz in the neck region of the 'special features'.

The term foliation boudinage was first used by Milnes (1964) in an unpublished thesis to describe boudins in foliated rocks which lacked competence variations. A relationship with the foliation was assumed and both symmetrical and asymmetrical foliation boudins were described **[Figure 3.2b]**. The symmetrical foliation boudins were inferred to relate to principal stresses perpendicular and parallel to the foliation, whilst the asymmetrical type related to principal stresses oblique to foliation. The presence of an initial fracture was not inferred in this study.

The study by Hambrey and Milnes (1975) is the first published on foliation boudinage, in which the structures were observed in Swiss glacier ice. Hambrey and Milnes (1975) stated that deformation of mechanically anisotropic and homogeneous bodies leads to structures which cannot be explained in terms of competence differences, supporting the inferences of Milnes (1964). Symmetrical foliation boudinage is stated to result from shear planes at high angles to the layering, displacing it at the boudin necks **[Figure 3.2c]**, with layering above and below the neck regions being continuous (Hambrey and Milnes, 1975). Hambrey and Milnes (1975) stated that this symmetrical type of foliation boudinage commonly results in voids near the ends of the individual boudins, which are then filled with new coarse ice, or in the case of rocks, new minerals. Hambrey and Milnes (1975) noted that the necks of the boudins correlated with joints in the glacier, suggesting boudinage occurred under extending flow as it passed through the crevasse zone. Hambrey and Milnes (1975) recognised that a characteristic of asymmetrical foliation boudinage is the displacement of the laminations along shear planes, with the curvature of the laminations towards the shear plane. They noted
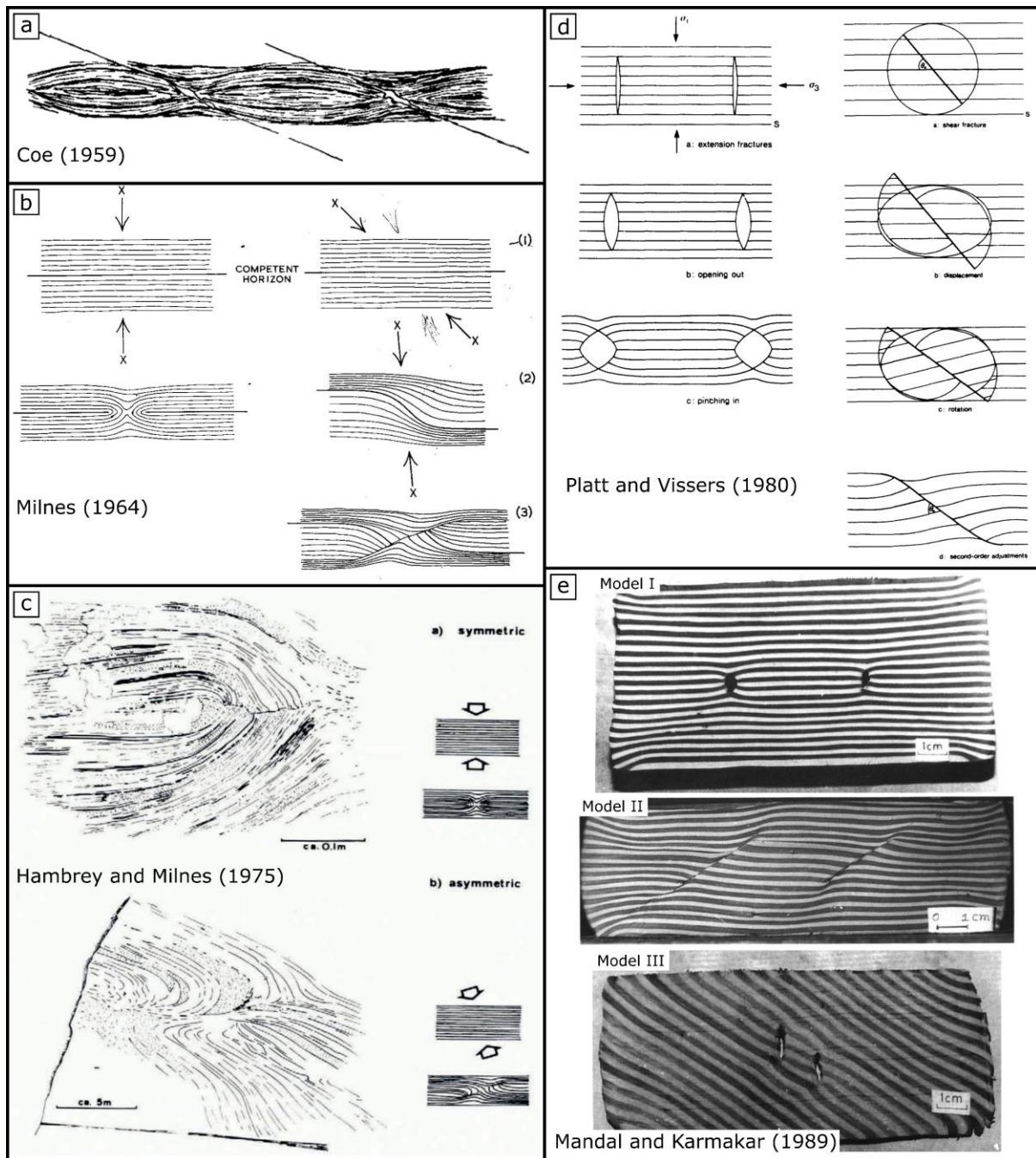
Figure 3.2: Observations, proposed formation mechanisms and models of foliation boudinage structures in the early literature. **a)** 'Special features' from Coe (1959), now recognised as foliation boudinage structures. **b)** A proposed formation mechanism for foliation boudinage structures. From Milnes (1964). **c)** Sketches and interpretation of foliation boudinage structures in rocks. From Hambrey and Milnes (1975). **d)** Origin of foliation boudinage structures as proposed by Platt and Vissers (1980). Left – symmetrical foliation boudinage structures; right – asymmetrical foliation boudinage structures. **e)** Plasticine models of Mandal and Karmakar (1989) showing the development of foliation boudin-like structures. Symmetrical opening of the structure. Model I – layer-normal shortening and layer-parallel extension of vertical extension fracture. Model II – layer-normal shortening and layer-parallel extension of an originally oblique fracture. Little to no opening of the structure is observed. Model III – vertical shortening and horizontal extension of extension fractures at an oblique angle to the layering. Asymmetrical opening of the structures.

this to be the opposite sense to what is expected if the curving was caused by drag during movement (Hambrey and Milnes, 1975).

Milnes (1964) and Hambrey and Milnes (1975) did not consider that an initial fracture was necessary for foliation boudinage (Milnes personal communication, 2019). However, Platt and Vissers (1980), who observed foliation boudinage structures in a metasedimentary sequence (Agnew, Australia), stated that an initial fracture appears to be essential to these structures **[Figure 3.2d]**. Platt and Vissers (1980) argued that the fractures form as the strong foliation limits the rate of ductile extension parallel to the layering, hence extensional fractures form normal to the layering. Therefore, they argue that the finite pinch and swell geometry is caused and preceded by brittle deformation. The formation mechanism proposed by Platt and Vissers (1980) assumes a constant shortening orientation perpendicular to the layering, with the orientation of the initial fracture changing relative to the layering.

Platt and Vissers (1980) indicate that symmetrical foliation boudinage structures form by an extensional fracture oriented parallel to the maximum principal stress and perpendicular to the layering. Extension parallel to the layering creates necking in the region of the fracture and the pinching of the layering **[Figure 3.2d]**. The fracture opens into a void which Platt and Vissers (1980) observed to be filled with coarse minerals and no internal deformation.

Platt and Vissers (1980) state that the asymmetrical foliation boudinage structures form by shear fractures developing oblique (~45°) to the layering and principal stresses. Shear failure relieves stress, inhibiting ductile deformation in the surroundings (Platt and Vissers, 1980). Extension parallel to the layering will result in rigid body rotation of the fracture towards the layering. The displacements in these cases are roughly parallel to the fracture, with slip taken up along it. Platt and Vissers (1980) state this does not lead to opening of the fracture and

voids do not generally form **[Figure 3.2d]**. The fractures curve towards the layering, where the displacement diminishes. Reverse drag of the layering agrees with that observed by Hambrey and Milnes (1975). Models of foliation boudinage proposed by Platt and Vissers (1980) show the final angle between the layering and the fracture approximates the initial angle of the fracture. Conjugate sets of foliation boudinage structures were observed as a result of ~35% shortening normal to the foliation (Platt and Vissers, 1980).

Lacassin (1988) built on the work of Platt and Vissers (1980) using field examples from the Cezarenque gneisses (France), demonstrating that a progression of structures form during deformation of both symmetrical and asymmetrical foliation boudins. In symmetrical foliation boudins, Lacassin (1988) noted pinching in the neck region towards the void almost resembled a fold. This was later described as a closed fish-mouth boudin (Swanson, 1992; Goscombe *et al.*, 2004; Arslan *et al.*, 2008). As inferred by Platt and Vissers (1980), oblique shear or fracture planes dipping at 20-50° to the layering caused asymmetrical pinching of the foliation. The quartz filled voids were smaller in these asymmetrical foliation boudinage structures compared to those that were symmetrical (Lacassin, 1988).

Mandal and Karmakar (1989) added to previous work by demonstrating another formation mechanism for asymmetrical foliation boudinage structures using layered plasticine stacks **[Figure 3.2e]**. In their models an extension fracture is created oblique to the layering (45°), with a maximum principal stress applied parallel to the fracture. Opening of the fracture occurs, forming a void with asymmetrical bending of the layers in the vicinity of the void **[Figure 3.2e]**. Therefore, the models of Mandal and Karmakar (1989) show that asymmetrical foliation boudinage structures will also form from extension fractures, providing the initial fracture is oblique to the layering. Mandal and Karmakar (1989) demonstrated that

symmetrical foliation boudins only form where the initial fracture is both normal to the layering and parallel to the maximum principal stress. However, for asymmetrical foliation boudinage structures, either the fracture or the stress directions, or both, must be oblique to the layering.

Arslan *et al.* (2008) describe four main types of foliation boudins from the Cine Massif in Turkey and the Furka Pass-Urseren Zone in central Switzerland. Arslan *et al.* (2008) also performed numerical modelling of the development of foliation boudinage structures using the 2-dimensional FLAC software. They model foliation boudinage structures with and without fracture propagation, the former producing the more common geometries that are also observed by others **[Figure 3.3]** (Hambrey and Milnes, 1975; Platt and Vissers, 1980; Mandal and Karmakar, 1989; Arslan *et al.*, 2008). Hence, propagation of the fracture tip during the formation may have a significant influence on the final geometry of the foliation boudinage structure (Arslan *et al.*, 2008). Arslan *et al.* (2008) concluded that foliation boudinage structures develop by the combination of brittle fracturing, ductile deformation, and deposition of vein material.

The models of Arslan *et al.* (2008) show that foliation boudinage structures can form in both coaxial and non-coaxial flow **[Figure 3.4]**. Symmetric foliation boudinage structures are shown to form only under pure shear conditions, with asymmetric foliation boudinage structures forming in both pure shear and simple shear (Arslan *et al.*, 2008). Asymmetric foliation boudinage structures forming under pure shear flow develop from fractures which have an initial distortion, such as sigmoidal shaped or folded fractures. Asymmetric foliation boudinage structures developing under non-coaxial flow form where the fracture is initially perpendicular to layering or at an angle inclined towards the direction of shearing.
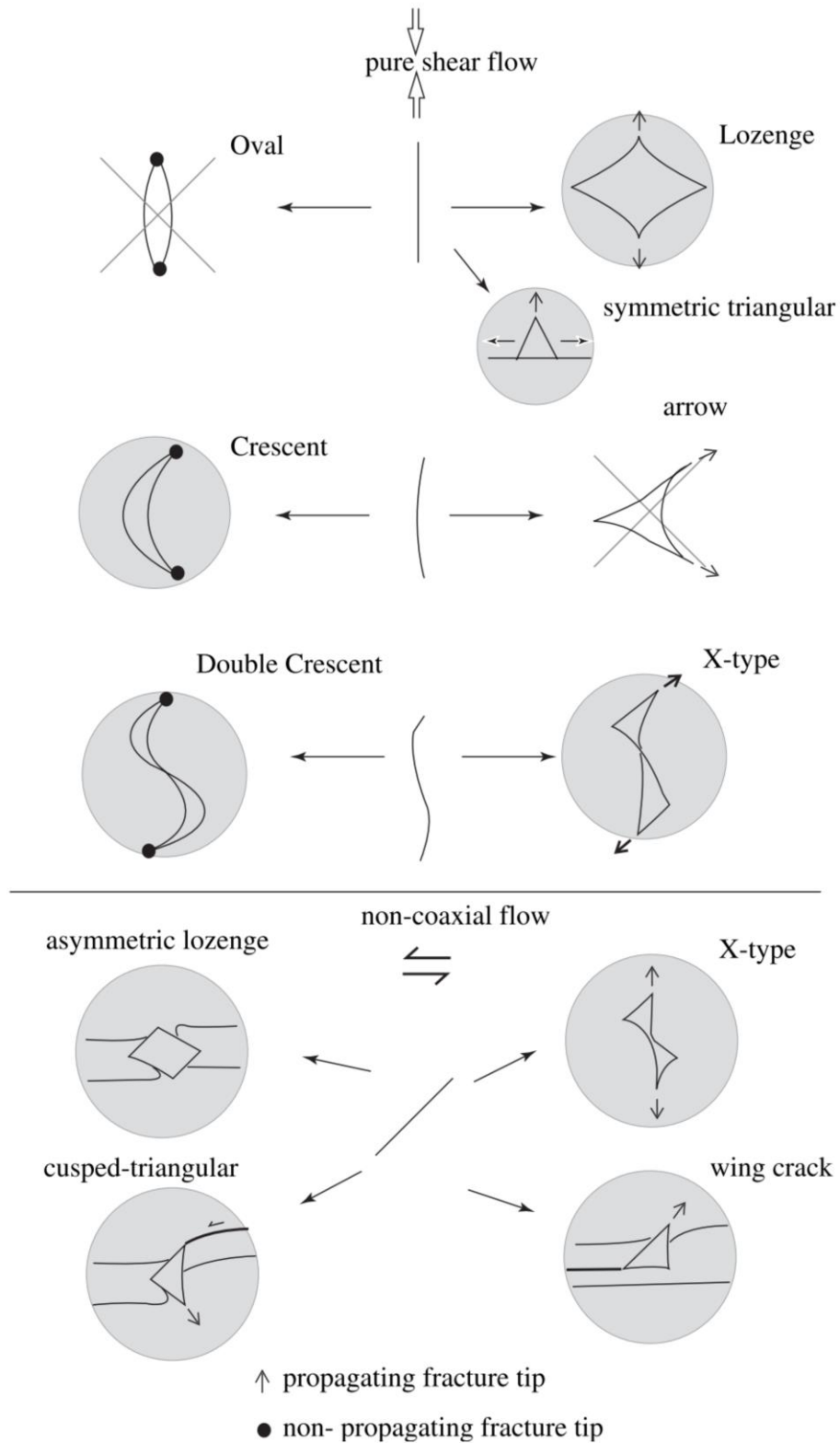
Figure 3.3: Schematic diagrams depicting the geometries of foliation boudinage structures. Geometries depend on initial fracture shape, fracture propagation, and flow type. Grey circles represent structures that have been observed in nature. From Arslan *et al.* (2008).
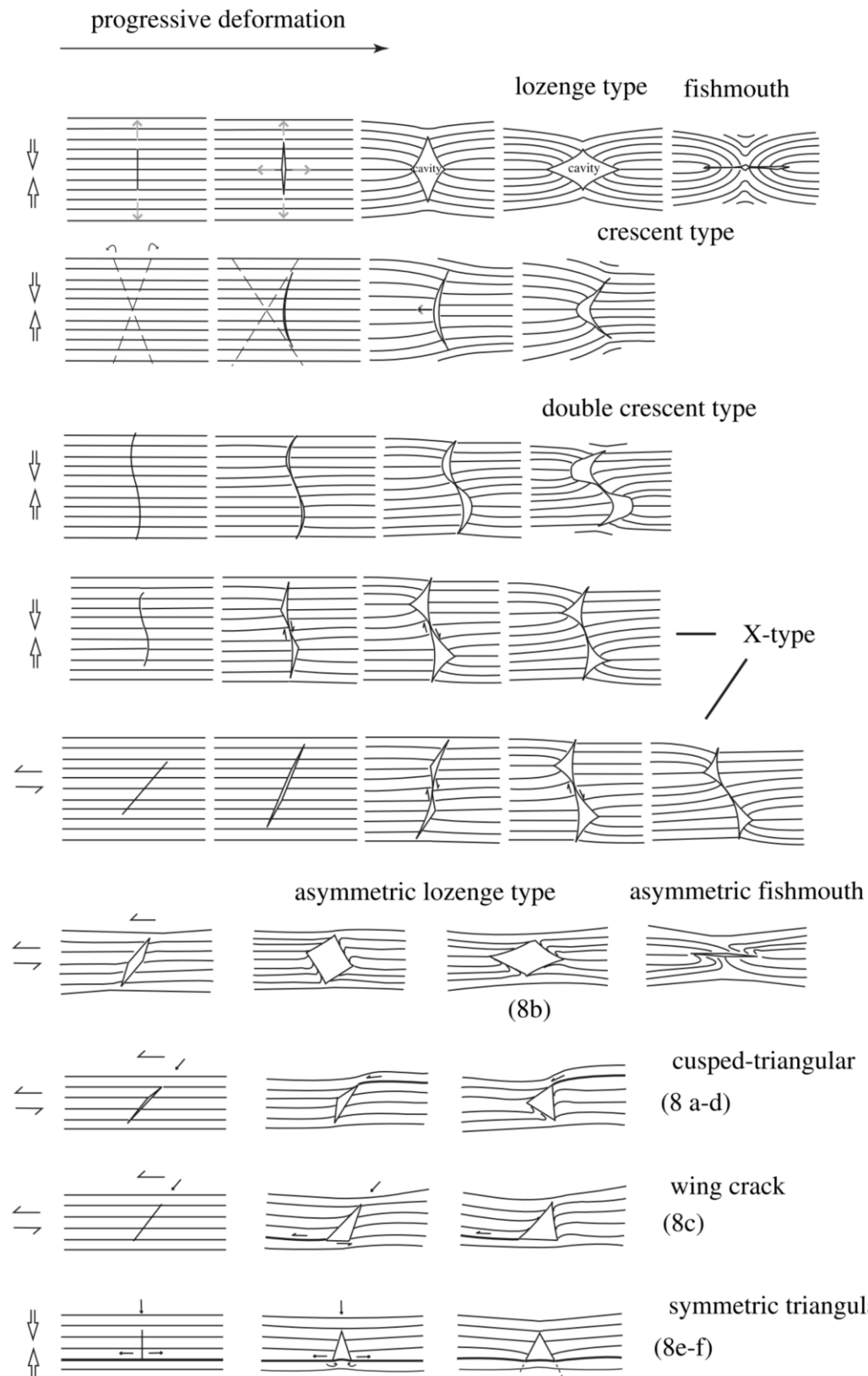
Figure 3.4: The inferred formation mechanisms of foliation boudinage structures. Fracture geometries depend on flow type, fracture propagation and fracture rotation.

Arslan *et al.* (2008) and Arslan *et al.* (2012) state that fractures and fluid filled cavities can form at any depth if fluid pressure exceeds the minimum principal stress by the tensile strength of the rock. Arslan *et al.* (2008) also infer that fluid-filled foliation boudinage structures could remain open for a significant period of time before mineral precipitation, providing the fluid pressure is kept above lithostatic to maintain open fractures. Arslan *et al.* (2008) demonstrate that some of the best examples of foliation boudinage structures are found in weakly foliated gneiss rather than strongly foliated mica-schist or mylonite. Therefore, they argue that the fluid pressure may be more critical than fabric strength for the development of foliation boudinage structures.

The presence of many different geometries of foliation boudinage structures shows a continuum of deformation and vein deposition, indicating vein filling can happen at all stages during the evolution of foliation boudinage structures **[Figure 3.4]** (Arslan *et al.*, 2008). In the foliation boudinage structures observed by Arslan *et al.* (2008) the infill is generally blocky crystals indicative of growth into open fluid filled cavities during foliation boudinage development. The vein infilling of the foliation boudinage structures is rarely deformed or recrystalised, supporting the similar observation made by Platt and Vissers (1980). The absence of deformation within the mineral infill has been used as evidence for a protracted period of time between the initial formation of the structure and the final infill stage (Arslan *et al.*, 2008). Based on these inferences there appears to be only minor, if any, further deformation after the infill is precipitated, potentially indicating the infill inhibits continued deformation.

Arslan *et al.* (2008) noted the presence of flanking folds within foliation boudinage structures, caused by the rotation of the fracture walls. This is a result of the fracture wall being bound

by a fluid filled void on one side. The fracture wall is unable to undergo shearing and only extension or shortening can occur in this direction (Arslan *et al.*, 2008). However, distal to the fracture wall, the resulting difference in the orientation of the stress field leads to the development of the flanking folds (Arslan *et al.*, 2008). The resulting angle between the foliation boudin fracture wall and the adjacent bending layers approximates the initial angle between the layers and the fracture (Arslan *et al.*, 2008).

Arslan *et al.* (2012) produced natural-looking foliation boudinage structures using numerical modelling of a 'random mica model', showing foliation boudin development under pure shear conditions. They show that small extension fractures and then shear fractures form early in the deformation history. Progressive deformation opens the fractures, leading to foliation boudinage structures (Arslan *et al.*, 2012). Increased deformation produced necks and flanking folds around extensional shear fractures and voids. Veins develop at 'pull-aparts', which look similar to the X-type foliation boudinage structures formed under pure shear flow of Arslan *et al.* (2008). The models of Arslan *et al.* (2012) demonstrate how a relatively high Young's modulus and viscosity will lead to shear fractures, but a low Young's modulus and viscosity will more commonly lead to mode I extension fractures. This implies that the material properties such as tensile and shear strengths in rocks (breaking strength in the models), Young's modulus and viscosity have strong influences on the geometry of fractures and the flow patterns surrounding them (Arslan *et al.*, 2012). Arslan *et al.* (2012) show that small, local variations in material properties can lead to both symmetric and asymmetric foliation boudinage structures being observed in the same models.

3.2.1.2 Synthesis of Foliation Boudinage Structure Literature

The previous work on foliation boudinage structures show that they form by the ductile (continuous deformation/low strain rate) deformation of foliation or layering around a brittle (high strain rate) fracture (Arslan *et al.*, 2008) and have been identified in multiple materials that exhibit significant anisotropy (Hambrey and Milnes, 1975; Platt and Vissers, 1980; Arslan *et al.*, 2008; Wiest *et al.*, 2020). The deformation of fractures during layer-normal shortening may lead to the opening of voids that accommodate infill (Arslan *et al.*, 2008). The characteristic bending or necking of the layering into the fracture defines the neck of the foliation boudinage structure (Arslan *et al.*, 2008) and is most readily identified in cross-section normal to the foliation boudin long-axis **[Figure 3.5]**. The observed angle between the wall of the foliation boudinage structure and the adjacent distorted layers approximates the initial angle between the layers and the original fracture (Arslan *et al.*, 2008). Goscombe *et al.* (2004) and Arslan *et al.* (2008) showed that the long-axes of boudins and foliation boudinage structures represent the intermediate principal strain axis.

Foliation boudins could be considered fractal structures identifiable on multiple scales from millimetres to at least 10's of metres (Arslan *et al.*, 2008). The largest structures contain at least 10's to 100's of cubic metres of infill and can form fishmouth structures as the central void recloses (Aerden, 1991; Swanson, 1992; Goscombe *et al.*, 2004; Arslan *et al.*, 2008). Infill is usually massive quartz and calcite, but also biotite, feldspar, chlorite, tourmaline and other common vein-forming minerals (Platt and Vissers, 1980; Swanson, 1992; Arslan *et al.*, 2008).
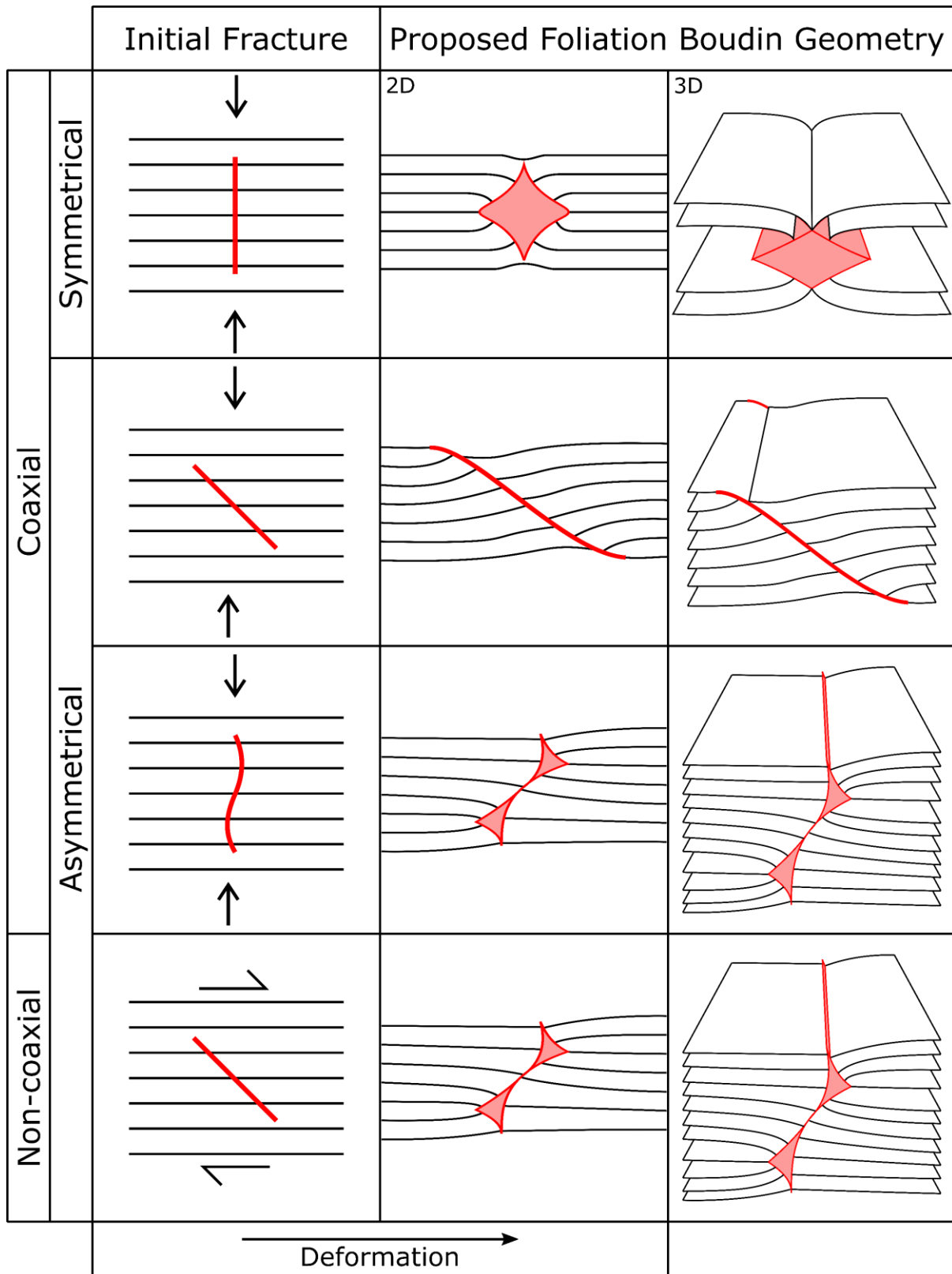
Figure 3.5: Summary of the formation mechanisms for the most common foliation boudinage structures as shown by previous studies. The geometry of the foliation boudinage structure depends on the initial fracture geometry and the deformation style. The 3-dimensional diagrams depict the assumed geometry of the foliation boudinage structures. Based on Platt and Vissers (1980) and Arslan *et al.* (2008).

Foliation boudinage structures can be separated into two broad type **[Figure 3.5]**: symmetrical and asymmetrical (Milnes, 1964; Hambrey and Milnes, 1975; Platt and Vissers, 1980). The symmetrical types form in coaxial flow around Mode I extension fractures and can produce infill in lozenge-shaped voids (Platt and Vissers, 1980; Mandal and Karmakar, 1989; Arslan *et al.*, 2008). Asymmetrical foliation boudinage structures can form under coaxial flow of oblique fractures or by non-coaxial flow of shear fractures where they display antithetic displacements (Platt and Vissers, 1980; Mandal and Karmakar, 1989; Arslan *et al.*, 2008). Asymmetrical foliation boudinage structures can form as single fractures or as conjugate sets (Sawyer, 1983; Arslan *et al.*, 2012).

Arslan *et al.* (2008) suggested that open fluid-filled voids could occur for a substantial period of time before mineral precipitation providing the fluid pressure is significantly high. The lack of deformation in the void fill material would seem to support this, as it implies a protracted period of time between foliation boudin formation and the final stage of mineral infill (Hambrey and Milnes, 1975; Platt and Vissers, 1980; Arslan *et al.*, 2008).

3.2.2 Internal Boudins

Internal boudins were first described by Cobbold *et al.* (1971) from experiments involving the shortening of statistically homogeneous, anisotropic materials. Rocks with anisotropic stress-strain properties may become unstable when shortened. These instabilities, which do not have to include a competency difference, are governed largely by the degree of anisotropy of the rock. Cobbold *et al.* (1971) produced models with stacks of lubricated plasticine layers **[Figure 3.6a]**. Model runs were performed with shortening directions parallel, oblique, and perpendicular to the layering.

Where the shortening direction was normal to the layering, the layers did not flatten uniformly. Instead, interlocking pinch and swell structures developed within individual layers, which Cobbold *et al.* (1971) termed 'internal boudins' **[Figure 3.6]**. These models do not predict brittle failure as the experiments are limited to infinitesimal deformation (Platt and Vissers, 1980). Further shortening of the internal boudins formed conjugate normal kink bands in the models of Cobbold *et al.* (1971). These experimental results were controlled by the angle between the layering and the maximum principal stress, as well as the degree of anisotropy. Internal boudinage appears to have a close resemblance to extensional crenulation cleavage and there are similarities between the formation of these two structures (Hanmer, 1986).

Kidan and Cosgrove (1996) experimented with layer-normal shortening of a statistically homogeneous and anisotropic material. They observed the formation of what they termed internal pinch and swell structures **[Figure 3.6b]**, identical to the internal boudins of Cobbold *et al.* (1971). Kidan and Cosgrove (1996) state that shortening normal to layering can produce two types of structures, controlled by the degree of anisotropy of the material. Where the degree of anisotropy is high, normal kink bands will form. Interlocking internal pinch and swell structures (internal boudins of Cobbold *et al.*, 1971) will form where the anisotropy is low.

In experiments by Kidan and Cosgrove (1996), internal boudins (their internal pinch and swell structures) formed after a small amount of shortening, whereby the deformation is then transferred to adjacent layers. Areas that are pinched align with areas of swell in adjacent layers, forming an interlocking network **[Figure 3.6c]**. As deformation continues, increased bulk shortening in these zones of failure is concentrated along a diagonal array of pinched neck regions. These regions link, forming a planar zone of localised shear deformation in the

form of conjugate normal kink bands (Cobbold *et al.*, 1971; Kidan and Cosgrove, 1996). There is some similarity to brittle shear, in which shear failure is commonly achieved by linking of individual tension fractures in an en-echelon array. An initial 30° angle between the kink bands and the layering is reduced as deformation is applied. The formation of internal boudins and then kink bands in the models of Kidan and Cosgrove (1996) agrees with Cobbold *et al.* (1971), suggesting kink bands can also form from the pinch and swells of internal boudinage structures in rocks with a low degree of anisotropy.
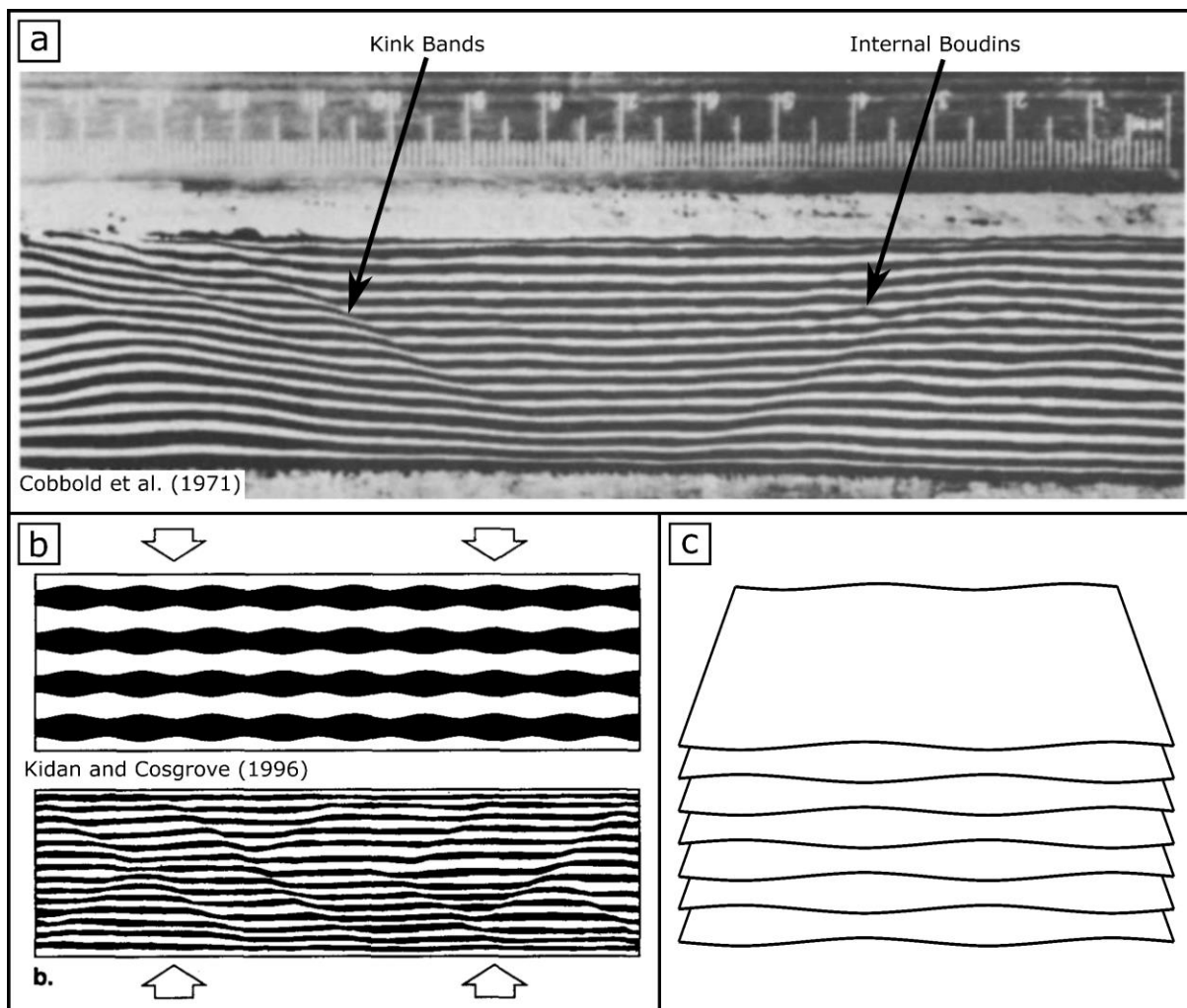
Figure 3.6: Diagrams and models of internal boudins in the previous literature. **a)** Experimental formation of internal boudins by layer-normal shortening of a plasticine model. Both internal boudins and kink bands were identified. From Cobbold *et al.* (1971). **b)** Diagrams of 'interlocking pinch and swell' structures (internal boudins) and kink bands showing their formation by layer-normal shortening. From Kidan and Cosgrove (1996). **c)** A 3-dimensional schematic diagram of internal boudins based on previous literature, depicting their characteristic pinch and swell geometries.

3.2.3 Flanking Structures

Flanking structures are defined as deflections of planar or linear fabric elements from their undisturbed orientations in a rock near pre-existing discontinuities, such as veins, dykes, fractures, or burrows (Grasemann and Stüwe, 2001; Passchier, 2001). Flanking structures are categorised into flanking shear bands and flanking folds and are developed by a variety of mechanisms (Passchier, 2001). Within these two sub-categories, they can be split further into s-, n- or a-type flanking structures **[Figure 3.7]**, based on the displacement of the host element (HE) along the cross-cutting element (CE; Passchier, 2001).

Flanking folds are generally the most common type of flanking structure, occurring from mm- to at least metre-scale (Passchier, 2001). Flanking folds form by flow perturbations where rheological heterogeneities are present during their development (Passchier *et al.*, 2005), and are therefore ductile structures which develop next to distinct discontinuities in rocks **[Figure 3.7]**.

Grasemann and Stüwe (2001) noted the similarities between a-type flanking folds and asymmetric foliation boudinage structures, with both structures demonstrating antithetic displacements **[Figure 3.7d]**. As Passchier (2001) describes flanking structures as forming adjacent to pre-existing discontinuities in the rock, this implies that the discontinuity is present prior to the development of the structures. However, Arslan *et al.* (2008) describe the bending of the layering adjacent to foliation boudinage structures as a category of flanking fold. This is despite the foliation boudinage structures forming simultaneously to the bending or flanking folds of Arslan *et al.* (2008).
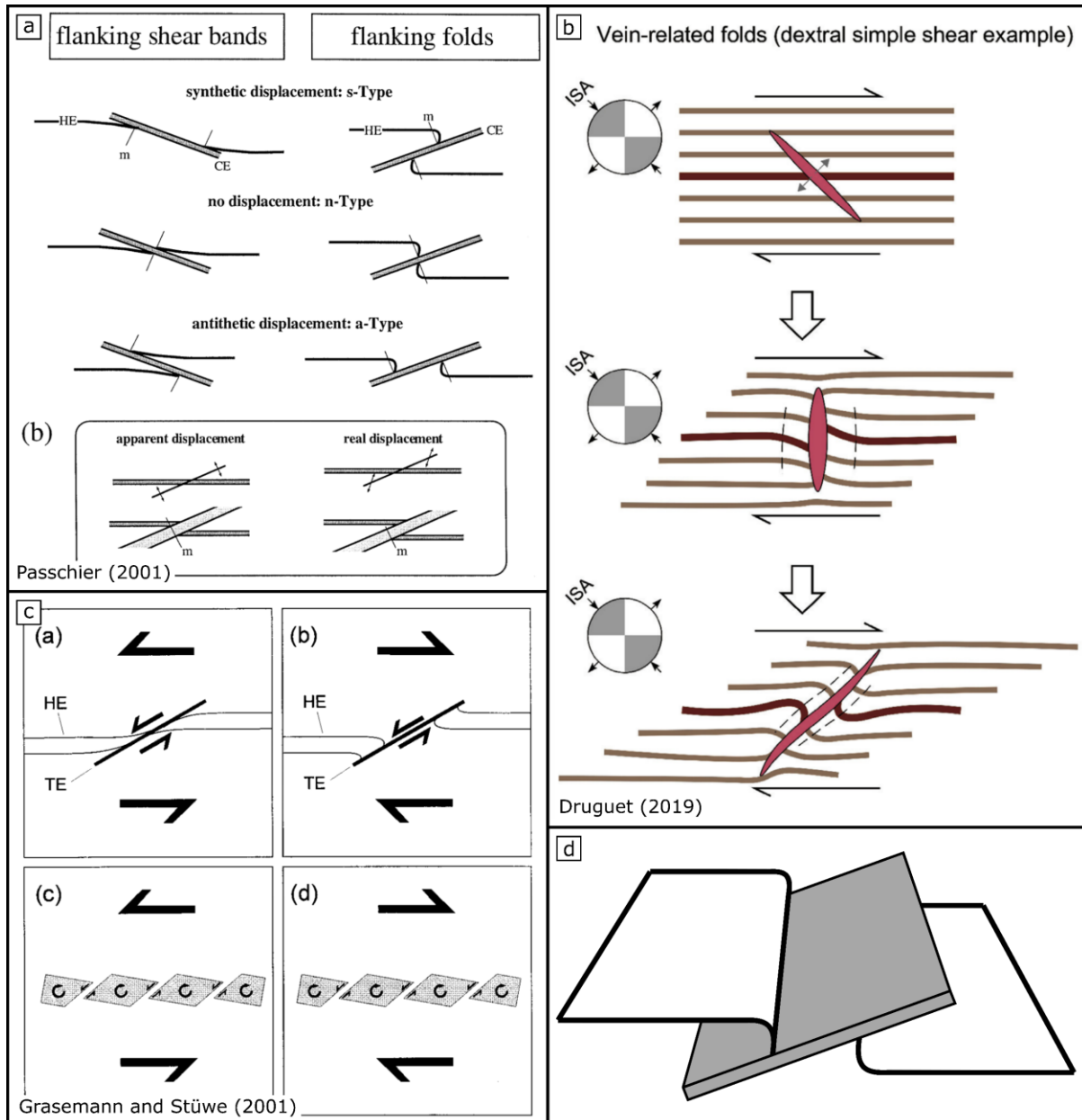
Figure 3.7: Flanking structure (flanking fold) classifications and diagrams in the previous literature. Most authors recognise s-type, n-type and a-type structures, characterised by their apparent synthetic, none and antithetic displacements, respectively. **a)** Classification of Passchier (2001) into flanking shear bands and flanking folds. HE – host element; CE – cross-cutting element. **b)** Diagrams of Druguet (2019) showing the formation of flanking structures adjacent to an existing vein. **c)** Flanking structure formation as proposed by Grasemann and Stüwe (2001). TE – transecting element. **d)** A schematic 3-dimensional diagram of an a-type flanking structure adjacent to an existing discontinuity. The a-type flanking structures that develop around existing discontinuties have a similar appearance to foliation boudinage structures.

3.3 Pressure-Temperature (PT) Conditions of Foliation Boudinage Structures

As the later chapters in this thesis focus on foliation boudinage structures, only the pressure-temperature (PT) conditions for these structures have been investigated here.

The metamorphic conditions during the formation of foliation boudinage structures have been investigated based on evidence from previous studies. Where the precise PT conditions of formation have been established from previous literature, they are shown in **Figure 3.8a**. The data points plot predominantly in the PT ranges of greenschist and amphibolite facies. **Figure 3.8b** includes all data points for foliation boudinage structure formation conditions, including where only metamorphic facies are known. **Figure 3.8** shows that foliation boudinage structures form under almost all metamorphic conditions above ~250 °C and ~200 MPa, including in ice. However, around 75% of occurrences are within the Greenschist and Amphibolite facies. This could be a genuine relationship or, more likely, it may reflect the abundance of studies on rocks in these metamorphic conditions.

Some high temperature foliation boudinage structures near the granite partial melt conditions are occasionally filled with leucosome or partial melt (McLellan, 1988; Allibone and Norris, 1992; Jain *et al.*, 2018), rather than the more commonly observed quartz and calcite (e.g. Ghosh and Sengupta, 1999; Druguet and Carreras, 2006; Arslan *et al.*, 2008). These results could show that temperature and possibly pressure are not as important as the presence of a strong structural anisotropy and high fluid pressures in the formation of foliation boudinage structures.
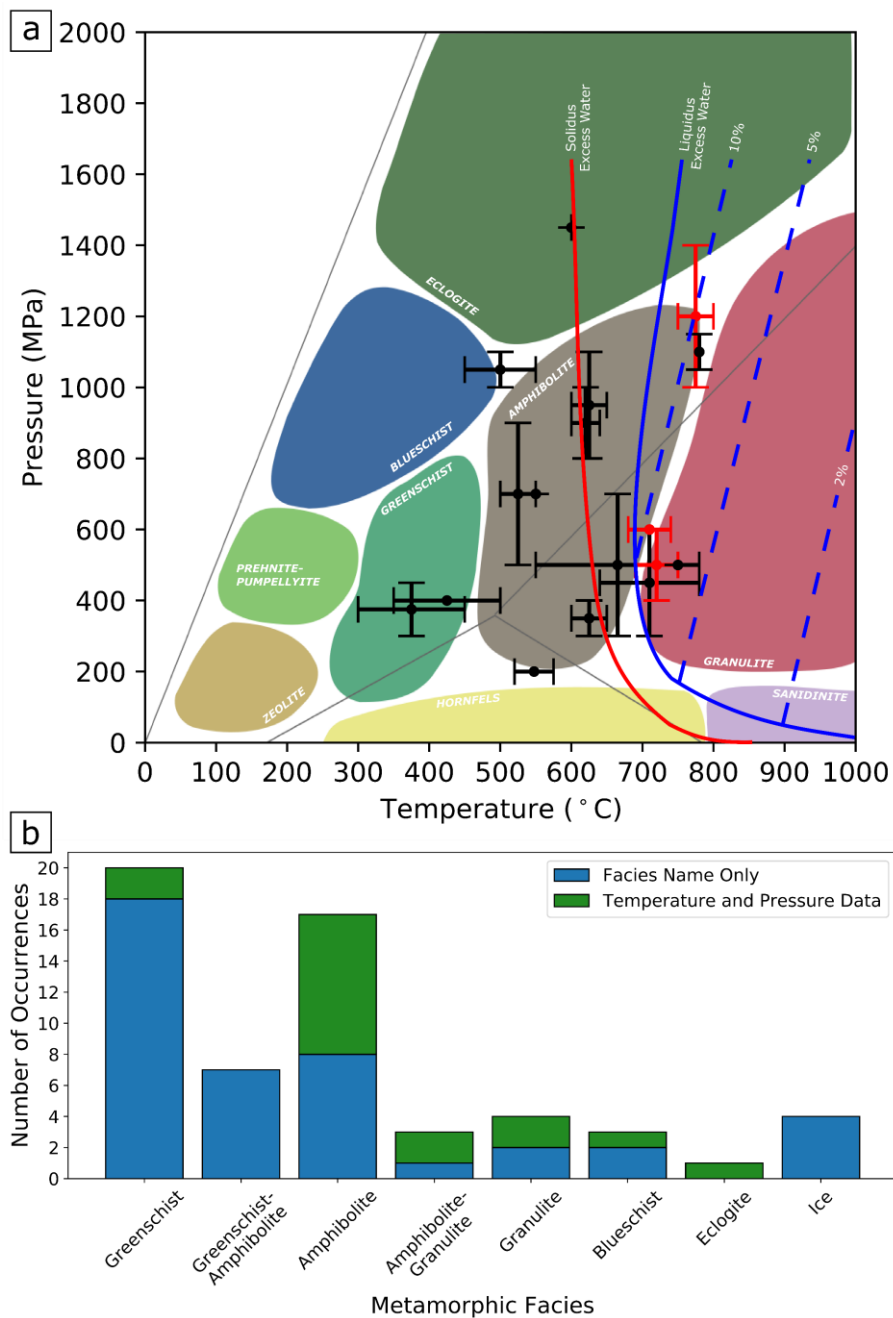
Figure 3.8: Metamorphic conditions during the formation of foliation boudinage structures. **a)** Quantitative data showing the pressure-temperature conditions. Error bars indicate the PT uncertainty as published in the literature. The high temperature foliation boudinage structures coincide with granite partial melt conditions and can be filled with leucosomes (red points). Metamorphic facies after Turner (1948) etc. Granite partial melt solidus and liquidus based on Stern *et al.*, (1975) and Weinberg and Hasalová (2015). **b)** Qualitative data showing the literature occurrence of foliation boudinage structures in the major metamorphic facies. Both the quantitative and qualitative data has been grouped to highlight the conditions where foliation boudinage structures are most commonly formed.

3.4 Geometric Descriptions of Structures in Anisotropic Rocks – Synthesis and Classification of End Members

The structures detailed in this chapter all form by shortening in anisotropic and homogeneous rocks. The orientation of the fracture or discontinuity seemingly plays a considerable role in the formation of most structures mentioned in this chapter. The foliation boudinage structures, internal boudins and flanking structures could be divided by the presence, absence, and timing of these discontinuities during deformation **[Figure 3.9]**.

The geometries of foliation boudinage structures, internal boudins and antithetic type flanking structures are observed in field examples, experiments and modelling. By comparing the final geometries of the structures after deformation, a new classification scheme can be proposed **[Figure 3.9]**. Further material can be found in **Appendix A**, including examples from Mount Isa.

Deformation is separated into pure shear (coaxial) and simple shear (non-coaxial), relative to the layering. In cases where general shear is involved, deformation with a non-coaxial component commonly results in asymmetric structures which closely resemble the simple shear end members. For simple shear, the synthetic or antithetic orientation of the oblique fracture to the shear direction is important. In pure shear, the fracture orientation is less important as the resulting structures are mirrored in the vertical axis.

	Coaxial		Non Coaxial	
	Initial Geometry	Final Geometry	Initial Geometry	Final Geometry
No Fracture	**a** Internal Boudin		**b** Shear bands - Extensional Crenulation Cleavage	
Pre-existing Vein	**c** Flanking Structure		**d** Flanking Structure	
Normal Fracture	**e** Symmetrical Foliation Boudinage Structure		**f** Asymmetrical Foliation Boudinage Structure	
Oblique Fracture (Antithetic)	**g** Asymmetrical Foliation Boudinage Structure - no fill		**h** Asymmetrical Foliation Boudinage Structure	
Oblique Fracture (Synthetic)	**i** Asymmetrical Foliation Boudinage Structure - no fill		**j** Asymmetrical Foliation Boudinage Structure - no fill	

Figure 3.9: (Previous page) Structures associated with the coaxial and non-coaxial deformation of anisotropic, homogeneous rocks, in scenarios where: no fractures form (**a-b**), veins are pre-existing (**c-d**), and where fractures form just subsequent to or during deformation (**e-j**). **a)** Internal boudins – coaxial, no fracture (Cobbold *et al.*, 1971). **b)** Extensional crenulation cleavage – non-coaxial, no fracture (Platt and Vissers, 1980). **c)** Flanking structure – coaxial, pre-existing vein (Grasemann and Stüwe, 2001; Passchier, 2001). **d)** Flanking structure – non-coaxial, pre-existing vein (Grasemann and Stüwe, 2001; Passchier, 2001). **e)** Symmetrical foliation boudinage structure – coaxial, fracture (Hambrey and Milnes, 1975; Platt and Vissers, 1980; Mandal and Karmakar, 1989; Arslan *et al.*, 2008). **f)** Asymmetrical foliation boudinage structure – non-coaxial, fracture (Mandal and Karmakar, 1989; Arslan *et al.*, 2008). **g)** Asymmetrical foliation boudinage structure (no fill) – coaxial, fracture ((Platt and Vissers, 1980; Mandal and Karmakar, 1989). **h)** Asymmetrical foliation boudinage structure – non-coaxial, fracture (Mandal and Karmakar, 1989; Arslan *et al.*, 2008). **i)** Asymmetrical foliation boudinage structure (no fill) – coaxial, fracture ((Platt and Vissers, 1980; Mandal and Karmakar, 1989). **j)** Asymmetrical foliation boudinage structure (no fill) – non-coaxial, fracture.

3.5 Conclusions and Recommendations

There is confusion in the previous literature over the terms associated with the deformation of anisotropic, homogeneous rocks. Past studies have often used the terms 'foliation boudins' and 'internal boudins' interchangeably, and further confusion may be seen with addition of the geometrically similar 'flanking structures' to the terminology. However, by carefully detailing the original, updated or accepted definitions and descriptions of all three structures, the differences are apparent.

No new definitions have been added in this chapter and all terminology throughout the thesis refers to the definitions outlined below. Where possible, the classification scheme in **Figure 3.9** is based on the definitions in the original literature. However, it is apparent that some terminology has changed over time and is the cause of most of the confusion in the literature. Where definitions have changed, the current most widely used terminology is used. Although, this contradicts the convention that precedence in definitions should be observed. The review and classification scheme in **Figure 3.9** may be a useful addition to the multitude of studies

on these structures. There are likely to be a host of intermediate structures between all of those observed and illustrated in **Figure 3.9**, which have not been taken into consideration here.

Foliation boudinage structures – these structures form from the deformation of a fracture, where the fracture forms either just prior to or during the deformation event. Platt and Vissers (1980) argue that an initial fracture is a precondition for foliation boudinage to occur, this is despite the original definitions of Milnes (1964) and Hambrey and Milnes (1975) not including a fracture. The symmetrical foliation boudinage structures form by the coaxial deformation of an extension fracture, whilst the asymmetrical types can form in many conditions, with or without mineral infill.

Internal boudins – these structures develop by the coaxial deformation of anisotropic layers without a fracture, where they form distinct pinch and swell geometries, as described by Cobbold *et al.* (1971). Extensional crenulation cleavages form under similar conditions, but during non-coaxial deformation (Platt and Vissers, 1980).

Flanking structures – these structures form by the deformation of layers around pre-existing, mineral filled veins. Deformation within the vein material may be apparent. Additional confusion arises with the introduction of the term flanking structure by Arslan *et al.* (2008) for the bending of layers within foliation boudinage structures.

Foliation boudinage structures form under most metamorphic conditions but are observed most commonly under greenschist and amphibolite facies conditions. However, the abundance of foliation boudinage structures in these rocks may be due to sampling biases, with the great number of studies on such rock types. At low metamorphic conditions the foliation boudinage structures are often filled with common rock forming minerals such as

quartz, calcite, biotite, among others. At higher metamorphic conditions, the structures can

be filled with partial melt and leucosomes.

CHAPTER 4

Methodology

The methods outlined in this chapter are common to the thesis and apply to most aspects of this study. More specific methods are detailed fully in the relevant chapters.

4.1 Materials

All drillholes examined in the study are from within the Mount Isa Cu system. Thirteen drillholes from the Mount Isa Copper Operations (MICO) and two from Resource Development (RD) were logged for structures of interest related to sulphide mineralisation. The MICO drillholes were drilled underground from a range of areas within the deposit but are generally close to or intersect high-grade Cu mineralisation **[Figure 4.1** and see geological map in **Figure 4.2]**. The two RD drillholes were drilled from the surface into the periphery of the Mount Isa system. The drill cores were chosen based on availability during core logging and represent various locations across the orebody **[Figure 4.1; Appendix C.1]**. Structural measurements were collected from both the MICO and RD drill cores, although only the RD drillholes (T667ED1 and T190ED1) are oriented.

4.2 Logging and Sampling

The long-axes of foliation boudinage structures **[Y-direction; Figure 4.3]** were defined by the pinching of the layering into the neck regions. Adapting the fold hinge method of Blenkinsop *et al.* (2015), orientations of the foliation boudinage structures were measured as lines connecting the neck regions observed on opposite sides of the drill core. Structural measurements were collected using an EZY-Logger goniometer and the orientations of the structures were determined using drill core α and β angles together with the drillhole survey data (Vearncombe and Vearncombe, 1998; Chapter 5). Most MICO drillholes were drilled using 'NQ2' (50.7 mm) diameter, whilst most RD drillholes were 'HQ3' (61.1 mm).
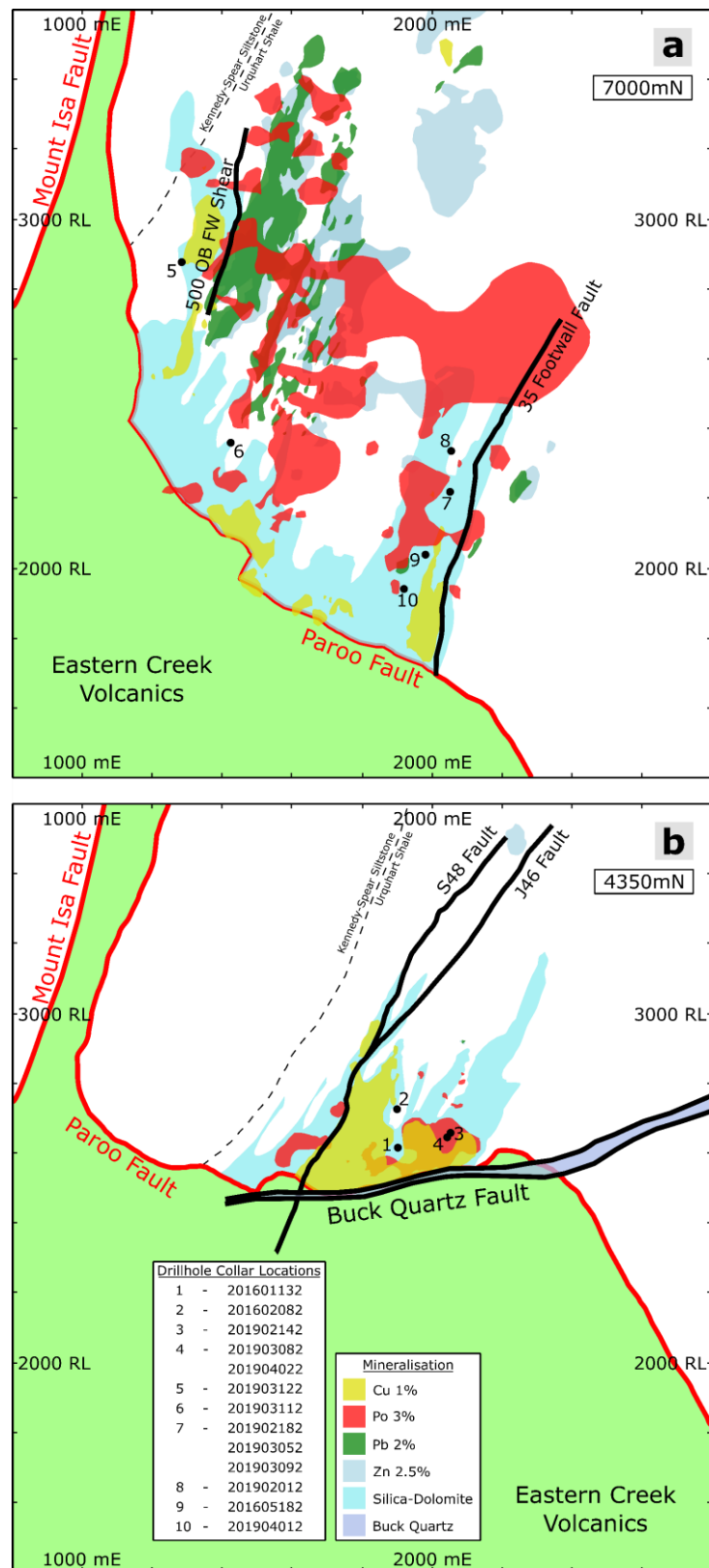
Figure 4.1: East-west cross-sections showing the collar locations displayed as points for drillholes analysed in this study and corresponding to their relative positions in relation to the mineralisation (see **Appendix C** for drillhole co-ordinates, downhole lengths, and orientations). The east-west cross-sections depict the relative positions of the Cu, Pb and Zn orebodies, pyrrhotite (Po) and silica-dolomite halos, and buck quartz at Mount Isa. **a)** Cross-section in the north of the mine at 7000mN. **b)** Cross-section in the south of the mine at 4350mN.
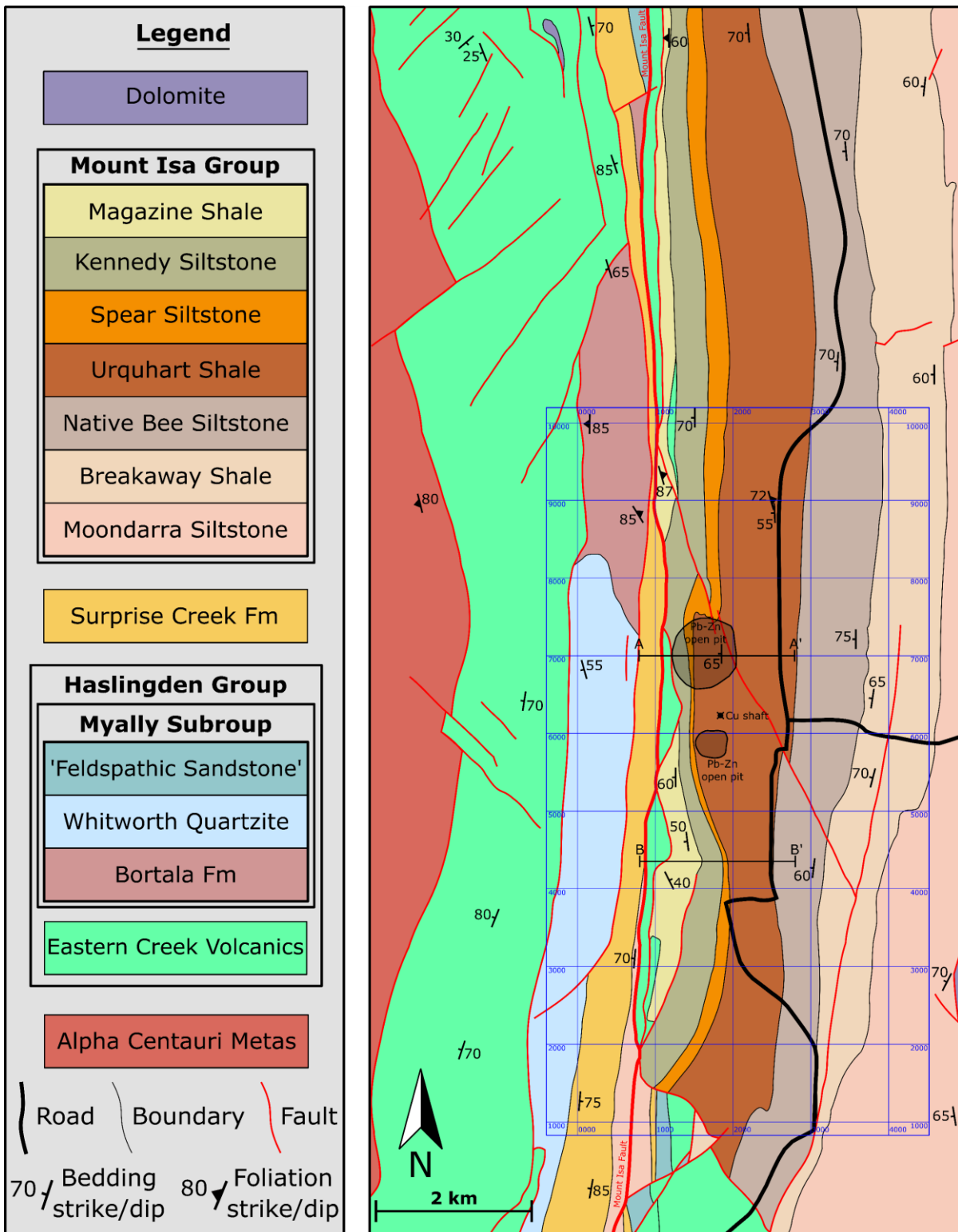
Figure 4.2: A geological map of the Mount Isa area with mine workings and local mine grid. After Spatial and Graphic Services, Statewide Operations, Department of Natural Resources (2020).
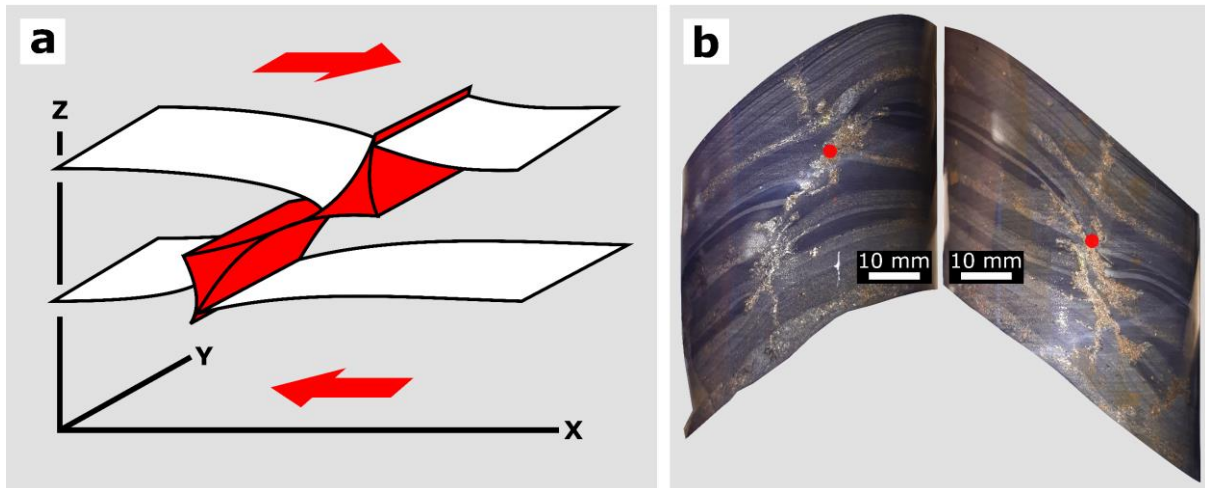
Figure 4.3: Measuring orientations of foliation boudinage structures in drill core. **a)** Reference axes of foliation boudinage structures showing the pinching of layering into the neck region. The long-axis of the structure is in the Y-direction and cross-section in the XZ-plane. **b)** A foliation boudinage structure from drillhole '201903092' as seen on opposite sides of the drill core. The sample was located at a downhole distance of 32.1 metres. Diameter of drill core is ~50 mm. The neck lineation is defined by the red dots**.**

The infills of the drill core-scale foliation boudinage structures were recorded and their positions logged as downhole distances. Some drill core lengths containing foliation boudinage structures were collected for further detailed analysis. Samples were cut in orientations of interest and polished thin sections were produced at Cardiff University. All samples of interest that were collected and where thin sections were produced are presented in **Appendix D**.

4.3 Provided Datasets

MICO and RD downhole assay and lithology logs were available. The logged rock types differentiate progressively deformed and altered lithologies and are termed 'Shale', 'Pyritic Shale (5–20% pyrite)', 'Pyritic Shale (>20% pyrite)', 'Recrystallised Shale', 'Irregularly

Brecciated and Recrystallised Shale', 'Siliceous Shale', 'Brecciated and Fractured Siliceous Shale', 'Carbonaceous Mylonite', 'Buck Quartz' and 'Greenschist'.

4.4 Surface Mapping

Some surface measurements were collected at the 'Airport', 'Lookout' and 'Shed 7' road-cuttings **[Appendix E]**. Measurements include bedding surfaces, cleavages, joints, fold axes, mineral veins, and shear planes.

Measurements were systemically collected using the MOVE 'Fieldmove Clino' mobile application (Petroleum Experts, 2023) on a Samsung A5. All measurements were collected with the device in one orientation (upright), to allow for consistency across all measurements.

CHAPTER 5

A Comparison of Drillhole Desurveying Methods: Examples from Mount Isa

5.1 Introduction

The orientations (azimuth and plunge) of drillholes are required to orient drill core, which can then be used to measure the orientations of geological structures (e.g. Marjoribanks, 1997; Vearncombe and Vearncombe, 1998; Blenkinsop and Doyle, 2010; Blenkinsop *et al.*, 2015). Knowledge of the exact 3-dimensional positions for points of interest along the drill core may be required to locate drillhole intersections with geological boundaries, faults or underground mine workings.

Desurveying is the calculation of drillhole paths from discontinuous drillhole survey data. The choice of desurveying method could have significant implications (outlined in section 5.2) for locating geological targets, including Cu mineralisation at Mount Isa. Developing a method for calculating positions for any point along the drillhole was necessary so that the foliation boudinage structures in this study can be accurately and consistently located in 3-dimensional mine grid co-ordinates. The method also ensures that original orientations of all structures can be accurately reconstructed from structural measurements. By deriving formulas to calculate the azimuth, plunge, and exact positions for any distance along the drillhole, the differences and limitations in the desurveying methods can also be highlighted.

The aims of this study are: (1) to provide a comparison between desurveying methods using different drillhole lengths and angles between the drill bit and the rock anisotropy; (2) to provide a solution for interpolating azimuth and plunge measurements between survey points; (3) to calculate the positions of any point along the drillhole in geographical coordinates (northing, easting and true vertical depth) from downhole measurements; (4) to make the desurveying method calculations available in an easily accessible computer code in both Python and R languages.

5.2 Background

Directional drilling of longer and deeper drillholes is becoming increasingly important as resources are being exploited at greater depths (Bourgoyne *et al.*, 1986; Howson and Sides, 1986; Blenkinsop *et al.*, 2015; 'MinEx CRC: A new frontier in mineral exploration', 2019). The ability to calculate and control the position of the drilling rod along the drill path is vital for many industries, such as mining, mineral exploration, degasification, water extraction, civil engineering, and geothermal energy.

The cutting head of the drill rod, known as the drill bit, can deviate both intentionally and unintentionally from its initial orientation. Targeted drilling to a specific location such as an oil reservoir beneath an inaccessible area is an example of an intentional deviation (Bourgoyne *et al.*, 1986), whilst unintentional deviations can occur due to drill bit interaction with anisotropic rock (Lubinski and Woods, 1953; Brown *et al.*, 1981; Singh, 1998).

Most drillholes surveys carried out in the past are able to track the deviation of the drillhole path by taking down hole surveys at constant intervals during drilling (Howson and Sides, 1986; Monterrosa *et al.*, 2016). Surveying devices are passed down the drillhole to measure the drillhole angle from the horizontal and the angle clockwise from north (Wilson, 1968; Walstrom *et al.*, 1972; Killeen and Elliott, 1997; Sindle *et al.*, 2006; Seibi *et al.*, 2009; Škrjanc and Vulic, 2016 etc.), which can be defined as the plunge and azimuth respectively, in accordance with linear measurement convention in structural geology. Recent developments in down hole surveying instruments include those that are able to survey continuously as the tool passes both in and out of the drillhole, such as the REFLEX GYRO SPRINT-IQ (REFLEX, 2021). Surveying devices used in the data collection include Electric Multishot Systems,

gyroscope and optical instruments (Killeen and Elliott, 1997; Sindle *et al.*, 2006; Seibi *et al.*, 2009; REFLEX, 2021).

The locations of the survey points are known only from their downhole distance (Mason and Taylor, 1972). In all circumstances other than continuous surveying, the positions of the drillhole and survey points must be estimated on the basis of adjacent survey measurements. With these discontinuous surveying methods, the true shape of the drillhole between survey points is unknown (Zaremba, 1973). Desurveying estimates the positions of the survey points by extrapolating the drillhole path between the survey points (Bourgoyne *et al.*, 1986). Naturally, a shorter distance between survey points results in a truer drillhole pathway after desurveying, with the continuous surveying methods plotting the most accurate drillhole path (REFLEX, 2021).

There is no unique solution to the desurveying problem, with a number of desurveying methods available. The *Basic Tangent*, *Average Angle*, *Balanced Tangent* (Walstrom *et al.*, 1972), *Minimum Curvature* (Mason and Taylor, 1972; Zaremba, 1973), and *Radius of Curvature* (Wilson, 1968) methods are the most widely described in the literature (Škrjanc and Vulic, 2016; Eren and Suicmez, 2020). Some methods such as the *Basic Tangent* and *Average Angle* methods have obscure or unknown origins (Bourgoyne *et al.*, 1986). Despite frequent use, desurveying calculations are often poorly described in the literature, or given as computer code within the text, meaning extraction of the desurveying calculation is cumbersome. Examples of this practice include Howson and Sides (1986), Ozkaya (1995), Khaled (2016), and Eren and Suicmez (2020).

All desurveying methods make assumptions about the drillhole path **[Figure 5.1]**. Straight line segments, sudden orientation changes and the restriction of drillhole plots to lie on planes

are examples of assumptions that are made in desurveying methods; these are quite unrealistic.
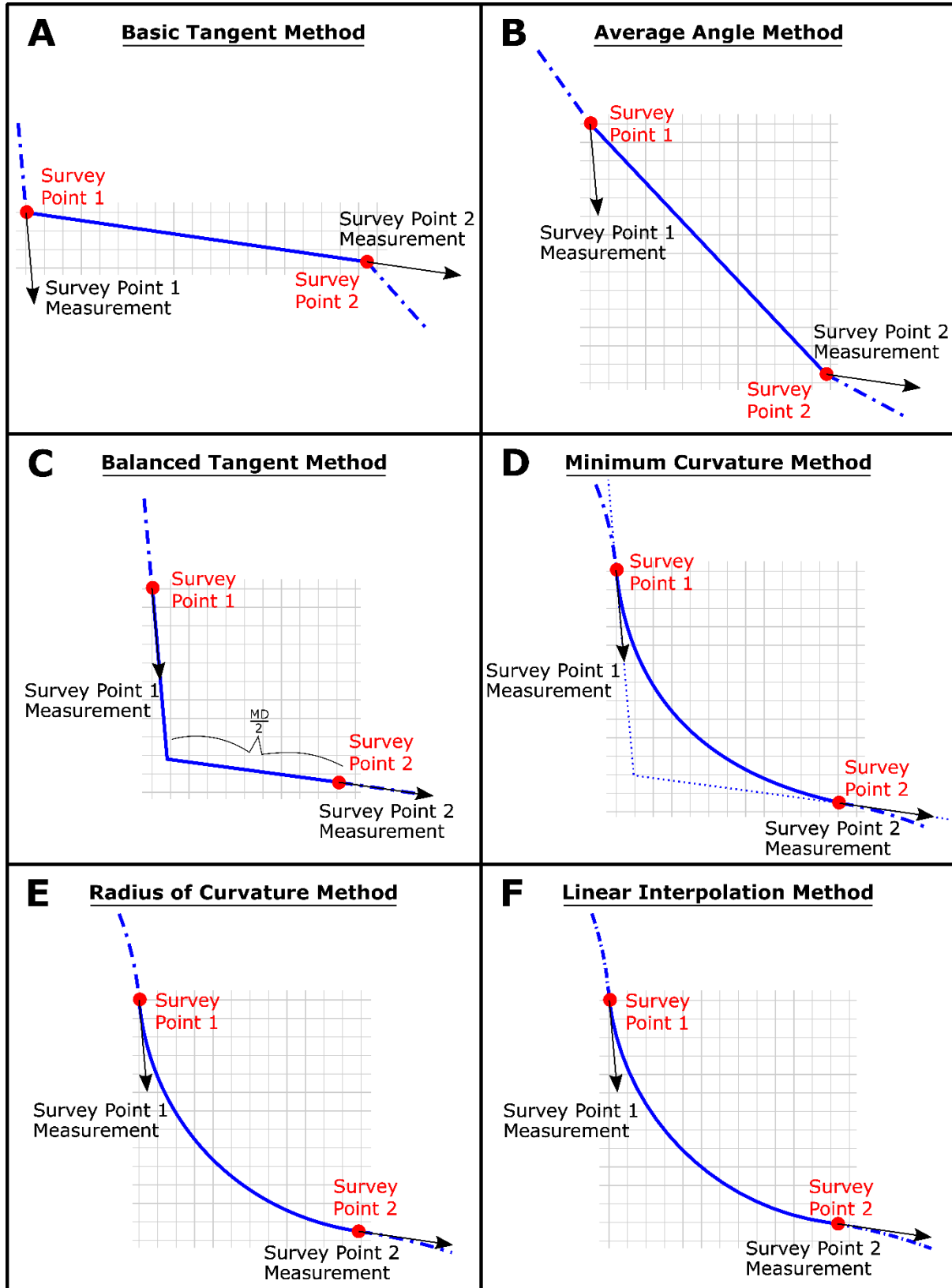
Figure 5.1: (Previous page) Cross-sectional view of adjacent survey points in an example drillhole. Different desurveying methods significantly influence the course of the drillhole. 'Survey Point 1' is placed at the same origin in all drillholes relative to a grid square, with 'Survey Point 2' positioned to scale in 2-dimensions using the desurveying methods: **A**) Basic Tangent Method. **B**) Average Angle Method. **C**) Balanced Tangent Method (*MD* is the total distance between survey points). **D**) Minimum Curvature Method. **E**) Radius of Curvature Method. **F**) Linear Interpolation Method.

There are few ways to test the accuracy of the desurveying methods without exact end of hole positions measured underground. One such method could be the creation and plotting of a random drillhole trajectory in computer code and then the calculation of the azimuth and plunge systemically along the curve, mimicking the capture of survey data. However, without such a test, the end of hole positions for each desurveying method can be compared relative to each other in order to assess their precision (Mason and Taylor, 1972; Walstrom *et al.*, 1972; Amorin and Broni-Bediako, 2010; Khaled, 2016; Škrjanc and Vulic, 2016; Eren and Suicmez, 2020).

Such comparisons show that differences between the methods at the start of the drillhole are initially low. However, the discrepancies are compounded when calculated cumulatively down the drillhole and distances between the survey points calculated by different methods are greatly amplified (Wilson, 1968), also resulting in 'sharp' unnatural discontinuities in the path of the drillhole at each survey point (Zaremba, 1973). Previous comparisons between desurveying methods have highlighted the relative differences between the survey point positions along the drillhole, with the *Basic Tangent* method interpreted to be the least precise when compared to other methods (Wilson, 1968; Mason and Taylor, 1972; Walstrom *et al.*, 1972; Škrjanc and Vulic, 2016 etc.). The *Minimum Curvature* method is generally accepted as the industry standard for desurveying calculations, with fewer compounding discrepancies (Sawaryn and Thorogood, 2005).

5.3 Assumptions of Desurveying Methods

The *Basic Tangent*, *Average Angle* and *Balanced Tangent* methods assume a series of straight-line segments between survey points as the drillhole deviates. Additionally, the *Basic Tangent* method uses only the downhole survey point measurements for each given interval, disregarding the initial survey measurements at the drillhole collar. In most cases, this method immediately produces an incorrect path from the drillhole collar **[Figure 5.1a]**.

The *Average Angle* and *Balanced Tangent* methods improve on the *Basic Tangent* method by giving equal weighting to both survey points 1 and 2, where survey point 1 is the first survey and survey point 2 is the second survey in each pair of measurements down the hole **[Figure 5.1]**. The *Average Angle* method **[Figure 5.1b]** gives equal weight to both measurements by averaging the Azimuth and Plunge values before plotting the straight line segment, whilst the *Balanced Tangent* method **[Figure 5.1c]** is similar to the *Basic Tangent* method, but uses half the measured distance between survey points (Walstrom *et al.*, 1972).

The *Minimum Curvature* method **[Figure 5.1d]** gives equal weight to measurements from both survey points 1 and 2 but assumes adjacent survey points lie on a circular arc (Mason and Taylor, 1972; Zaremba, 1973). This arc lies on a plane, the orientation of which is determined by the adjacent azimuth and plunge of the survey points. The drillhole is therefore always co-planar between survey point pairs, curving in only 2-dimensions between survey points. Consequently, the *Minimum Curvature* method still results in unnatural discontinuities at the survey points when viewed in 3-dimensions. The *Minimum Curvature* method uses a complex formula to produce a ratio factor determined by the angle between survey point pairs. The ratio factor is then used to multiply the results of the *Balanced Tangent* method.

The *Radius of Curvature* method **[Figure 5.1e]** plots a smooth curve in both the vertical and horizontal projections by drawing a curved drillhole around a cylinder (Wilson, 1968; Škrjanc and Vulic, 2016). This method uses the azimuth and plunge from both survey points in a survey point pair, giving equal weighting to both the first and second measurements. The *Radius of Curvature* method may still result in unnatural discontinuities at the survey points when viewed in 3-dimensions as the drillhole 'passes' from one cylinder to the next down the drillhole. Furthermore, the *Radius of Curvature* method results in a division by zero error if either the Azimuth or Plunge are the same at adjacent survey points, requiring a different calculation to be made or one of the values to be changed by a small amount (Eren and Suicmez, 2020). This results in a user induced error into the formula, further complicating the calculation process.

The *Linear Interpolation* method **[Figure 5.1f]** interpolates between each pair of survey points by dividing the distance between survey points into intervals. The length of each interval can be compared to the total distance between the pair of survey points, thus enabling the incremental change of azimuth and plunge measurements between survey points. The *Linear Interpolation* method assumes incremental straight drillhole segments, in addition to the assumption that the drillhole orientation changes gradationally between survey points. This method is not widely used in the desurveying literature.

5.4 Calculation of Positions at Survey Points

Formulae for the down hole desurveying methods using plunge are presented in **Table 5.1**. From these calculations, the entire drillhole can be plotted and the positions of the survey points in 3-dimensional space are known. *D1* and *D2* are the downhole distances along the

drillhole for successive survey points; *MD* is the downhole distance between successive survey points (*D2 - D1*); *P1* and *P2* are the plunges, and *Az1* and *Az2* are the azimuths, at successive survey points. *North*, *East* and *TVD* are the northings, eastings, and true vertical depths from the drillhole collar, respectively. *ΔNorth, ΔEast* and *ΔTVD* represent the change in the relative positions from one survey point to the next, cumulatively plotting the entire drillhole length. **Figure 5.2** details the derivation of the *Minimum Curvature* method.

Method	Equations
Basic Tangent	MD = $D2-D1$ ΔTVD = $MD * \sin(P2)$ $\Delta North$ = $MD * \cos(Az2) * \cos(P2)$ $\Delta East$ = $MD * \sin(Az2) * \cos(P2)$
Average Angle	MD = $D2-D1$ ΔTVD = $MD * [\sin((P1 + P2) / 2)]$ $\Delta North$ = $MD * [\cos((Az1 + Az2) / 2)] * [\cos((P1 + P2) / 2)]$ $\Delta East$ = $MD * [\sin((Az1 + Az2) / 2)] * [\cos((P1 + P2) / 2)]$
Balanced Tangent	MD = $D2-D1$ ΔTVD = $MD/2 * [\sin(P1) + \sin(P2)]$ $\Delta North$ = $MD/2 * [\cos(Az1) * \cos(P1) + \cos(Az2) * \cos(P2)]$ $\Delta East$ = $MD/2 * [\sin(Az1) * \cos(P1) + \sin(Az2) * \cos(P2)]$
Minimum Curvature	$A.B$ = $[\sin(Az1) * \cos(P1) * \sin(Az2) * \cos(P2)] + [\cos(Az1) * \cos(P1) * \cos(Az2) * \cos(P2)] + [\sin(P1) * \sin(P2)]$ $\lvert A\rvert\lvert B\rvert = \sqrt{[(\sin(Az1) * \cos(P1))^2 + (\cos(Az1) * \cos(P1))^2 + (\sin(P1))^2]} * \sqrt{[(\sin(Az2) * \cos(P2))^2 + (\cos(Az2) * \cos(P2))^2 + (\sin(P2))^2]}$ $\beta = \dfrac{A.B}{\lvert A\rvert\lvert B\rvert}$ $\qquad\qquad RF = \dfrac{\tan(\beta/2)}{(\beta/2)}$ MD = $D2-D1$ ΔTVD = $MD/2 * [\sin(P1) + \sin(P2)] * RF$ $\Delta North$ = $MD/2 * [\cos(Az1) * \cos(P1) + \cos(Az2) * \cos(P1)] * RF$ $\Delta East$ = $MD/2 * [\sin(Az1) * \cos(P1) + \sin(Az2) * \cos(P2)] * RF$
Radius of Curvature	MD = $D2-D1$ ΔTVD = $MD * [\cos(P2) - \cos(P1)] / [P1 - P2]$ $\Delta North$ = $MD * [\sin(P2) - \sin(P1)] * [\sin(Az2) - \sin(Az1)] / [(P2 - P1) * (Az2 - Az1)]$ $\Delta East$ = $MD * [\sin(P2) - \sin(P1)] * [\cos(Az1) - \cos(Az2)] / [(P2 - P1) * (Az2 - Az1)]$

Table 5.1: Desurveying calculations for the *Basic Tangent*, *Average Angle*, *Balanced Tangent* (Walstrom *et al.*, 1972), *Minimum Curvature* (Mason and Taylor, 1972; Zaremba, 1973) and *Radius of Curvature* (Wilson, 1968) methods. A and B represent the 3-dimensional direction vectors of *D1* and *D2*, respectively. *A.B* is equal to the dot product of the direction vectors *A* and *B*, where *A* and *B* are the direction vectors of adjacent survey points calculated using the orientation measurements at each survey point. $\lvert A\rvert\lvert B\rvert$ is equal to the product of the vector lengths of *A* and *B*. β is therefore the angle between *D1* and *D2* lying on a plane, as shown in **Figure 5.2**. *RF* is the Ratio Factor, used to multiply the Balanced Tangent calculations.
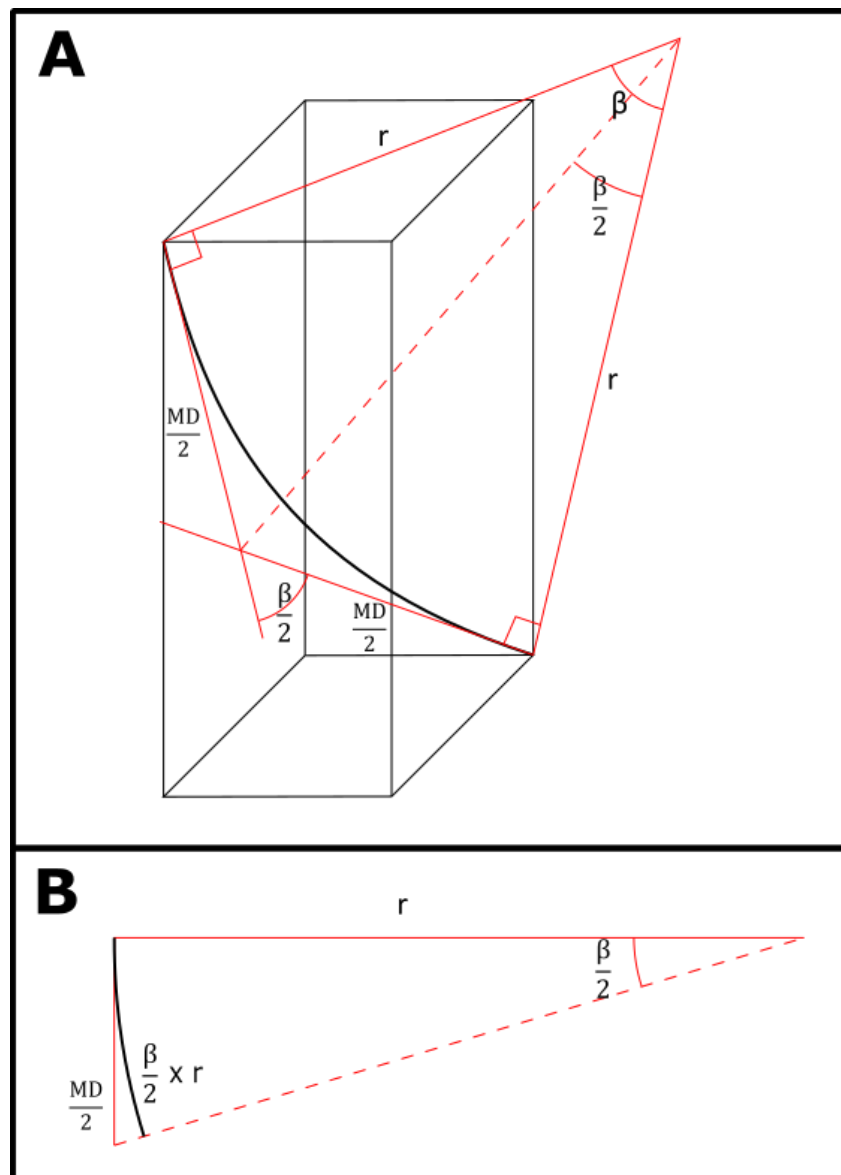
Figure 5.2: Derivation of the minimum curvature method. **A)** The minimum curvature method uses the balanced tangent method, along with the plunges and azimuths to calculate the beta (β) angle between successive survey points lying on an arc. **B)** The view normal to the plane on which the drillhole arc is calculated.

5.5 Calculation of Positions at Any Distance Along the Drillhole

New formulae to derive the position relative to the drillhole collar for any point along the

drillhole are described in **Table 5.2**. The formulas are based on the geometry of the drillhole

plotted for each method in **Figure 5.1**. The calculations in **Table 5.2** are used in the R and

Python code for the *Basic Tangent, Average Angle, Balanced Tangent and Minimum Curvature*

Method	Equations
Basic Tangent	MDn = $Dn - D1$ ΔTVD = $MDn * \sin(P2)$ $\Delta North$ = $MDn * \cos(Az2) * \cos(P2)$ $\Delta East$ = $MDn * \sin(Az2) * \cos(P2)$
Average Angle	MDn = $Dn - D1$ ΔTVD = $MDn * [\sin((P1 + P2) / 2)]$ $\Delta North$ = $MDn * [\cos((Az1 + Az2) / 2)] * [\cos((P1 + P2) / 2)]$ $\Delta East$ = $MDn * [\sin((Az1 + Az2) / 2)] * [\cos((P1 + P2) / 2)]$

Balanced Tangent	MD = $D2 - D1$
	ΔTVD :
	    If Dn < (D1 + MD/2)
	    = $(Dn - D1) * (\sin(P1))$
	    If Dn > (D1 + MD/2)
	    = $[(Dn - D1 - (MD/2)) * \sin(P2)] + [(MD/2) * \sin(P1)]$
	$\Delta North$:
	    If Dn < (D1 + MD/2)
	    = $[(Dn - D1) * \cos(P1) * \cos(Az1)]$
	    If Dn > (D1 + MD/2)
	    = $[(Dn - D1 - (MD/2)) * \cos(P2) * \cos(Az2)] + [(MD/2) * \cos(P1) * \cos(Az1)]$
	$\Delta East$:
	    If Dn < (D1 + MD/2)
	    = $[(Dn - D1) * \cos(P1) * \sin(Az1)]$
	    If Dn > (D1 + MD/2)
	    = $[(Dn - D1 - (MD/2)) * \cos(P2) * \sin(Az2)] + [(MD/2) * \cos(P1) * \sin(Az1)]$

Minimum Curvature	MD = $D2 - D1$
	ΔTVD :
	    If Dn < (D1 + MD/2)
	    = $[(Dn - D1) * (\sin(P1))] * RF$
	    If Dn > (D1 + MD/2)
	    = $([(Dn - D1 - (MD/2)) * \sin(P2)] + [(MD/2) * \sin(P1)]) * RF$
	$\Delta North$:
	    If Dn < (D1 + MD/2)
	    = $[(Dn - D1) * \cos(P1) * \cos(Az1)] * RF$
	    If Dn > (D1 + MD/2)
	    = $([(Dn - D1 - (MD/2)) * \cos(P2) * \cos(Az2)] + [(MD/2) * \cos(P1) * \cos(Az1)]) * RF$
	$\Delta East$:
	    If Dn < (D1 + MD/2)
	    = $[(Dn - D1) * \cos(P1) * \sin(Az1)] * RF$
	    If Dn > (D1 + MD/2)
	    = $([(Dn - D1 - (MD/2)) * \cos(P2) * \sin(Az2)] + [(MD/2) * \cos(P1) * \sin(Az1)]) * RF$

Table 5.2: Calculations for the easting, northing, and true vertical depth (*TVD*) relative to the drillhole collar for any point along the drillhole using the *Basic Tangent*, *Average Angle*, *Balanced Tangent* and *Minimum Curvature* methods. See text for details.

desurveying methods given in **Appendix F.1** and **Appendix F.2**. *Dn* is given as the input distance of interest along the core between *D1* and *D2*; *MDn* is the downhole distance between the point of interest (*Dn*) and the uphole distance along core measurement (*D1*); all other variables are as previously given. The method works iteratively down the hole, to the depth *Dn*.

5.6 Azimuth and Plunge Calculation at Any Drillhole Distance

Using the *Basic Tangent, Average Angle, Balanced Tangent and Minimum Curvature* desurveying methods, both the azimuth and plunges can be calculated in the R and Python codes for any point along the drillhole, summarised in **Table 5.3**. All variables are as previously given.

Method	Equations
Basic Tangent	*D1 ≤ Dn ≤ D2* Azimuth = *Az2* Plunge = *P2*
Average Angle	*D1 ≤ Dn ≤ D2* Azimuth = (*Az1* + *Az2*) / 2 Plunge = (*P1* + *P2*) / 2
Balanced Tangent AND *Minimum Curvature*	*If Dn < (D1 + MD/2)* Azimuth = *Az1* Plunge = *P1* *If Dn > (D1 + MD/2)* Azimuth = *Az2* Plunge = *P2*

Table 5.3: Calculations for the azimuth and plunge at any point along the drillhole using the *Basic Tangent*, *Average Angle*, *Balanced Tangent* and *Minimum Curvature* methods.

5.7 Comparison of Desurveying Methods

Desurveying methods are compared using drillhole data from Mount Isa Mines, where the drillholes generally pass through an anisotropic shale. The dominant anisotropy at Mount Isa is the ~65° west dipping bedding and bedding sub-parallel foliations. The drillholes examined in this study were drilled using the diamond drilling technique to collect whole rock core. Drillhole positions are compared for the *Basic Tangent*, *Average Angle*, *Balanced Tangent¸ Minimum Curvature* and *Radius of Curvature* desurveying methods for different drillhole lengths and angles between the drillhole and anisotropy.

5.7.1 Drillhole Length

The impact of drillhole length on the precision of the end of hole positions for the desurveying methods are shown in **Table 5.4**. Short (132.8 m – '201605182') **[Figure 5.3]** and long (627.3 m – '197506312') **[Figure 5.4]** Mount Isa drillholes with similar initial orientations have been plotted for each desurveying method. Both the short and long drillholes have an initial angle to the dominant anisotropy of ~65°.

For both drillholes, the end of hole position for the *Basic Tangent* method has the greatest difference from all methods **[Figure 5.3b and Figure 5.4b]**, confirming results from previous studies (Wilson, 1968; Mason and Taylor, 1972; Walstrom *et al.*, 1972; Amorin and Broni-Bediako, 2010; Khaled, 2016; Škrjanc and Vulic, 2016).

Apart from the *Basic Tangent* method, the end of hole positions differ on a scale of millimetres for the short drillhole when comparing the *Average Angle, Balanced Tangent, Minimum Curvature* and *Radius of Curvature* methods. The greatest distance between the end of hole

points for these desurveying methods in the short (132.8 m – '201605182') drillhole is 16 mm, between the *Average Angle* and the *Balanced Tangent*. All end of hole points for these desurveying methods lie within a cube of side 20 mm **[Figure 5.3c]**. The side of the cube is smaller than the 47 mm diameter of the short drill core, indicating the choice between these methods is irrelevant for such short drillholes.

	Short Drillhole (132.8 m) - 201605182 Azimuth = 90° Plunge = 0°			Long Drillhole (627.3 m) - 197506312 Azimuth = 89.92° Plunge = 0.5°		
	East Position (m)	North Position (m)	TVD Position (m)	East Position (m)	North Position (m)	TVD Position (m)
Basic Tangent	132.648	-1.954	-4.328	584.652	-5.265	-204.867
Average Angle	132.690	-1.284	-3.707	586.562	-4.219	-198.296
Balanced Tangent	132.674	-1.284	-3.707	586.430	-4.210	-198.263
Minimum Curvature	132.685	-1.284	-3.707	586.517	-4.210	-198.289
Radius of Curvature	132.685	-1.285	-3.707	586.518	-4.219	-198.285

Table 5.4: Summary table of the *Basic Tangent*, *Average Angle*, *Balanced Tangent, Minimum Curvature* and *Radius of Curvature* methods of two real drillholes, showing the end of hole positions in metres to the nearest millimetre, referenced from the collar coordinates (0,0,0). Both a short (132.8 metre – '201605182') and a long (627.3 metre – '197506312') drillhole are plotted in order to compare the impact the length of the drillhole has on the variance in the methods. As there is no base line for the actual position of the end of hole, this can only be used as a comparison between each of the methods.

Figure 5.4c shows the end of hole positions for the *Average Angle*, *Balanced Tangent*, *Minimum Curvature* and *Radius of Curvature* methods for the long (627.3 m – '197506312') drillhole. The separation of end of hole points between the methods is on a centimetre scale, with the greatest distance of 13.6 cm between the *Average Angle* and *Balanced Tangent* desurveying methods. All end of hole positions for this long drillhole fall within a cube with sides 15 cm.
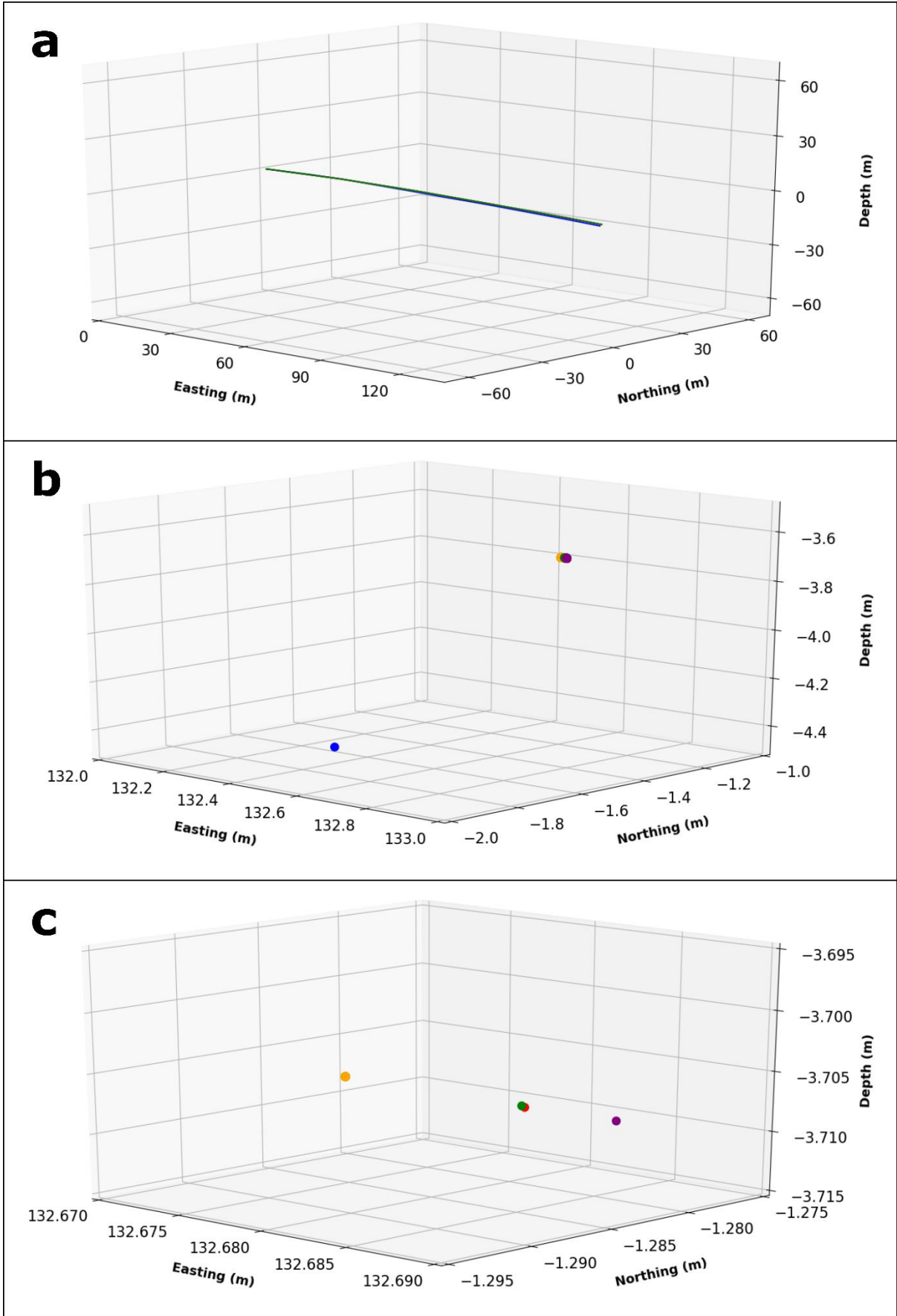
Figure 5.3: (Previous page) The short (132.8 metre – '201605182') drillhole showing the end of hole positions. Blue = *Basic Tangent*; Purple = *Average Angle*; Orange = *Balanced Tangent*; Red = *Minimum Curvature*; Green = *Radius of Curvature*. **a)** All drillhole methods plotted to scale. **b)** End of hole positions for all drillhole methods, plotted within a cube of side 1 metre. The *Average Angle*, *Balanced Tangent*, *Minimum Curvature* and *Radius of Curvature* methods plot in close proximity, with the *Basic Tangent* method located at a greater distance. **c)** End of hole positions of the *Average Angle*, *Balanced Tangent*, *Minimum Curvature* and *Radius of Curvature* methods located in a cube of side 2 cm. The drill core diameter of 4.7 cm is greater than this box size.

Figure 5.4: (Following page) The long (627.3 metre – '197506312') drillhole showing the end of hole positions. Blue = *Basic Tangent*; Purple = *Average Angle*; Orange = *Balanced Tangent*; Red = *Minimum Curvature*; Green = *Radius of Curvature*. **a)** All drillhole methods plotted to scale. **b)** End of hole positions for all desurveying methods located in a cube of side 8 metres. The *Basic Tangent* is located distal to the *Average Angle*, *Balanced Tangent*, *Minimum Curvature* and *Radius of Curvature* methods. **c)** End of hole positions for the *Average Angle*, *Balanced Tangent*, *Minimum Curvature* and *Radius of Curvature* methods, situated in a cube of side 0.15 metres.
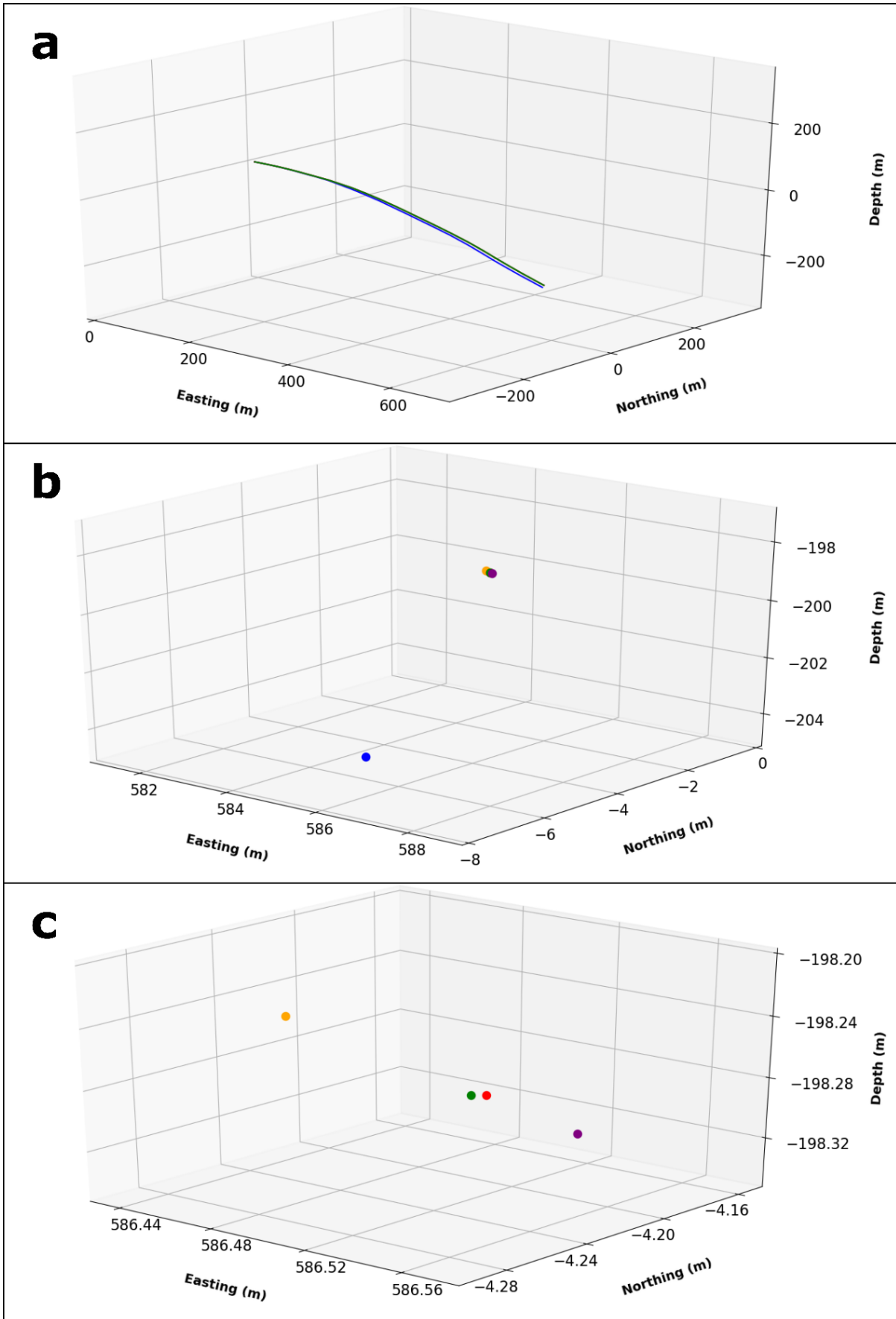
5.7.2 Anisotropy

Additional short (168 m – '199012092') and long (1200 m – 'T667ED1') drillholes with different orientations to the those previously shown, have been plotted **(Table 5.5)** in order to investigate the impact of anisotropy. The initial orientation of these drillholes are at a smaller angle (~40°) to the dominant anisotropy at Mount Isa.

In both drillholes the *Basic Tangent* method is the least precise compared to the other methods, with the end of hole positions consistently plotting at greater distances (199012092 – ~1.37 m; T667ED1 – ~4.92 m) from the other desurveying methods.

	Short Drillhole (168 m) - 199012092 Azimuth = 87.35° Plunge = -75°			Long Drillhole (1200 m) – T667ED1 Azimuth = 87° Plunge = -75°		
	East Position (m)	**North Position (m)**	**TVD Position (m)**	**East Position (m)**	**North Position (m)**	**TVD Position (m)**
Basic Tangent	59.472	0.848	-156.777	445.314	-79.134	-1105.763
Average Angle	58.202	0.792	-157.279	442.361	-75.639	-1107.382
Balanced Tangent	58.190	0.789	-157.255	442.192	-75.625	-1107.372
Minimum Curvature	58.195	0.789	-157.272	442.215	-75.631	-1107.421
Radius of Curvature	58.198	0.792	-157.271	442.306	-75.626	-1107.379

Table 5.5: Summary table of the *Basic Tangent*, *Average Angle*, *Balanced Tangent, Minimum Curvature* and *Radius of Curvature* methods of two real drillholes, showing the end of hole positions in metres to the nearest millimetre, referenced from the collar coordinates (0,0,0). Both a short (168 m – '199012092') and a long (1200 m – 'T667ED1') drillhole are plotted in order to compare the impact the length of the drillhole has on the variance in the methods. As there is no base line for the actual position of the end of hole, this can only be a comparison between each method.

For the other methods, short holes have smaller distances between end of hole points compared to the long drillholes. Comparing the distances between each desurveying method end of hole points as a proportion of the drillhole length, the long (1200 m – 'T667ED1') drillhole has smaller values than the short (168 m – '199012092') (**Table 5.6**). This is the opposite relationship to that seen in the previous two drillholes with the greater initial angles between the drillhole and anisotropy.

	Short (132.8 m) – '201605182'	Long (627.3 m) - '197506312'	Short (168 m) – '199012092'	Long (1200 m) – 'T667ED1'
Initial Angle between drillhole and anisotropy	~65°	~65°	~40°	~40°
Final Angle between drillhole and anisotropy	~68°	~89°	~51°	~56°
Maximum Distance between end of hole points (mm)	16	136	27	170
Maximum Distance as % of drillhole length	0.012%	0.021%	0.016%	0.014%

Table 5.6: Table of all four drillholes showing the initial and final angles between the drillhole and the dominant anisotropy. The maximum distance between desurveying method end of hole points are shown, excluding the *Basic Tangent*. The maximum distance between end of hole points in all four holes is between the *Balanced Tangent* and *Average Angle* methods. The end of hole distances between desurveying methods increase with increasing drillhole length. However, when displayed as a percentage of the drillhole length, the drillholes at smaller initial angles to the anisotropy ('199012092' and 'T667ED1') in fact decrease with drillhole length.

5.8 Discussion

5.8.1 Drillhole Terminology

In drilling engineering and structural geology, the term 'azimuth' is used for the angle of the horizontal projection of a line (the drillhole) measured clockwise from north. However,

differences in terminology arise when describing the angle from the vertical or horizontal. Structural geologists record measurements of lines in terms of 'inclination' or 'plunge' for the angle from horizontal. However, 'inclination' in drilling engineering is described as the angle of the drillhole from the vertical. Drilling engineers express the angle of the drillhole from the horizontal as its 'dip'. The term 'dip' is used in structural geology to record the angle of planes from the horizontal and should not be used for lineations. Therefore, the term 'plunge' is preferred as the cross-disciplinary resolution for describing the angle of the drillhole from the horizontal.

5.8.2 Comparison of the Effects of Drillhole Length on Desurveying Results

The *Basic Tangent* method is shown to have the least precision for all drillhole lengths. Differences between the end of hole positions for each desurveying method increase with drillhole length. The desurveying method that is employed is less important in short drillholes than for long drillholes. The calculated end of hole coordinates for the short (132.8 m – '201605182') drillhole in the *Average Angle*, *Balanced Tangent*, *Minimum Curvature* and *Radius of Curvature* methods all lie within a cube of side less than the drillhole diameter in the example from Mount Isa. The criterion that the end of hole positions lie within the drillhole diameter could act as an upper limit of acceptability when the choice of desurveying method becomes more important.

Other methods exist for measuring the deviation of drillholes, such as that shown by Bustos *et al.* (2020), which defines the deviation as a horizontal distance between the calculated and the projected end of hole points, if the drillhole were to follow the initial orientation of the drillhole. However, this method does not directly compare the desurveying methods and is

predominantly a function of the rock mass properties, such as anisotropy, that the drillholes pass through.

End of hole coordinates measured underground would be needed for a complete comparison of desurveying methods or by using more recent drillhole examples which use continuous surveying tools. In the absence of such data, the precision of each desurveying method has been compared. The significant assumptions of straight drillhole segments in the *Basic Tangent* method would suggest this to be the least accurate method in general. This method may only be accurate in rare examples such as straight drillholes with incremental dog-legs caused by rock anisotropies as described by Lubinski and Woods (1953), and Brown *et al.* (1981).

The *Minimum Curvature* and *Radius of Curvature* should be the most realistic and accurate desurveying methods, as they both plot the drillholes as curves. These methods are the industry standard methods for desurveying as they are consistently the most precise. However, all desurveying methods have inherent problems, including the *Minimum Curvature* and *Radius of Curvature* which still do not eliminate the unnatural discontinuities at survey points.

5.8.3 Effect of Rock Anisotropy on Desurveying Method Precision

A smaller initial angle between the drillhole and anisotropy resulted in a greater precision in the end of hole points when considering the distance as a proportion of the drillhole length for the long drillhole. This could suggest that the current desurveying methods have a higher precision as the drillhole gets longer when the initial angle is smaller. However, this result

could also be explained by unintentional deviation of the drillhole due to anisotropy, with the drillhole tending to deviate towards either parallel or normal to the anisotropy. Longer drillholes can reach either one of these preferred deviation directions within the length of the drillhole. A constant rate of deviation is then reached, with the drillhole continuing relatively straight, decreasing the deviation as a proportion of the drillhole as it lengthens. This decrease in deviation of the drillhole might result in smaller distances between end of hole points for each desurveying method as a proportion of the drillhole length.

5.8.4 Using Positions, Azimuth and Plunge

The R and Python codes available in **Appendix F.1** and **Appendix F.2** can be used to plot drillholes using the most commonly used desurveying methods, the *Basic Tangent*, *Balanced Tangent*, *Average Angle* and *Minimum Curvature*. The user is able to choose the desurveying method to quickly visualise the drillhole simultaneously calculating the position, azimuth, and plunge at any point of interest along the drillhole.

The R and Python codes require an input survey of the drillhole of interest in the form of a *.csv* file, named *Survey*. A point of interest can be stipulated in metres as a distance along the drillhole, defined as *Dn* within the code. This code allows the visualisation of the drillholes as 3-dimensional interactive plots. The position, azimuth and plunge of the point of interest are also made available as a printed statement.

5.9 Conclusions

Assumptions made in the desurveying calculations for drillholes by any existing method mean that the azimuths and plunges at survey points, which are used to define the drillhole along its length, do not give an accurate path of the drillhole after desurveying. Desurveying methods which plot drillholes as smooth curves are considered to be the best options for drillhole plotting.

The data show there is a high precision for the *Average Angle*, *Balanced Tangent*, *Minimum Curvature*, and *Radius of Curvature* methods for both long and short drillholes. The *Basic Tangent* method is the least precise. Excluding the *Basic Tangent,* the greatest distances between end of hole points in all drillholes are between the *Balanced Tangent* and the *Average Angle* methods. The end of hole points for the *Minimum Curvature* and *Radius of Curvature* methods consistently plot at the centre of the group and these are regarded as the most precise methods.

The length of the drillhole has a large impact on the consistency between the end of hole positions of the desurveying methods. For shorter drillholes the method used does not appear to be important. Disparity between the desurveying methods increases with drillhole length. When calculated as a proportion of the drillhole length, longer drillholes at smaller angles between the drillhole and rock anisotropy have shorter distances between each desurveying end of hole point.

Codes in R and Python are supplied to plot the drillhole using the various desurveying methods and output a 3-dimensional figure, allowing the quick calculation and visualisation of the drillhole data without sophisticated or commercial software. The codes allow azimuths,

plunges, and positions relative to the drillhole collar to be calculated for any distance along

the drillhole using the existing desurveying methods.

CHAPTER 6

Foliation Boudinage Structures in the Mount Isa Cu System

6.1 Introduction

The Mount Isa deposit has experienced a long and complex deformation history **[Figure 6.1]**, which has undergone some recent revisions (e.g. section 2.3). Perkins (1984), Swager (1985), Bell *et al.* (1988), Davis (2004) and Miller (2007) have all argued for Cu mineralisation at a late stage in the deformation sequence. However, even within this consensus there are different interpretations for the controls on Cu orebody orientations and relative timings (e.g. Perkins, 1984; Miller, 2007). The relative timings of deformation and mineralisation have previously been determined using small-scale structures and past studies have also shown the importance of these small-scale structures in elucidating the structural controls on orebodies at a larger scale (Perkins, 1984; Swager, 1985; Bell *et al.*, 1988; Davis, 2004). This chapter gives details of the previously undescribed foliation boudinage structures at Mount Isa, where they have been observed at the drill core-scale, proximal to the high-grade Cu orebodies.

This chapter aims to highlight the presence of drill core scale foliation boudinage structures at Mount Isa and their potential importance for Cu mineralisation by answering the following questions:

- What is the location, geometry, and timing of foliation boudinage structures?

- Is there any relationship between the foliation boudinage structures and Cu grades at Mount Isa?

Figure 6.1: (Following page) Summary of deformation events at Mount Isa based on previous deformation schemes (Perkins, 1984; Swager, 1985; Bell *et al.*, 1988; O'Dea and Lister, 1995; O'Dea *et al.*, 1997a, 1997b; Davis, 2004; Miller, 2007; Wilde, 2011). **D1** – localised reverse reactivation of normal faults as a result of north-south shortening; **D2** – east-west shortening; **D3** – top to the east shear, weakly developed at Mount Isa Mine; **D4a** – ENE-WSW shortening and mineralisation at Mount Isa; **D4b** – WNW-ESE shortening and mineralisation at Mount Isa; **D5a** – top to the east transport direction on west-dipping reverse faults; **D5b** – conjugate sinistral-reverse and dextral-reverse faults with top to the east or west transport directions consistent with continued east-west shortening.
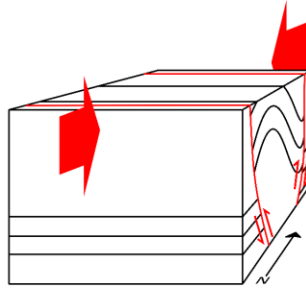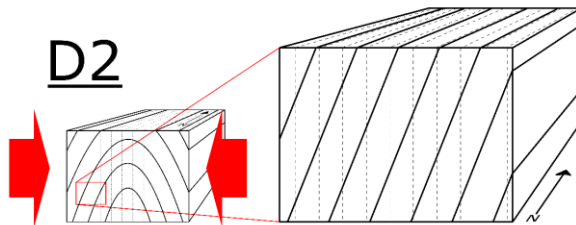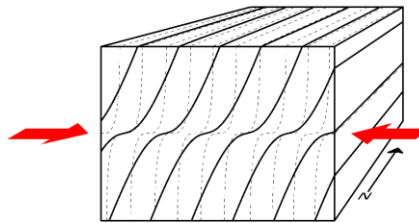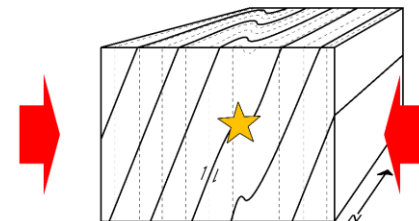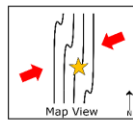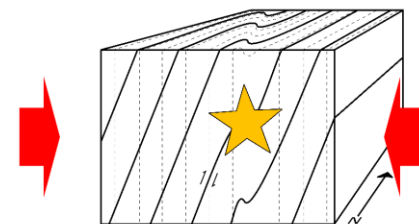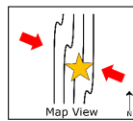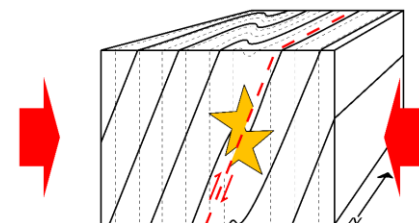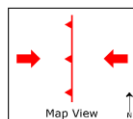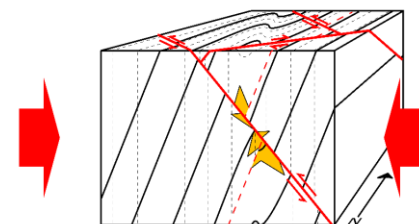
6.2 Methods

As previously stated in Chapter 4, only the two RD drillholes (T667ED1 and T190ED1) are oriented, thus only the structural measurements from the RD drillholes have been used in this chapter. The assay and lithology logs from section 4.3 are used in this chapter and compared to the positions of the foliation boudinage structures. For this chapter, samples of foliation boudinage structures were cut in cross-section (XZ-plane) as this produced the best visible depictions of the structures for petrographic analysis. Polished thin sections were made for petrographic analysis and mineral phase maps were collected using a scanning electron microscope (SEM).

6.3 Results

6.3.1 Petrography

In the host rock surrounding the orebodies, fine-grained pyrite replaces shale selectively along layers **[Figure 6.2a** and **Figure 6.3]**. Small veinlets of quartz occur normal or oblique to layering; their timing is generally early, forming after the fine-grained pyrite and before the coarse-grained pyrite **[Figure 6.2a,b]**. Coarse-grained pyrite comprises euhedral to subhedral crystals ranging in size from 500 µm to mm, occurring as single porphyroblasts or in trains at contacts between particular shale beds **[Figure 6.2a]**. The coarse-grained pyrite is commonly zoned **[Figure 6.2c]** and is associated with later arsenopyrite growth rims (Cave *et al.*, 2020). Dolomite replaces shale layering, occurring throughout layers or as lenses **[Figure 6.2d, Figure 6.4c** and **Figure 6.5a,b,d,f]**. Brecciation occurs with silica-dolomite infilling between shale clasts with some alteration of the shale **[Figure 6.2b]**. Pyrrhotite occurs as infill in silica-

dolomite breccia and replacement in dolomitic layers **[Figure 6.2d]**. Chalcopyrite occurs as

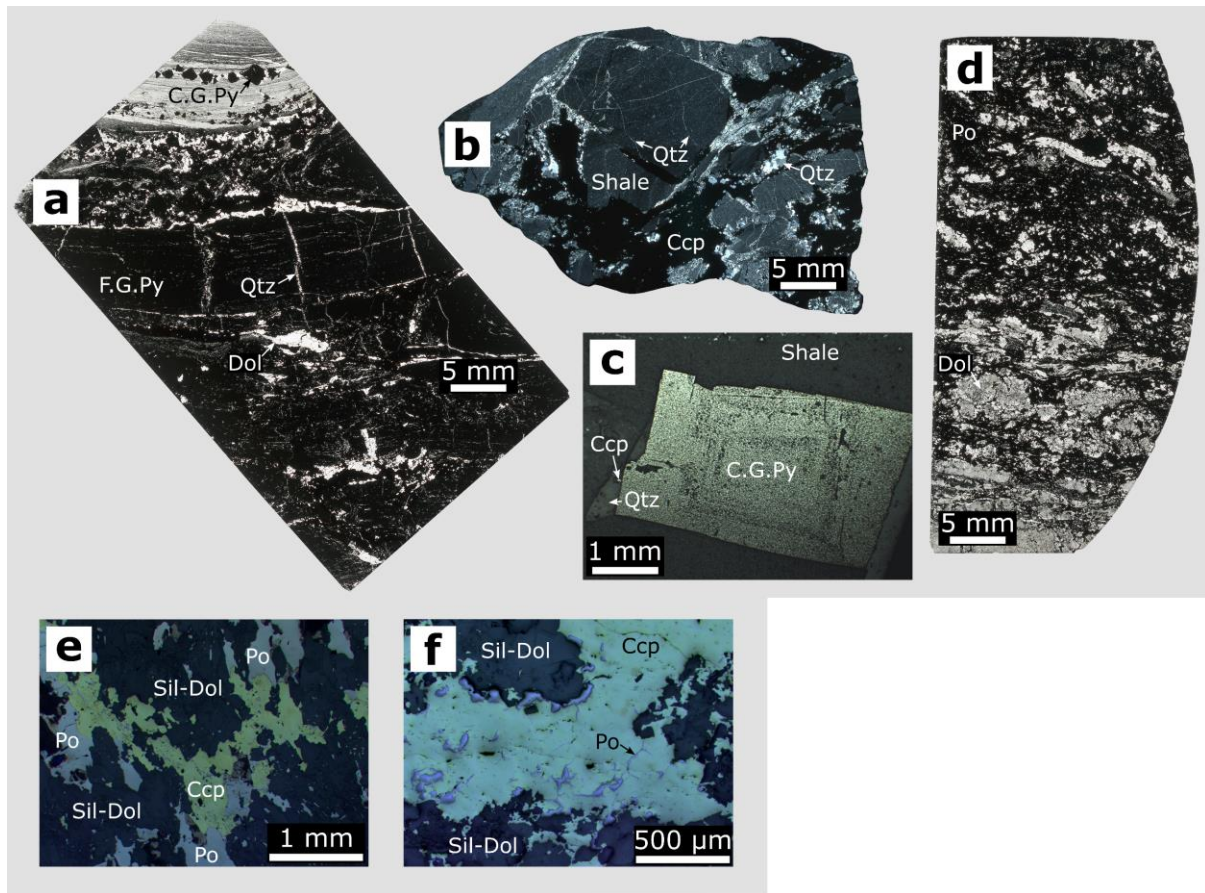veins and replacement and varies in samples from pre-, syn- to post-pyrrhotite **[Figure 6.2e,f]**.

Figure 6.2: Polished sections from underground samples and drill core in the Mount Isa system. **a)** Fine-grained pyrite selectively replacing shale layers, with later quartz veinlets. Coarse-grained pyrite restricted to contacts between select shale layers. Sample BW304B, Drillhole № '201904012', 36.65 m, (PPL). **b)** Silica-dolomite and chalcopyrite breccia associated with the main Cu mineralisation event. Shale clasts show small pre-brecciation quartz veinlets. Sample BW308, collected from underground proximal to Cu orebodies, (XPL). **c)** Zoned coarse-grained pyrite with quartz and chalcopyrite in strain shadow. Sample 'F', Drillhole № '201903092', 32.1 m, (RL). **d)** Coarse-grained dolomite alteration of shale layering which is subsequently replaced by pyrrhotite. Sample BW205, Drillhole № '201903092', 152.8 m, (PPL). **e)** Early-pyrrhotite and later chalcopyrite in silica-dolomite. Sample BW201B, Drillhole № '201904012', 175.5 m, (RL). **f)** Early chalcopyrite with later pyrrhotite in silica-dolomite. Sample BW402, Drillhole № '201903092', 168 m, (RL). **Key:** Ccp = chalcopyrite, C.G.Py = coarse-grained pyrite, Dol = dolomite, Po = pyrrhotite, Qtz = quartz, Shale = unaltered shale, Sil-Dol = silica-dolomite, Sul = multiple sulphides, PPL = Plane-polarised light, XPL = Cross-polarised light, RL = Reflected light.

Asymmetrical foliation boudinage structures are the most common type observed in Mount Isa drill core **[Figure 6.4]**. Foliation boudinage structures and polished sections of cross-sections through the structures are shown in **[Figure 6.5]**. Dolomite replaces shale layers and forms lenses adjacent to some foliation boudin samples **[Figure 6.4c** and **Figure 6.5b,d]**. Regular boudins are observed in these dolomitic layers close to the foliation boudinage structures where they show an equivalent petrography, with silica-dolomite rims and sulphide infills **[Figure 6.5d,f]**. Coarse-grained pyrite with quartz strain shadows are observed in close proximity to the foliation boudinage structures in some samples. Quartz veins normal to the layering and veinlets oblique to the layering are cross-cut and deformed by the foliation boudinage structures **[Figure 6.5a,b,c,g]**.

Mineral	Pre-FBS		FBS Infill	
Pyrite (F.G)	▬			
Quartz	▬		▬▬	
Pyrite (C.G)		▬		
Arsenopyrite		▬		
Dolomitisation		▬		
Silicification		▬		
Dolomite			▬	
Pyrrhotite			···▬	▬
Chalcopyrite			···▬	▬
Deformation stage	Pre-D4a	D4a (early)	D4a N-plunge FBS	D4b S-plunge FBS

Brecciation

Figure 6.3: Paragenetic chart of the main mineralisation associated with foliation boudinage structures at Mount Isa.
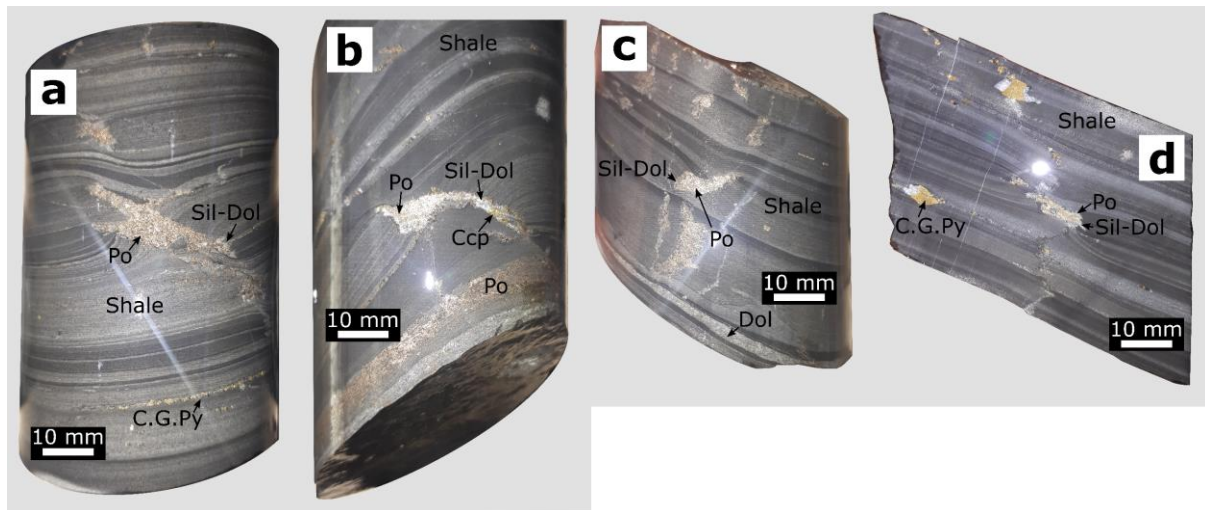
Figure 6.4: Photographs of asymmetrical foliation boudinage structures from Mount Isa drill core. **a)** Pyrrhotite filled foliation boudinage structure with silica-dolomite rim. Coarse-grained pyrite can be seen along one shale layer interface. Drillhole № '201903052', 23.5 m (all depths downhole). **b)** Pyrrhotite and chalcopyrite filled foliation boudinage structure with silica-dolomite rim. Pyrrhotite replacement also along a shale layer. Drillhole № '201902182', 16.1 m. **c)** Pyrrhotite filled foliation boudinage structure with silica-dolomite rim. Dolomite replacing shale layering. Drillhole № '201903092', 2.4 m. **d)** Pyrrhotite filled foliation boudinage structure with silica-dolomite rim. Coarse-grained pyrite has bedding parallel strain shadows and is cut by a bedding normal vein. Drillhole № 'T667ED1', 1202.2 m. **Key:** Ccp = chalcopyrite, C.G.Py = coarse-grained pyrite, Dol = dolomite, Po = pyrrhotite, Qtz = quartz, Shale = relatively unaltered shale, Sil-Dol = silica-dolomite, Sul = multiple sulphides.

All foliation boudinage structures analysed in this study are completely filled by a combination of quartz, dolomite, pyrrhotite and minor chalcopyrite. Quartz infilling around the edges of the interior of the foliation boudinage structures creates a rim of quartz growth into the structures **[Figure 6.4** and **Figure 6.5]**. Later coarse-grained dolomite is the dominant non-sulphide infill in the foliation boudinage structures and occurs within the quartz rim. The dolomite infill and quartz rim both show deformation in the form of deformation twins and undulose extinction, respectively. In places, the silica-dolomite also alters the wall rock and appears to propagate from the foliation boudinage structure **[Figure 6.5b]**.

Pyrrhotite is the most abundant mineral found within the foliation boudinage structures. The pyrrhotite shows an infill texture around dolomite and quartz grains and is observed replacing dolomite **[Figure 6.5e]**. Chalcopyrite is observed in only a few foliation boudinage structures on the drill core scale, where it is intergrown with pyrrhotite **[Figure 6.4b]**. Within one foliation boudinage structure, chalcopyrite cross-cuts the pyrrhotite as a vein style or late infill mineralisation, giving a post-pyrrhotite timing **[Figure 6.5g]**.
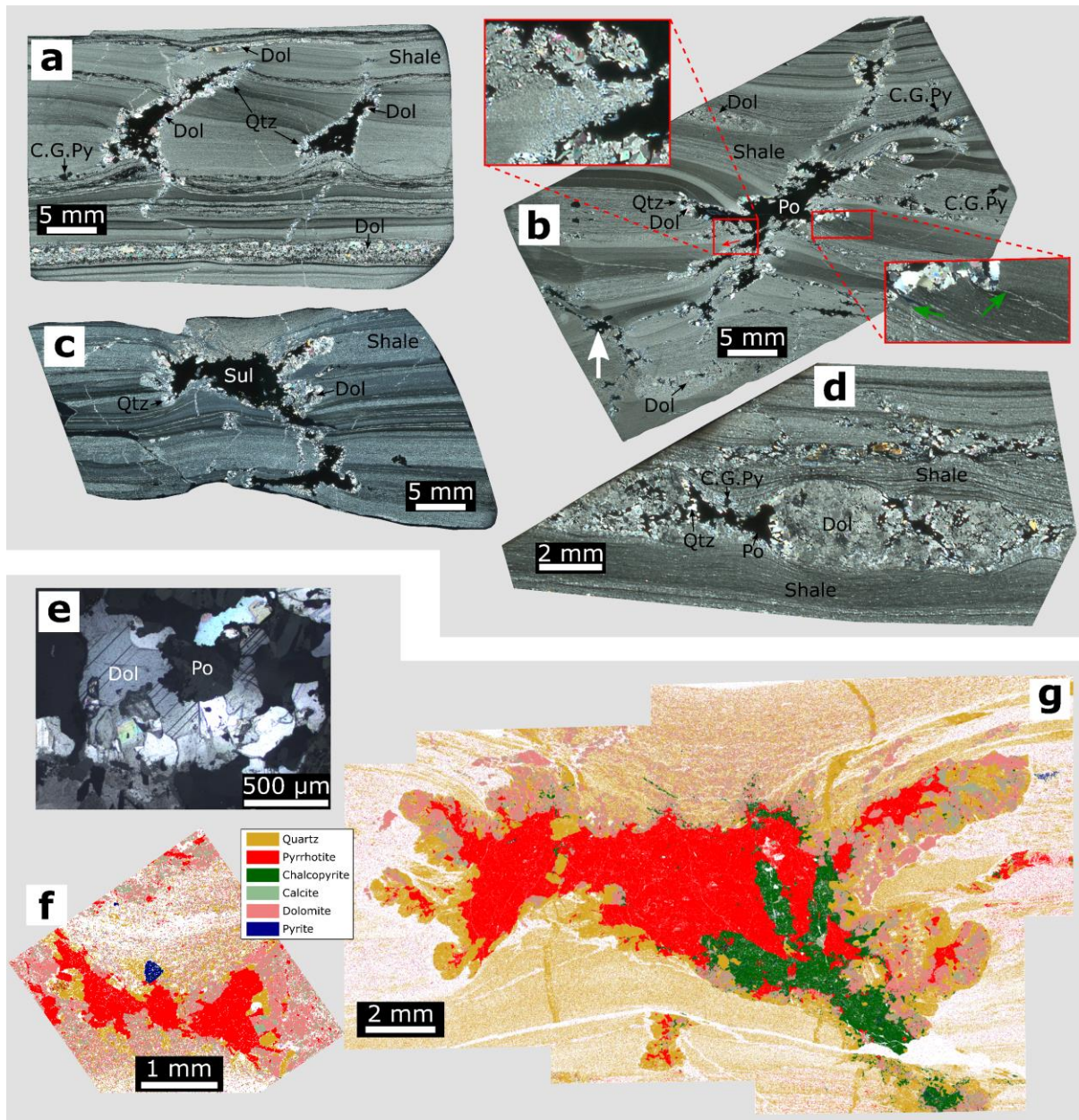
Figure 6.5: (Previous page) Polished sections and scanning electron microscope (SEM) phase maps of foliation boudinage structures from drill core in the Mount Isa system. **a)** Pyrrhotite filled foliation boudinage structures with silica-dolomite rims. Coarse-grained pyrite along a layer interface and dolomite replacing shale. Sample 'BW302', Drillhole № '201903092', 8.0 m, (XPL). **b)** Pyrrhotite filled foliation boudinage structure with silica-dolomite rim. Coarse-grained pyrite throughout sample. A lens of dolomite replaces shale. Silica-dolomite alteration of the shale away from the foliation boudinage structure is represented by a red arrow. Pre-foliation boudinage veins are cross-cut and deformed by the foliation boudinage structure (green arrows). A smaller foliation boudinage structure indicating a conjugate set is seen at bottom left of polished thin section (white arrow). Sample 'E', Drillhole № '201903092', 32.1 m, (XPL). **c)** Pyrrhotite and chalcopyrite infilled foliation boudinage structure with silica-dolomite rim. Pre-foliation boudinage veins are cross-cut and deformed by the foliation boudinage structure. Sample 'BW303', Drillhole № '201904012', 159.3 m, (XPL). **d)** Pyrrhotite filled boudin within a dolomite layer adjacent to a foliation boudinage structure. The competency difference between the shale and the dolomite enables the formation of boudins. A coarse-grained pyrite grain can be seen in the pinched neck of the boudin. Sample 'G', Drillhole № '201903092', 32.1 m, (XPL). **e)** Pyrrhotite replacing dolomite grain within the interior of a foliation boudinage structure. Sample 'BW205', Drillhole № '201903092', 152.8 m, (XPL+RL). **f)** Phase map of the boudin within the dolomite layer in '(d)', showing the pyrrhotite infill similarly to the foliation boudinage structures (key in figure). Sample 'G', Drillhole № '201903092', 32.1 m. **g)** Phase map of the interior of '(c)' showing the quartz and dolomite rim. The later pyrrhotite infills around and replaces earlier grains of dolomite. A later vein-like chalcopyrite mineralisation cuts through the pyrrhotite mass. Sample 'BW303', Drillhole № '201904012', 159.3 m. **Key:** Ccp = chalcopyrite, C.G.Py = coarse-grained pyrite, Dol = dolomite, Po = pyrrhotite, Qtz = quartz, Shale = unaltered shale, Sil-Dol = silica-dolomite, Sul = multiple sulphides, PPL = Plane-polarised light, XPL = Cross-polarised light, RL = Reflected light.

6.3.2 Foliation Boudinage Structure Orientations

The long-axes of drill core scale foliation boudinage structures form a predominant north-south lineation with gentle to moderate plunges **[Figure 6.6]**. Bedding orientations change slightly from a WSW to a WNW dip direction with increasing depth down RD drillhole T667ED1 **[Figure 6.6]** and are representative of the dominant orientations in the mine. The long-axis orientations of foliation boudinage structures also vary with depth, changing from NNW-SSE to NNE-SSW trends at greater depths **[Figure 6.6]**. The foliation boudinage structures always lie on or close to the local bedding **[Appendix C.3]**. A Terzaghi correction (Terzaghi, 1965;

Wallis *et al.*, 2020) was performed on the bedding measurements but made no discernible

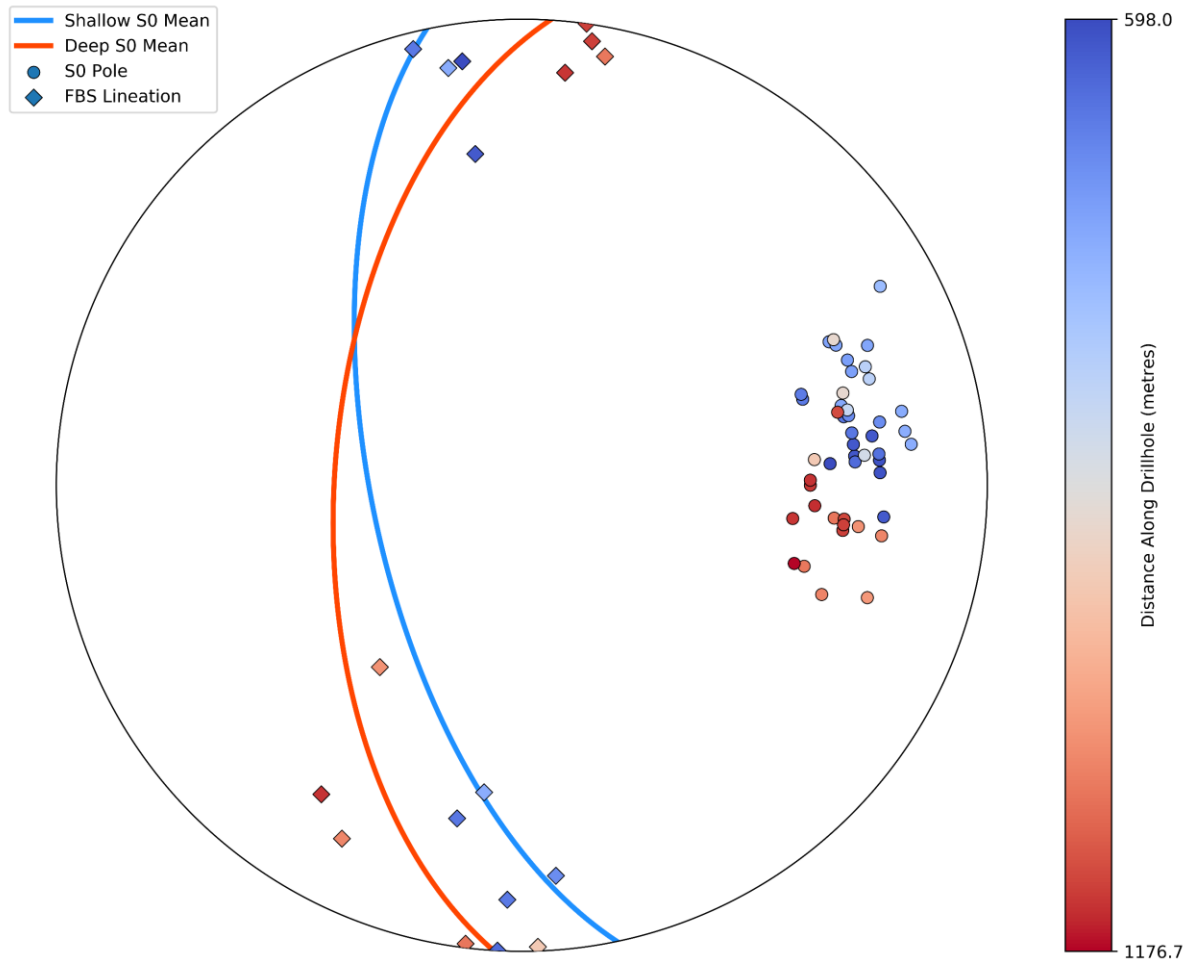difference as the drilling orientation is at a high angle to bedding.

Figure 6.6: Lower hemisphere, equal area stereoplot of poles to bedding (circles) and foliation boudinage structures (diamonds) shaded by distance along drillhole T667ED1. Mean bedding planes are shown as great circles for shallow (blue) and deep (red) measurements that coincide with foliation boudin orientation changes with distance. Drillhole № 'T667ED1', drillhole collar azimuth = 087° and plunge = -75°.

6.3.3 Distribution of Foliation Boudinage Structures by Rock Type

A total of 255 foliation boudinage structures were observed in the MICO and RD drill core and have been normalised by the total length of the lithologies in which they were located **[Figure 6.7]**. By far the most common rock type for foliation boudinage structures is the relatively undeformed Urquhart Shale **[Appendix C.2]**, and when normalised, also has the greatest number of foliation boudinage structures per metre **[Figure 6.7]**. No foliation boudinage structures were identified in the 'pyritic shale (>20% pyrite)', 'carbonaceous mylonite', 'buck quartz' or 'greenschist' lithologies.
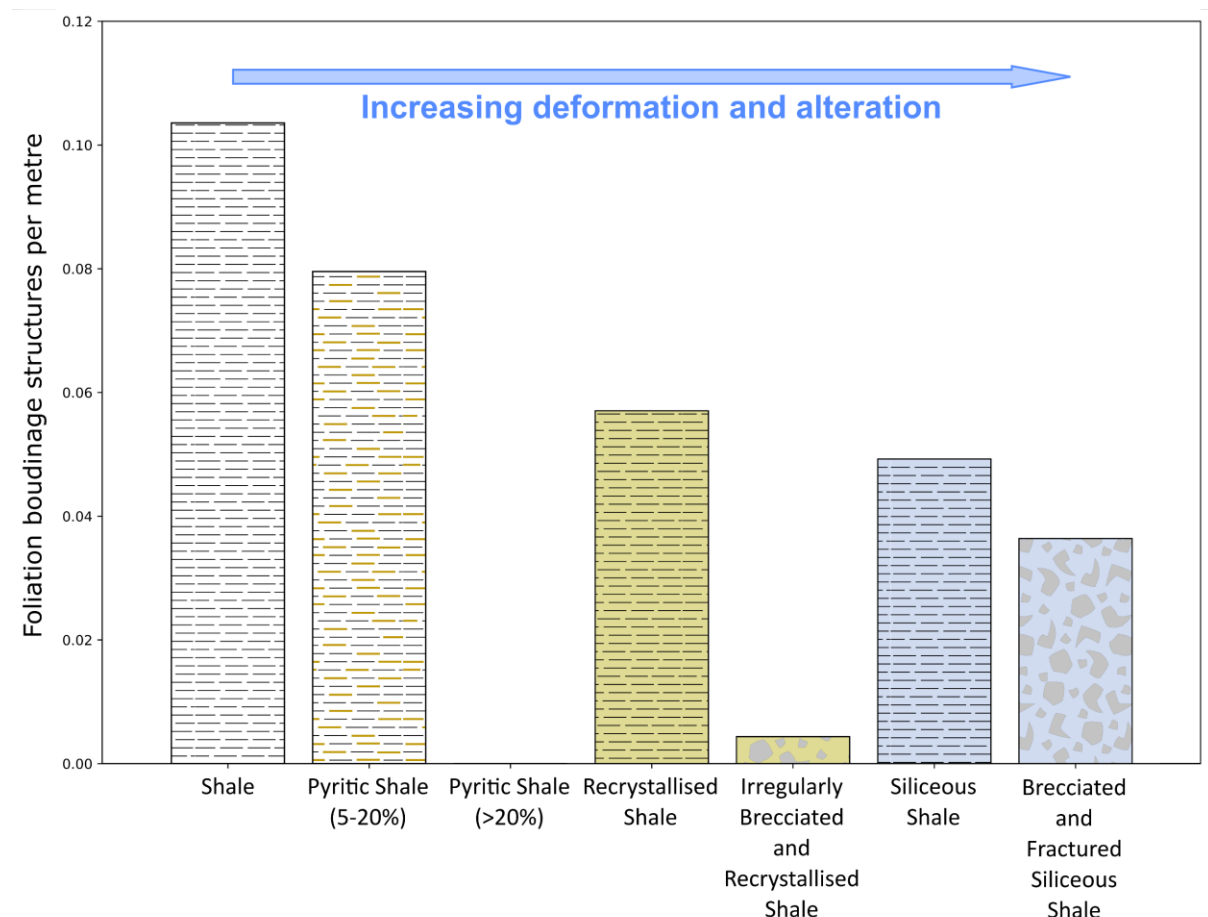

Figure 6.7: Normalised occurrences of foliation boudinage structures per lithology in the Mount Isa drill core. Foliation boudinage structures are identified most commonly in the less deformed lithologies.

6.3.4 Distribution of Ore-Grade Cu by Rock Type

Lengths of drill core intervals with ore-grade Cu (>3% Cu) are normalised to the total lengths of each lithology and plotted against the logged drill core lithologies **[Figure 6.8; Appendix C.2]**. In the 47.7 metres of drill core at greater than 3% Cu, the most common rock type is the 'brecciated and fractured siliceous shale'. The ore-grade Cu is situated primarily in the brecciated and altered lithologies, with no Cu greater than 3% in the 'pyritic shale (>20% pyrite)', 'carbonaceous mylonite', 'buck quartz' or 'greenschist'.
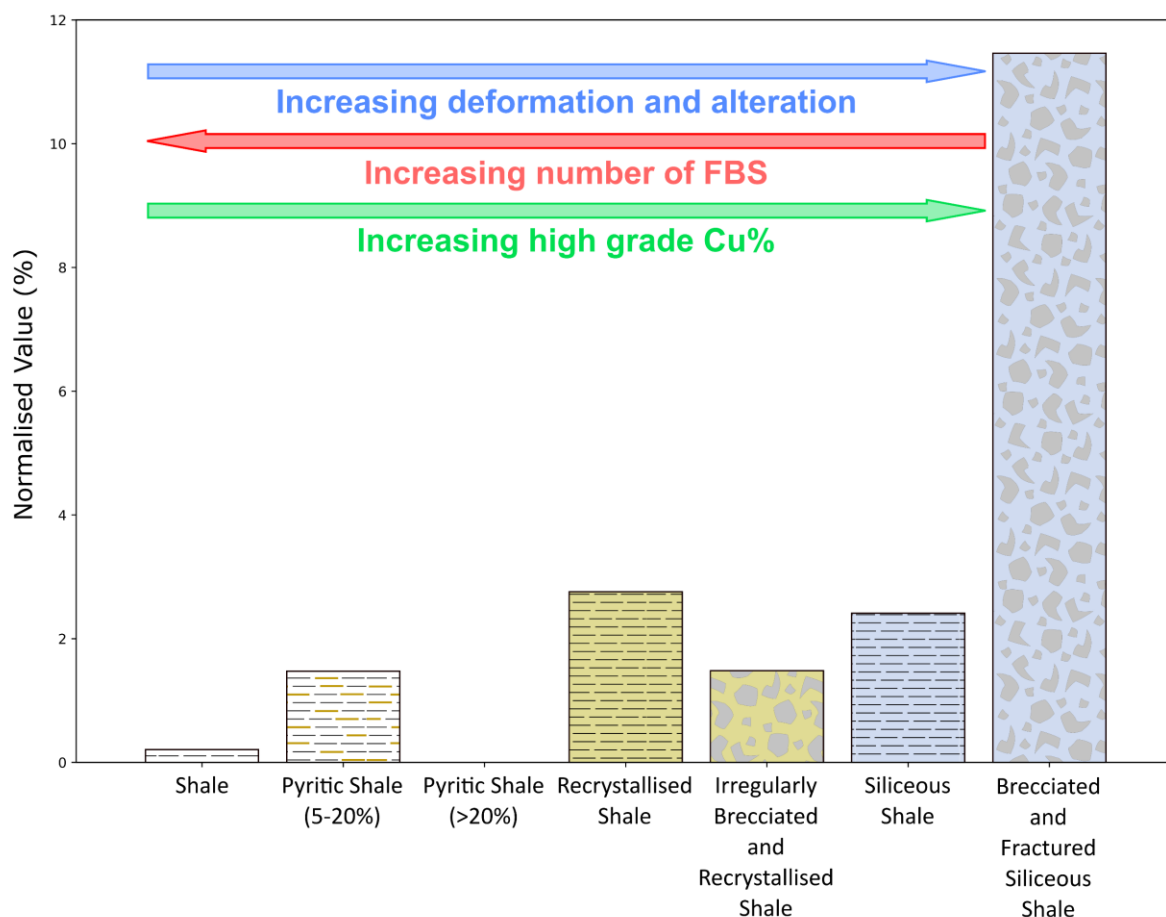

Figure 6.8: Lengths of drill core intervals with ore-grade Cu (>3% Cu) normalised to the total lengths of each lithology in the studied drillholes. The plot shows a strong correlation between ore-grade Cu and alteration and deformation.

6.3.5 Cu Grade of Foliation Boudinage Structures

Downhole Cu percentages and locations of foliation boudinage structures for three example drillholes are presented in **Figure 6.9**. Foliation boudinage structures are predominantly located in drillhole intervals with the lowest Cu percentages and almost always below the 3% Cu grade **[Appendix C.4]**.
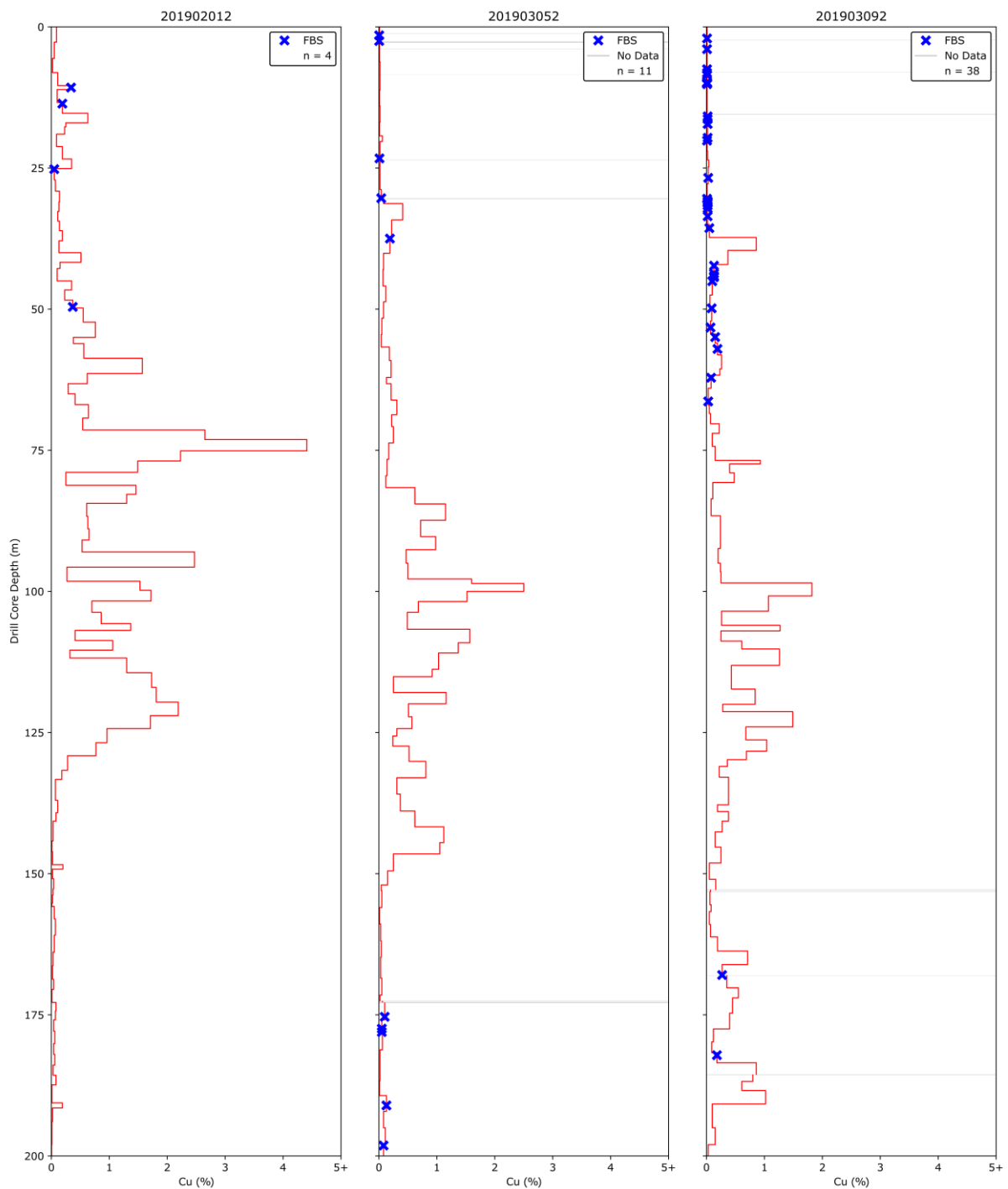
Figure 6.9: (Previous page) Downhole logs of Cu % in three MICO drillholes showing the locations of foliation boudinage structures and associated Cu %. Foliation boudinage structures are predominantly located in drillhole intervals with the lowest Cu %.

6.4 Discussion

6.4.1 Paragenesis

The petrographic observations in this study show that quartz forms an initial rim inside the foliation boudinage structures with a subsequent dolomite infill **[Figure 6.3** and **Figure 6.5]**. This characteristic, seen in all the sampled foliation boudinage structures from Mount Isa, suggests that the infill mineralisation of the foliation boudinage structures is syn-silica-dolomite and the structures developed during this event. Within the Cu orebodies, the silica-dolomite generally forms a breccia fill around shale clasts (Perkins, 1984; Bell *et al.*, 1988; Cave *et al.*, 2020) and is not conducive to the formation or preservation of the foliation boudinage structures as the breccia lacks the necessary anisotropy. No samples of foliation boudinage structures have yet been identified in brecciated shale clasts at Mount Isa. The foliation boudinage structures may have a pre- to syn-breccia timing, forming within the silica-dolomite halo, but distally to the breccia zone.

Pyrrhotite both replaced and infilled around the earlier silica-dolomite grains within the foliation boudinage structures **[Figure 6.5]**, consistent with the post-silica-dolomite timing of most pyrrhotite at Mount Isa (Perkins, 1984; Cave *et al.*, 2020). Pyrrhotite is the most abundant sulphide mineral within the foliation boudinage structures and occurs within every sampled structure. Miller (2007) noted that the pyrrhotite has a strong correlation with the Cu, dolomite, and siliceous inner core and the data presented in this study broadly agrees with this relationship.

Only around 8% of the sampled drill core scale foliation boudinage structures contain chalcopyrite. Where chalcopyrite is present, it occurs either coeval with the pyrrhotite or as vein-like mineralisation cross-cutting the pyrrhotite infill **[Figure 6.5g]**. Pyrrhotite has been observed to be intimately associated with the chalcopyrite, and textural evidence shows both quartz and dolomite dissolution during chalcopyrite formation (Wilde *et al.*, 2006). Perkins (1984) and Miller (2007) describe strain free quartz associated with the chalcopyrite mineralisation. However, quartz and dolomite within the foliation boudinage structures have indications of strain.

6.4.2 Foliation Boudinage Structure Logging and Scaling Limitations

Foliation boudinage structures are predominantly located within the less deformed and altered lithologies **[Figure 6.7]** as a result of the shale layering or a layer-parallel foliation providing the anisotropy and homogeneity of these rock types. Foliation boudinage structures could not form in rocks that lost their anisotropy during brecciation, deformation and alteration. The dolomitisation and silicification of the shale is generally considered to be an early alteration with subsequent brecciation associated with the silica-dolomite and Cu ore (Perkins, 1984; Swager, 1985; Cave *et al.*, 2020).

Perkins (1984) showed that dolomite porphyroblasts truncate and overgrow S2 cleavages, indicating a post-D2 age for this dolomitisation. Perkins (1984) also observed that the dolomite is both truncated by and overgrows the S4 cleavages and this has been used as evidence for a syn-D4a timing for dolomite porphyroblast growth (Miller, 2007). Foliation boudinage structures are generally absent in the dolomitised layers, possibly due to their heterogeneity and increased shear strength. Instead, regular boudins can be seen in these

layers, owing to the development of a competency contrast between the ductile shale and more competent dolomite **[Figure 6.5d,f]**. The foliation boudinage structures are interpreted to have formed coeval with and adjacent to the regular boudins, and both have a post-dolomitisation timing.

Silicification of the shale is considered to have a post-dolomitisation timing (Perkins, 1984; Swager, 1985; Cave *et al.*, 2020). Siliceous shales and brecciated siliceous shales generally form the inner core of the deposit, with most Cu mineralisation associated with these lithologies (Perkins, 1984). Relatively few foliation boudinage structures formed in the siliceous shale lithology **[Figure 6.7]**. Where they are observed, they are interpreted to have a post-silicification timing as the foliation boudinage structures are not overprinted by the silicification process. The foliation boudinage structures located in the siliceous shale are commonly filled with chalcopyrite, reflecting the closer proximity to the high-grade Cu mineralisation.

The ore-grade Cu is located in the more deformed and altered lithologies, close to or within the zone of brecciation as shown in **Figure 6.8**. A greater proportion of high-grade Cu in the more altered lithologies is expected as the silica-dolomite alteration and brecciation are generally understood to lay the groundwork for the subsequent Cu mineralisation (Perkins, 1984; Swager, 1985; Bell *et al.*, 1988; Miller, 2007; Cave *et al.*, 2020). The shale lithology has by far the most foliation boudinage structures **[Appendix C.2]**, but is not typically associated with high-grade Cu (e.g. Perkins, 1984; Swager, 1985; Swager *et al.*, 1987; Bell *et al.*, 1988; Davis, 2004; Miller, 2007; Cave *et al.*, 2020). Contrary to this general relationship, **Figure 6.8** shows that there is some high-grade Cu in the shale lithology. This may be due to narrow chalcopyrite veins that intersect the shale.

Arslan *et al.* (2008) showed that foliation boudinage structures occur on scales similar to those found at Mount Isa and also on scales much larger than drill core. Aerden (1991) demonstrated the importance of these large-scale foliation boudinage structures on the control of orebodies at the Rosebery deposit, Tasmania. The orebodies at Rosebery occur in similar rock types and deformation styles to those at Mount Isa. Although they have not been identified during this study, large-scale foliation boudinage structures may exist and exert controls on the Cu orebodies at Mount Isa. Davis (2004) showed that the Mount Isa Cu orebodies were steeply dipping with gentle to moderate plunges to the north and NW, consistent with the orientations of the NW-plunging small-scale foliation boudinage structures observed in this study. The drillholes may intersect large-scale foliation boudinage structures that are indistinguishable on the drill core scale from structures such as breccia, recrystallisation or veins. Foliation boudinage structures larger than the drill core diameter could be distinguished by the bending of bedding adjacent to these zones, but this is difficult to assess without oriented drill core close to the Cu orebodies**.**

Currently, foliation boudinage structures have only been found at Mount Isa mine. However, they may exist at other deposits, and a search for their distribution at other Pb-Zn and Cu deposits in the area would allow their evaluation as a possible vector to ore.

6.4.3 Structural Measurements and Timing of Foliation Boudinage Structures

The most common foliation boudinage structures observed at Mount Isa are the asymmetrical x-type of Arslan *et al.* (2008) **[Figure 6.3** and **Figure 6.5]**. Asymmetrical foliation boudinage structures can form in both simple and pure shear conditions, depending on initial

fracture geometries **[Figure 3.5]**. The asymmetrical structures at Mount Isa are likely to have formed through simple shear from fractures sub-perpendicular to bedding. Asymmetrical x-type foliation boudinage structures which open into fluid filled voids and form by simple shear can have many initial fracture geometries, compared to those forming by pure shear which require a specific sigmoidal-shaped fracture to form **[Figure 3.5]** (Arslan *et al.*, 2008). It is considered unlikely that all foliation boudinage structures at Mount Isa formed by pure shear from fractures with this specific geometry. Therefore, it is more likely the asymmetrical foliation boudinage structures formed by simple shear of fractures with various orientations.

The necks of foliation boudinage structures are shown to have both north and south plunges in the same drill core independently of depth **[Figure 6.6]**, implying that the plunge directions are not domainal in the deposit. The long-axes of foliation boudinage structures lie on the great circles of the Urquhart Shale bedding planes **[Figure 6.6; Appendix C.3]**. This relationship is preserved as the orientation of the bedding changes along the drillhole. Therefore, the shale bedding or a bedding-parallel foliation must be the controlling fabric anisotropy in the development of the foliation boudinage structures at Mount Isa. The homogeneous nature of the Urquhart Shale and anisotropy provided by the fine laminations favour the formation of foliation boudinage structures.

The north-south orientations of the foliation boudin long-axes indicate the intermediate principal strain axis during their formation (Arslan *et al.*, 2008) and when combined with the steep orientation of the anisotropy, show approximate east-west shortening **[Figure 6.10]**. The deformation history at Mount Isa is complex (Bell *et al.*, 1988; Davis, 2004; Miller, 2007) with D2, D3, D4a, the D4b syn-Cu event of Miller (2007), D5a and D5b all corresponding to approximately east-west shortening.
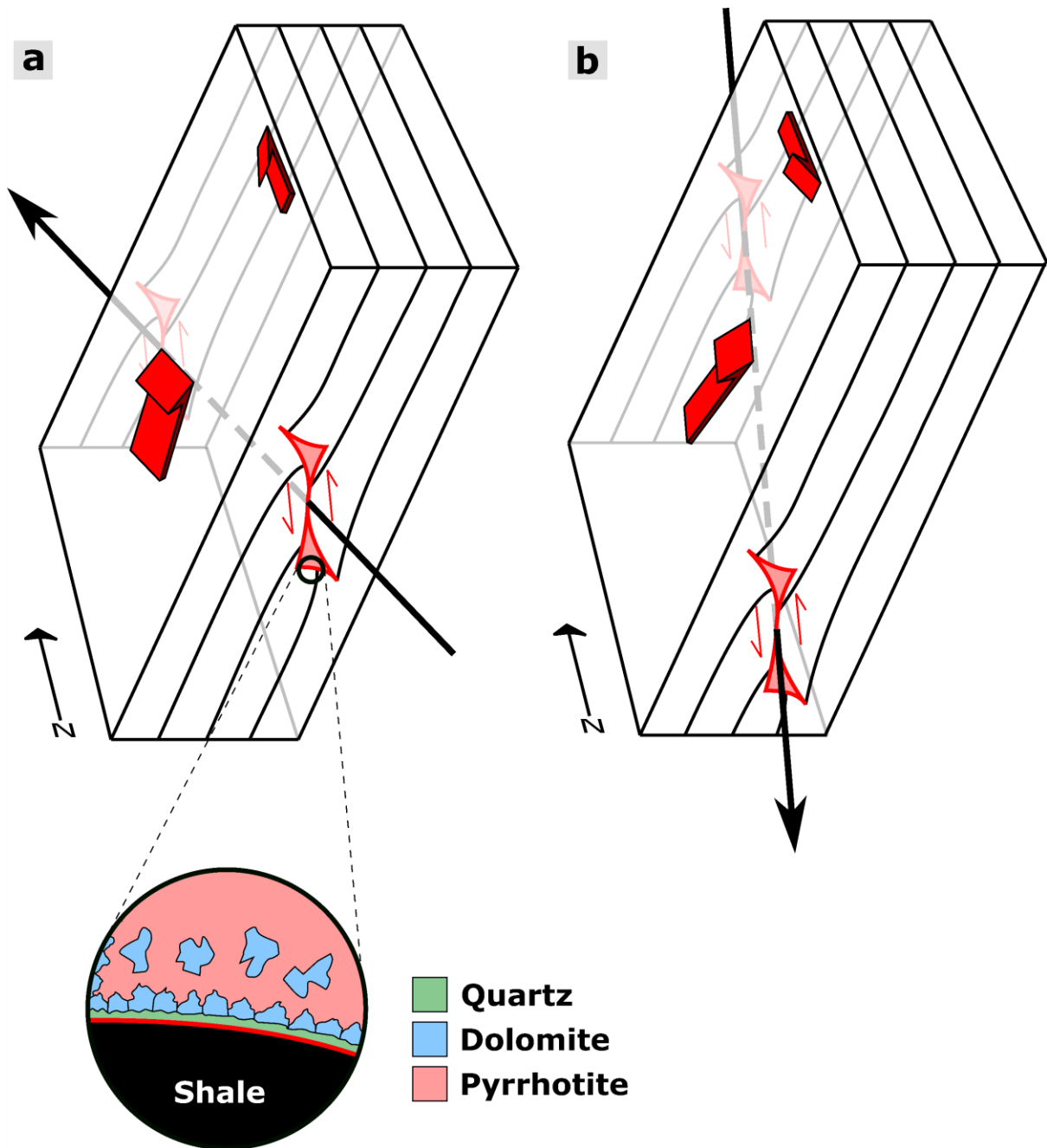
Figure 6.10: The formation of asymmetrical foliation boudinage structures at Mount Isa by approximately east-west shortening and up-dip, layer-parallel extension, showing the long-axis of the foliation boudinage structures: **a)** plunging to the north as a result of east-west shortening and dextral-reverse shear during D4a; **b)** plunging to the south as a result of east-west shortening and sinistral-reverse shear during D4b. Red arrows at foliation boudinage structures show relative displacements of the fracture walls. An enlarged diagram of the foliation boudinage structure infilling shows the initial quartz rim and subsequent dolomite, with later sulphide (pyrrhotite ± chalcopyrite) infill and replacement.

The D5a and D5b events are shown by Miller (2007) to have post-silica-dolomite, pyrrhotite and Cu mineralisation timings and therefore they also have a post-foliation boudin timing. Some of the deformation events with an east-west shortening may be compatible, however, a protracted period of foliation boudin formation is favoured based on their north and south plunges. The variation in the plunge of the foliation boudinage structures is interpreted to reflect an evolution from D4a through to the D4b syn-Cu event. The ENE-WSW shortening of the steeply west-dipping Urquhart Shale during D4a resulted in dextral-reverse shear along bedding surfaces with a top to the NE shear direction **[Figure 6.10a]**. Foliation boudinage structures formed as a result of this deformation have long-axes that plunge to the north **[Figure 6.10a]**. Miller's (2007) unnamed NW-SE shortening sinistral-reverse shear event (D4b), which he interprets as having a syn-Cu mineralisation timing, has a top to the SE shear direction and resulted in foliation boudinage structures plunging to the south **[Figure 6.10b]**.

All foliation boudinage structures in this study have sulphide infills of pyrrhotite ± chalcopyrite. The foliation boudinage structures have an identical mineral paragenesis to the rest of the deposit (e.g. Perkins, 1984; Cave *et al.*, 2020) and no evidence has been found in this study to suggest the silica-dolomite + pyrrhotite ± chalcopyrite infills of the foliation boudinage structures have been remobilised and precipitated at a later stage. This agrees with the observations of Perkins (1984) that, once precipitated, chalcopyrite does not redissolve and reprecipitate.

Arslan *et al.* (2008) state that a high fluid pressure is critical for the formation of foliation boudinage structures and in maintaining open fluid-filled fractures. High fluid pressures during the silica-dolomite alteration could be a contributing factor to the formation of foliation boudinage structures at Mount Isa. The drop in fluid pressure during the brecciation

(Perkins, 1984; Bell *et al.*, 1988) may have resulted in the cessation of silica-dolomite, pyrrhotite and minor chalcopyrite infilling of the foliation boudinage structures. The initial infill was followed by continuing pyrrhotite ± chalcopyrite replacement of the silica-dolomite within the foliation boudinage structures during the Cu brecciation event.

The results in this study largely support Miller's (2007) unnamed sinistral-reverse (D4b) timing for Cu brecciation at the Mount Isa deposit. However, a prolonged Cu mineralisation episode from late-D4a through to the main Cu brecciation during D4b is favoured based on the infill characteristics of the foliation boudinage structures. A Cu mineralisation event that initiates in late D4a and progresses through to the main Cu brecciation and mineralisation event in D4b would show an initial infill and then replacement of silica-dolomite in both the north and south plunging structures. However, a similar infill could be observed in foliation boudinage structures by a Cu event restricted to D4b if the D4b south-plunging structures were infilled and the D4a north-plunging structures were largely mineralised by replacement of the existing silica-dolomite infill.

6.5 Conclusions

- Petrographic analysis at the Mount Isa copper deposit shows that foliation boudinage structures in drill core have an infill of quartz, dolomite and pyrrhotite, with minor chalcopyrite in some samples. Pyrrhotite replaces and infills around quartz and dolomite in all analysed samples. Chalcopyrite has a coeval or post-pyrrhotite timing.

- The foliation boudinage structures plunge gently to the north and south as a result of layer-normal shortening and layer-parallel extension of the steeply west-dipping Urquhart Shale.

- Drill core scale foliation boudinage structures at Mount Isa are identified almost exclusively within the unaltered and undeformed Urquhart Shale and 'pyritic shale (5-20% pyrite)' lithologies, where the anisotropy required for their formation was still intact. The homogeneous nature of the Urquhart Shale at the small scale, combined with the anisotropy provided by the shale layering or layer-parallel foliation, was conducive to the formation of foliation boudinage structures at Mount Isa.

- The drill core scale foliation boudinage structures are generally located outside the zone of high-grade Cu mineralisation, though within the silica-dolomite and pyrrhotite mineralisation halos.

- Foliation boudinage structures formed after dolomitisation and silicification along bedding. Infilling of the structures occurred during a protracted silica-dolomite, pyrrhotite and chalcopyrite mineralisation event. The paragenesis of the foliation boudinage structures is consistent with the established paragenesis of the main Cu mineralisation at Mount Isa.

- The orientations and mineral infills show a continued formation of foliation boudinage structures from ENE-WSW dextral-reverse shortening during D4a through to the main Cu mineralisation during Miller's (2007) unnamed WNW-ESE sinistral-reverse shortening event (D4b).

CHAPTER 7

Strain in Sulphide Filled Foliation Boudinage Structures at the Mount Isa Cu Deposit

7.1 Introduction

Recent studies highlight the importance of geological structures in the localisation of the Cu deposit at Mount Isa (Davis, 2004; Miller, 2007; Cave *et al.*, 2020; Williams *et al.*, 2023 and Chapter 6). However, the timing and the detailed controls on sulphide deposition are still controversial. A currently accepted view is that the Cu and possibly Pb-Zn orebodies were syn-tectonic and hydrothermally precipitated, and that some deformation events followed ore formation (Perkins, 1984; Cave *et al.*, 2020). However, deformation of ore-related sulphides, which might be expected in this scenario, has not been previously demonstrated.

Foliation boudinage structures are known to be important controls on mineralisation at other ore deposits, such as the Rosebery Pb-Zn deposit in Tasmania (Aerden, 1991), as well as being identified in the Mount Isa Cu system (Chapter 6 and Williams *et al.*, 2023). The foliation boudinage structures at Mount Isa are predominantly filled with quartz, dolomite, and later ore-related sulphides (pyrrhotite ± chalcopyrite) that are associated with the Cu mineralisation event (Chapter 6 and Williams *et al.*, 2023). The fillings of these structures can be used to test the possibility of post-mineralisation deformation events, even though previous studies on foliation boudinage structures in general have identified little to no deformation within their mineral infill. The infills can also be examined to elucidate the mechanism of formation of foliation boudinage structures.

Electron backscatter diffraction EBSD analysis was used to evaluate the relationship between the finite strain geometry, crystallographic orientations, and deformation mechanisms of pyrrhotite. If relationships exist between shape preferred orientation (SPO), crystallographic preferred orientation (CPO) and grain finite strain geometry, then they can be used to determine the relative timing of formation and deformation of the foliation boudinage

structure infill by comparison with the deformation sequence (Chapter 2). This chapter aims to determine the magnitude and orientation of the strain ellipsoid within the sulphide infill of the foliation boudinage structures, in order to reveal the deformation of ore related sulphides at Mount Isa.

7.2 Deformation of Pyrrhotite

Under most conditions of mechanical deformation in the crust, pyrrhotite behaves as a ductile material (Handin, 1966; Graf and Skinner, 1970). Brittle failure of pyrrhotite predominates at room temperature (Graf and Skinner, 1970). An increase in temperature reduces the strength of pyrrhotite and increases the intracrystalline deformation (Graf and Skinner, 1970; Clark and Kelly, 1973; Kelly and Clark, 1975). Pyrrhotite is one of the strongest sulphides at room temperature but becomes significantly weaker at higher temperatures **[Figure 7.1]** (Clark and Kelly, 1973; Kelly and Clark, 1975). Experimental studies have shown that pyrrhotite aggregates are weaker than dolomite rock at temperatures greater than 125 °C (Clark and Kelly, 1973; Kelly and Clark, 1975).

The pyrrhotite basal plane serves as the dominant shear plane during plastic deformation (Kübler, 1985). Pyrrhotite is strongest perpendicular to the (0001) plane and weakest at a 55° angle (Graf and Skinner, 1970). The pyrrhotite critical resolved shear stress (CRSS) for basal slip, at a strain rate of 10^{-5} (s^{-1}) and confining pressure of 300 MPa, changes significantly with temperature (Kübler, 1985; Niederschlag and Siemes, 1996). At temperatures of 200 °C, 300 °C and 400 °C, the CRSS for basal slip is 60 MPa, 8 MPa and 4.7 MPa, respectively.
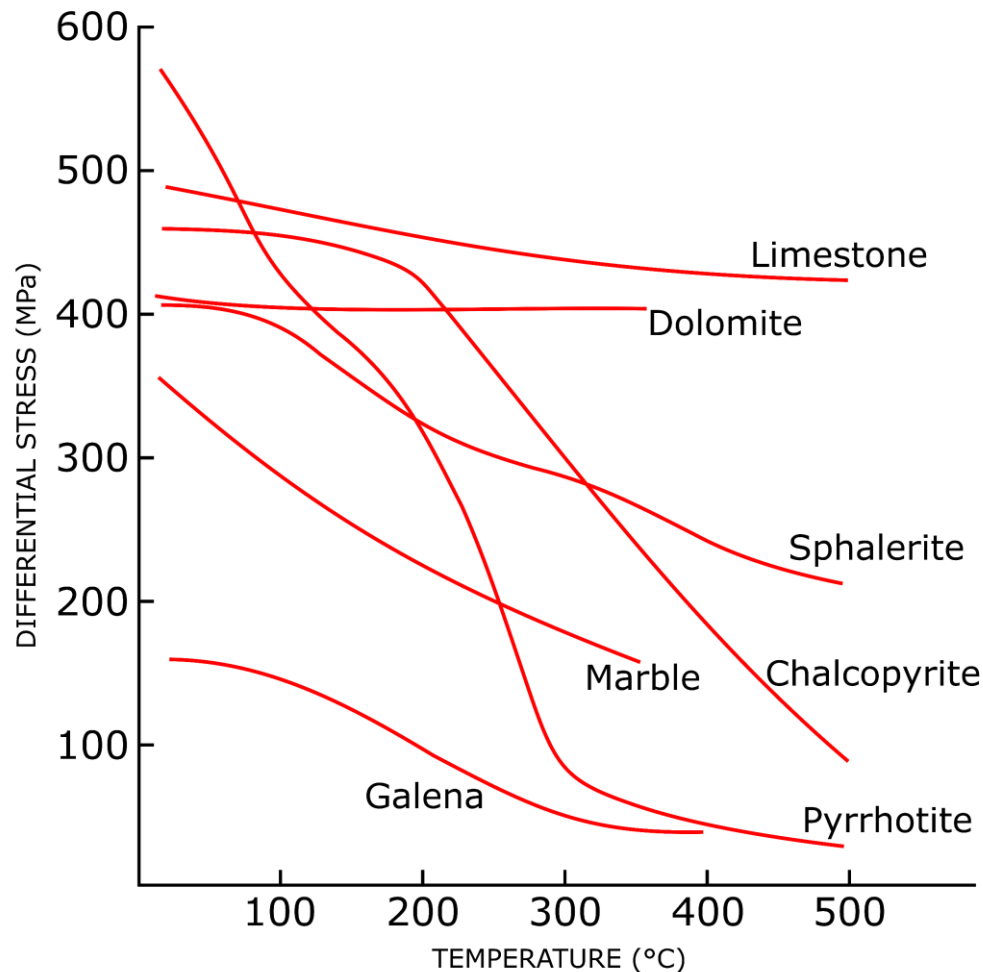
Figure 7.1: Experimental deformation showing the strengths (differential stress) of mineral aggregates and carbonate rocks as a function of temperature at a strain rate of ~7.5x10^{-5} s^{-1} and 100 MPa confining pressure. Modified from Clark and Kelly (1973) and Kelly and Clark (1975).

7.3 Methodology

7.3.1 Materials

Foliation boudinage structures in this chapter were collected from several drill cores that represented various locations in the deposit **[Figure 7.2]**. The samples were cut, and polished thin sections were made either in cross-section, through the long-axes or horizontally through the structures as represented by the XZ-, YZ- and XY-planes in **Figure 7.3**. One sample (FBS3/FBS4) was cut in two orthogonal directions (XZ and YZ; **Figure 7.4**) and two samples

(FBS1 and FBS2) were cut in three orthogonal directions (XZ, YZ, XY; **Figure 7.4**). FBS3 includes

two adjacent foliation boudinage structures and is further divided into FBS3 (left) and FBS4

(right) in **Figure 7.4g**. Results for the YZ-plane shown in **Figure 7.4h** are used for both FBS3

and FBS4 throughout this study.

Figure 7.2: (Following page) East-west cross-sections through the Mount Isa deposit, showing the relative positions of the Pb-Zn and Cu orebodies, pyrrhotite and silica-dolomite. Sample locations are shown for each foliation boudinage structure analysed in this study and correspond to their relative positions in relation to the mineralisation. **a)** Cross section in the south of the mine at 4350mN. B-B' in **Figure 4.2**. **b)** Cross-section in the north of the mine at 7000mN. A-A' in **Figure 4.2**.
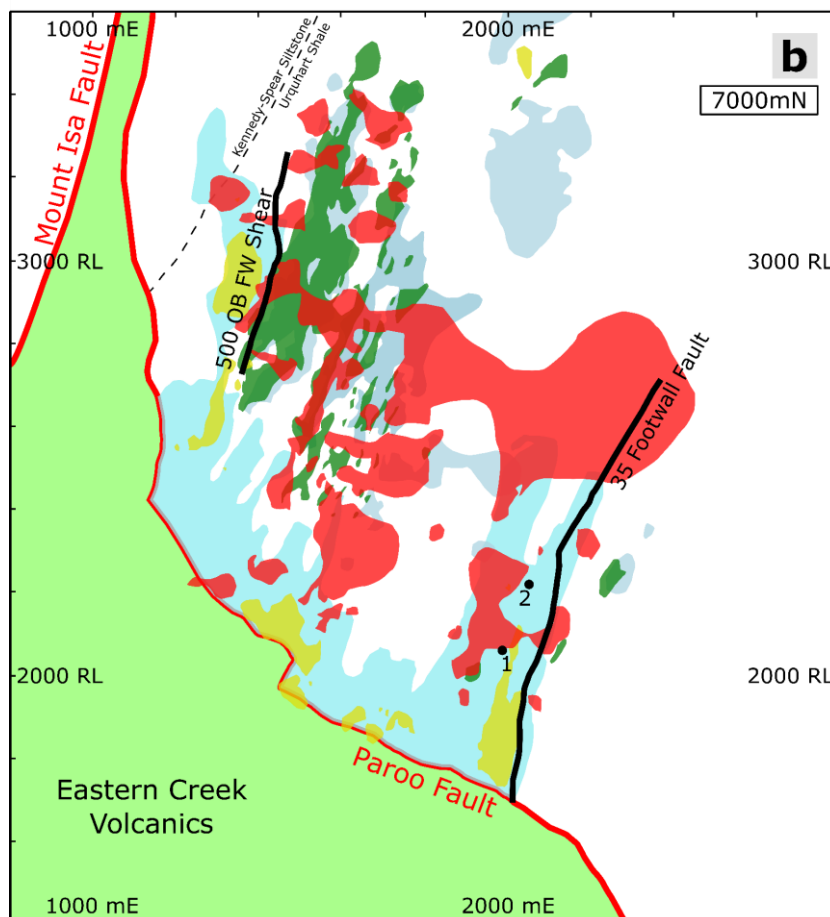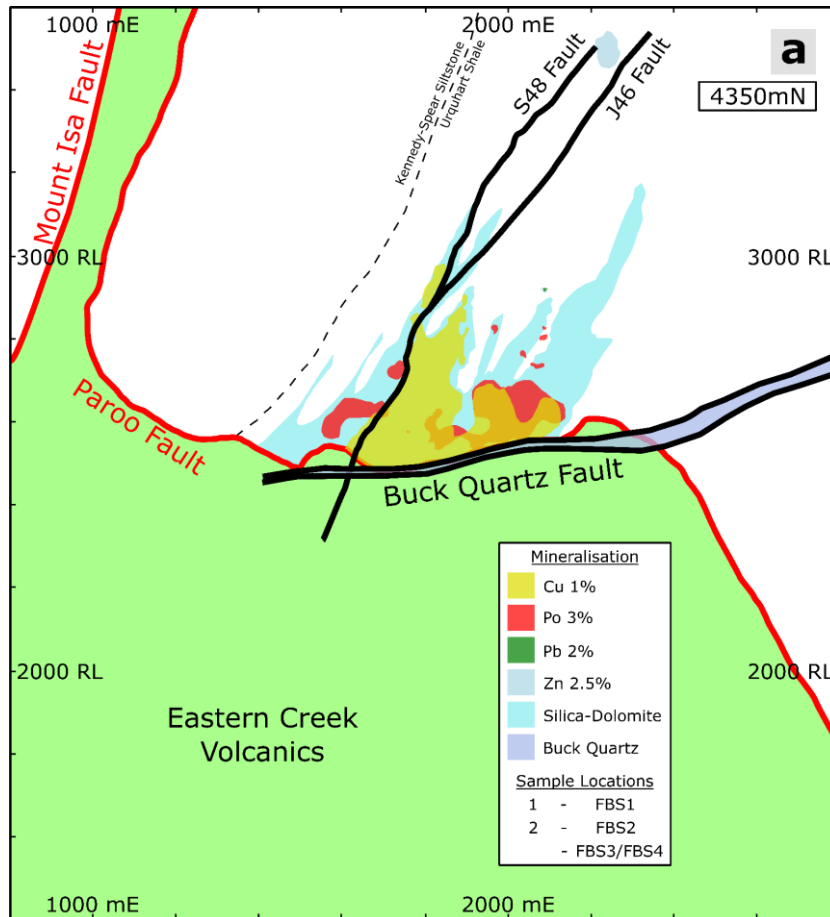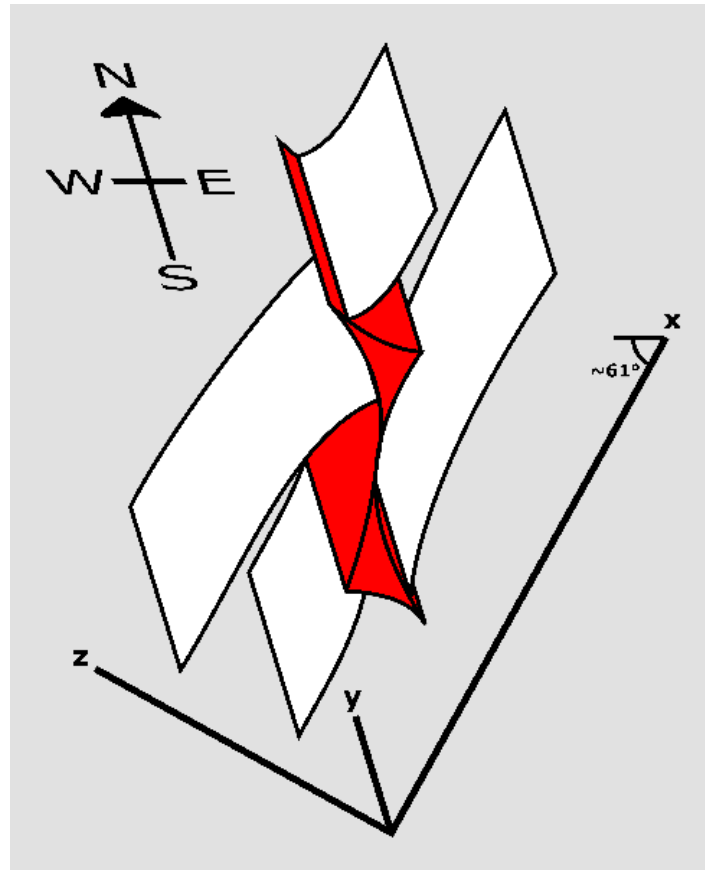
Figure 7.3: Oriented reference axes of foliation boudinage structures at Mount Isa.

Figure 7.4: Samples of foliation boudinage structures cut in a minimum of two orthogonal directions, represented by the XZ-, YZ- and XY-planes.

7.3.2 Electron Backscatter Diffraction (EBSD) Preparation

EBSD analysis was performed using the Zeiss Sigma HD scanning electron microscope in the School of Earth and Environmental Sciences, Cardiff University. The eight representative polished thin sections were initially polished with colloidal silica for 10 minutes and then washed with de-ionised water before being checked under the microscope. A second 10 minute polish was performed on the samples, which were then placed in an ultrasonic bath for 5 minutes in de-ionised water. A thorough clean with de-ionised water is essential as colloidal silica can crystallise onto the slide if left uncleaned. A tissue was used to dry all the samples prior to them being given a thin carbon coat of 4-8 nm using an Agar Turbo carbon coating vacuum chamber. The carbon coat minimises electron charge across the sample yet maintains a strong crystallographic signal. All samples were analysed within 48 hours of polish to minimise tarnishing (oxidation) of exposed sulphide minerals.

7.3.3 Electron Backscatter Diffraction (EBSD) Analysis Set-up

Phases were indexed as consistently as possible between samples **[Appendix G.1]**. X-ray diffraction (XRD) analysis was used to determine that the pyrrhotite at Mount Isa is monoclinic ($Fe_{1-x}S$, where x=0 to 0.125) **[Appendix G.2]**. Monoclinic pyrrhotite is absent from the EBSD phase databases, therefore the hexagonal phase Troilite (FeS) was used to index all pyrrhotite in samples in this study. For EBSD analysis, the properties of monoclinic pyrrhotite (Fe_7S_8) are almost identical to the hexagonal FeS phase.

EBSD data were collected using a 20 keV beam with high-current turned on. Raw data were collected at step-sizes between 6 and 14.1 μm, with an aperture size of 120 μm and EBSD

detector insertion distance of ~190 mm for all samples **[Appendix G.3]**. Mean angular deviation (MAD) was less than 1° for all samples.

7.3.4 Data Processing

The EBSD data were processed using the open-source MTEX toolbox for MATLAB (Bachmann *et al.*, 2010, 2011; Mainprice *et al.*, 2015). The EBSD data clean-up procedure is described below:

- Grains were determined using 10° bins

- Grains ≤5 pixels were removed

- Grains were redetermined using 10° bins

- Grains that had an area of non-indexed pixels >50% of the total grain area were removed, leaving only the well-constrained grains

- The remaining grains were extrapolated to fill the missing pixels and smoothed

- If required, the EBSD maps were rotated so the shale layering was horizontal in all maps

- Boundary grains that intersected the EBSD map edge were removed, leaving only those grains whose entire area was within the map

7.3.5 Relict and Recrystallised Grain Identification – GOS Method

The grain orientation spread (GOS) has previously been used to define the threshold between relict (high strain) and recrystallised (low strain) grains **[Figure 7.5]** (Cross *et al.*, 2017). Intragranular lattice distortions represented by the misorientation angle between each pixel

and the mean orientation of the grain allows the calculation of the GOS for each grain **[Figure 7.6]**. The GOS value is equivalent to the average misorientation relative to the mean grain orientation for each grain (Wright *et al.*, 2011). A trade-off curve of the number of grains in the sample against their GOS value is used to calculate the threshold between relict and recrystallised grains **[Figure 7.5]**. Relict grains are defined as grains with GOS values greater than the knee of the GOS curve and recrystallised grains as those with GOS values lower than the knee (Cross *et al.*, 2017). Separation of relict and recrystallised grains using the GOS values is used for the pyrrhotite infill of the foliation boudinage structures. Unless otherwise stated, only relict grains are used for grain analyses as they represent the earliest pyrrhotite grains to form and should have accumulated the greatest amount of strain within the pyrrhotite infill.
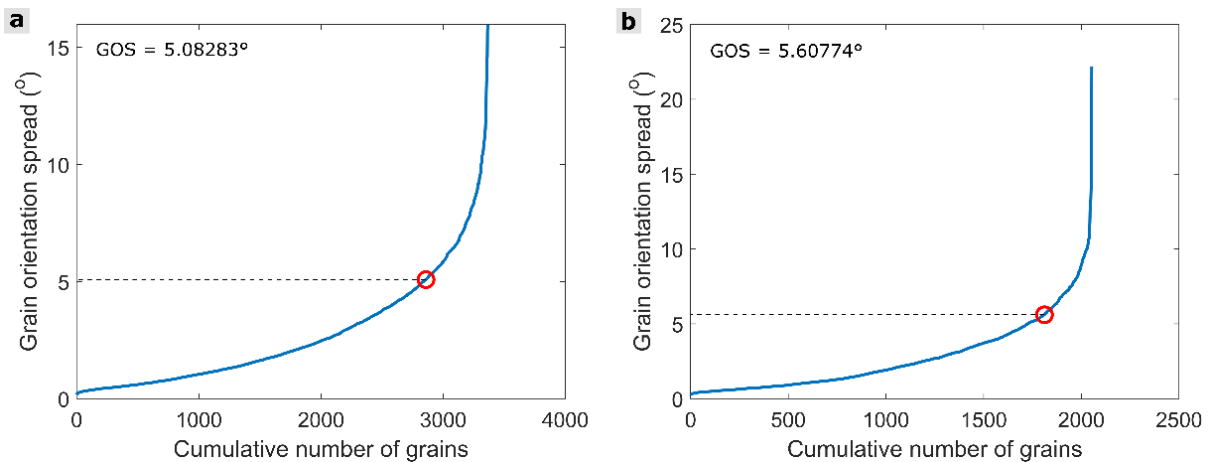
Figure 7.5: Cumulative plot of the number of pyrrhotite grains versus the grain orientation spread (GOS). The GOS threshold (red circles) defines the difference between relict (above threshold) and recrystallised grains (below threshold). **a)** GOS graph of the XZ-plane for FBS1. **b)** GOS graph of the YZ-plane for FBS1.
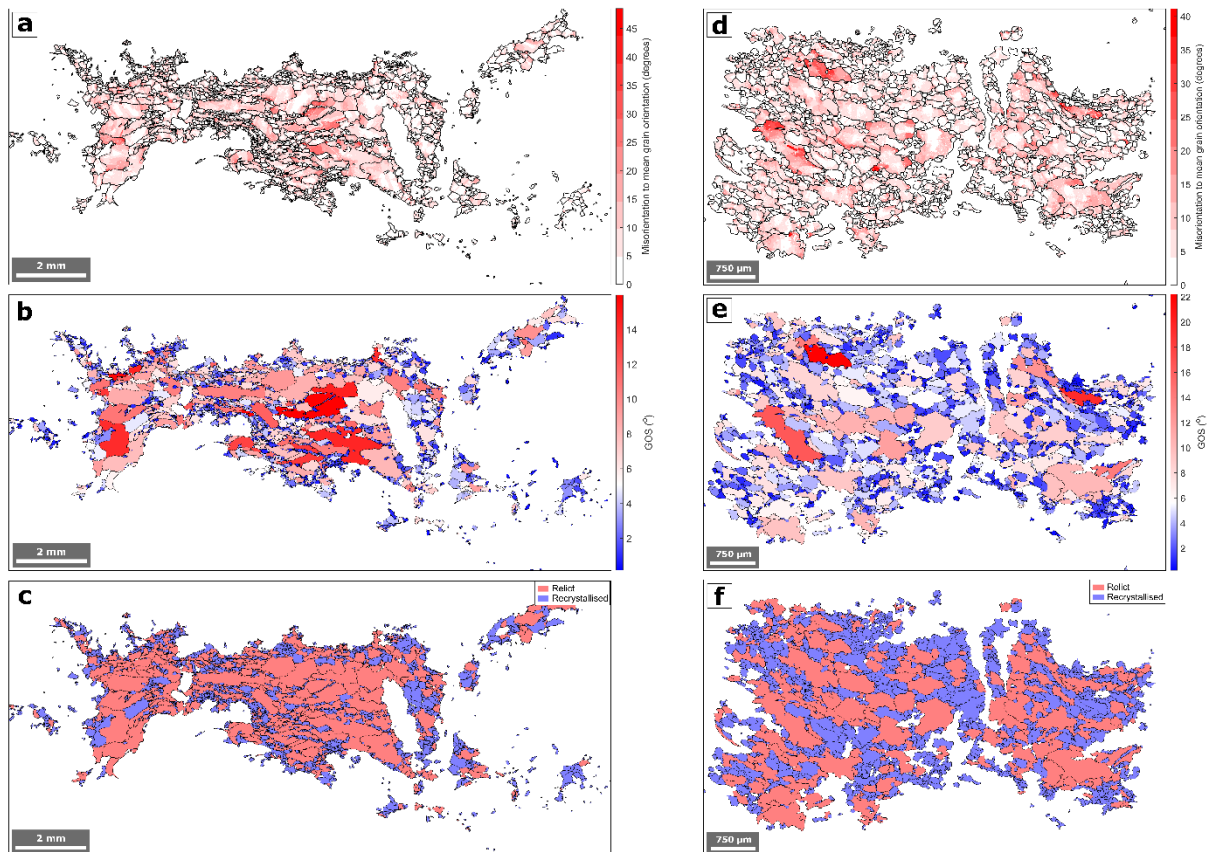
Figure 7.6: EBSD maps of pyrrhotite infills of FBS1 in cross sections XZ-plane (left) and YZ-plane (right). **a)** Map of all pyrrhotite grains showing the local misorientations within each grain. **b)** Grain orientation spread (GOS) value for each grain. **c)** Relict and recrystallised grains as determined by the GOS threshold in **Figure 7.2a**. **d)** Map of all pyrrhotite grains showing the local misorientations within each grain. **e)** GOS value for each grain. **f)** Relict and recrystallised grains as determined by the GOS threshold in **Figure 7.2b**.

7.3.6 Grain Analysis

Mulchrone and Choudhury (2004) showed that ellipses can be fitted to arbitrary shapes that are not necessarily elliptical, such as grains. Best fit ellipses were calculated for individual grains in each EBSD map using the ellipse fitting calculation in the MTEX toolbox (Mulchrone and Choudhury, 2004; Bachmann *et al.*, 2010, 2011; Mainprice *et al.*, 2015). Data for individual grains were extracted as grain centre co-ordinates (X and Y), grain aspect ratios (Rf) and grain long-axis orientations (omega).

2-dimensional grain analyses were performed on samples analysed in this study using the open-source EllipseFit program (v.3.8.2) (Vollmer, 2018) to create Rf/ɸ plots (Ramsay, 1967; Dunnet, 1969) in order to obtain the mean ellipse ratio (Rs) for the combined relict grains and angle of the longest axis of the best-fitted ellipses (X). Rf/ɸ plots are widely used in strain analysis (Ramsay and Huber, 1983; Lisle, 1985) where the Rf parameter is most commonly plotted in the logarithmic ln(Rf) form (Vollmer, 2018).

3-dimensional grain analyses were performed by creating Flinn plots (Flinn, 1965), strain ellipsoids and lower hemisphere equal area stereographic projections for each foliation boudin sample in order to give the orientations of the principal strains within the pyrrhotite infill of the foliation boudinage structures. 3-dimensional Flinn plots were created by combining two orthogonal orientations of 2-dimensional finite strain ellipses.

7.3.7 Drill Core Reorientation

Foliation boudinage samples were collected from drill cores that are unoriented in the structural framework. Drill core was reoriented based on a modified method of Holcombe (2016) for partially oriented core which is outlined in **Appendix G.4**. Measurements of shale layering from the oriented Resource Development (RD) drillhole 'T667ED1' were used to calculate the mean dip and dip direction of the bedding (61° towards 263°). Measurements of shale layering orientations near the underground drillhole locations are, in general, in close agreement with the calculated mean.

7.3.8 Section Reorientation

Polished sections that contain the drillhole edge can be reoriented using the drillhole direction **[Appendix G.5]**. The straight edge of the drillhole in the section must be in the direction of the drillhole at the point where the sample was taken. The sample can be reoriented by rotating the section about this known direction until the bedding is in the correct orientation, based on oriented samples proximal to the sample location, reoriented drill core bedding measurements (section 7.3.7), or an assumed bedding dip and dip direction based on bedding measurements in the Mount Isa area **[Appendix E]**.

7.4. Results

7.4.1 Strain in Grains

7.4.1.1 Misorientations

The misorientations of each pixel to the mean grain orientation within each grain are shown in **Figure 7.6a** and **Figure 7.6d**. In general, larger grains show greater misorientations and the development of subgrains are apparent. Checkerboard style subgrains are visible in some samples.

7.4.1.2 GOS Analysis

Grain orientation spread (GOS) analysis has been used to differentiate relict from recrystallised grains **[Figure 7.5** and **Figure 7.6c,f]**. The GOS analysis also identifies the significant intragranular lattice distortions of up to 20° in some grains **[Figure 7.6b,e]**. Relict grains are generally elongate, or ribbon shaped. Recrystallised grains are slightly elongate and form networks surrounding relict grains.

7.4.1.3 Grain Shape Preferred Orientations (SPO)

Orientations of the pyrrhotite grain long-axes from the infill of foliation boudinage structures are shown in **Figure 7.7**. Both the XZ- and YZ-planes for the four foliation boudinage structures are plotted as equal area moving average rose diagrams using the MARD software in MATLAB (Munro and Blenkinsop, 2012). A weighting factor of 0.9 and aperture of 9° was used during plotting as recommended by Munro and Blenkinsop (2012). Grain shape preferred orientations (SPO) that are approximately horizontal can be observed in all samples for both the relict and recrystallised grains. The horizontal SPO is approximately parallel to the far-field shale layering in all samples.

7.4.1.4 Crystallographic Preferred Orientations (CPO)

Equal area, lower hemisphere pole figures of pyrrhotite grains within foliation boudinage structures are shown in **Figure 7.8**. Pyrrhotite *c*-axes show a well-defined crystallographic preferred orientation (CPO) in all samples **[Appendix G.6]**. The CPO patterns show the normal to the *c*-plane to be sub-perpendicular to the shale layering. Normals to the *m*- and *a*-planes are within the plane of shale layering and are rotated about the perpendicular to the shale layering (*c*-axis).

Measures of fabric strength are shown by the M-index (0.11 in the XZ-plane and 0.13 in the YZ-plane) and J-index (1.76 in the XZ-plane and 1.80 in the YZ-plane), indicating a moderate fabric strength of the CPO in FBS1 **[Figure 7.8]**. There is little difference between the CPO produced using all grain data and using only relict grains **[Appendix G.6]**; as a result, the whole dataset is used.
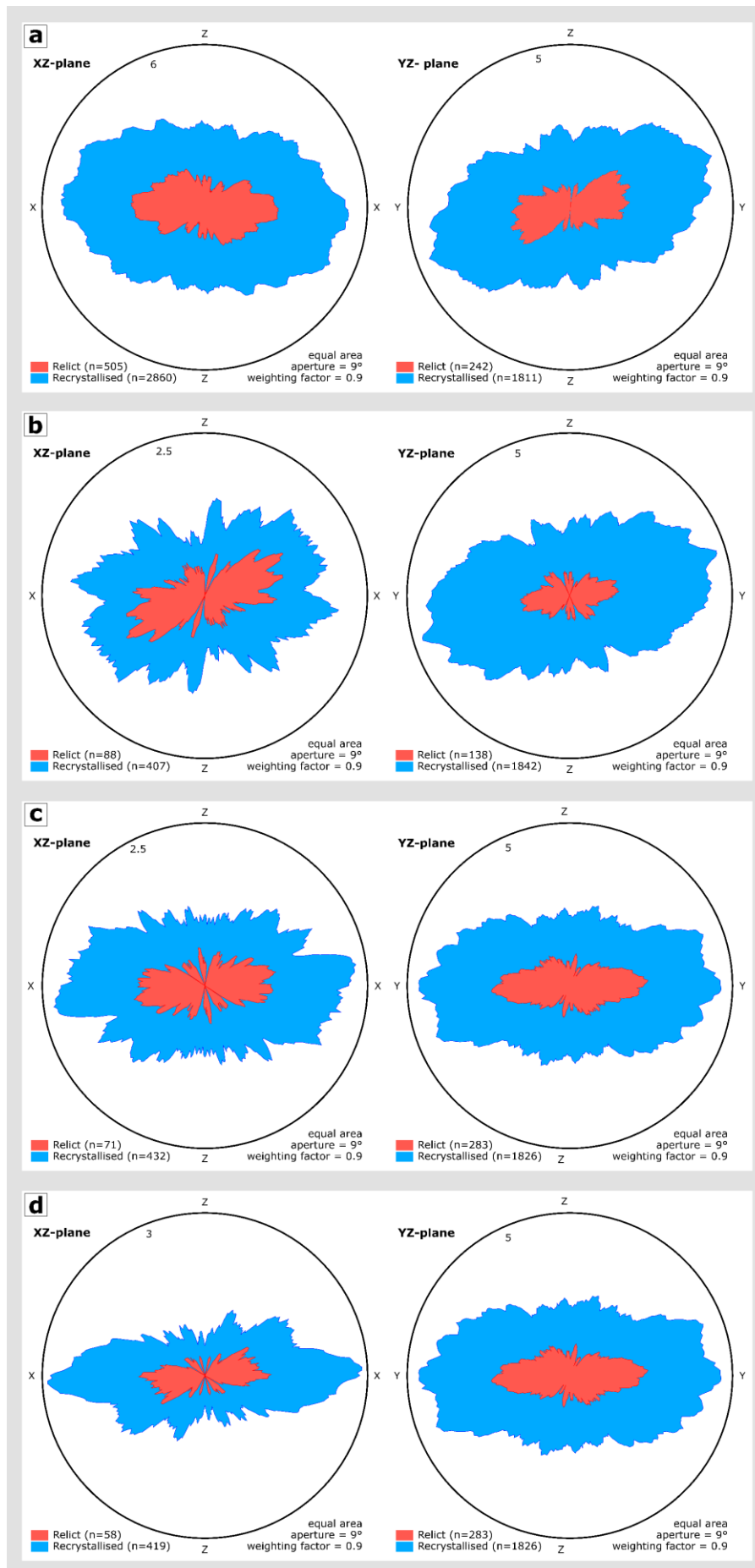
Figure 7.7: (Previous page) Rose plot of relict and recrystallised pyrrhotite grain long-axes in two perpendicular planes (sample XZ-plane and YZ-plane). **a)** FBS1. **b)** FBS2. **c)** FBS3. **d)** FBS4.
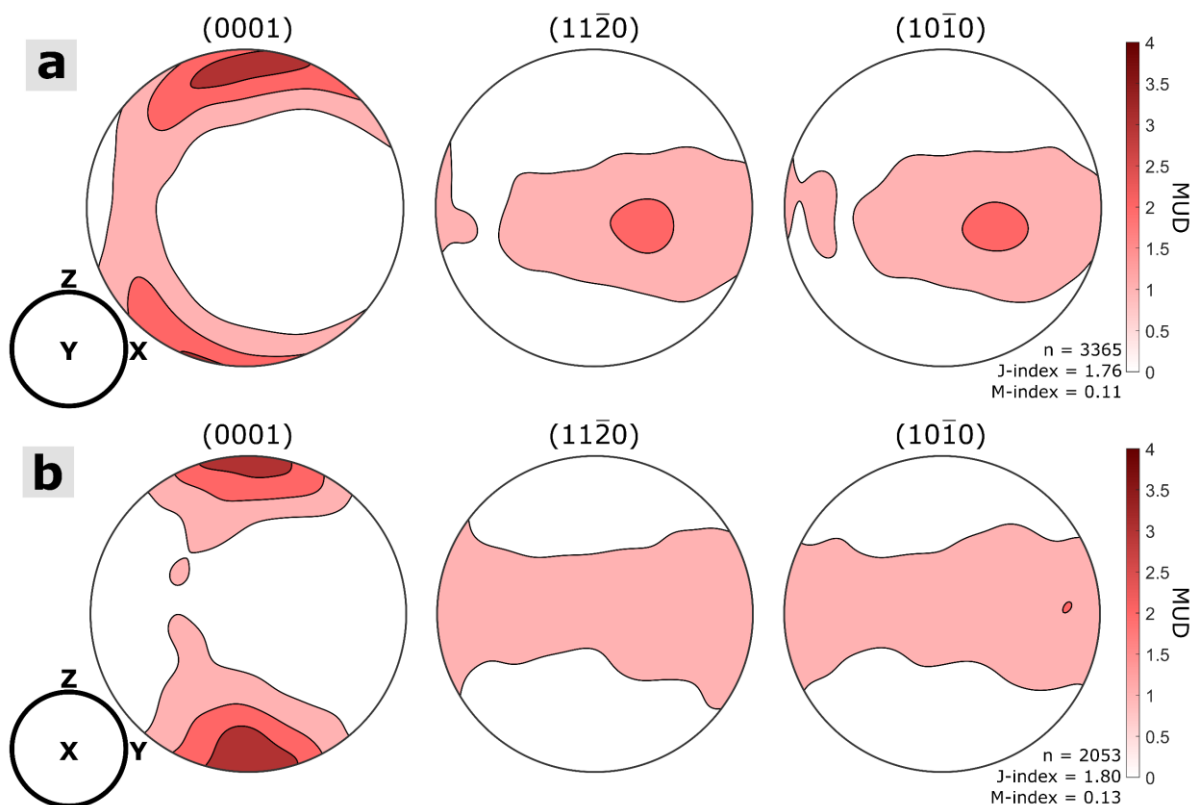

Figure 7.8: Equal area, lower hemisphere pole figures for pyrrhotite grain orientations within FBS1, with one point per grain. Contours in units of multiples of uniform distribution (MUD). Pyrrhotite $(11\bar{2}0)$ and $(10\bar{1}0)$ planes form a girdle parallel to the shale layering. Pyrrhotite (0001) planes show a defined crystallographic preferred orientation (CPO), with c-axes normal to the shale layering. n is equal to the number of grains. Fabric strengths are presented using the J-index and M-index for both **a)** XZ-plane of FBS1 and **b)** YZ-plane of FBS1.

7.4.2 2D Strain Analysis

Strain analyses of relict pyrrhotite grains are illustrated in 2-dimensions by ln(Rf)/ϕ plots

[Figure 7.9; Appendix G.7]. The ln(Rf)/phi plots for the four foliation boudinage structures

show a dominant shale layer-parallel orientation of the pyrrhotite grains in the XZ- and YZ-

planes of **Figure 7.4**, supporting the evidence for the SPO fabric in **Figure 7.7**. The mean R-values (ellipticity of the grains) of the combined pyrrhotite grain ellipses estimate the 2-dimensional finite strain within the infill of the foliation boudinage structures. R-values vary from 1.43 to 1.62 in the XZ-plane, 1.36 to 1.60 in the YZ-plane and 1.04 to 1.28 in the XY-plane. For the two foliation boudinage structures with R-values in the XY-plane, they approximate the ratio between the R-values in the XZ- and YZ-planes.
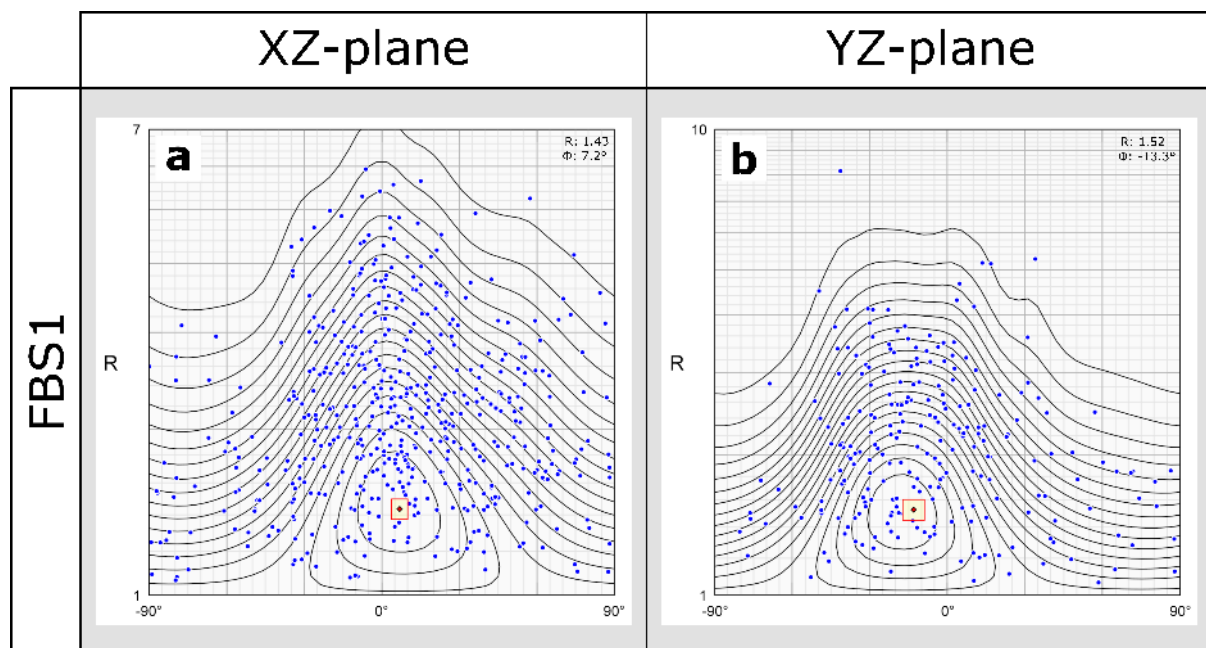
Figure 7.9: Logarithmic ln(Rf)/Φ plots of relict pyrrhotite grains within FBS1. Rf/phi plots of XZ- and YZ-planes are shown with the mean R-value and grain long-axis orientation. R-values of the pyrrhotite approximate the 2-dimensional finite strain within the foliation boudinage structure infill. **a)** XZ-plane of FBS1. **b)** YZ-plane of FBS1.

7.4.3 3D Strain Analysis

7.4.3.1 Flinn Plots

The shape of the 3-dimensional finite strain ellipsoid is shown in **Figure 7.10** as a Flinn plot of the four foliation boudinage structures. The shape of the finite strain ellipsoid is calculated using the combined 2-dimensional strain values in **Figure 7.9** for the two orthogonal XZ- and

YZ-planes. All foliation boudinage structures analysed in this study plot in the flattening strain region of the diagram. FBS2 and FBS4 have maximum principal strain directions in the X-axis of the foliation boudinage structure, whilst FBS1 and FBS3 have maximum principal strain directions in the Y-axis of the foliation boudinage structure.
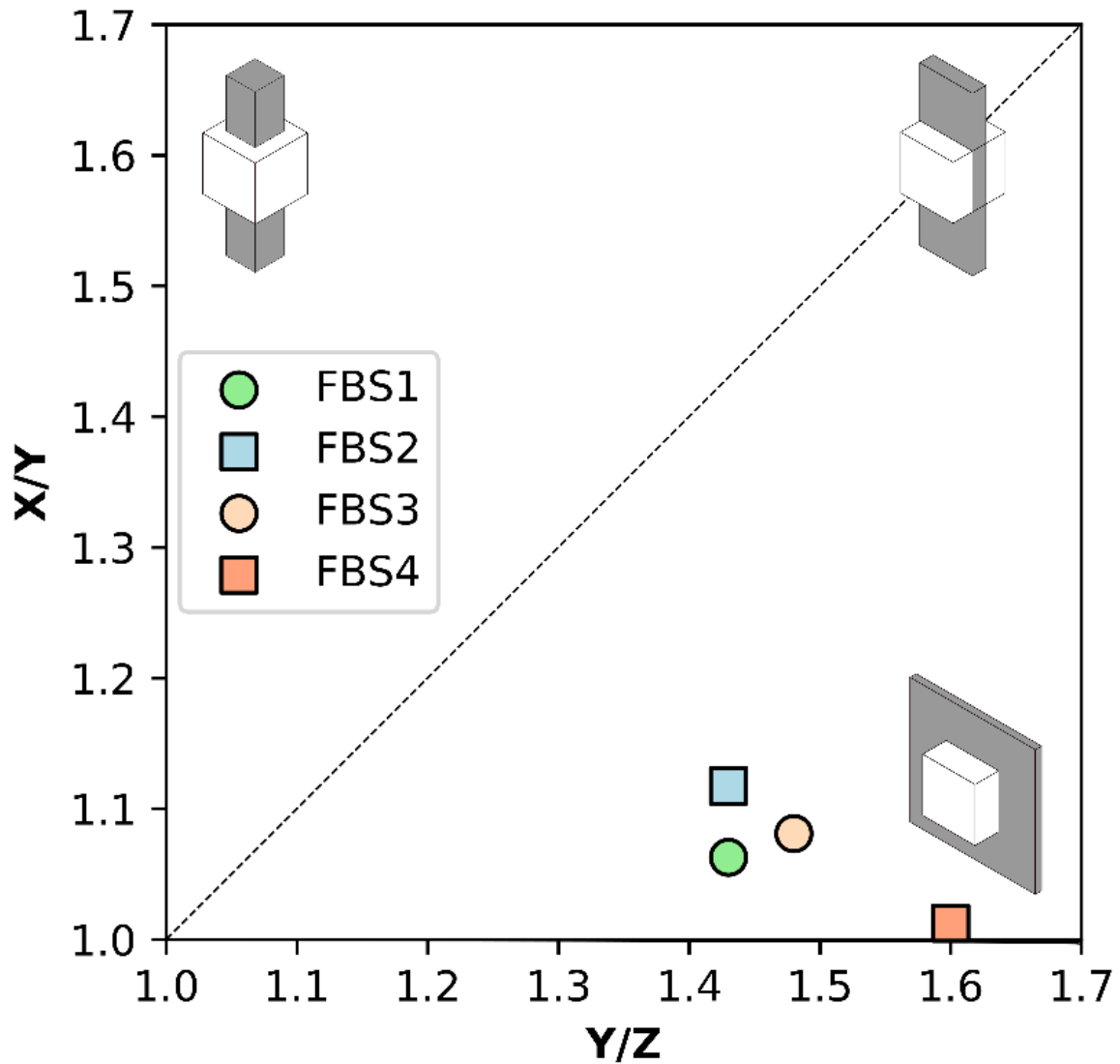

Figure 7.10: Flinn plot showing the 3-dimensional shape of the finite strain ellipsoid in the pyrrhotite infill of four foliation boudinage structures. The strain ellipsoid is calculated using the 2-dimensional strain values in **Figure 7.3**. The foliation boudinage structures plot in the flattening strain region of the diagram. Square: X-axis of foliation boudinage structure = direction of maximum principal strain; Circle: X-axis of foliation boudinage structure = intermediate strain direction.

7.4.3.2 Orientation of Principal Strain Axes

Shortening directions for the relict pyrrhotite grain infill of the four foliation boudinage structures are plotted in **Figure 7.11**. Using the reorientation method in section 7.3.8, shortening directions are calculated as normals to the plane passing through the directions of the longest axes for the mean relict grain ellipses in the XY- and YZ-planes. Neck-lines of foliation boudinage structures are estimated from the normal to the XZ-plane and are plotted for reference. Foliation boudinage structure neck-lines plot close to the mean shale layering in Chapter 6 and Williams *et al.* (2023). The shortening direction within the relict pyrrhotite grain infill is the local minimum principal strain direction. The maximum principal strain direction is assumed to be up-dip, based on the typically north-south orientations of oriented foliation boudinage structures in Chapter 6 and Williams *et al. (*2023). Shortening directions
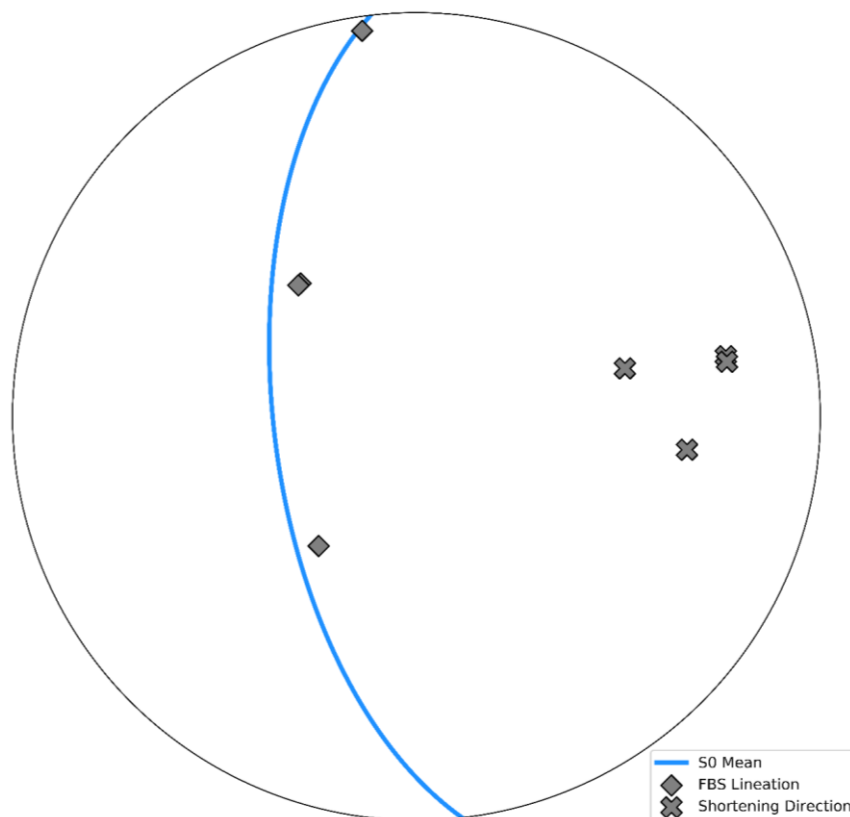
Figure 7.11: Shortening directions for the relict pyrrhotite grains within the four foliation boudinage structures. Shortening directions, neck-lines of foliation boudinage structures and the mean shale layering orientation in Chapter 6 and Williams et al. (2023) are plotted.

for the northerly-plunging foliation boudinage structures are ENE-WSW and southerly-plunging structures are WNW-ESE. Errors between ±1° and ±9° for the plunge and ±3° and ±12° for the azimuth of the shortening direction were calculated during the reorientation of polished thin sections **[Appendix G.8** and **Appendix G.9]**.

7.5 Discussion

7.5.1 Pyrrhotite Indexing

Few studies have investigated pyrrhotite using EBSD analysis (Qian *et al.*, 2011; Vukmanovic *et al.*, 2014, 2019; Uwanyuze *et al.*, 2022) and as far as it is known, only one recent study has specified the mineral system used during pyrrhotite indexing (Uwanyuze *et al.*, 2022). The pyrrhotite at Mount Isa is weakly magnetic and is characteristic of monoclinic Fe_7S_8. In additional agreement to this, XRD analysis has determined Mount Isa pyrrhotite as type 29-0723 monoclinic phase **[Appendix G.2]**. Despite this determination, there is no monoclinic pyrrhotite in the available EBSD indexing databases. As there is essentially no difference in lattice parameters between the hexagonal FeS Troilite phase and the monoclinic Fe_7S_8 pyrrhotite phase, indexing using the hexagonal phase has a good efficiency (MAD of <1°, >90% indexing for the total EBSD map and approximately >98% of pyrrhotite pixels indexed). Therefore, the hexagonal FeS phase has been used throughout this study for pyrrhotite indexing.

7.5.2 Deformation Mechanism of Pyrrhotite

The strong CPO patterns **[Figure 7.8]** with *c*-axes sub-perpendicular to the shale layering and large local misorientations (average relict grain misorientation ~9°; **Figure 7.6**) for the pyrrhotite show that dislocation creep is the dominant deformation mechanism within the infill of the foliation boudinage structures. Cox (1987) showed that pyrrhotite commonly exhibits dislocation creep at the greenschist facies conditions, as at Mount Isa during the formation of foliation boudinage structures (Perkins, 1984, 1997; Bell and Hickey, 1998).

The CPO shows basal slip sub-parallel to the shale layering dominates in the pyrrhotite samples. Pyrrhotite is weakest along the basal plane, where only a small non-parallelism between the compression axis and the *c*-axis is sufficient to induce basal slip (Kübler, 1985). Kübler (1985) has also identified prism slip, twinning and kinking of pyrrhotite occurring at higher temperatures.

It is likely the pyrrhotite deformation was dominated by coaxial flow (pure shear), with an element of non-coaxial flow (simple shear) owing to the fabric shown in the CPO. However, it is difficult to ascertain the degree of coaxial vs non-coaxial deformation. Determining the vorticity requires additional analysis that is beyond the scope of this study.

A strong *c*-axis texture shown in **[Figure 7.8]** is in agreement with the experiments of Niederschlag and Siemes (1996), which show a strengthening of the pyrrhotite *c*-axis texture in pole figures where the angle between the compression axis and the initial *c*-axis is less than 35°. At these angles, the *c*-axes show a progressive tendency to orient parallel to the compression axis (Niederschlag and Siemes, 1996). Pyrrhotite pole figures in **Figure 7.8** show *c*-axes approximately normal to the horizontal shale layering and parallel to the approximate shortening direction. The experiments of Niederschlag and Siemes (1996) also suggest that at

greater compression angles, the (0001) planes reorient perpendicular to the compression axis and the resulting pyrrhotite pole figures show this progressive reorientation. A similar behaviour may be occurring in some samples where the *c*-axes form a weak girdle **[Appendix G.6]**.

7.5.3 Dynamic Recrystallisation of Pyrrhotite

The populations of relict and recrystallised grains are differentiated using the grain orientation spread (GOS) value. The GOS method is an EBSD based method for measuring intragranular distortions and hence determines recrystallised populations from relict grains independently of grain geometry. Unlike other methods, this method does not make assumptions that relict grains are larger and less spherical than recrystallised grains. This method has been used with success in dynamically recrystallised quartz grains (Cross *et al.*, 2017; Tulley, 2021). The pyrrhotite grain geometry characteristics in **Figure 7.6** show evidence of dynamic recrystallisation by subgrain rotation (SGR). SGR is a response to the migration of dislocations into subgrain walls during progressive deformation, eventually forming recrystallised grains (Hirth and Tullis, 1992). Recrystallised grains are defined by the creation of subgrain boundaries at high angles (>10°) to the relict grains. SGR is dominant at intermediate temperatures (~500-1000 °C) and strains (~10^{-7}-10^{-5} s^{-1}) in quartz (Hirth and Tullis, 1992). SGR in pyrrhotite is expected at lower temperatures than quartz and indicates the deformation conditions at Mount Isa during the development of foliation boudinage structures.

Studies on quartz have shown that relict grains tend to be penetratively deformed and elongate or ribbon-shaped and contain numerous subgrains, whilst recrystallised grains

usually have a minor elongation (Hobbs, 1968; Hirth and Tullis, 1992; Stipp *et al.*, 2002a, 2002b, 2010; Stipp and Tullis, 2003). These characteristics are observed in the pyrrhotite infills of foliation boudinage structures **[Figure 7.6a,d]** and may explain why SPOs are found in both the relict and recrystallised grain populations **Figure 7.7**. Newly recrystallised pyrrhotite grains occur in sheets between old grain relicts forming a network of smaller recrystallised grains across the sample **[Figure 7.6]**, similar to the fabric observed by Hirth and Tullis (1992) and Stipp *et al.* (2002b). CPO patterns can also develop in recrystallised grain aggregates and may originate from large relict grains that have been partially recrystallised (Passchier and Trouw, 2005).

7.5.4 Shape Fabric

The XZ- and YZ-planes of the foliation boudinage structures show grain shape preferred orientations (SPO) of the pyrrhotite grains **[Figure 7.7].** Both the XZ- and YZ-planes have a dominant horizontal SPO, that is parallel or sub-parallel to the shale layering seen in **Figure 7.4**. The SPO is perpendicular to the *c*-axes of pyrrhotite grains and this is also present in studies by Bayer and Siemes (1971), Ostwald and Lusk (1978) and McQueen (1987). Despite the relict grains typically having greater R-values (aspect ratios) than the recrystallised grains, the orientation of the SPO for both populations are remarkably consistent. It is difficult to make the distinction between the relict and recrystallised grains from looking solely at the rose plots of the SPO. The similarity in the orientations of relict and recrystallised pyrrhotite grain axes is probably caused by the recrystallisation process which forms slightly elongate recrystallised grains (Hobbs, 1968; Hirth and Tullis, 1992; Stipp *et al.*, 2002a, 2002b, 2010; Stipp and Tullis, 2003). In all foliation boudinage structures analysed in this study,

recrystallised pyrrhotite grains typically have a smaller area and are more numerous than the relict grains.

SPO fabrics can develop through dislocation creep (Passchier and Trouw, 2005), consistent with the results observed in the CPO. The deformation of the pyrrhotite resulted from dislocation creep along the basal planes. These orientations of pyrrhotite grains will deform more readily and this could explain the relative lack of strain observed in some larger grains.

If the SPO is produced by coaxial flow, the SPO seen in **Figure 7.7** will be approximately parallel to the finite strain axes. The non-coaxial component has not been determined in this study but is thought to be relatively small within the foliation boudinage structures due to the fabric observed in the CPO, meaning the finite strain ellipse will only minimally rotate away from the instantaneous stretching axes (ISA) with progressive deformation. The SPO will therefore lie between the orientation of the ISA and the finite strain axes.

7.5.5 Strain in Pyrrhotite Filled Foliation Boudinage Structures

The Rf/ϕ method has been used to calculate the mean aspect ratio (R-value) and long-axis orientation for the relict pyrrhotite grain ellipses **[Figure 7.9]**. Fry plots were also created and showed similar results for the strain ellipses. The long-axis orientation calculated in the Rf/ϕ analysis is consistent with that calculated by the SPO. A benefit of the Rf/ϕ method is the ability to consider the probable non-sphericity of the pre-deformation pyrrhotite grains. Recrystallised pyrrhotite grains were removed for the Rf/ϕ analysis to reduce the skew error in the resultant strain and no volume change is assumed during the deformation process.

The directions of shortening during the pyrrhotite grain finite strain are gently plunging towards either the ENE or ESE **[Figure 7.11]**. These shortening directions approximate the normal to the steeply west-dipping Urquhart Shale layering and can be explained as a strain response to the shortening of the steep anisotropy.

7.5.6 Timing of Pyrrhotite Deformation

Previous studies have shown that foliation boudinage structures form by plane strain deformation through layer-normal shortening and layer-parallel extension of a foliation or shale fabric (Platt and Vissers, 1980; Mandal and Karmakar, 1989; Arslan *et al.*, 2008, 2012). This plane strain deformation results in the long-axis of foliation boudinage structures in a single orientation parallel to the intermediate principal strain (Platt and Vissers, 1980; Mandal and Karmakar, 1989; Arslan *et al.*, 2008, 2012). Aerden (1991) showed evidence of 'chocolate tablet' foliation boudinage as a result of two boudinage axes parallel to the principal directions of the strain ellipsoid. This combination of strain directions is not observed at Mount Isa. As shown in Chapter 6 and Williams *et al.* (2023), oriented foliation boudinage structures at Mount Isa have long-axes that plunge gently to both the north and south. These orientations have been used as evidence for a progressive development from D4a ENE-WSW dextral-reverse shortening through to the D4b WNW-ESE sinistral-reverse shortening event of Miller (2007).

The maximum principal strain direction of FBS2 and FBS4 are in the X-direction of the foliation boudinage structures. This is to be expected as the foliation boudinage structures develop by the extension of layering in the X-axis. However, the maximum principal strain axis of FBS1 and FBS3 are in the Y-direction of the foliation boudinage structures. This is not expected

based on the assumed foliation boudin formation mechanism and is evidence for flattening post-pyrrhotite infill. The evidence of one dominant linear orientation of foliation boudinage structures (north-south; Chapter 6 and Williams *et al.*, 2023), implies the plane strain is dominant during their initial formation. A flattening strain during their initial formation would result in the presence of two orthogonal orientations of foliation boudinage structures, similar to Rosebery Mine (Aerden, 1991).

For this reason, the flattening strain recorded in the pyrrhotite infills is likely to have post-dated the initial development of the foliation boudinage structures. The change from plane strain during the initial formation to a late stage flattening strain in the pyrrhotite infills is interpreted as an evolutionary strain over the entire time of foliation boudin development at Mount Isa. The flattening strain may also be a result of strain partitioning in the weaker pyrrhotite infills of the foliation boudinage structures, but this does not account for the plane strain required for the initial formation of the structures. It cannot be ruled out that this strain was completely post-mineralisation during the later D5 events.

Importantly however, the shortening directions of the pyrrhotite infills **[Figure 7.11]** are the same as the shortening of the foliation boudinage structures in Chapter 6 and Williams *et al.* (2023). North-plunging foliation boudinage structure lineations have a shortening direction that is to the ENE, whilst the south-plunging structure have shortening directions to the ESE. This agrees with the evidence presented in Chapter 6 and Williams *et al.* (2023) that north-plunging foliation boudinage structures are formed by dextral-reverse slip during D4a ENE-WSW shortening and south-plunging structures resulting from the sinistral-reverse slip during the D4b WNW-ESE shortening event.

7.6 Conclusions

In this study multiple foliation boudinage structures have been analysed using electron backscatter diffraction. The electron backscatter diffraction maps show pyrrhotite grains within foliation boudinage structures have significant intracrystalline deformation, resulting in large local misorientations within grains. The deformation observed within the pyrrhotite filled foliation boudinage structures have allowed some conclusions to be made about the deformation mechanism, grain fabric, finite strain geometry and timing of deformation.

- Deformation of pyrrhotite in foliation boudinage structures is by dislocation creep and is dominated by basal slip. Deformation was likely dominated by coaxial flow, with a component of non-coaxial deformation. Pyrrhotite grain *c*-axes are normal to the shale layering at Mount Isa and parallel to the approximate shortening direction.

- Dynamic recrystallisation of pyrrhotite was by subgrain rotation.

- Both relict and recrystallised grains show a grain shape preferred orientation as a result of deformation. Recrystallised grains form a network of typically smaller grains between relict grains.

- The shape preferred orientation of the relict grains is sub-parallel to the shale layering and mimics the geometry of the 3-dimensional strain ellipsoid. 2-dimensional strain analyses using the Rf/ϕ method show that the orientations of the long-axes of relict pyrrhotite grains agree with the orientation of the shape preferred orientation fabric.

- Shortening directions of the pyrrhotite grains are approximately east-west and are similar to the shortening directions of the foliation boudinage structures. This evidence for the shortening directions agree with the results in Chapter 6 and Williams *et al.* (2023).

- Foliation boudinage structures at Mount Isa developed during plane strain deformation in D4a through to D4b. Deformation of the pyrrhotite infill shows flattening strain that post-dates the initial formation of the foliation boudinage structures. The change from plane to flattening strain may reflect progressive deformation during foliation boudinage.

- Strain in the sulphide infills of foliation boudinage structures at Mount Isa shows that these structures may not remain as open voids throughout their formation. The measured strains may be preserved due to the weakness of pyrrhotite at these conditions.

- There is clear evidence for deformation of ore-related, hydrothermal sulphides at Mount Isa.

CHAPTER 8

A 3-Dimensional Insight into the Development of Foliation Boudinage Structures from Serial Section Modelling

8.1 Introduction

The 3-dimensional geometry of foliation boudinage structures are not well understood. Although foliation boudinage structures have been illustrated and described in cross-section **[Figure 8.1]**, no studies have illustrated their geometries in 3-dimensions. Previous modelling of foliation boudinage structures has focused on their formation mechanisms. These include analogue modelling using plasticine layers (Mandal and Karmakar, 1989), simulated computer modelling using the FLAC software (Arslan *et al.*, 2008) and a visco-elastic lattice-particle model (Arslan *et al.*, 2012). These studies have emphasised 2-dimensional sections through foliation boudinage structures.

Swanson (1992) and Arslan *et al.* (2008, 2012) show that foliation boudinage structures can close to a fishmouth as an end-member structure. However, it is unclear whether these fishmouth foliation boudins occur at the centre of the long-axis, or closer to the fracture tips, as no study has shown how foliation boudinage structures close along their long-axes. Previous studies suggest that there are at least two stages in the development of foliation boudinage structures along their long-axes, as illustrated by the symmetrical structures in **Figure 8.2**. *Stage 1* shows the opening of the foliation boudinage structure where there is an increase in the cross-sectional area at the centre. *Stage 2* shows the closing of the structure by further shortening. There are two possible models for how this closure occurs based on the models proposed in the previous literature (e.g. Platt and Vissers, 1980; Mandal and Karmakar, 1989; Swanson, 1992; Arslan *et al.*, 2008, 2012). *Model I* shows the largest cross-sectional areas near the mid-point of the long-axis, with the structure closing to a fishmouth near the fracture tips **[Figure 8.2]**. *Model II* shows a decrease in cross-sectional area at the centre of the structure as it closes to a fishmouth **[Figure 8.2]**.

The aim of this chapter is to investigate the 3-dimensional geometry of asymmetrical foliation boudinage structures from Mount Isa and to infer how these structures evolved. MOVE modelling software (Petroleum Experts) and computerised tomography (CT) scanning is used. A specific aim is to distinguish between the alternative models for fishmouth development described above.
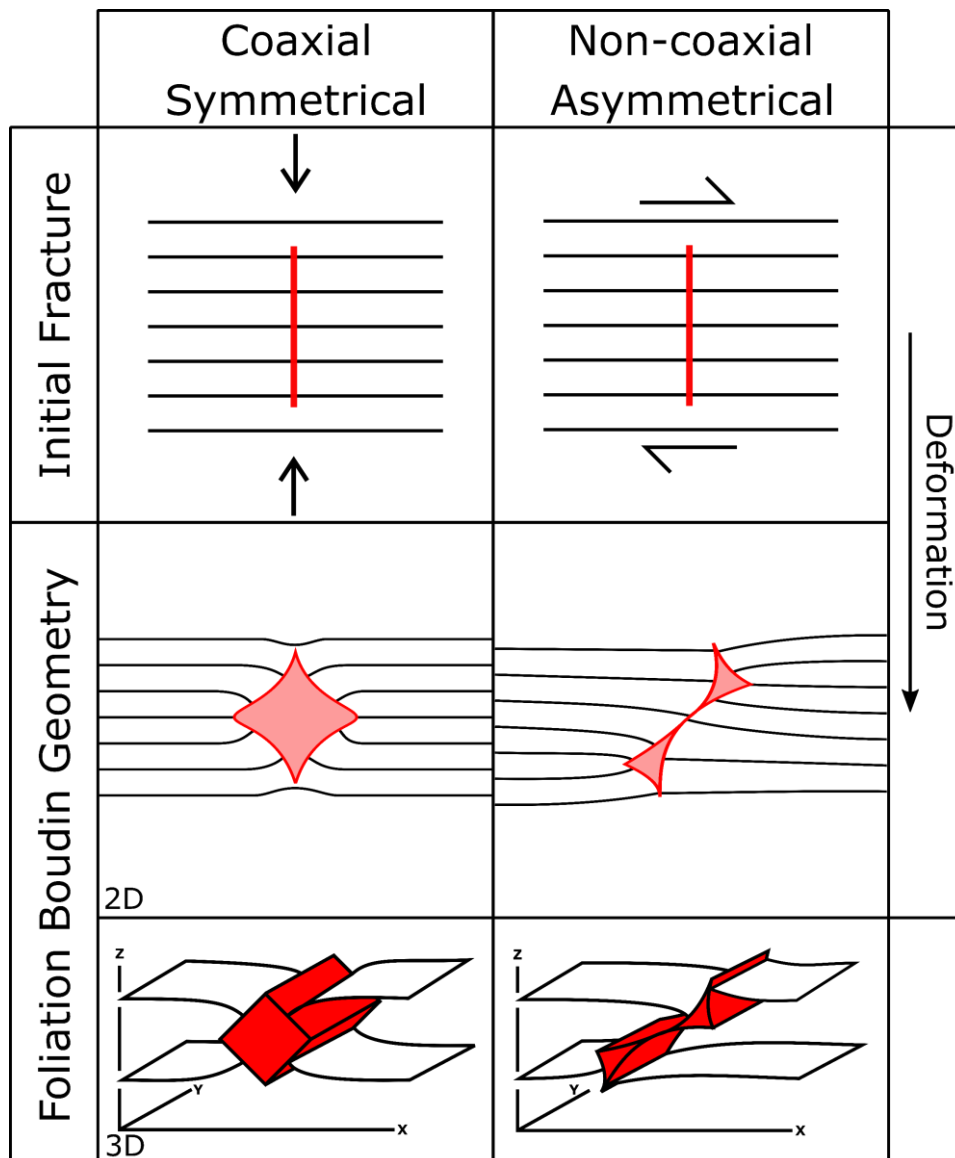
Figure 8.1: Schematic diagrams showing the formation mechanisms and cross-sectional geometries of symmetrical and asymmetrical foliation boudinage structures during opening based on Hambrey and Milnes (1975), Platt and Vissers (1980), Mandal and Karmakar (1989), Arslan *et al.* (2008, 2012), Williams *et al.* (2023) and Chapter 6. Symmetrical foliation boudinage structures forming by coaxial, layer-normal shortening and layer-parallel extension and asymmetrical structures by non-coaxial shortening and layer-parallel extension. Additional figure in **Appendix F.3** and **Appendix F.4**.
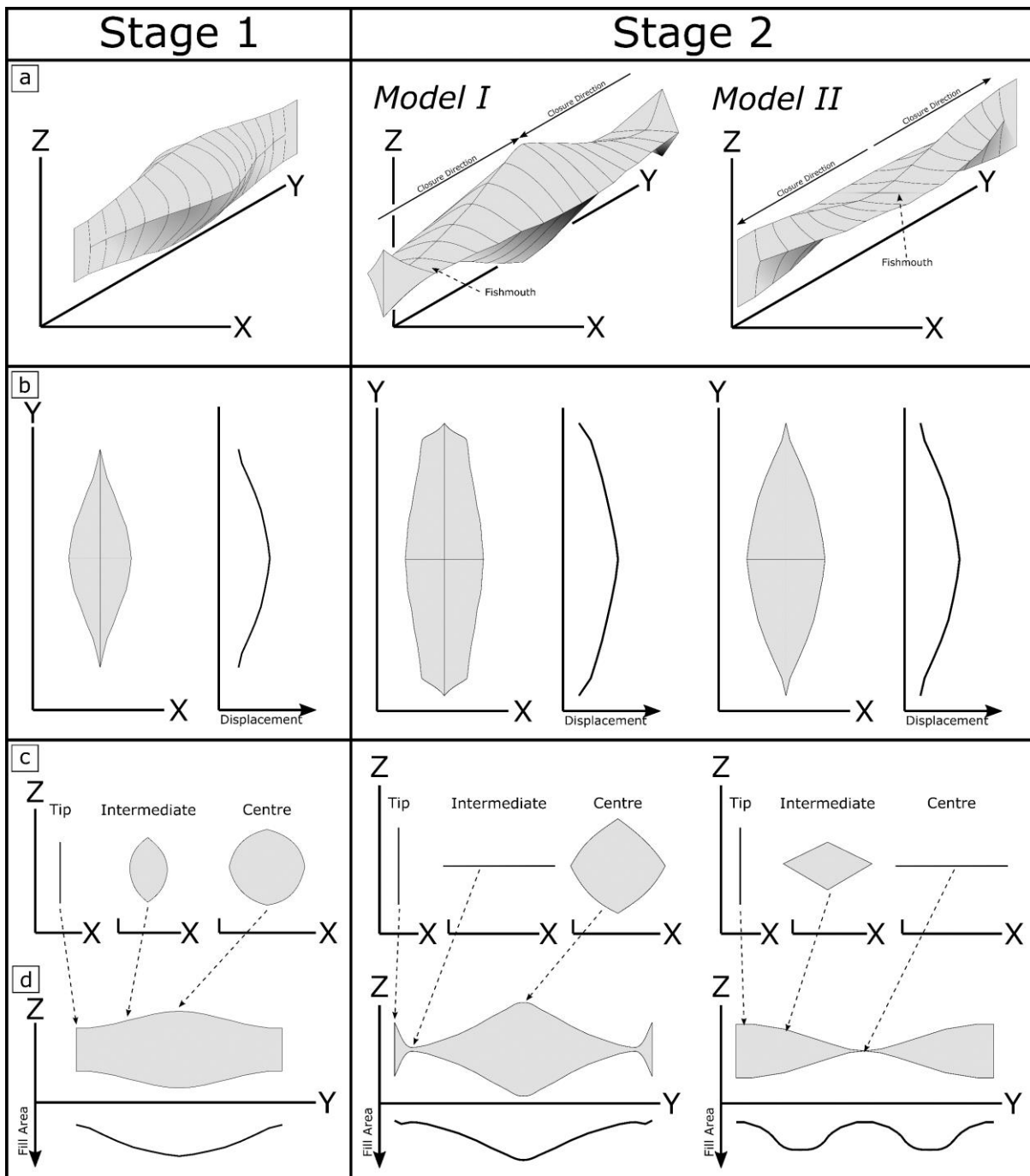
Figure 8.2: Diagrams showing two stages in the formation of symmetrical fishmouth foliation boudinage structures by layer-normal shortening in the Z-direction **[Figure 8.1]**. *Stage 1* shows the opening of the structure, with the largest cross-sectional areas near the centre of the void. *Stage 2* depicts the closure of the structure by further shortening and two possible models for their 3-dimensional geometries, based on previous literature (e.g. Arslan *et al.*, 2008, 2012). *Model I* shows the closure of the structure initiates near the fracture tips, with the largest cross-sectional areas near the mid-point of the long-axis. *Model II* shows the closure of the structure initiates near to the mid-point of the long-axis, with the fishmouth progressing towards the fracture tips. Co-ordinates are given as sample axes, where the XY-plane is parallel to the shale layers and Z-direction is normal to the shale layers. **a)** 3-dimensional geometry of the foliation boudinage structure. **b)** Plan view of the foliation

boudinage structure in the XY-plane, with the change in relative displacement along the structure. **c)** Cross-sectional views through the foliation boudinage structure in the XZ-plane. **d)** Cross section view through the foliation boudinage structure in the YZ-plane, with the change in relative areas along the structure.

8.2 Methodology

8.2.1 Sample Preparation

Core samples containing foliation boudinage structures were collected from drillholes at Mount Isa Mine. The samples were assessed and a single foliation boudin sample was chosen based on the criteria that (1) the foliation boudinage structure intersects opposite sides of the drill core and (2) the structure fits onto a thin section glass slide. The drillhole was cored with an 'NQ2' size (50.7 mm) drill bit. A small loss of core diameter, probably owing to movement of the drill bit, meant the diameter of the sample was roughly 50 mm.

Co-ordinates are given as sample axes, where the XY-plane is parallel to the shale layers, Z-direction is normal to the shale layers and Y-direction is the long-axis of the foliation boudinage structure (Chapter 6 and Williams *et al.*, 2023). The sample was cut normal to the long-axis (Y-direction) of the foliation boudinage structure **[Figure 8.3]**. Some loss of material during cutting resulted in nine approximately 5 mm thick rock chips. Polished sections were produced from the rock chips. The chip at the edge of the drill core **[**rock chip 'A'; **Figure 8.3]** was too thin to produce a polished section and has not been included. The eight serial sections were scanned using an Epson scanner at 6400 dpi.

Similar to all drill core scale foliation boudinage structures at Mount Isa, this sample had a silica-dolomite rim and a sulphide filled interior (Chapter 6 and Williams *et al.*, 2023). The outer limit of the silica-dolomite is typically the outer edge of the foliation boudinage

structure, with sulphides almost exclusively restricted to the interior (Chapter 6 and Williams *et al.*, 2023).
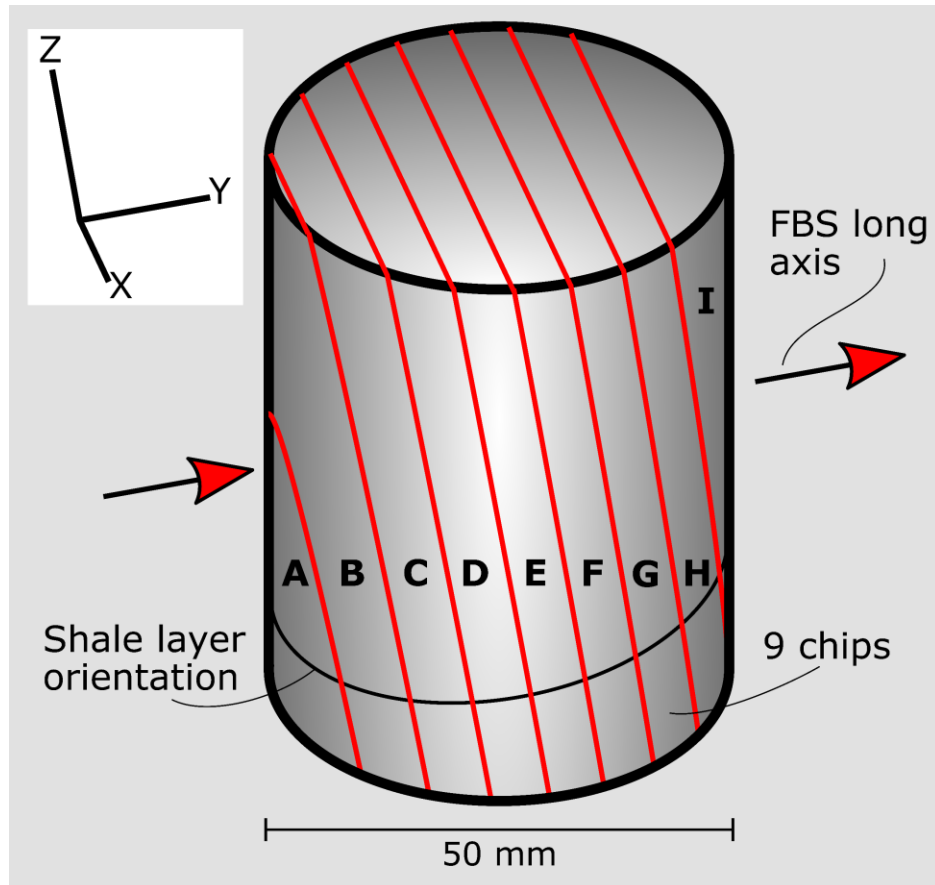
Figure 8.3: Drill core cut into nine 5 mm chips normal to the length of the foliation boudinage structure. Eight of which were used to create polished sections. Co-ordinates are given as sample axes, where the XY-plane is parallel to the shale layers and Z-direction is normal to the shale layers.

8.2.2 Modelling

8.2.2.1 MOVE Software

The MOVE software (Petroleum Experts) is a 3-dimensional model building application that allows the input, building and export of geological models. MOVE was chosen in this study owing to the relative ease of use and because it is one of the most complete structural geology modelling and analysis toolkits available.

Seven of the eight polished section scans were imported into the MOVE software as cross-sections at an equivalent scale of 5 mm distances. Sample 'B' was not included, as a substantial part of the foliation boudinage structure is missing in the polished section. The shale layering and the outer edge of the foliation boudinage structure were traced using the line drawing tool in each cross-section. The traced shale layers in each section were then joined using the surface creation tool, modelling the shale surfaces throughout the structure. The circumference of each foliation boudinage structure was split into lengths between distinguishable points, such as significant changes in geometry, in each section **[Figure 8.4]**. Surfaces were created between each line using the surface creation tool and joined into one surface, forming the outer surface of the foliation boudinage structure.
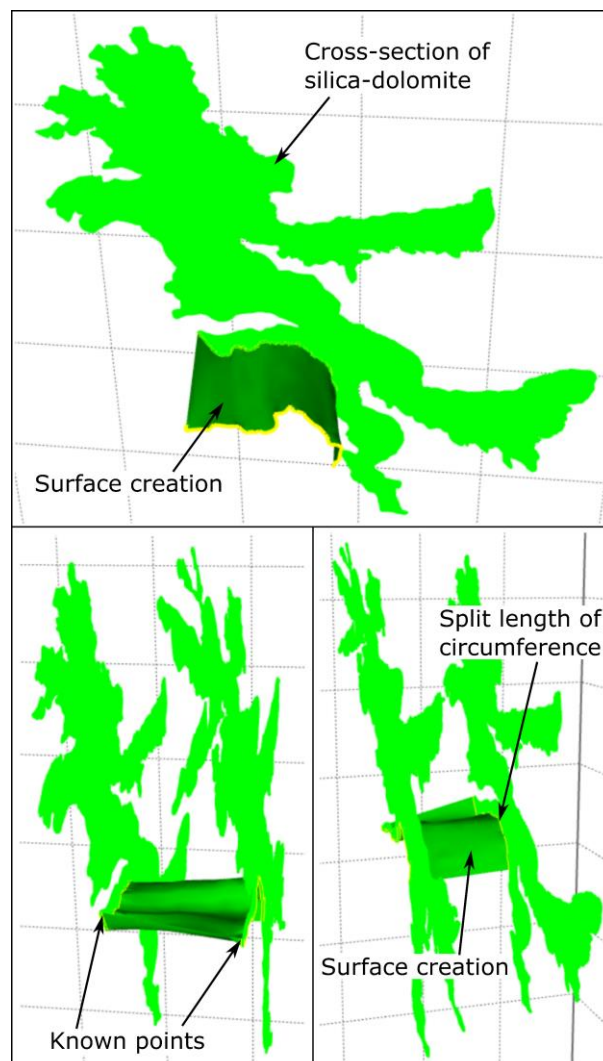
Figure 8.4: (Previous Page) Building the MOVE model by separating the circumference of the foliation boudinage structure between known points in each cross-section. Individual surfaces are created between the known points in adjacent sections, which are subsequently joined to form a single surface of the foliation boudinage structure. Background grids represent 10 mm squares and silica-dolomite cross-sections have a separation of 5 mm.

8.2.2.2 CT Scanning

Computerised tomography (CT) scanning of drill core samples is a non-destructive technique allowing visualisation of the interior of the foliation boudinage structures. CT scanning was chosen for this study as it allows the complete imaging of the structures in 3-dimensions. CT scanning was performed at the Henry Royce Institute at the University of Manchester using the Nikon XTEK 320/225 kV Custom Bay 3D X-Ray Computerised Tomography Scanner. Owing to the high power needed to achieve enough X-Ray transmission through the drill core samples, the resolution was limited to approximately 70 μm. Features smaller than 70 μm were not captured in the scanning and may have resulted in the loss of definition of the model. A segmentation intensity threshold of 64-255 was used to differentiate the sulphide material as it provided the best observable results. Segmentation intensity is displayed as a histogram plot and scaled from 0 to 255 similar to that associated with RGB colours.

CT scanning of the foliation boudinage structures from Mount Isa was unable to distinguish the shale layering from the silica-dolomite rim due to their similar density and contrast qualities, resulting in only the high contrast sulphides being readily identified in the model.

8.2.3 Geometrical Properties of the Foliation Boudinage Structure

8.2.3.1 Perimeter and Area

The seven complete serial sections were imported into the Inkscape drawing software (version 0.92.4) at 1:1 scale. The perimeters of both the silica-dolomite (outer edge of foliation boudinage structure) and the sulphides were then traced **[Figure 8.5; Appendix H.1]**. All lines were traced using the Inkscape 'Bezier curve and straight lines' tool in the 'straight line segment' mode. Using this single method for all serial sections allowed for consistency in line drawing and speed in drawing. The inbuilt measuring functions of Inkscape were used to calculate the area and perimeter length in each foliation boudinage structure. Errors in the perimeter and area measurements were calculated from the mean of three repeated traces of the foliation boudinage structure in sample F. Sample F was chosen as it is the midpoint of the serial sections. Ellipses that represented the approximate geometry of each foliation boudin were fitted to show the general trend in aspect ratios through the structure.

Figure 8.5: (Following page) Diagrams of the modelled foliation boudinage structure in section G, showing: **a)** the polished thin section in plane polarised light (PPL). **b)** areas and perimeters of the silica-dolomite (green) and sulphides (red). **c)** simplified cartoon diagram of the shape of the structure and orientations of displacement. **d)** shale layer point-to-point displacements. **e)** displacement vectors of the shale layers. All diagrams are shown to the same scale. Sample 'G', Drillhole № '201903092', 32.1 m. Additional material in **Appendix H.1**.

a Section G

10 mm

b Area

c Cartoon Structure

d Displacement

7.35
9.86
16.48
19.98
17.93
9.47 15.58
18.52
22.65 20.15
16.90
11.62
6.63
9.26
15.04
2.94
11.58
1.44

e Displacement Vector
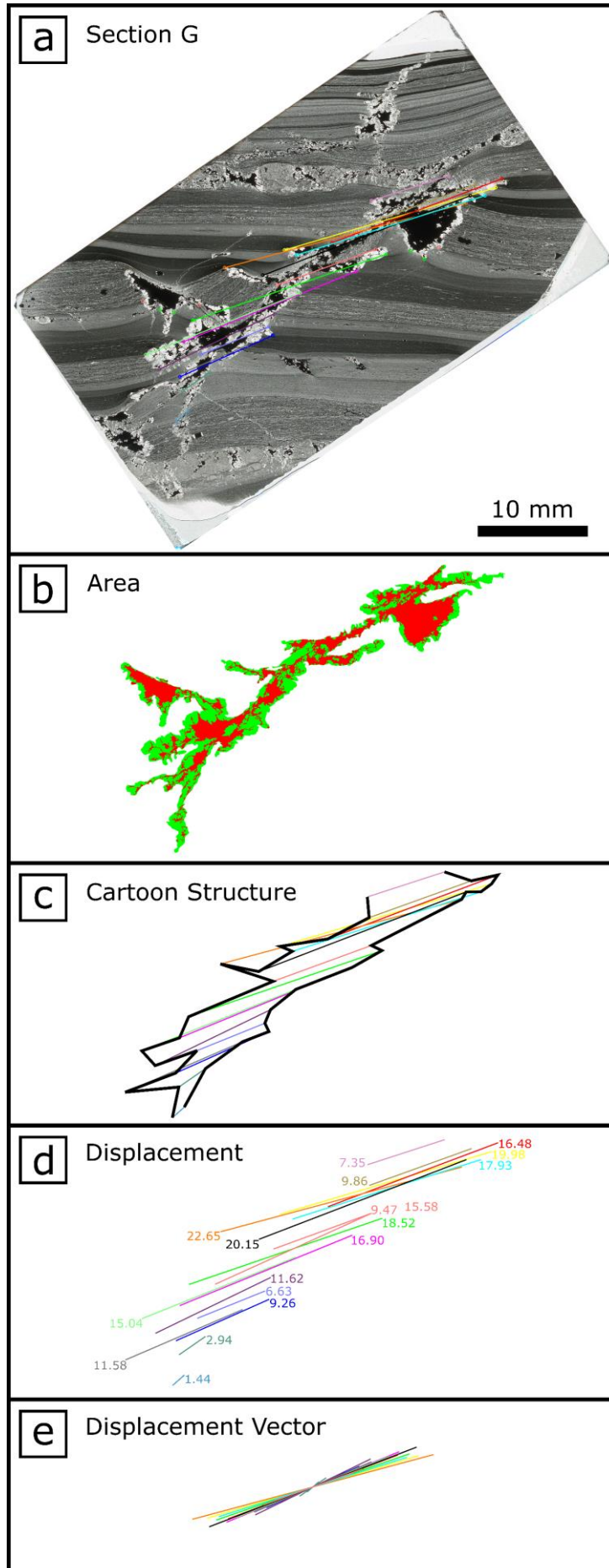
8.2.3.2 Volume

The total volume of the modelled portion of the foliation boudinage structure was calculated using the mean area of adjacent cross-sections with the known separation of 5 mm. The same process was repeated for the sulphides within the structure. The volume of the silica-dolomite rim material was calculated as the difference between the total foliation boudin volume and the sulphides. Errors in the volume calculation derive from the error in the area and ±0.5 mm in the section separation distance.

8.2.3.3 Sphericity

The irregularity of the perimeter of both the foliation boudinage structures and the sulphides were calculated from the perimeter and area. Sphericity can be used to measure grain boundary irregularity by showing how closely the grain resembles the circumference of a circle. Sphericity was measured as it may correlate with the extent of replacement, with a lower sphericity of the foliation boudins possibly indicating a longer and more complex replacement process. Sphericity of a sphere is equal to 0.5 and decreases to 0 as the boundary becomes infinitely irregular. Sphericity was calculated using **Equation 1** and **Equation 2**.

$$Sphericity = \frac{A}{P*R}$$

Equation 1

Where *A* is equal to the area, *P* is the perimeter and *R* is the area equivalent radius **[Equation 2]**.

$$R = \sqrt{\left(\frac{A}{\pi}\right)}$$

Equation 2

Errors in the sphericity calculation are derived from errors in both the perimeter and area measurements.

8.2.3.4 Displacements

Points of intersection between each shale layer and the foliation boudinage structure were highlighted **[Figure 8.5]**. Point-to-point displacements of individual shale layers were measured in each section across the foliation boudinage structure. Each shale thickness (individual layer distance) was measured normal to the layer and averaged across each cross-section (total layer distance). Errors in the displacement measurement are negligible.

8.2.4 Restoration

Three polished thin sections of foliation boudinage structures were traced using Inkscape. One sample (E) in the XZ-plane has been used from the previously mentioned serial sectioning. Two samples (BW302 and BW502) are from additional foliation boudinage structures collected from Mount Isa drill core. Sample BW302 is in the XZ-plane and BW502 in the YZ-plane of the structure. All three samples are representative of those at Mount Isa and show similar characteristics, such as silica-dolomite rims and sulphide infills. Multiple diagrams were created to restore the foliation boudins in stages to undeformed shale from complete structures with silica-dolomite and sulphide infills. Polished thin sections, offcut rock chips, drill core samples and previous petrographic work (Chapter 6.3.1) were used to develop the diagrams.

8.3 Results

8.3.1 Models

The 3-dimensional MOVE model is shown in **Figure 8.6**. The model is also available as a 3D

PDF in **Appendix F.5** and as a fly around video in **Appendix F.6**. The model identifies significant

displacement and changes in geometry through the structure, with new portions opening and

closing through the model.
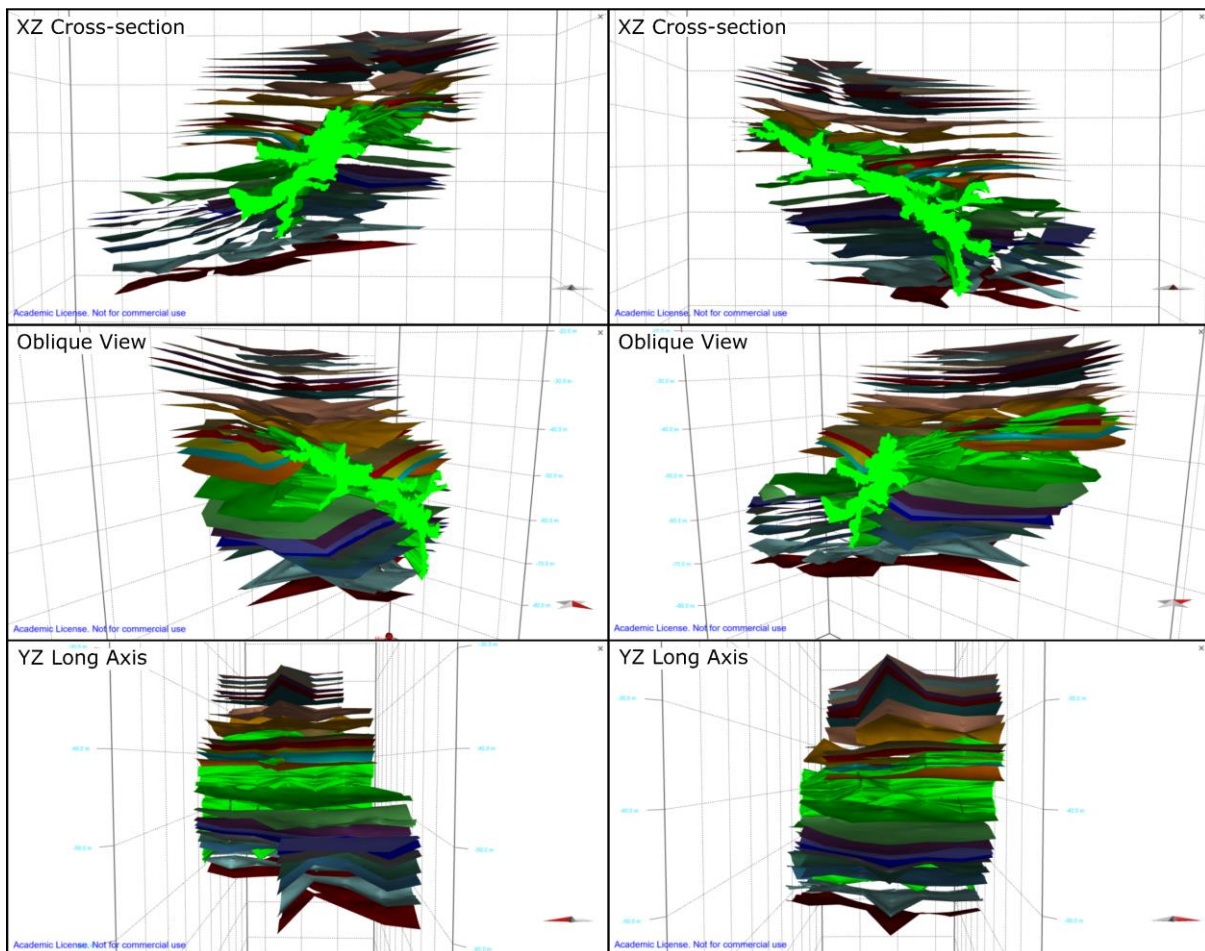
Figure 8.6: Images of the foliation boudinage structure modelled using serial sections in the MOVE software. The silica-dolomite volume (green) changes geometry along the long-axis and the shale layers bend into the central structure. The model is shown at a x1000 scale, where 1 mm is equal to 1 metre. The background grids represent 10 mm squares. Sample from Drillhole № '201903092', 32.1 m. Additional material in **Appendix F.5** and **Appendix F.6**.

The CT scan of the foliation boudinage structure is shown in **Figure 8.7** and is available as a fly around video in **Appendix F.7**. The CT scan shows the most complete view of the 3-dimensional geometry of the sulphide fill within the foliation boudin.
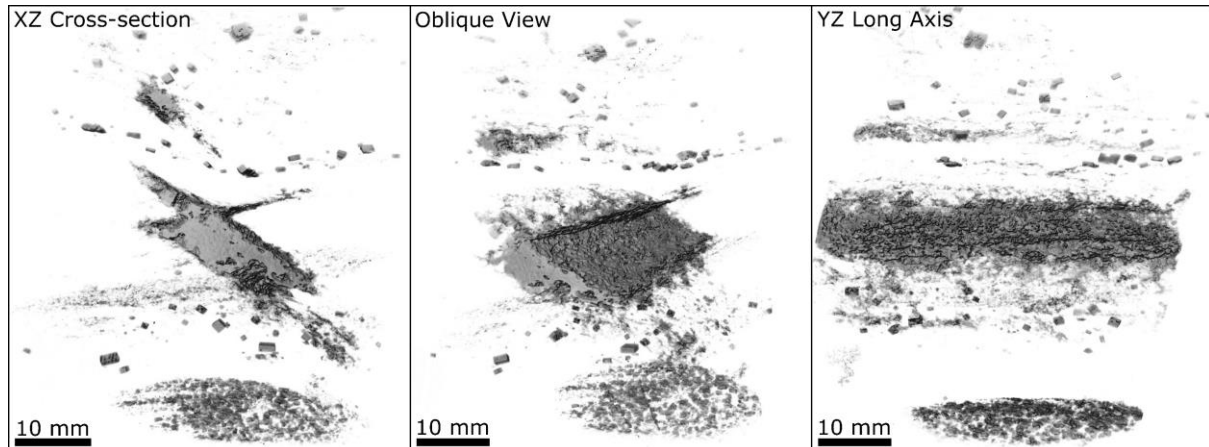
Figure 8.7: Computerised tomography (CT) images of the sulphide fill within the foliation boudinage structures. Sample from Drillhole № '201903052', 23.5 m.

8.3.2 Geometry

8.3.2.1 Perimeters

The perimeters of the foliation boudinage structures and sulphide infill for each section are shown in **Table 8.1**. **Figure 8.8** shows how the perimeters in each section change with distance along the long-axis of the foliation boudinage structure. In general, the perimeters of both the foliation boudin and the sulphides increase from section C (0 mm) to section I (30 mm). Errors of +1.27% and -2.53% were calculated for the perimeter measurements.

	Distance (mm)	FBS Area (mm²)	FBS Perimeter (mm)	FBS Sphericity	Sulphide Area (mm²)	Sulphide Perimeter (mm)	Sulphide Sphericity	Silica-Dolomite Area (mm²)	FBS Aspect Ratio
C	0	115.90	160.80	0.118667	55.01	477.01	0.027559	60.89	1.81
D	5	126.47	167.44	0.119045	59.66	363.76	0.037636	66.81	1.87
E	10	118.09	162.59	0.118464	51.34	389.1	0.032639	66.75	1.56
F	15	128.44	224.10	0.089636	56.83	540.26	0.024732	71.61	1.88
G	20	125.98	239.44	0.083086	55.12	610.15	0.021567	70.86	3.31
H	25	121.84	190.14	0.102896	63.01	524.54	0.026823	58.83	3.94
I	30	120.39	236.87	0.082103	55.81	593.58	0.022308	64.58	3.17

Table 8.1: Perimeters, areas, sphericity, and ellipse aspect ratios of the foliation boudinage structures (FBS), sulphides, and silica-dolomite in each section.
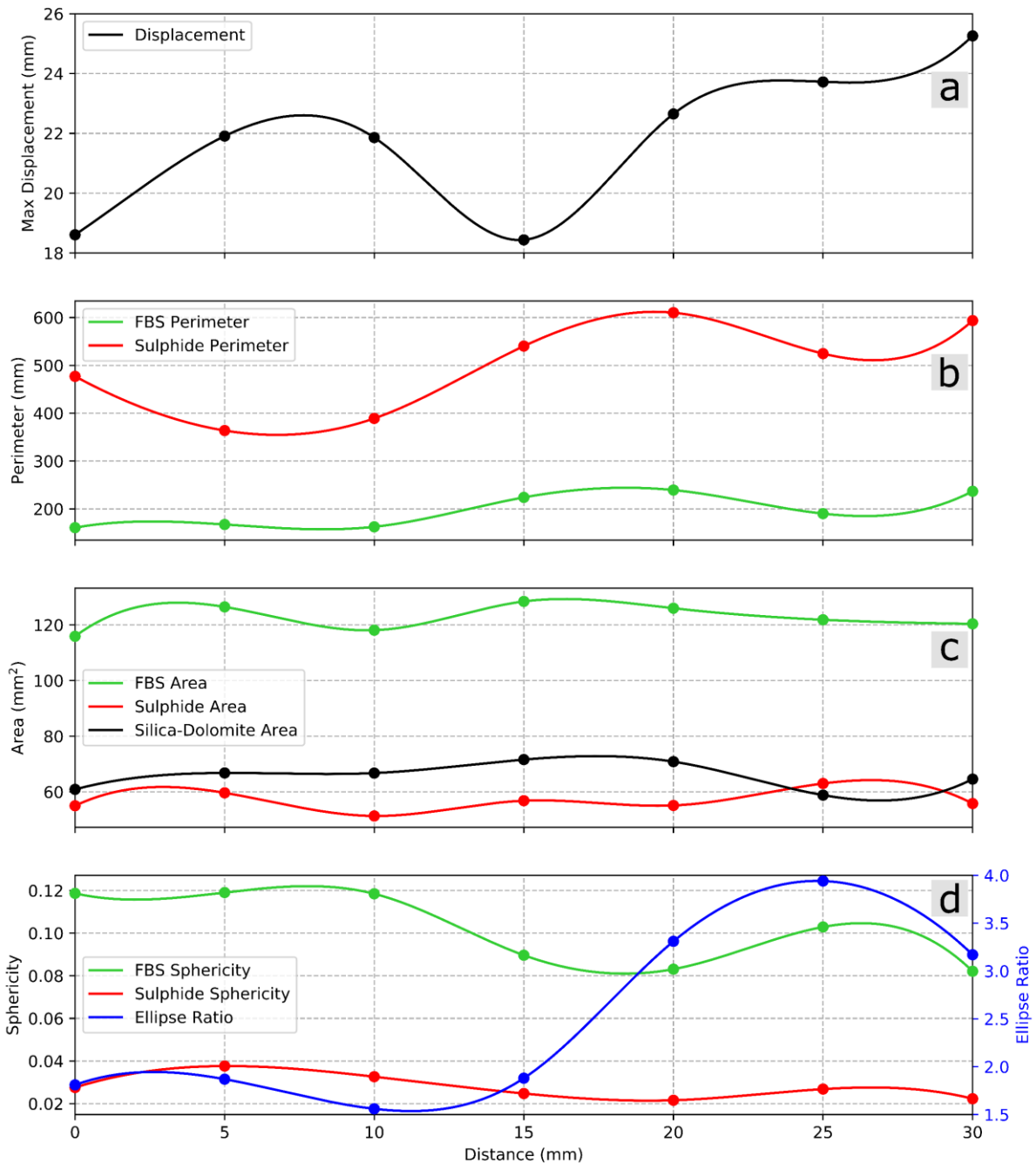
Figure 8.8: Graphs of foliation boudinage structure features against distance through the serial cross-sections (section C = 0 mm; section I = 30 mm). **a)** Distance against maximum displacement in each cross-section. **b)** Distance against perimeter lengths for the foliation boudin and sulphide infill. **c)** Distance against areas for the foliation boudin, sulphide and silica-dolomite. **d)** Shape parameters showing distance against sphericity for the foliation boudin and sulphide infill; and distance against ellipse aspect ratio of the foliation boudin geometry.

8.3.2.2 Areas

The areas of the foliation boudinage structures and interior sulphides in each section are shown in **Table 8.1**. **Figure 8.8** shows how the areas of the foliation boudinage structure, sulphides and silica-dolomite change with distance along the long-axis. Errors of +1.41% and -1.70% were calculated for the area measurements.

8.3.2.3 Volume

Volumes between adjacent sections are shown in **Table 8.2**. The resulting total volume of the modelled foliation boudinage structure is 3695 mm^3, sulphide volume is 1707 mm^3, and silica-dolomite volume is 1988 mm^3. An error of ±11.55% was calculated for the volume measurements, based on errors in the area and on a possible error of ±0.5 mm in the separation distance.

Sections	FBS Volume	Sulphide Volume	Silica-Dolomite Volume
C/D	605.93	286.68	319.25
D/E	611.40	277.50	333.90
E/F	616.33	270.43	345.90
F/G	636.05	279.88	356.17
G/H	619.55	295.33	324.22
H/I	605.58	297.05	308.53
TOTAL	**3694.83**	**1706.85**	**1987.98**

Table 8.2: Table of volumes for the foliation boudinage structure (FBS), sulphide and silica-dolomite.

8.3.2.4 Sphericity

Inspection of individual sections shows that irregularity of the foliation boudin margins is related to the amount of replacement **[e.g. Figure 8.5]**. **Table 8.1** shows the sphericity of the foliation boudinage structures, sulphides, and silica-dolomite in each section. An overall trend of decreasing sphericity with distance along the structure from C (mm) to I (30 mm) is

observed **[Figure 8.8]**. Both the foliation boudin and sulphides develop a more complex geometry through the structure. Errors of +3.32% and -2.10% were calculated for the sphericity.

8.3.2.5 Displacements

The point-to-point displacement distances of each shale layer have been calculated for each section along the foliation boudinage structure **[Table 8.3]**. The layer distances on **Figure 8.9a** are the mean cumulative thicknesses of the individual shale layers **[Figure 8.9b,c]**. The 2-dimensional contour map shows displacement is greatest close to the centre of each cross-section **Figure 8.9**. The 3-dimensional displacement surface is shown in **Figure 8.10** and **Appendix F.8**.

The maximum displacements in each section are presented in **Table 8.4** and are shown as a graph of maximum section displacements with long-axis distance in **Figure 8.8**. In general, the displacements increase along the structure from section C (0 mm) to section I (30 mm).
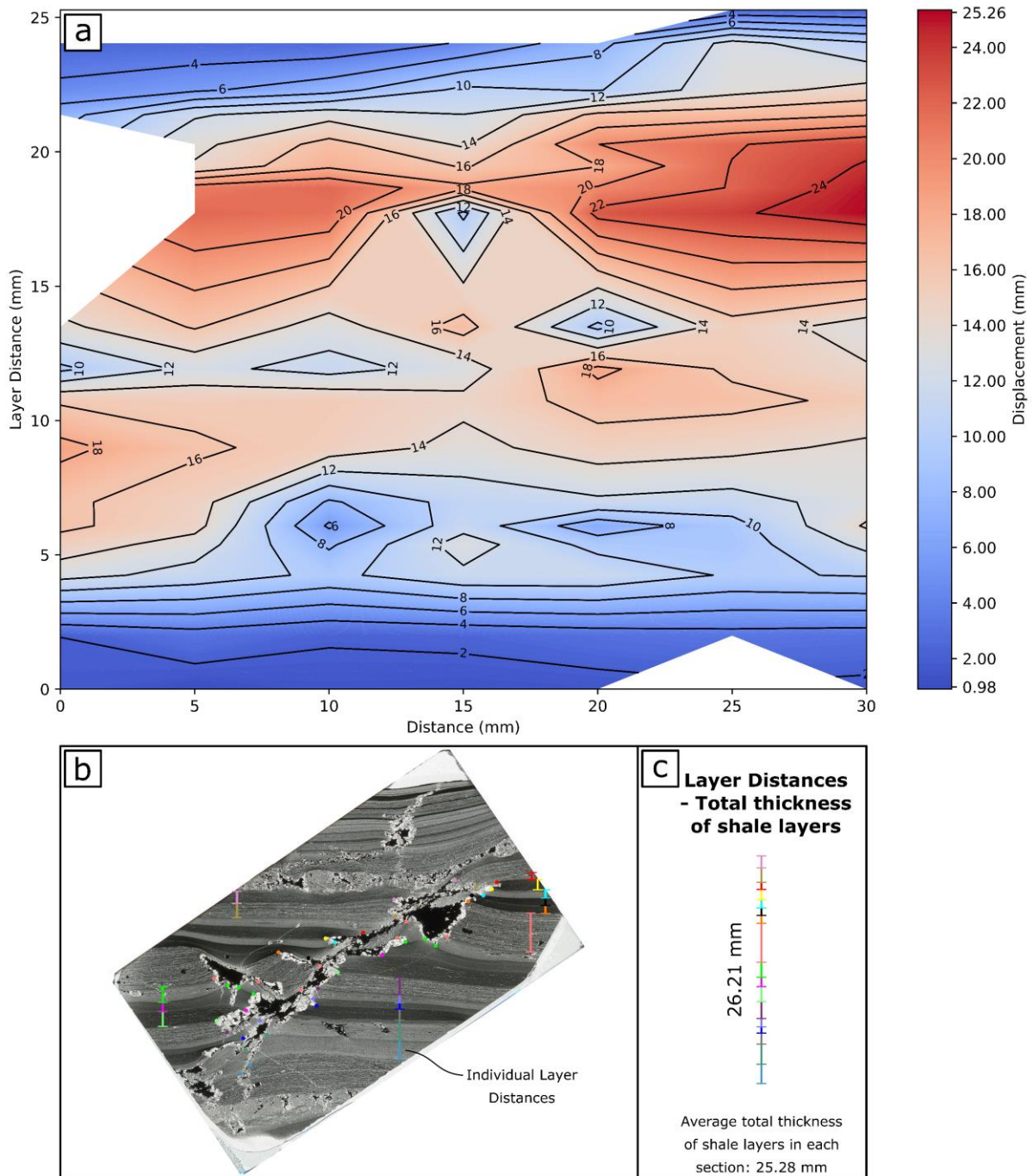
Figure 8.9: a) 2-dimensional contour map of distance along the foliation boudinage structure against distances of shale layers, showing the displacement at each shale layer and for all cross-sections. The plot was created using linear interpolation. **b)** Measuring individual shale layer thicknesses (layer distance) in all sections. Example shown is sample 'G', Drillhole № '201903092', 32.1 m. **c)** Calculating the total thickness of the shale layers in each section in order to calculate the mean.
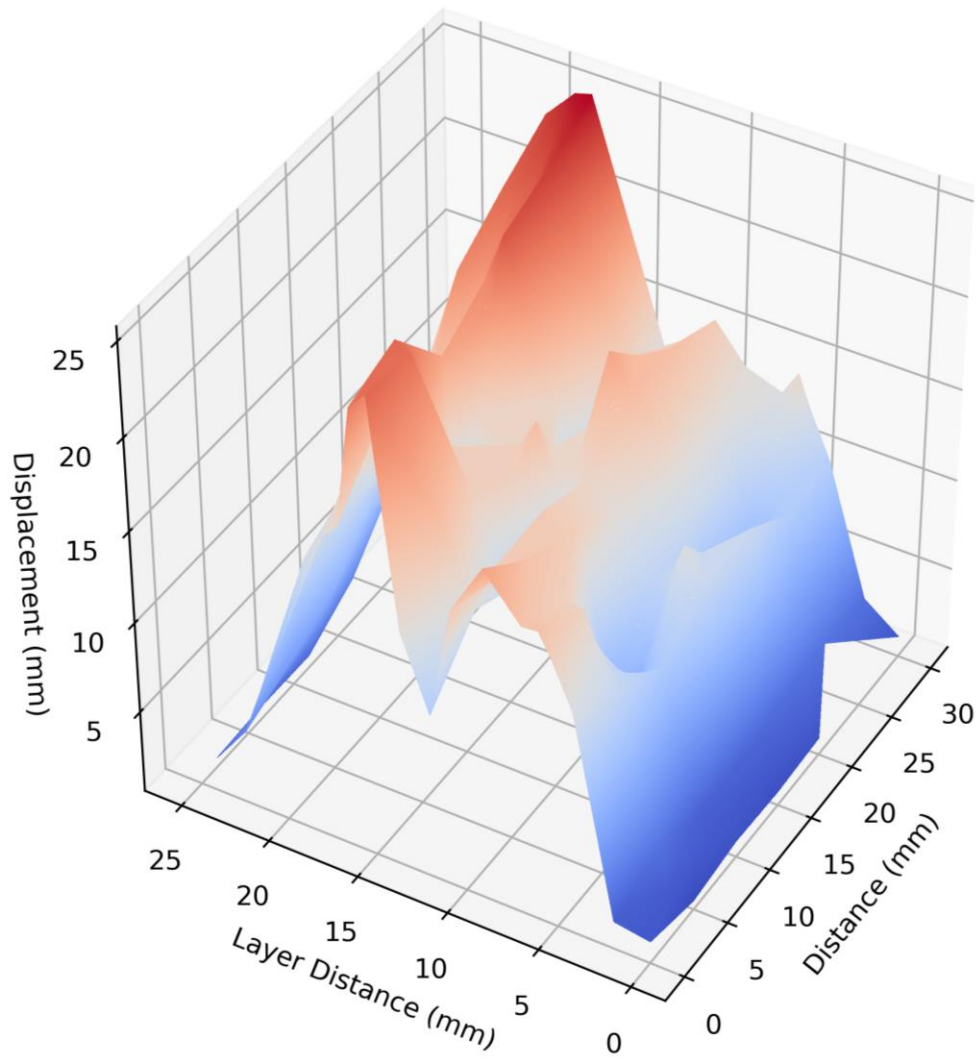
Figure 8.10: Plot of the 3-dimensional displacement surface of the entire modelled foliation boudinage structure. Additional figure in **Appendix F.8**. The surface plot was created using linear interpolation.

Section	Distance (mm)	Grey Blue	Dark Green	Grey	Blue	Lilac	Purple	Light Green	Pink	Green	Peach	Orange	Black	Light Blue	Yellow	Red	Brown	Light Pink	Dark Brown
C	0	1.70	2.01	12.74	15.19	16.42	16.33	18.61	15.72	9.56	13.51	N/A	N/A	N/A	N/A	7.14	4.57	2.36	N/A
D	5	0.98	3.13	11.24	13.00	14.75	15.00	16.33	15.37	12.55	16.17	21.91	20.87	14.23	13.45	11.77	5.68	2.55	N/A
E	10	1.39	2.18	9.50	7.69	5.69	7.69	15.25	15.57	11.25	12.96	21.38	21.86	17.64	16.68	13.25	7.23	2.50	N/A
F	15	1.26	2.38	11.53	13.00	11.27	10.81	13.38	14.52	12.81	16.81	9.54	18.44	15.87	13.71	12.03	10.48	4.18	N/A
G	20	1.44	2.94	11.58	9.26	6.63	11.62	15.04	16.90	18.52	9.47	22.65	20.15	17.93	19.98	16.48	9.86	7.35	N/A
H	25	N/A	3.27	9.74	8.94	9.22	11.17	14.53	16.58	15.59	15.19	23.72	22.11	22.09	21.81	16.98	13.31	12.74	2.41
I	30	1.62	3.06	10.14	12.52	14.25	12.89	13.59	15.55	14.21	12.98	25.26	25.01	24.20	23.40	17.89	14.66	10.28	2.17

Table 8.3: Table of point-to-point displacement-distances for each shale layer and cross-section through the foliation boudinage structure. The colours of the layers are as shown in **Figure 8.5**.

Section	Distance (mm)	Max Displacement (mm)	Shale Layer
C	0	18.61	L Green
D	5	21.91	Orange
E	10	21.86	Black
F	15	18.44	Black
G	20	22.65	Orange
H	25	23.72	Orange
I	30	25.26	Orange

Table 8.4: Table of maximum point-to-point displacements in each section of the foliation boudinage structure. The highlighted colour of the traced shale layer indicates where the maximum displacement occurs in each section.

8.3.3 Evolution of Foliation Boudinage Structures from Restoration

Diagrams created from the restoration of three foliation boudinage structures reveal how the structures evolved **[Figure 8.11]**. The foliation boudinage structures develop from an initially undeformed shale to shale with dolomite lenses, shale with veins, deformation of veins, foliation boudin development with silica-dolomite fill and finally sulphide filled structures. Samples E and BW302 are cross-sections through the XZ-plane of the foliation boudinage structure. Sample BW502 is a cross-section through the YZ-plane (long-axis) of the structure.

Figure 8.11: (Following page) Diagrams showing the evolution of three foliation boudinage structures. Samples BW302 and E are in cross-section (XZ-plane) and sample BW502 displays the long-axis (YZ-plane) of the foliation boudinage structure. **a)** Undeformed shale. **b)** Lenses of dolomite selectively replace shale layers in the otherwise unaltered shale. Sample BW302 also contains sporadic pyrite grains in the dolomite lens. **c)** Undeformed veins, veinlets, and cleavages typically at high angles to shale layers. **d)** Some veins become fluid filled and/or deformation initiates within existing veins. **e)** Deformation, predominantly layer-normal shortening but some non-coaxial flow, continues with foliation boudinage structures forming with a silica-dolomite infill. **f)** Deformation continues and influx of sulphide mineralisation, both infilling and replacing existing silica-dolomite grains. Some rotation of structures occurs with increased shortening and non-coaxial component. The diagrams show the final geometries of the foliation boudinage structures. **g)** Polished thin sections of the three foliation boudinage structures, in plane polarised light (PPL). All diagrams are shown to the same scale. Sample 'BW502', Drillhole № '201903052', 1.0 m. Sample 'E', Drillhole № '201903092', 32.1 m. Sample 'BW302', Drillhole № '201903092', 8.0 m.

BW502   E   BW302

Evolution

a Undeformed Shale | Undeformed Shale | Undeformed Shale

10 mm | 10 mm | 10 mm

b Undeformed Lenses | Undeformed Lenses | Undeformed Lenses

c Undeformed Veins | Undeformed Veinlets/ Cleavage | Undeformed Veinlets/ Cleavage

d Deforming veins (No FBS) | Undeformed Veinlets/ Cleavage + Fluid Filled Veins | Deforming Veinlets/Cleavage + Fluid Filled Veins (No FBS)

e Deforming (FBS) - Silica-Dolomite | Deforming (FBS) - Silica-Dolomite | Deforming (FBS) - Silica-Dolomite

f Deforming (FBS) - Silica-Dolomite + Sulphides | Deforming (FBS) - Silica-Dolomite + Sulphides | Deforming (FBS) - Silica-Dolomite + Sulphides

10 mm | 10 mm | 10 mm

g Polished Thin Section | Polished Thin Section | Polished Thin Section

181

8.4 Discussion

8.4.1 Models

The CT model shows that there are some finer scale complexities to the sulphide infill compared to the MOVE serial section model. Nevertheless, the CT scans validate the use of extrapolation between the serial sections in the MOVE model and in the geometrical analysis. Having justified the serial section approach, it is possible to take advantage of its ability to separate the silica-dolomite from the host rock, which cannot be done in the CT scans. A limitation of this study is the that the entire length of the foliation boudinage structure was not sampled.

8.4.2 Geometry

Previous work on foliation boudinage structures at Mount Isa has shown the sulphides both infilled space around and replaced silica-dolomite (Chapter 6 and Williams *et al.*, 2023). The total volume of the silica-dolomite (54%) in the modelled part of the structure is greater than the volume of sulphides (46%). As at least some of the silica-dolomite has been replaced by the paragenetically later sulphides, the original volume of the silica-dolomite was likely higher than measured here.

The silica-dolomite areas in the sections are on average 13% greater than the sulphide areas. This is much larger than the average measurement error of +1.41% and -1.70% for the area measurements. The great error in the volume calculations means that the silica-dolomite and sulphide volumes are within error of each other. However, there is no likelihood that the relative volumes are in the incorrect order, as that would have required systematic

underestimation of the sulphide area and overestimation of the silica-dolomite area in each section. Since the extra error is due to the section separation, it is unlikely to have introduced such a systematic bias.

The displacement-distance analysis of the foliation boudinage structure is similar to the approach taken for displacements on faults, where the maximum displacements are typically identified around the centre of the fault (e.g. Walsh and Watterson, 1988; Gillespie *et al.*, 1992; Dawers *et al.*, 1993; Childs *et al.*, 2003). The maximum displacement of the layers is also likely to be at the centre of the foliation boudinage structure, where the structure is oldest. This analysis assumes displacement is entirely within the section plane, but there may be a minor component of displacement out of this plane. However, samples in the long-axis (Y-direction) of the foliation boudinage structure, such as BW502 in **Figure 8.11**, show that displacement is negligible in this plane.

The maximum displacement generally increases through the structure, from the serial section at 0 mm (C) to the section at 30 mm distance (I) **[Figure 8.8a]**. This implies that section I is closest to the mid-point along the length of the whole foliation boudinage structure. The reduction in the displacement at 15 mm (F) can be related to the opening of another void within the structure at this point **[Appendix H.1]**. The second void has transferred some of the displacement onto a parallel structure, in a similar way that displacements are transferred in linked faults. Additional displacements of the same shale layers can be seen on the second void adjacent to the main structure, which have not been included in the point-to-point displacements.

The results of the sulphide and silica-dolomite area analyses show that the areas vary little through the structure **[Figure 8.8c]**. The cross-sectional areas do not increase where the layer

displacements are greatest and are inconsistent with an increasing volume at the centre of the foliation boudinage structure, as in *Stage 1* and the proposed closure in *Model I*. Therefore, *Model II* is favoured as the likely closure mechanism, as displacement increases but cross-sectional area remains more or less constant as predicted by this model. Further, the results of this study also allow the modelled portion of the foliation boudinage structure to be located within a specific part along the long-axis of the whole structure, as shown in **Figure 8.12**.

A change in the aspect ratio and orientation of the foliation boudinage structure with distance is evident in **Figure 8.8d** and **Appendix H.1**. The overall increase in the ellipse aspect ratio from the serial section at 0 mm (C) to the section at 30 mm (I) would suggest an increase in the finite strain from section C to I. The increase in the finite strain is likely due to section I having been open for a longer period of time, as the fracture propagates away from the mid-point. The clockwise rotation of the long-axes of the foliation boudin aspect ratios **[Appendix H.1]** towards the horizontal (XY-plane and shale layer) from 0 mm (C) to 30 mm (I), indicates the apparent dextral sense of sub-simple shear involved **[Figure 8.12]**.

A similar inference can be made from the sphericity. The sphericity of the foliation boudinage structure in each cross-section indicates the surface irregularity and the extent of replacement and infill. Therefore, a decrease in the sphericity from 0 mm (C) to 30 mm (I) **[Figure 8.8d]** suggests section I was open for a longer period of time. The lower value of sphericity for the sulphides compared to the outer edge of the foliation boudinage structure implies a more complex process of replacement and infill during the sulphide mineralisation.
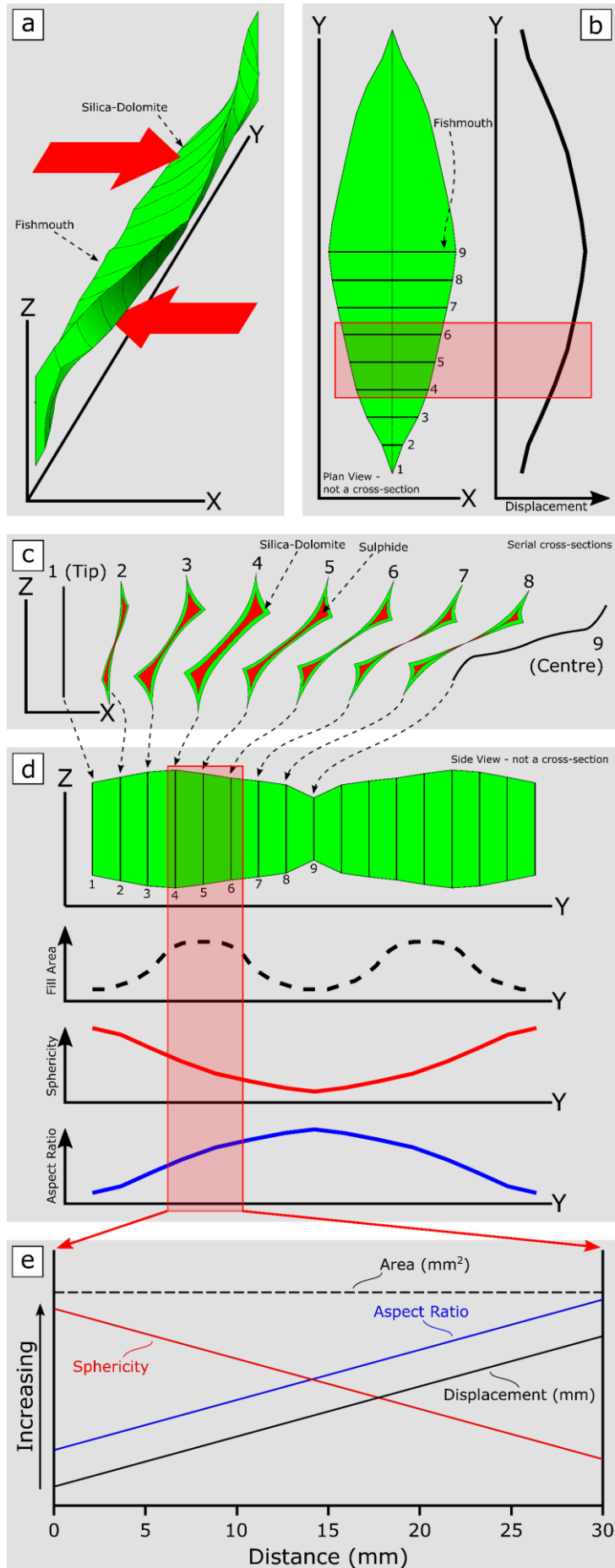
Figure 8.12: (Previous page) Schematic diagrams of the asymmetrical foliation boudinage structure from Mount Isa that was modelled in this study. The structure formed by layer-parallel extension and approximate layer-normal shortening, with a component of non-coaxial deformation **[e.g. Figure 8.1]**, as shown by shear arrow directions. The Y-direction is the long-axis of the structure. **a)** 3-dimensional geometry of the foliation boudinage structure. **b)** Plan view of the foliation boudinage structure in the XY-plane, with the change in relative displacement along the structure. **c)** Cross-sections at multiple positions along the long-axis of the foliation boudinage structure showing the observed relationship between the silica-dolomite rim and the sulphide infill. **d)** Side view of the foliation boudinage structure in the YZ-plane, showing the relative changes in area, sphericity, and aspect ratio along the long-axis. **e)** Graph of the modelled portion of the foliation boudinage structure in this study representing the general trends in the area, sphericity, aspect ratio and displacement from 0 mm (section C) to 30 mm (section I). The red highlighted areas reflect the position within the foliation boudinage structure which have been modelled in this study.

8.4.3 Evolution of Foliation Boudinage Structures

The diagrams in **Figure 8.11** show the interpreted sequence of events that led to the present geometry of the foliation boudinage structures at Mount Isa. Despite a few minor discrepancies in the timing of some vein features, the overall paragenesis of the structures remains consistent with previous work (Chapter 6 and Williams *et al.*, 2023). Unaltered shales first underwent layer replacement forming dolomite lenses. Veins in several orientations and possible cleavages formed next.

The foliation boudinage structures appear to have initiated from a discontinuity, which may have been a pre-existing vein. Veins at high angles to the shale layers can be exploited as a weak discontinuity to form the foliation boudinage structures. The diagrams show that some early low angle veins are crosscut by the foliation boudinage structure and did not develop into foliation boudinage structures . In some foliation boudinage structures, pre-existing veins increase the geometrical complexity of the structure. An example of this is sample F, detailed in section 8.4.2, where part of the displacement has been taken up by an adjacent structure as a result of the linkage of multiple pre-existing discontinuities.

Previous studies, such as Arslan *et al.* (2008, 2012), suggest that fluid pressures in foliation boudinage structures must (1) exceed lithostatic pressures by at least the tensile strength of the rock in order to form brittle fractures and (2) be lithostatic to allow the growth of minerals into a fluid-filled void. However, such high fluid pressures is not required during the initiation of foliation boudinage if the discontinuity is already present. At Mount Isa, once the early veins or fractures formed, the fluid pressure could have reduced. Therefore, the exploitation of these early discontinuities indicate that fluid pressures during the formation of foliation boudinage structures are not as high as in a scenario where there were no pre-existing veins or fractures.

Sample E contains a smaller conjugate foliation boudinage structure at the bottom left of the section **[Figure 8.11e,f,g]**, which has less infill compared to the main structure. This could be because the direction of maximum shortening is at a relatively high angle to this structure. The direction of shortening is likely to be at a lower angle to the main foliation boudin in the sample, favouring the opening and infill of this structure.

8.5 Conclusions

- The foliation boudinage structures are filled by silica-dolomite and sulphides (pyrrhotite and chalcopyrite). The areas of both the silica-dolomite and sulphides vary little through the foliation boudinage structure, although the areas of the silica-dolomite are typically greater than the sulphides in each section.

- The volume of sulphide infill is slightly lower than the volume of silica-dolomite. Some of the silica-dolomite has been replaced by later sulphides. The foliation boudinage structures act as structural traps during sulphide mineralisation.

- The aspect ratio of the foliation boudinage structure increases towards the centre of the foliation boudin (section I) as the finite strain is greatest in the oldest parts of the structure. The orientation of the longest axis of the aspect ratio rotates clockwise towards the horizontal shale layers, indicating the apparent dextral sense of sub-simple shear **[Figure 8.12]**.

- Lower sphericities of the foliation boudinage structure likely indicate a longer replacement history as the geometry of the infills become more sophisticated. The sphericity of both the foliation boudinage structure and the sulphide infill decrease from 0 mm (section C) to 30 mm (section I), indicating an increase in age and more elaborate replacement towards section I.

- Displacements increase from 0 mm (section C) to 30 mm (section I), also indicating the oldest parts of the structure are more proximal to section I.

- Foliation boudinage structures at Mount Isa are consistent with a model in which they have evolved by increasing displacement in cross-section, implying propagation along their long-axes. In this model, the oldest parts of the structures are near the central point along the long-axes, similar to fault propagation.

- The foliation boudinage structures probably developed similar to *Model II* **[Figure 8.2]**. In this model, the structures close to a fishmouth at their centre with little or no infill, low sphericities, maximum displacements, and high aspect ratios. Displacements decrease towards the end of the structure (tips), with the largest infill areas midway between the centre and the tips. Hence, the oldest parts of the structures are likely to have less potential for mineral infill.

- At Mount Isa, pre-foliation boudinage discontinuities, such as veins, acted as planes of weakness and were exploited during foliation boudinage. Therefore, significantly

high fluid pressures and/or differential stresses are not required during foliation boudinage.

- Multiple orientations of pre-existing discontinuities, as well as alteration, had significant impacts on the final geometries and orientations of the foliation boudinage structures. Linkage of discontinuities increased the geometrical complexity of the foliation boudinage structures where displacement is transferred onto adjacent structures.

CHAPTER 9

Conclusions

9.1 Context and Aims

The demand for copper is substantially increasing as the global economy becomes more reliant on the use of electricity from renewable energy sources (Harmsen *et al.*, 2013). The introduction of copper bearing fluids and precipitation of copper bearing minerals at Mount Isa have resulted in the formation of a 'world-class' deposit, as defined by Singer (1995). The Mount Isa Cu deposit is the second largest copper producer in Australia, yet controversy still remains over the origin, formation, and geometry of the orebodies. These controversies add to the difficulty involved in mine and near mine exploration for new orebodies that, if located, would help contribute to the increasing demand for Cu.

Foliation boudinage structures have recently been identified at Mount Isa and may have some structural control on the copper orebodies. Foliation boudinage structures are known to have some structural control on the formation of other deposits in similar rock types, such as at the Rosebery Mine, Tasmania (Aerden, 1991). The aims of this study were to show the distribution and geometry of foliation boudinage structures in relation to the Cu orebodies at Mount Isa. This study is the first systematic investigation into foliation boudinage structures at the Mount Isa Cu deposit, with potential consequences for mineral exploration in similar deposit styles, deformation histories, and rock types in the Mount Isa Inlier and worldwide.

Despite many previous studies on foliation boudinage structures, there is still a lack of knowledge of the 3-dimensional geometry, evolution, and ore hosting potential of real foliation boudinage structures. Therefore, this study aimed to demonstrate the evolution of foliation boudinage structures and is the first study to model real structures in 3-dimensions. Further, confusions in the use of nomenclature surrounding the term 'foliation boudinage'

have been identified in this study and a synthesis of the nomenclature was created in order to allow the aims and objectives to be achieved.

9.2 Conclusions of Research Objectives

(1) Develop a method to calculate 3-dimensional coordinates and orientations of foliation boudinage structures by combining measurements on oriented and unoriented core with drillhole surveys. (1.1) 'Desurveying' methods will be investigated to find the optimum procedure for determining the location and orientation of drill core samples. (1.2) A method to orient the foliation boudinage structures in unoriented core relative to an assumed orientation of bedding in the core will be developed.

- A method has been developed to plot drillholes using simple computer code, without sophisticated or commercial software. The code also allows the azimuth, plunge and 3-dimensional coordinates to be calculated for any point along the drillhole. These results have been used to reorient foliation boudinage structures and the code has been used to locate the structures relative to mineralisation within the Mount Isa system. **[Chapter 5]**

- There is a high precision for all desurveying methods, except the *Basic Tangent*, which is consistently the least precise method. With the short (168 m) drillhole in this study, the distance between the end of hole points for the Basic Tangent and the other methods is approximately 1.37 metres. The long (1200 m) drillhole has a distance of almost 5 metres (4.92 m) between predicted end of hole points in the *Basic Tangent* and the other methods. With end of hole points consistently plotting in close

proximity, the *Minimum Curvature* and *Radius of Curvature* are recommended for use as they most realistically plot drillhole pathways. **[Chapter 5]**

- Disparities between the plotted end of hole positions for each desurveying method increase with increasing drillhole length and increasing angle between the drill bit and the dominant rock anisotropy. At high initial angles between the drill bit and rock anisotropy, the maximum distance between the end of hole points increases with increasing drillhole length, when calculated as a percentage of the total drillhole length. However, at small initial angles, the maximum distance between end of hole points decreases with increasing drillhole length, when calculated as a percentage of the drillhole length. **[Chapter 5]**

- Analysis of the existing desurveying methods shows that they place unrealistic constraints on the geometry of the predicted drillhole path. There is a potential for a new desurveying method that overcomes these problems. **[Chapter 5; Future Work]**

- A method for reorienting unoriented drill core has been developed in this study using knowledge of the dominant westward dip direction of the Urquhart Shale. An additional method has been developed in order to reorient polished thin section samples from unoriented drill core by combining the recorded measurements of the drillhole orientations with the assumed westward dip direction of the Urquhart Shale. These methods may be useful in reorienting unoriented drill core from other locations and deposits. **[Chapter 7; Appendix G]**

(2) Describe the orientation and distribution of foliation boudinage structures and their importance in mineralisation at Mount Isa.

- Petrographic analysis has shown that drill core scale foliation boudinage structures have an outer, initial rim of quartz and dolomite, with infill and replacement by later sulphides in the central parts, predominantly pyrrhotite with some chalcopyrite. The chalcopyrite and pyrrhotite are generally cogenetic and both can be associated with the main Cu mineralisation event. **[Chapter 6; Chapter 7]**

- Drill core scale foliation boudinage structures at Mount Isa are found almost exclusively in the unaltered and least deformed lithologies, proximal to, but outside the zone of high-grade Cu mineralisation, though within the zones of silica-dolomite and pyrrhotite mineralisation. Therefore, the drill core scale foliation boudinage structures may have played a role in controlling the mineralisation in the outer parts of the orebodies. **[Chapter 6]**

- The foliation boudinage structures likely formed by a combination of coaxial and non-coaxial deformation (general shear), as evidenced by their asymmetrical geometries and deformation within the pyrrhotite infill. All of the foliation boudinage structures in this study have some filling, therefore do not form a closed structure like those that develop by the coaxial shortening of an initially oblique fracture. The elongation of the foliation boudinage structures and rotation of the aspect ratios towards the horizontal both increase with strain, meaning there has to be a non-coaxial component to the deformation. **[Chapter 6; Chapter 7; Chapter 8]**

- The foliation boudinage structures plunge gently to the north and south as a result of approximately layer-normal and reverse shortening of the anisotropic, steeply west-dipping Urquhart Shale. The north plunging foliation boudinage structures formed

during ENE-WSW dextral-reverse shortening during D4a and the south plunging structures formed during WNW-ESE sinistral-reverse shortening during the D4b deformation event. **[Chapter 6; Chapter 7]**

(3) Describe the geometry of the mineral infill in foliation boudinage structures to determine their relative timing of formation and subsequent deformation history of ore-related sulphides at Mount Isa.

- This study is the first to demonstrate significant deformation in the mineral infilling of foliation boudinage structures. Previous studies have shown little to no deformation within the mineral infill, which has been used to infer that the mineral filling is late or post-deformation associated with the formation of the foliation boudinage structures. Pyrrhotite grains in the central part of the foliation boudin underwent dynamic recrystallisation by subgrain rotation. Both the relict and recrystallised grains show a grain shape preferred orientation, that is sub-parallel to the shale layering, as a result of deformation. **[Chapter 7]**

- The pyrrhotite grains within the foliation boudinage structures have *c*-axes that are normal to the shale layering and parallel to the approximate shortening direction at Mount Isa. **[Chapter 7]**

- The strain ellipsoid for the deformed infill indicates shortening was approximately east-west, similar to the shortening directions of the foliation boudinage structures. A change from plane strain during the formation of foliation boudinage structures to a flattening strain, shown by the strain ellipsoid, may reflect a continuous, progressive deformation during the formation of the foliation boudinage structures. **[Chapter 7]**

- The foliation boudinage structures at Mount Isa are unlikely to have remained as fluid filled voids throughout their formation as shown by the finite strain accumulated in the sulphide infills. **[Chapter 7]**

*(4) **Ascertain the 3-dimensional geometries and the evolution of foliation boudinage structures using examples from Mount Isa.***

- Natural examples of foliation boudinage structures have been modelled in 3-dimensions for the first time. Foliation boudinage structures likely develop by propagation along their long-axes (Y-direction) from the central, oldest parts of the structures, towards the fracture tips. In this model, the structures eventually close to fishmouth foliation boudins at their centres, where there is little or no infill, maximum displacements, low shape sphericities, and high shape aspect ratios. The oldest parts of the foliation boudinage structures have greater displacements and the displacements can be transferred between adjacent discontinuities within the same foliation boudinage structure, analogous to the propagation and linkage of faults. The largest volumes of infill are midway between the centre and fracture tip. The central, oldest parts of the foliation boudinage structure are likely to have a decreasing potential for significant mineral infill as they closed. **[Chapter 8]**

- Samples from Mount Isa that contain foliation boudinage structures formed through several stages: 1) dolomite replacement of shale layers forming lenses. 2) Veins and possibly cleavages formed approximately normal to the shale layers. 3) The veins underwent some deformation which had a large component of layer-normal shortening. 4) Foliation boudinage structures began developing from pre-existing

discontinuities, as a result of shortening at an oblique angle to the shale layers. Discontinuities that were at a low angle to the shale layers are truncated and offset by the developing structure. The dominant infills at this early stage were quartz and dolomite (silica-dolomite). 5) Continued oblique shortening of the shale further developed the foliation boudinage structures into asymmetrical geometries. The infill at this stage was dominated by pyrrhotite and chalcopyrite. **[Chapter 6; Chapter 7; Chapter 8]**

- The fluid pressures required for the formation of foliation boudinage structures at Mount Isa are likely to have been lower than in other examples of the structures. This is owing to the presence of pre-existing discontinuities that were exploited as planes of weakness during the formation of foliation boudinage structures. These pre-existing discontinuities add further complexity to the geometry of the foliation boudinage structures at Mount Isa. **[Chapter 8]**

9.3 Implications for Exploration and Future Work

The conclusions presented in this thesis raise several questions regarding the ore host potential of foliation boudinage structures, both at Mount Isa and further afield. Some directions of research that future work could explore are also detailed below:

- Future work should aim to develop a new method of desurveying for plotting drillhole paths, that does not have significant assumptions. Such a method is currently being developed as an outcome of this project that overcomes the limitations of the existing methods. This is being undertaken with Professor Owen Jones from the School of Mathematics at Cardiff University. This method should then be tested against the previous

desurveying methods using either: (1) a drillhole path with known collar and end of hole points, or (2) a random drillhole trajectory, plotted using computer code, where measurements can be taken systemically down the curve at hypothetical survey points.

- Foliation boudinage structures are fractal and have been observed on scales of 10s to 100s of metres. Future work should investigate the possibility of larger scale foliation boudinage structures at Mount Isa to answer some important questions. What scale do foliation boudinage structures extend to at Mount Isa? Are larger scale foliation boudinage structures in closer proximity to the bulk of ore-grade Cu mineralisation than the more peripheral small scale structures? Do large scale foliation boudinage structures host significant Cu mineralisation within their mineral infills? If so, are the largest scale foliation boudinage structures actually controlling the locations, orientations, and geometries of the Cu orebodies (i.e., are the orebodies at Mount Isa actually large scale foliation boudinage structures?). To answer these questions, detailed underground mapping, reanalysis of level plans, and updated 3-dimensional modelling of the Mount Isa deposit need to be undertaken.

- This study has focused primarily on foliation boudinage structures in the Cu deposit. However, if the Cu-Pb-Zn-Ag is in fact a linked mineralisation sequence, as described by some authors (e.g. Cave *et al.*, 2020), then some questions arise about the other orebodies in the Mount Isa system. Are foliation boudinage structures observed in the Pb-Zn-Ag orebodies? If so, do they have a similar deformation history and paragenesis to those observed in the Cu system? Do they host significant Pb-Zn-Ag ore? To answer these questions, a detailed reanalysis and relogging of drill core from the now closed Pb-Zn-Ag orebodies needs to be undertaken.

- The foliation boudinage structures at Mount Isa occur within the Urquhart Shale unit of the Mount Isa Group, an anisotropic and homogeneous lithology, that is common to several other ore deposits. Future work could investigate other ore deposits in the Mount Isa region with similar rock types and deformation histories. The results presented in this thesis could lead to the reinterpretation of other ore deposit models.

- Some recent studies (e.g. Miller, 2007) have shown that Cu mineralisation began during D4a and continued through to the main Cu mineralisation during D4b. The results presented in this thesis show that foliation boudinage structures also developed during both the D4a and D4b deformation events. Therefore, is there a more fundamental link between the origins of both the foliation boudinage structures and mineralising fluids at Mount Isa? Did the introduction of Cu bearing fluids lead to the formation of foliation boudinage structures? Or did the formation of foliation boudinage structures create space that permitted the influx of fluids?

References

Aerden, D. G. A. (1991) 'Foliation-boudinage control on the formation of the Rosebery Pb-Zn orebody, Tasmania', *Journal of Structural Geology*, 13(7), pp. 759–775. doi: 10.1016/0191-8141(91)90002-Z.

Allen, L. (2020) *The metal leading the way to a green, circular economy – ILA*, *International Lead Association*. Available at: https://ila-lead.org/the-metal-leading-the-way-to-a-green-circular-economy/ (Accessed: 27 February 2023).

Allibone, A. H. and Norris, R. J. (1992) 'Segregation of leucogranite microplutons during syn-anatectic deformation: an example from the Taylor Valley, Antarctica', *Journal of Metamorphic Geology*, 10(4), pp. 589–600. doi: 10.1111/j.1525-1314.1992.tb00107.x.

Amorin, R. and Broni-Bediako, E. (2010) 'Application of Minimum Curvature method to wellpath calculations', *Research Journal of Applied Sciences, Engineering and Technology*, 2(7), pp. 679–686.

Andrew, A. S., Heinrich, C. A., Wilkins, R. W. T. and Patterson, D. J. (1989) 'Sulfur isotope systematics of copper ore formation at Mount Isa, Australia', *Economic Geology*, 84(6), pp. 1614–1626. doi: 10.2113/gsecongeo.84.6.1614.

Andrew, B. S. (2020) *Recognising cryptic alteration surrounding the Mount Isa Copper Deposits: Implications for controls on fluid flow, and mineral exploration*. University of Waikato.

Arslan, A., Koehn, D., Passchier, C. W. and Sachau, T. (2012) 'The transition from single layer to foliation boudinage: A dynamic modelling approach', *Journal of Structural Geology*, 42, pp. 118–126. doi: 10.1016/j.jsg.2012.06.005.

Arslan, A., Passchier, C. W. and Koehn, D. (2008) 'Foliation boudinage', *Journal of Structural Geology*, 30(3), pp. 291–309. doi: 10.1016/J.JSG.2007.11.004.

Austin, J. R. and Blenkinsop, T. G. (2010) 'Cloncurry Fault Zone: strain partitioning and reactivation in a crustal-scale deformation zone, Mt Isa Inlier', *Australian Journal of Earth Sciences*, 57(1), pp. 1–21. doi: 10.1080/08120090903416187.

Bachmann, F., Hielscher, R. and Schaeben, H. (2010) 'Texture analysis with MTEX- Free and open source software toolbox', *Solid State Phenomena*, 160, pp. 63–68. doi: 10.4028/www.scientific.net/SSP.160.63.

Bachmann, F., Hielscher, R. and Schaeben, H. (2011) 'Grain detection from 2d and 3d EBSD data-Specification of the MTEX algorithm'. doi: 10.1016/j.ultramic.2011.08.002.

Bayer, H. and Siemes, H. (1971) 'Zur Interpretation von Pyrrhotin-Gefugen', *Mineralium Deposita*, 6, pp. 225–244.

Bell, T. H. (1983) 'Thrusting and duplex formation at Mount Isa, Queensland, Australia', *Nature*, 304(5926), pp. 493–497. doi: 10.1038/304493a0.

Bell, T. H. (1991) 'The role of thrusting in the structural development of the Mount Isa Mine and its relevance to exploration in the surrounding region', *Economic Geology*, 86(8), pp. 1602–1625. doi: 10.2113/gsecongeo.86.8.1602.

Bell, T. H. and Hickey, K. A. (1998) 'Multiple Deformations with Successive Subvertical and Subhorizontal Axial Planes in the Mount Isa Region; Their Impact on Geometric Development and Significance for Mineralization and Exploration', *Economic Geology*, 93(8), pp. 1369–1389. doi: 10.2113/gsecongeo.93.8.1369.

Bell, T. H., Perkins, W. G. and Swager, C. P. (1988) 'Structural Controls on Development and

Localization of Syntectonic Copper Mineralization at Mount Isa, Queensland', *Economic Geology*, 83(1), pp. 69–85. doi: 10.2113/gsecongeo.83.1.69.

Betts, P. G., Giles, D., Mark, G., Lister, G. S., Goleby, B. R. and Aillères, L. (2006) 'Synthesis of the proterozoic evolution of the Mt Isa Inlier', *Australian Journal of Earth Sciences*, 53(1), pp. 187–211. doi: 10.1080/08120090500434625.

Betts, P. G., Lister, G. S. and O'Dea, M. G. (1998) 'Asymmetric extension of the Middle Proterozoic lithosphere, Mount Isa terrane, Queensland, Australia', *Tectonophysics*, 296(3–4), pp. 293–316. doi: 10.1016/S0040-1951(98)00144-9.

Betts, P. G., Lister, G. S. and Pound, K. S. (1999) 'Architecture of a Palaeoproterozoic Rift System: Evidence from the Fiery Creek Dome region, Mt Isa terrane', *Australian Journal of Earth Sciences*, 46(4), pp. 533–554. doi: 10.1046/j.1440-0952.1999.00721.x.

Blackmon, D. (2022) *New Study Finds That The Future of Copper Is Coming At Us Fast*, *Forbes*. Available at: https://www.forbes.com/sites/davidblackmon/2022/08/16/new-study-finds-that-the-future-of-copper-is-coming-at-us-fast/.

Blake, D. H. (1987) *Geology of the Mount Isa Inlier and environs, Queensland and Northern Territory*.

Blake, D. H. and Stewart, A. J. (1992) 'Stratigraphy and tectonic framework, Mount Isa Inlier', *Australian Geological Survey Organisation Bulletin*, 243, pp. 1–11.

Blenkinsop, T. G. and Doyle, M. G. (2010) 'A method for measuring the orientations of planar structures in cut core', *Journal of Structural Geology*, 32(6), pp. 741–745. doi: 10.1016/j.jsg.2010.04.011.

Blenkinsop, T. G., Doyle, M. and Nugus, M. (2015) 'A unified approach to measuring structures

in orientated drill core', *Geological Society Special Publication*, 421(1), pp. 99–108. doi: 10.1144/SP421.1.

Bourgoyne, A. T., Millheim, K. K., Chenevert, M. E. and Young, F. S. (1986) *Applied Drilling Engineering*, *Applied Drilling Engineering*. Society of Petroleum Engineers. doi: 10.2118/9781555630010.

Brown, A., Spandler, C. and Blenkinsop, T. G. (2023) 'New age constraints for the Tommy Creek Domain of the Mount Isa Inlier, Australia', *Australian Journal of Earth Sciences*. doi: 10.1080/08120099.2023.2171124.

Brown, E. T., Green, S. J. and Sinha, K. P. (1981) *The influence of rock anisotropy on hole deviation in rotary drilling- A review*, *International Journal of Rock Mechanics and Mining Sciences and*. doi: 10.1016/0148-9062(81)90003-6.

Bustos, N., Villaescusa, E. and Onederra, I. (2020) 'Analysis of drillhole deviation during drawbell construction in block caving', pp. 883–896. doi: 10.36487/acg_repo/2063_63.

Cave, B., Lilly, R. and Barovich, K. (2020) 'Textural and geochemical analysis of chalcopyrite, galena and sphalerite across the Mount Isa Cu to Pb-Zn transition: Implications for a zoned Cu-Pb-Zn system', *Ore Geology Reviews*, p. 103647. doi: 10.1016/j.oregeorev.2020.103647.

Cave, B., Perkins, W. and Lilly, R. (2022) 'Linking uplift and mineralisation at the Mount Novit Zn-Pb-Ag Deposit, Northern Australia: Evidence from geology, U–Pb geochronology and sphalerite geochemistry', *Geoscience Frontiers*, 13(2), p. 101347. doi: 10.1016/j.gsf.2021.101347.

Childs, C., Nicol, A., Walsh, J. J. and Watterson, J. (2003) 'The growth and propagation of synsedimentary faults', *Journal of Structural Geology*, 25(4), pp. 633–648. doi:

10.1016/S0191-8141(02)00054-8.

Ciacci, L., Fishman, T., Elshkaki, A., Graedel, T. E., Vassura, I. and Passarini, F. (2020) 'Exploring future copper demand, recycling and associated greenhouse gas emissions in the EU-28', *Global Environmental Change*, 63(102093). doi: 10.1016/j.gloenvcha.2020.102093.

Clark, B. R. and Kelly, W. C. (1973) 'Sulfide Deformation Studies: I. Experimental Deformation of Pyrrhotite to 2,000 bars and 500°C', *Economic Geology*, 68, pp. 332–352. doi: 10.2113/gsecongeo.70.3.431.

Clark, G. J. (1968) *A mineralogical examination of the 1100 copper orebody. Unpublished internal company report of Mount Isa Mines Limited*.

Cobbold, P. R., Cosgrove, J. W. and Summers, J. M. (1971) 'Development of internal structures in deformed anisotropic rocks', *Tectonophysics*, 12(1), pp. 23–53. doi: 10.1016/0040-1951(71)90065-5.

Coe, K. (1959) 'Boudinage Structure in West Cork, Ireland', *Geological Magazine*, 96(3), pp. 191–201. doi: 10.1017/S0016756800060179.

Connor, A. G., Johnson, I. R. and Muir, M. D. (1990) 'Dugald River zinc-lead deposit', in Hughes, F. E. (ed.) *Geology of the mineral deposits of Australia and Papua New Guinea*. Australasian Institute of Mining and Metallurgy, Monograph 14, pp. 949–953.

Connors, K. A. and Page, R. W. (1995) 'Relationships between magmatism, metamorphism and deformation in the western Mount Isa Inlier, Australia', *Precambrian Research*, 71, pp. 131–153. doi: 10.1016/0301-9268(94)00059-Z.

Cox, R. and Curtis, R. (1977) 'The discovery of the Lady Loretta zinc-lead-silver deposit, northwest Queensland, Australia - A geochemical exploration case history', *Journal of*

Geochemical Exploration, 8(1–2), pp. 189–202. doi: 10.1016/0375-6742(77)90051-6.

Cox, S. F. (1987) 'Flow mechanisms in sulphide minerals', *Ore Geology Reviews*, 2(1–3), pp. 133–171. doi: 10.1016/0169-1368(87)90026-6.

Cross, A. J., Prior, D. J., Stipp, M. and Kidder, S. (2017) 'The recrystallized grain size piezometer for quartz: An EBSD-based calibration', *Geophysical Research Letters*, 44(13), pp. 6667–6674. doi: 10.1002/2017GL073836.

Davis, T. P. (2004) 'Mine-Scale Structural Controls on the Mount Isa Zn-Pb-Ag and Cu Orebodies', *Economic Geology*, 99(3), pp. 543–559. doi: 10.2113/gsecongeo.99.3.543.

Dawers, N. H., Anders, M. H. and Scholz, C. H. (1993) 'Growth of normal faults: displacement-length scaling', *Geology*, 21(12), pp. 1107–1110. doi: 10.1130/0091-7613(1993)021<1107:GONFDL>2.3.CO;2.

Day, R. W., Whitaker, W. G., Murray, C. G., Wilson, I. H. and Grimes, K. G. (1983) *Queensland geology. A companion volume to the 1:2 500 000 scale geological map (1975)*, *Geological Survey of Queensland, Publication 383*.

Department for Foreign Affairs and Trade (2020) *United Kingdom country brief*. Available at: https://www.dfat.gov.au/geo/united-kingdom/Pages/united-kingdom-country-brief.

Derrick, G. M. (1982) 'A Proterozoic rift zone at Mount Isa, Queensland, and implications for mineralisation', *BMR Journal of Australian Geology & GeophysicsJournal of Australian Geology & Geophysics*, 7, pp. 81–92.

Domagala, J., Southgate, P. N., Mc Conachie, B. A. and Pidgeon, B. A. (2000) 'Evolution of the Palaeoproterozoic Prize, Gun and lower Loretta Supersequences of the Surprise Creek Formation and Mt Isa Group', *Australian Journal of Earth Sciences*, 47(3), pp. 485–507. doi:

10.1046/j.1440-0952.2000.00796.x.

Druguet, E. (2019) 'Deciphering the presence of axial-planar veins in tectonites', *Geoscience Frontiers*, 10(6), pp. 2101–2115. doi: 10.1016/j.gsf.2019.02.005.

Druguet, E. and Carreras, J. (2006) 'Analogue modelling of syntectonic leucosomes in migmatitic schists'. doi: 10.1016/j.jsg.2006.06.015.

Duncan, R. J., Wilde, A. R., Bassano, K. and Maas, R. (2006) 'Geochronological constraints on tourmaline formation in the Western Fold Belt of the Mount Isa Inlier, Australia: Evidence for large-scale metamorphism at 1.57 Ga?', *Precambrian Research*, 146(3–4), pp. 120–137. doi: 10.1016/j.precamres.2006.01.010.

Dunnet, D. (1969) 'A technique of finite strain analysis using elliptical particles', *Tectonophysics*, 7(2), pp. 117–136. doi: 10.1016/0040-1951(69)90002-X.

Eren, T. and Suicmez, V. S. (2020) 'Directional drilling positioning calculations', *Journal of Natural Gas Science and Engineering*, 73, p. 103081. doi: 10.1016/j.jngse.2019.103081.

Finlow-Bates, T. and Stumpfl, E. F. (1979) 'The copper and lead zinc silver orebodies of Mt. Isa Mine, Queensland; products of one hydrothermal system', *Annales de la Societe Geologique de Belgique*, 102, pp. 497–517.

Flinn, D. (1965) 'On the Symmetry Principle and the Deformation Ellipsoid', *Geological Magazine*, 102(1), pp. 36–45. doi: 10.1017/S0016756800053851.

Ford, A. and Blenkinsop, T. G. (2008a) 'Combining fractal analysis of mineral deposit clustering with weights of evidence to evaluate patterns of mineralization: Application to copper deposits of the Mount Isa Inlier, NW Queensland, Australia', *Ore Geology Reviews*, 33, pp. 435–450. doi: 10.1016/j.oregeorev.2007.01.004.

Ford, A. and Blenkinsop, T. G. (2008b) 'Evaluating geological complexity and complexity gradients as controls on copper mineralisation, Mt Isa Inlier', *Australian Journal of Earth Sciences*, 55(1), pp. 13–23. doi: 10.1080/08120090701581364.

Forrestal, P. J. (1990) 'Mount Isa and Hilton silver-lead-zinc deposits', in Hughes, F. E. (ed.) *Geology of the mineral deposits of Australia and Papua New Guinea*. Australasian Institute of Mining and Metallurgy, Monograph 14, pp. 927–934.

Foster, D. R. W. and Rubenach, M. J. (2006) 'Isograd pattern and regional low-pressure, high-temperature metamorphism of pelitic, mafic and calc-silicate rocks along an east-west section through the Mt Isa Inlier Isograd pattern and regional low-pressure, high-te', *Australian Journal of Earth Sciences*, 53(1), pp. 167–186. doi: 10.1080/08120090500434617.

Garside, M. (2021) *Refined copper usage worldwide from 2010 to 2020*, *statista*. Available at: https://www.statista.com/statistics/267849/global-copper-consumption/.

Geological Survey of Queensland (2011) *North-West Queensland Mineral and Energy Province Report*. Queensland Department of Employment, Economic Development and Innovation, Brisbane.

Ghosh, S. and Sengupta, S. (1999) 'Boudinage and composite boudinage in superposed deformations and syntectonic migmatization', *Journal of Structural Geology*, 21(1), pp. 97–110. doi: 10.1016/S0191-8141(98)00096-0.

Giles, D., Ailléres, L., Jeffries, D., Betts, P. and Lister, G. (2006) 'Crustal architecture of basin inversion during the Proterozoic Isan Orogeny, Eastern Mount Isa Inlier, Australia', *Precambrian Research*, 148, pp. 67–84. doi: 10.1016/j.precamres.2006.03.002.

Gillespie, P. A., Walsh, J. J. and Watterson, J. (1992) 'Limitations of dimension and

displacement data from single faults and the consequences for data analysis and interpretation', *Journal of Structural Geology*, 14(10), pp. 1157–1172. doi: 10.1016/0191-8141(92)90067-7.

Glencore (2022) *Mount Isa Mines*. Available at: https://www.glencore.com.au/operations-and-projects/qld-metals/operations/mount-isa-mines.

Goscombe, B. D., Passchier, C. W. and Hand, M. (2004) 'Boudinage classification: end-member boudin types and modified boudin structures', *Journal of Structural Geology*, 26, pp. 739–763. doi: 10.1016/j.jsg.2003.08.015.

Graf, J. L. and Skinner, B. J. (1970) *Strength and Deformation of Pyrite and Pyrrhotite*, *Economic Geology*. doi: 10.2113/gsecongeo.65.2.206.

Grasemann, B. and Stüwe, K. (2001) 'The development of flanking folds during simple shear and their use as kinematic indicators', *Journal of Structural Geology*, 23(4), pp. 715–724. doi: 10.1016/S0191-8141(00)00108-5.

Gregory, M. J. (2006) 'Copper mobility in the Eastern Creek Volcanics, Mount Isa, Australia: Evidence from laser ablation ICP-MS of iron-titanium oxides', *Mineralium Deposita*, 41(7), pp. 691–711. doi: 10.1007/s00126-006-0086-2.

Gregory, M. J., Schaefer, B. F., Keays, R. R. and Wilde, A. R. (2008) 'Rhenium–osmium systematics of the Mount Isa copper orebody and the Eastern Creek Volcanics, Queensland, Australia: implications for ore genesis', *Mineralium Deposita*, 43(5), pp. 553–573. doi: 10.1007/s00126-008-0182-6.

Grondijs, H. F. and Schouten, C. (1937) 'A study of the Mount Isa ores [Queensland, Australia]', *Economic Geology*, 32(4), pp. 407–450. doi: 10.2113/gsecongeo.32.4.407.

Gulson, B. L., Perkins, W. G. and Mizon, K. J. (1983) 'Lead isotope studies bearing on the genesis of copper orebodies at Mount Isa, Queensland', *Economic Geology*, 78(7), pp. 1466–1504. doi: 10.2113/gsecongeo.78.7.1466.

Hambrey, M. J. and Milnes, A. G. (1975) 'Boudinage in Glacier Ice — Some Examples', *Journal of Glaciology*, 14(72), pp. 383–393. doi: 10.1017/s0022143000021912.

Hancock, M. C. and Purvis, A. H. (1990) 'Lady Loretta silver-lead-zinc deposit', in Hughes, F. E. (ed.) *Geology of the mineral deposits of Australia and Papua New Guinea*. Australasian Institute of Mining and Metallurgy, Monograph 14, pp. 943–948.

Handin, J. (1966) 'Strength and ductility', in Clark, Jr, S. P. (ed.) *Handbook of Physical Constants, Geol. Soc. Am., Memoir.* 97th edn, pp. 223–289.

Hanmer, S. (1986) 'Asymmetrical pull-aparts and foliation fish as kinematic indicators', *Journal of Structural Geology*, 8(2), pp. 111–122. doi: 10.1016/0191-8141(86)90102-1.

Hannan, K. W., Golding, S. D., Herbert, H. K. and Krouse, H. R. (1993) 'Contrasting alteration assemblages in metabasites from Mount Isa, Queensland: implications for copper ore genesis', *Economic Geology*, 88(5), pp. 1135–1175. doi: 10.2113/gsecongeo.88.5.1135.

Harmsen, J. H. M., Roes, A. L. and Patel, M. K. (2013) 'The impact of copper scarcity on the efficiency of 2050 global renewable energy scenarios', *Energy*, 50(1), pp. 62–73. doi: 10.1016/j.energy.2012.12.006.

Heinrich, C. A., Bain, J. H. C., Fardy, J. J. and Waring, C. L. (1993) 'Br/Cl geochemistry of hydrothermal brines associated with Proterozoic metasediment-hosted copper mineralization at Mount Isa, northern Australia', *Geochimica et Cosmochimica Acta*, 57(13), pp. 2991–3000. doi: 10.1016/0016-7037(93)90288-8.

Heinrich, C. A., Bain, J. H. C., Mernagh, T. P., Wyborn, L. A. I., Andrew, A. S. and Waring, C. L. (1995) 'Fluid and mass transfer during metabasalt alteration and copper mineralization at Mount Isa, Australia', *Economic Geology*, 90(4), pp. 705–730. doi: 10.2113/gsecongeo.90.4.705.

Hirth, G. and Tullis, J. (1992) 'Dislocation creep regimes in quartz aggregates', *Journal of Structural Geology*, 14(2), pp. 145–159. doi: 10.1016/0191-8141(92)90053-Y.

Hobbs, B. E. (1968) 'Recrystallization of single crystals of quartz', *Tectonophysics*, 6(5), pp. 353–401. doi: 10.1016/0040-1951(68)90056-5.

Howson, M. and Sides, E. J. (1986) 'Borehole desurvey calculation', *Computers & Geosciences*, 12(1), pp. 97–104. doi: 10.1016/0098-3004(86)90022-1.

Islam, M. M., Sohag, K., Hammoudeh, S., Mariev, O. and Samargandi, N. (2022) 'Minerals import demands and clean energy transitions: A disaggregated analysis', *Energy Economics*, 113(106205), p. 106205. doi: 10.1016/j.eneco.2022.106205.

Jackson, M. J., Scott, D. L. and Rawlings, D. J. (2000) 'Stratigraphic framework for the Leichhardt and Calvert superbasins: Review and correlations of the pre-1700 Ma successions between Mt Isa and McArthur River', *Australian Journal of Earth Sciences*, 47(3), pp. 381–403. doi: 10.1046/j.1440-0952.2000.00789.x.

Jain, A. K., Sushmita, Singh, S. and Mukherjee, P. K. (2018) 'Migmatization, granite generation and melt accumulation in the Himalayan Orogenic Channel, Central and Eastern Bhutan', *Research Articles*. doi: 10.18520/cs/v114/i09/1903-1912.

Jaques, A. L., Jaireth, S. and Walshe, J. L. (2002) 'Mineral systems of Australia: An overview of resources, settings and processes', *Australian Journal of Earth Sciences*, 49(4), pp. 623–660.

doi: 10.1046/j.1440-0952.2002.00946.x.

Kelly, A. (1967) *A petrological study of the silica-dolomites and associated copper mineralization at Mount Isa with an interpretation of their origins*.

Kelly, W. C. and Clark, B. R. (1975) 'Sulfide deformation studies; III, Experimental deformation of chalcopyrite to 2,000 bars and 500 degrees C', *Economic Geology*, 70(3), pp. 431–453. doi: 10.2113/gsecongeo.70.3.431.

Kelso, I., Briggs, T. and Basford, P. (2001) 'The Century Zinc Deposit – Geological Update', *Australian Institute of Geoscientists*, (January 2001), pp. 1–3.

Khaled, S. M. (2016) 'A New Model for Calculating Well Trajectory', *International Advanced Research Journal in Science, Engineering and Technology*, 3(11), pp. 108–111. doi: 10.17148/IARJSET.2016.31121.

Kidan, T. W. and Cosgrove, J. W. (1996) 'The deformation of multilayers by layer-normal compression; an experimental investigation', *Journal of Structural Geology*, 18(4), pp. 461–474. doi: 10.1016/0191-8141(95)00099-Y.

Killeen, P. and Elliott, B. (1997) 'Surveying the path of boreholes: a review of developments and methods since 1987', in *Proceedings of Exploration 97: Fourth Decennial International Conference on Mineral Exploration*, pp. 709–712.

Kleijn, R., van der Voet, E., Kramer, G. J., van Oers, L. and van der Giesen, C. (2011) 'Metal requirements of low-carbon power generation', *Energy*, 36(9), pp. 5640–5648. doi: 10.1016/j.energy.2011.07.003.

Knights, J. G. (1976) *The 1100 orebody from zero to 1000 m. Unpublished internal company report of Mount Isa Mines Ltd*.

Kübler, L. (1985) 'Deformation mechanisms in experimentally deformed single crystals of pyrrhotite, Fe1-xS', *Physics and Chemistry of Minerals*, 12(6), pp. 353–362. doi: 10.1007/BF00654346.

Lacassin, R. (1988) 'Large-scale foliation boudinage in gneisses', *Journal of Structural Geology*, 10(6), pp. 643–647. doi: 10.1016/0191-8141(88)90030-2.

Large, R. R., Bull, S. W., McGoldrick, P. J., Walters, S., Derrick, G. M. and Carr, G. R. (2005) 'Stratiform and Strata-Bound Zn-Pb-Ag Deposits in Proterozoic Sedimentary Basins, Northern Australia', in *One Hundredth Anniversary Volume*. Society of Economic Geologists, pp. 931–963. doi: 10.5382/AV100.28.

Large, R. R., Bull, S. W., Selley, D., Yang, J., Cooke, D., Garven, G. and McGoldrick, P. J. (2002) 'Controls on the formation of giant stratiform sediment-hosted Zn-Pb-Ag deposits: With particular reference to the north Australian Proterozoic', in Cooke, D. R. and Pongratz, J. (eds) *Giant Ore Deposits: Characteristics, Genesis and Exploration*, pp. 107–150.

Law, S. R. (1999) *The Mount Isa Deep Copper Orebodies - Characteristics and Structural Controls on Mineralisation*. University of Tasmania.

Lazenby, H. (2022) *Copper deficit a critical destabilizing threat to international security, says S&P Global*, *The Northern Miner*. Available at: https://www.northernminer.com/news/copper-deficit-a-critical-destabilizing-threat-to-international-security-says-sp-global/ (Accessed: 15 November 2022).

Lisle, R. J. (1985) 'The use of the orientation tensor for the description and statistical testing of fabrics', *Journal of Structural Geology*, 7(1), pp. 115–117. doi: 10.1016/0191-8141(85)90119-1.

Logan, R. G., Murray, W. J. and Williams, N. (1990) 'HYC silver-lead-zinc deposit, McArthur River', in Hughes, F. E. (ed.) *Geology of the mineral deposits of Australia and Papua New Guinea*. Australasian Institute of Mining and Metallurgy, Monograph 14, pp. 907–911.

Long, R. D. (2010) *The Paroo Fault and the Mount Isa Copper Orebodies; A Revised Structural and Evolutionary Model, Mt Isa, Queensland, Australia*. James Cook University.

Lubinski, A. and Woods, H. B. (1953) 'Factors affecting the angle of inclination and dog-legging in rotary bore holes', in *Drilling and Production Practice 1953*, pp. 222–250.

Mainprice, D., Bachmann, F., Hielscher, R. and Schaeben, H. (2015) 'Descriptive tools for the analysis of texture projects with large datasets using MTEX : strength, symmetry and components', *Geological Society, London, Special Publications*, 409(1), pp. 251–271. doi: 10.1144/SP409.8.

Mandal, N. and Karmakar, S. (1989) 'Boudinage in homogeneous foliated rocks', *Tectonophysics*, 170(1–2), pp. 151–158. doi: 10.1016/0040-1951(89)90109-1.

Marjoribanks, R. W. (1997) *Geological Methods in Mineral Exploration and Mining*. Springer Netherlands. doi: 10.1007/978-94-011-5822-0.

Mathias, B. V. and Clark, G. J. (1975) 'Mount Isa copper and silver-lead-zinc orebodies. Isa and Hilton mines, in Knight, C. L, ed., Economic geology of Australia and Papua New Guinea, I. Metals', *Australasian Inst. Mining Metallurgy Mon.*, 5, pp. 351–371.

Matthäi, S. K., Heinrich, C. A. and Driesner, T. (2004) 'Is the Mount Isa copper deposit the product of forced brine convection in the footwall of a major reverse fault?', *Geology*, 32(4), p. 357. doi: 10.1130/G20108.2.

McGoldrick, P. J. and Keays, R. R. (1990) 'Mount Isa copper and lead-zinc-silver ores;

coincidence or cogenesis?', *Economic Geology*, 85(3), pp. 641–650. doi: 10.2113/gsecongeo.85.3.641.

McGoldrick, P. and Large, R. (1998) 'Proterozoic stratiform sediment-hosted Zn-Pb-Ag deposits', *Journal of Australian Geology & Geophysics*, 17(4), pp. 189–196.

McLellan, E. L. (1988) 'Migmatite structures in the Central Gneiss Complex, Boca de Quadra, Alaska', *Journal of Metamorphic Geology*, 6(4), pp. 517–542. doi: 10.1111/j.1525-1314.1988.tb00437.x.

McLellan, J. G., O'Sullivan, R., Miller, B. and Taylor, D. (2014) 'Geomechanical modelling of the Mount Isa copper deposit–predicting mineralisation', *Proceedings Ninth International Mining Geology Conference 2014*, (March), pp. 197–206.

McQueen, K. G. (1987) 'Deformation and remobilization in some Western Australian nickel ores', *Ore Geology Reviews*, 2(1–3), pp. 269–286. doi: 10.1016/0169-1368(87)90032-1.

Miller, J. M. (2007) *Structural controls on the Mount Isa Copper deposit, QLD - Project I7 Final Report*.

Milnes, A. G. (1964) *Unpublished Thesis*. University of Basel.

'MinEx CRC: A new frontier in mineral exploration' (2019) *Preview*, 2019:201, pp. 30–33. doi: 10.1080/14432471.2019.1646696.

Monterrosa, L. C., Rego, M. F., Zegarra, E. and Lowdon, R. (2016) 'Statistical analysis between different surveying instruments to understand the reliability of MWD/RSS high resolution surveys and its effect in well trajectory characterization', in *SPE/IADC Drilling Conference, Proceedings*. doi: 10.2118/178830-ms.

Mróz, M. (2022) 'Energy Security in Danger? A Comparative Analysis of Oil and Copper Supply', *Energies*, 15(2). doi: 10.3390/en15020560.

Mulchrone, K. F. and Choudhury, K. R. (2004) 'Fitting an ellipse to an arbitrary shape: implications for strain analysis', *Journal of Structural Geology*, 26(1), pp. 143–153. doi: 10.1016/S0191-8141(03)00093-2.

Munro, M. A. and Blenkinsop, T. G. (2012) 'MARD-A moving average rose diagram application for the geosciences', *Computers and Geosciences*, 49, pp. 112–120. doi: 10.1016/j.cageo.2012.07.012.

Murray, W. J. (1961) 'Notes on Mount Isa geology', *Proceedings of the Australian Institute of Mining and Metallurgy*, 197, pp. 105–136.

Neudert, M. K. (1983) *A depositional model for the Upper Mount Isa Group and implications for ore formation*. Australian National University.

Neumann, N. L., Southgate, P. N., Gibson, G. M. and MCintyre, A. (2006) 'New SHRIMP geochronology for the Western Fold Belt of the Mt Isa Inlier: developing a 1800 – 1650 Ma event framework', *Australian Journal of Earth Sciences*, 53(6), pp. 1023–1039. doi: 10.1080/08120090600923287.

Newbery, S. P., Carswell, J. T., Allnutt, S. L. and Mutton, A. J. (1993) 'The Dugald River zinc-lead-silver deposit: an example of a tectonised Proterozoic stratabound sulphide deposit', in *World Zinc '93*, pp. 7–21.

Niederschlag, E. and Siemes, H. (1996) 'Influence of Initial Texture, Temperature and Total Strain on the Texture Development of Polycrystalline Pyrrhotite Ores in Deformation Experiments', *Textures and Microstructures*, 28(1–2), pp. 129–148. doi: 10.1155/TSM.28.129.

O'Dea, M. G. and Lister, G. S. (1995) 'The role of ductility contrast and basement architecture in the structural evolution of the Crystal Creek block, Mount Isa Inlier, NW Queensland, Australia', *Journal of Structural Geology*, 17(7), pp. 949–960. doi: 10.1016/0191-8141(94)00117-I.

O'Dea, M. G., Lister, G. S., Betts, P. G. and Pound, K. S. (1997a) 'A shortened intraplate rift system in the Proterozoic Mount Isa terrane, NW Queensland, Australia', *Tectonics*, 16(3), pp. 425–441. doi: 10.1029/96TC03276.

O'Dea, M. G., Lister, G. S., MacCready, T., Betts, P. G., Oliver, N. H. S., Pound, K. S., Huang, W. and Valenta, R. K. (1997b) 'Geodynamic evolution of the Proterozoic Mount Isa Terrain', *Geological Society, London, Special Publications*, 121(1), pp. 99–122. doi: 10.1144/gsl.sp.1997.121.01.05.

Office for National Statistics (2020) *UK trading partners and trade relationships: 2020*.

Ostwald, J. and Lusk, J. (1978) 'Sulfide fabrics in some nickel sulfide ores from Kambalda, Western Australia', *Canadian Journal of Earth Sciences*, 15(4), pp. 501–515. doi: 10.1139/e78-057.

Ozkaya, S. I. (1995) 'Two EXCEL macros for tracing deviated boreholes using cubic splines and calculation of formation depth and thickness', *Computers & Geosciences*, 21(7), pp. 851–858. doi: 10.1016/0098-3004(95)00021-Y.

Page, R. W. (1983) 'Timing of superposed volcanism in the Proterozoic Mount Isa Inlier, Australia', *Precambrian Research*, 21(3–4), pp. 223–245. doi: 10.1016/0301-9268(83)90042-6.

Page, R. W. (1993a) 'Geological constraints given by U-Pb geochronology in the Mount Isa

inlier', *Australian Geological Survey Organisation Bulletin*, 93, pp. 13–15.

Page, R. W. (1993b) 'Mount Isa Geochronology', *Australian Geological Survey Organisation Bulletin*, 93, p. 60.

Page, R. W. and Bell, T. H. (1986) 'Isotopic and structural responses of granite to successive deformation and metamorphism', *Journal of Geology*, 94(3), pp. 365–379. doi: 10.1086/629035.

Page, R. W., Jackson, M. J. and Krassay, A. A. (2000) 'Constraining sequence stratigraphy in north Australian basins: SHRIMP U-Pb zircon geochronology between Mt Isa and McArthur river', *Australian Journal of Earth Sciences*, 47(3), pp. 431–459. doi: 10.1046/j.1440-0952.2000.00797.x.

Page, R. W. and Sun, S. S. (1998) 'Aspects of geochronology and crustal evolution in the Eastern Fold Belt, Mt Isa Inlier', *Australian Journal of Earth Sciences*, 45(3), pp. 343–361. doi: 10.1080/08120099808728396.

Page, R. W. and Sweet, I. P. (1998) 'Geochronology of basin phases in the western Mt Isa Inlier, and correlation with the McArthur Basin', *Australian Journal of Earth Sciences*, 45(2), pp. 219–232. doi: 10.1080/08120099808728383.

Page, R. W. and Williams, I. S. (1988) 'Age of the Barramundi Orogeny in northern Australia by means of ion microprobe and conventional U-Pb zircon studies', *Precambrian Research*, 40–41, pp. 21–36. doi: 10.1016/0301-9268(88)90059-9.

Painter, M. G. M., Golding, S. D., Hannan, K. W. and Neudert, M. K. (1999) *Sedimentologic, petrographic, and sulfur isotope constraints on fine-grained pyrite formation at Mount Isa Mine and environs, northwest Queensland, Australia*, *Economic Geology*. doi:

10.2113/gsecongeo.94.6.883.

Passchier, C. W. (2001) 'Flanking structures', *Journal of Structural Geology*, 23, pp. 951–962. doi: 10.1016/S0191-8141(00)00166-8.

Passchier, C. W., Mancktelow, N. S. and Grasemann, B. (2005) 'Flow perturbations: a tool to study and characterize heterogeneous deformation', *Journal of Structural Geology*, 27, pp. 1011–1026. doi: 10.1016/j.jsg.2005.01.016.

Passchier, C. W. and Trouw, R. A. J. (2005) *Microtectonics*. 2nd edn. Springer-Verlag Berlin Heidelberg. doi: 10.1007/3-540-29359-0.

Pearce, D. W., Markandya, A. and Barbier, E. B. (1989) *Blueprint for a Green Economy*. book. Earthscan.

Perkins, C., Heinrich, C. A. and Wyborn, L. A. I. (1999) '40Ar/39Ar Geochronology of Copper Mineralization and Regional Alteration, Mount Isa, Australia', *Economic Geology*, 94(1), pp. 23–36. doi: 10.2113/gsecongeo.94.1.23.

Perkins, W. G. (1984) 'Mount Isa Silica Dolomite and Copper Orebodies; The Result of a Syntectonic Hydrothermal Alteration System', *Economic Geology*, 79(4), pp. 601–637. doi: 10.2113/gsecongeo.79.4.601.

Perkins, W. G. (1997) 'Mount Isa lead-zinc orebodies: Replacement lodes in a zoned syndeformational copper-lead-zinc system?', *Ore Geology Reviews*, 12(2), pp. 61–110. doi: 10.1016/S0169-1368(97)00004-8.

Perkins, W. G. (1998) 'Timing of formation of Proterozoic stratiform fine-grained pyrite; post-diagenetic cleavage replacement at Mount Isa?', *Economic Geology*, 93(8), pp. 1153–1164. doi: 10.2113/gsecongeo.93.8.1153.

Petroleum Experts (2023) *Digital Field Mapping*. Available at: https://www.petex.com/products/move-suite/digital-field-mapping/ (Accessed: 12 March 2023).

Platt, J. P. and Vissers, R. L. M. (1980) 'Extensional structures in anisotropic rocks', *Journal of Structural Geology*, 2(4), pp. 397–410. doi: 10.1016/0191-8141(80)90002-4.

Potgieter, G. (2015) 'Work conducted in preparation for partial extraction of X41 shaft pillar at Mount Isa Mines', in *Proceedings of the International Seminar on Design Methods in Underground Mining*, pp. 273–290. doi: 10.36487/ACG_rep/1511_15_Potgieter.

Potma, W. A. and Betts, P. G. (2007) 'Australian Journal of Earth Sciences Extension-related structures in the Mitakoodi Culmination: Implications for the nature and timing of extension, and effect on later shortening in the eastern Mt Isa Inlier', *Australian Journal of Earth Sciences*, 53(1), pp. 55–67. doi: 10.1080/08120090500432421.

Qian, G., Xia, F., Brugger, J., Skinner, W. M., Bei, J., Chen, G. and Pring, A. (2011) 'Replacement of pyrrhotite by pyrite and marcasite under hydrothermal conditions up to 220 °C: An experimental study of reaction textures and mechanisms', *American Mineralogist*, 96(11–12), pp. 1878–1893. doi: 10.2138/am.2011.3691.

Ramberg, H. (1955) *Natural and Experimental Boudinage and Pinch-and-Swell Structures*, *The Journal of Geology*. doi: 10.1086/626293.

Ramsay, J. G. (1967) *Folding and Fracturing of Rocks*. New York McGraw-Hill Book Company.

Ramsay, J. G. and Huber, M. I. (1983) *The Techniques of Modern Structural Geology: Volume 1: Strain Analyses.* Academic Press Ltd.

REFLEX (2021) *REFLEX GYRO SPRINT-IQ^{TM} - REFLEX*. Available at:

https://reflexnow.com/product/reflex-gyro-sprint-iq/ (Accessed: 25 February 2023).

Riegel, B. (2020) *Lead is not dead – it's a critical foundation for Europe's low carbon future*, *Charge The Future*. Available at: https://chargethefuture.org/blog/lead-is-not-dead-its-a-critical-foundation-for-europes-low-carbon-future/ (Accessed: 27 February 2023).

Robertson, C. W. (1982) 'The role of pre-existing sulphides in coppper-ore formation at Mount Isa, Queensland', *BMR Journal of Australian Geology & Geophysics*, 7, pp. 119–124.

Rubenach, M. J. (1992) 'Proterozoic low-pressure/high-temperature metamorphism and an anticlockwise P-T-t path for the Hazeldene area, Mount Isa Inlier, Queensland, Australia', *Journal of Metamorphic Geology*, 10(3), pp. 333–346. doi: 10.1111/j.1525-1314.1992.tb00088.x.

S&P Global (2022) *Looming Copper Supply Shortfalls Present a Challenge to Achieving Net-Zero 2050 Goals, S&P Global Study Finds*.

Sawaryn, S. J. and Thorogood, J. L. (2005) 'A compendium of directional calculations based on the minimum curvature method', *SPE Drilling and Completion*, 20(1), pp. 24–36. doi: 10.2118/84246-PA.

Sawyer, E. W. (1983) 'The structural history of a part of the Archaean Quetico Metasedimentary Belt, superior province, Canada', *Precambrian Research*, 22(3–4), pp. 271–294. doi: 10.1016/0301-9268(83)90052-9.

Schipper, B. W., Lin, H. C., Meloni, M. A., Wansleeben, K., Heijungs, R. and van der Voet, E. (2018) 'Estimating global copper demand until 2100 with regression and stock dynamics', *Resources, Conservation and Recycling*, 132, pp. 28–36. doi: 10.1016/j.resconrec.2018.01.004.

Scott, D. L., Rawlings, D. J., Page, R. W., Tarlowski, C. Z., Idnurm, M., Jackson, M. J. and Southgate, P. N. (2000) 'Basement framework and geodynamic evolution of the Palaeoproterozoic superbasins of north-central Australia: An integrated review of geochemical, geochronological and geophysical data Basement framework and geodynamic', *Australian Journal of Earth Sciences*, 47, pp. 341–380. doi: 10.1046/j.1440-0952.2000.00793.x.

Seibi, A., Karrech, A., Boukadi, F. and Pervez, T. (2009) 'Wellbore Path Estimation Using Measurement While Drilling Techniques: A Comparative Study and Suggestions for Improvements', *Energy Sources, Part A: Recovery, Utilization and Environmental Effects*, 31(14), pp. 1205–1216. doi: 10.1080/15567030802087502.

Sindle, T. G., Mason, I. M., Hargreaves, J. E. and Cloete, J. H. (2006) *Adding Value to Exploration Boreholes by Improving Trajectory Survey Accuracy*.

Singer, D. A. (1995) 'World Class Base and Precious Metal Deposits-A Quantitative Analysis', *Economic Geology*, 90(1), pp. 88–104. doi: 10.2113/gsecongeo.90.1.88.

Singh, S. P. (1998) 'The effects of rock mass characteristics on blast hole deviation', *CIM Bulletin*, 91, pp. 90–95.

Škrjanc, Z. and Vulic, M. (2016) 'Comparison of the directional survey calculation methods applied on real well data', *Measurement*, 94, pp. 239–244. doi: 10.1016/j.measurement.2016.08.002.

Smith, J. W., Burns, M. S. and Croxford, N. J. W. (1978) 'Stable isotope studies of the origins of mineralization at Mount Isa. I.', *Mineralium Deposita*, 13(3), pp. 369–381. doi: 10.1007/BF00206570.

Smith, S. E. and Walker, K. R. (1971) *Primary Element Dispersions Associated with Mineralization at Mount Isa, Queensland*.

Southgate, P. N., Bradshaw, B. E., Domagala, J., Jackson, M. J., Idnurm, M., Krassay, A. A., Page, R. W., Sami, T. T., Scott, D. L., Lindsay, J. F., McConachie, B. A. and Tarlowski, C. (2000) 'Chronostratigraphic basin framework for Palaeoproterozoic rocks (1730-1575 Ma) in northern Australia and implications for base-metal mineralisation', *Australian Journal of Earth Sciences*, 47(3), pp. 461–483. doi: 10.1046/j.1440-0952.2000.00787.x.

Spatial and Graphic Services Statewide Operations Department of Natural Resources Mines and Energy (2020) *Mount Isa Surface Geology*.

Stanton, R. L. (1962) 'Elemental constitution of the Black Star orebodies, Mount Isa, Queensland and its interpretation', *Inst. Mining Metallurgy Trans*, 72, pp. 61–144.

Stanton, R. L. (1963) 'Constituitonal features of the Mount Isa sulphide ores and their interpretation', *Australasian Inst. Mining Metallurgy Proc*, 205, pp. 131–153.

Stern, C. R., Huang, W. L. and Wyllie, P. J. (1975) 'Basalt-andesite-rhyolite-H2O: Crystallization intervals with excess H2O and H2O-undersaturated liquidus surfaces to 35 kilobars, with implications for magma genesis', *Earth and Planetary Science Letters*, 28(2), pp. 189–196. doi: 10.1016/0012-821X(75)90226-5.

Stipp, M., Stünitz, H., Heilbronner, R. and Schmid, S. M. (2002a) 'Dynamic recrystallization of quartz: Correlation between natural and experimental conditions', *Geological Society Special Publication*, 200, pp. 171–190. doi: 10.1144/GSL.SP.2001.200.01.11.

Stipp, M., Stünitz, H., Heilbronner, R. and Schmid, S. M. (2002b) 'The eastern Tonale fault zone: A "natural laboratory" for crystal plastic deformation of quartz over a temperature

range from 250 to 700 °C', *Journal of Structural Geology*, 24(12), pp. 1861–1884. doi: 10.1016/S0191-8141(02)00035-4.

Stipp, M. and Tullis, J. (2003) 'The recrystallized grain size piezometer for quartz', *Geophysical Research Letters*, 30(21), pp. 6667–6674. doi: 10.1002/2017GL073836.

Stipp, M., Tullis, J., Scherwath, M. and Behrmann, J. H. (2010) 'A new perspective on paleopiezometry: Dynamically recrystallized grain size distributions indicate mechanism changes', *Geology*, 38(8), pp. 759–762. doi: 10.1130/G31162.1.

Swager, C. P. (1985) 'Syndeformational Carbonate-Replacement Model for the Copper Mineralization at Mount Isa, Northwest Queensland: A Microstructural Study', *Economic Geology*, 80(1), pp. 107–125. doi: 10.2113/gsecongeo.80.1.107.

Swager, C. P., Perkins, W. G. and Knights, J. G. (1987) 'Stratabound phyllosilicate zones associated with syntectonic copper orebodies at Mt Isa, Queensland', *Australian Journal of Earth Sciences*, 34(4), pp. 463–476. doi: 10.1080/08120098708729426.

Swanson, M. T. (1992) 'Late Acadian-Alleghenian transpressional deformation: evidence from asymmetric boudinage in the Casco Bay Area, coastal Maine', *Journal of Structural Geology*, 14(3), pp. 323–341. doi: 10.1016/0191-8141(92)90090-J.

Taylor, H. L. and Mason, M. C. (1972) 'A Systematic Approach to Well Surveying Calculations', *Society of Petroleum Engineers Journal*, 12(06), pp. 474–488. doi: 10.2118/3362-PA.

Terzaghi, R. D. (1965) 'Sources of Error in Joint Surveys', *Géotechnique*, 15(3), pp. 287–304. doi: 10.1680/GEOT.1965.15.3.287.

Tulley, C. J. (2021) *Geology of the subduction thrust: insights from exhumed shear zones on Kyushu, SW Japan*. Cardiff University.

Turner, F. J. (1948) *Mineralogical and structural evolution of the metamorphic rocks.* Geological Society of America. doi: 10.1130/MEM30.

Uwanyuze, R. S., Enright, L., Zhang, J. and Schafföner, S. (2022) 'Preparation of concrete specimen for internal sulfate attack analysis using electron backscatter diffraction', *International Journal of Applied Ceramic Technology*, 19(3), pp. 1195–1207. doi: 10.1111/IJAC.13973.

Valenta, R. (2018) *NW Queensland Mineral Province Deposit Atlas Prototype Report - the Mount Isa and Ernest Henry Deposits*, *DNRME-GSQ Commisioned study and report*.

Vearncombe, J. and Vearncombe, S. (1998) 'Structural data from drill core', in Davis, B. and Ho, S. . (eds) *More meaningful sampling in the mining industry. Australian Insitute of Geoscientists, Bulletins, 22*, pp. 67–82.

Venditti, B. (2022) *Zinc is a critical metal for developing a low-carbon economy | World Economic Forum*, *World Economic Forum*. Available at: https://www.weforum.org/agenda/2022/04/zinc-low-carbon-economy-construction/ (Accessed: 27 February 2023).

Vollmer, F. W. (2018) 'Automatic contouring of geologic fabric and finite strain data on the unit hyperboloid', *Computers & Geosciences*, 115, pp. 134–142. doi: 10.1016/j.cageo.2018.03.006.

Vukmanovic, Z., Fiorentini, M. L., Reddy, S. M. and Godel, B. (2019) 'Microstructural constraints on magma emplacement and sulfide transport mechanisms', *Lithosphere*, 11(1), pp. 73–90. doi: 10.1130/L743.1.

Vukmanovic, Z., Reddy, S. M., Godel, B., Barnes, Stephen J., Fiorentini, M. L., Barnes, Sarah-

Jane and Kilburn, M. R. (2014) 'Relationship between microstructures and grain-scale trace element distribution in komatiite-hosted magmatic sulphide ores', *Lithos*, 184–187, pp. 42–61. doi: 10.1016/j.lithos.2013.10.037.

Wallis, I., Rowland, J., Dempsey, D., Allan, G., Sidik, R., Martikno, R., McLean, K., Sihotang, M., Azis, H. and Baroek, M. (2020) 'Approaches to imaging feedzone diversity with case studies from Sumatra, Indonesia and the Taupō Volcanic Zone, New Zealand', in *Proceedings 42nd New Zealand Geothermal Workshop*.

Walsh, J. J. and Watterson, J. (1988) 'Analysis of the relationship between displacements and dimensions of faults', *Journal of Structural Geology*, 10(3), pp. 239–247. doi: 10.1016/0191-8141(88)90057-0.

Walstrom, J. E., Harvey, R. P. and Eddy, H. D. (1972) 'A Comparison of Various Directional Survey Models and an Approach To Model Error Analysis', *Journal of Petroleum Technology*, 24(08), pp. 935–943. doi: 10.2118/3379-pa.

Walters, S. and Bailey, A. (1998) 'Geology and mineralization of the Cannington Ag-Pb-Zn deposit: An example of broken hill-type mineralization in the eastern succession, Mount Isa Inlier, Australia', *Economic Geology*, 93(8), pp. 1307–1329. doi: 10.2113/gsecongeo.93.8.1307.

Waring, C. L. (1990) *Genesis of the Mount Isa Cu ore system (unpublished)*. Monash University.

Waring, C. L., Andrew, A. S. and Ewers, G. R. (1998a) 'Use of O, C and S stable isotopes in mineral exploration', *AGSO Journal of Australian Geology & Geophysics*, 17(4), pp. 301–313.

Waring, C. L., Heinrich, C. A. and Wall, V. J. (1998b) 'Proterozoic metamorphic copper deposits', *AGSO Journal of Australian Geology & Geophysics*, 17(4), pp. 239–246.

Watari, T., Nansai, K. and Nakajima, K. (2021) 'Major metals demand, supply, and environmental impacts to 2100: A critical review', *Resources, Conservation and Recycling*, 164. doi: 10.1016/J.RESCONREC.2020.105107.

Weinberg, R. F. and Hasalová, P. (2015) 'Water-fluxed melting of the continental crust: A review', *Lithos*, 212–215, pp. 158–188. doi: 10.1016/j.lithos.2014.08.021.

Wiest, J. D., Fossen, H. and Jacobs, J. (2020) 'Shear zone evolution during core complex exhumation – Implications for continental detachments', *Journal of Structural Geology*, 140, p. 104139. doi: 10.1016/j.jsg.2020.104139.

Wilde, A. R. (2011) 'Mount Isa copper orebodies: improving predictive discovery', *Australian Journal of Earth Sciences*, 58(8), pp. 937–951. doi: 10.1080/08120099.2011.571285.

Wilde, A. R., Jones, P. A., Gessner, K., Aillères, L., Gregory, M. J. and Duncan, R. J. (2006) 'A geochemical process model for the Mount Isa copper orebodies', *Economic Geology*, 101(8), pp. 1547–1567. doi: 10.2113/gsecongeo.101.8.1547.

Williams, B. J., Blenkinsop, T. G., Lilly, R., Thompson, M. P. and Ila'ava, P. (2023) 'Foliation boudinage structures in the Mount Isa Cu system', *Australian Journal of Earth Sciences*, pp. 1–18. doi: 10.1080/08120099.2022.2153384.

Williams, P. J. (1998a) 'An introduction to the metallogeny of the mcarthur river-mount isa-cloncurry minerals province', *Economic Geology*, 93(8), pp. 1120–1131. doi: 10.2113/gsecongeo.93.8.1120.

Williams, P. J. (1998b) 'Metalliferous economic geology of the Mt Isa Eastern Succession, Queensland', *Australian Journal of Earth Sciences*, 45(3), pp. 329–341. doi: 10.1080/08120099808728395.

Wilson, G. J. (1968) 'An Improved Method for Computing Directional Surveys', *Journal of Petroleum Technology*, 20(08), pp. 871–876. doi: 10.2118/1992-pa.

Wilson, I. H., Derrick, G. M. and Perkin, D. J. (1985) 'Eastern Creek Volcanics: their geochemistry and possible role in copper mineralisation at Mount Isa, Queensland.', *B.M.R. Journal of Australian Geology & Geophysics, Canberra*, 9(4), pp. 317–328.

Winsor, C. N. (1986) 'Intermittent folding and faulting in the lake moondarra area, mount isa, Queensland', *Australian Journal of Earth Sciences*, 33(1), pp. 27–42. doi: 10.1080/08120098608729348.

Wright, S. I., Nowell, M. M. and Field, D. P. (2011) 'A review of strain analysis using electron backscatter diffraction', *Microscopy and Microanalysis*, 17(3), pp. 316–329. doi: 10.1017/S1431927611000055.

Wyborn, L. A. I. (1987) 'The Petrology and Geochemistry of Alteration Assemblages in the Eastern Creek Volcanics, as a Guide to Copper and Uranium Mobility Associated with Regional Metamorphism and Deformation, Mount Isa, Queensland', *Geological Society, London, Special Publications*, 33(1), pp. 425–434. doi: 10.1144/GSL.SP.1987.033.01.29.

Zaremba, W. A. (1973) 'Directional Survey by the Circular Arc Method', *Society of Petroleum Engineers Journal*, 13(01), pp. 5–11. doi: 10.2118/3664-PA.

APPENDIX A

Foliation Boudinage Structure Literature Review Additional Material: Examples from Mount Isa

Most structures detailed in Chapter 3 are also found at Mount Isa. Some synthesis of the classification scheme has been detailed in each section, with examples of the structures observed during this study.
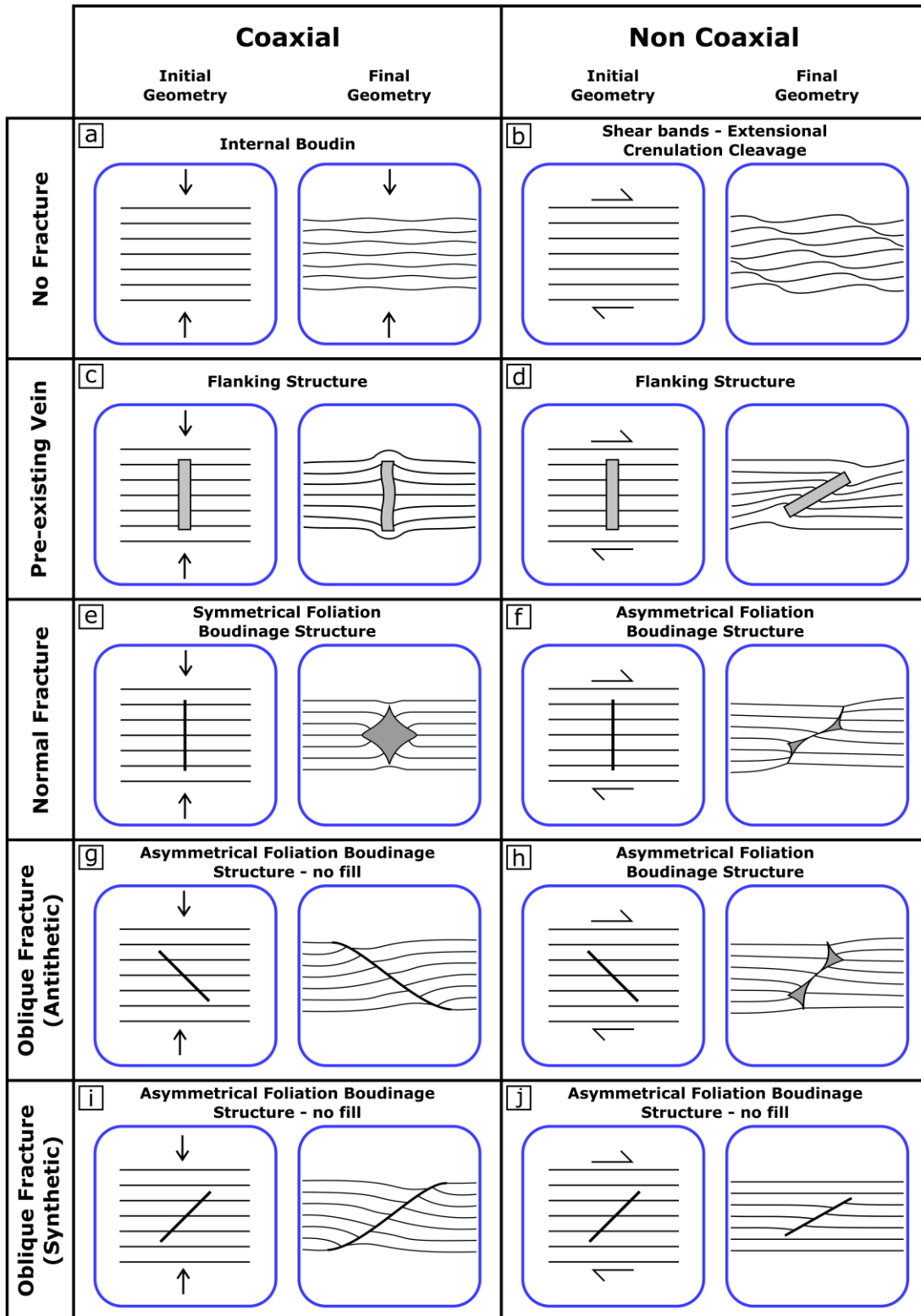
Figure 2.9: Repeat of **Figure 2.9** in foliation boudinage structure literature review. See caption in **Figure 2.9** for details.

A.1 Internal Boudinage (Coaxial – No Fracture): Figure 2.9a

Where no fracture forms, either due to lower fluid pressures, lower differential stresses or rheology, the structures vary depending on the direction of shortening. Based on the previous literature and the classification scheme, internal boudins will occur when shortening normal to the layering and extension parallel to the layering. Areas that are pinched align with areas of swell in adjacent layers, forming an interlocking network **[Figure A.1]**. This has been demonstrated in plasticine models by Cobbold *et al.* (1971), shown in diagrams by Kidan and Cosgrove (1996) and can be seen in drill core at Mount Isa **[Figure A.1]**. Continued layer-normal shortening of the internal boudins has been shown to form kink bands (Cobbold *et al.*, 1971; Kidan and Cosgrove, 1996).
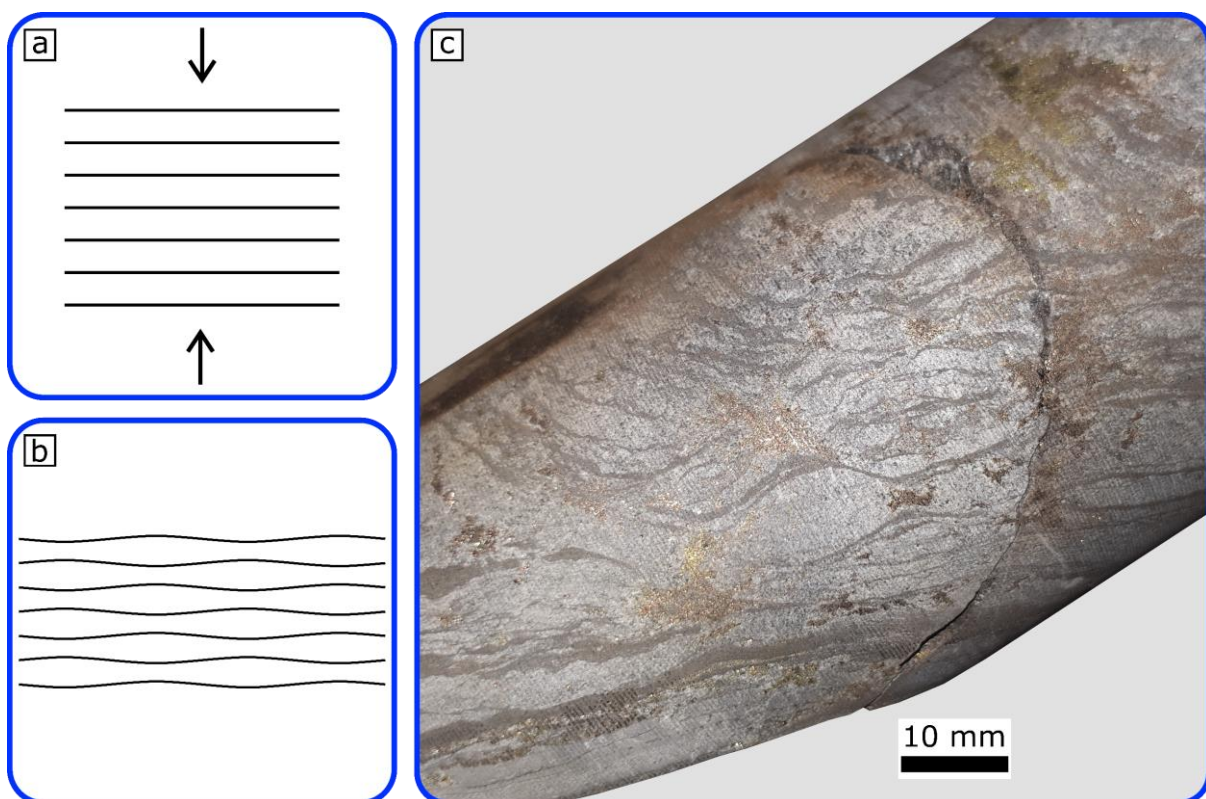
Figure A.1: Development of the distinct pinch and swell geometry of internal boudinage by layer-normal shortening of anisotropic and homogeneous lithologies, without the formation of a fracture. **a)** Initial shortening; **b)** After development of internal boudins; **C)** An example of internal boudinage as seen in drill core at Mount Isa Mines.

A.2 Shear – Extensional Crenulation Cleavage (Non-Coaxial – No Fracture): Figure 2.9b

Extensional crenulation cleavage and incipient shears develop when no fracture forms during non-coaxial shortening of anisotropic and homogeneous layering. Platt and Vissers (1980) show that extensional crenulation cleavage can form by asymmetric, non-coaxial deformation. They suggest that in zones of bulk simple shear, a single set of extensional crenulation cleavages should form parallel to the bulk shear direction. Extensional crenulation cleavage can be seen in Mount Isa drill core **[Figure A.2]**.
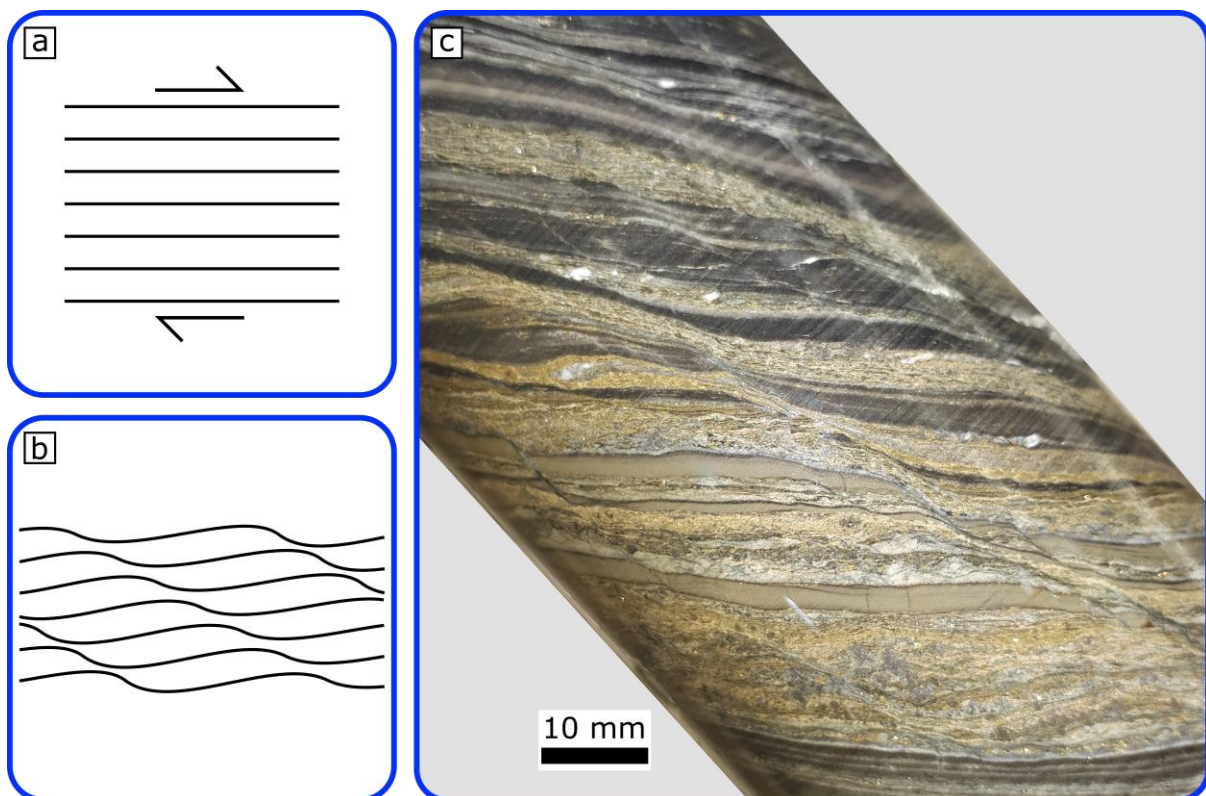
Figure A.2: Development of extensional crenulation cleavage by simple shear of anisotropic and homogeneous layering, without the formation of a fracture. **a)** Orientation of initial shear; **b)** Development of extensional crenulation cleavages; **c)** An example of extensional crenulation cleavage as seen in drill core at Mount Isa Mines.

A.3 Symmetrical Foliation Boudinage Structures (Coaxial – Normal Fracture): Figure 2.9e

It appears that for foliation boudinage structures to form, the timing of the initial fracture is important. The fracture forms either during the deformation event associated with the formation of the foliation boudinage structures or prior to the event, though remaining as a fluid filled fracture, without precipitation.

Where a fracture forms normal to the foliation or layering, and undergoes layer-normal shortening and layer-parallel extension, the resulting structure will be symmetric about a central vertical line **[Figure A.3]**. Arslan *et al.* (2008) show that providing fluid pressure is high, the fracture will open parallel to the layering, resulting in a fluid filled void. Most foliation boudinage structures are filled by common vein forming minerals such as quartz and calcite, which undergo little or no deformation after precipitation and filling of the void (Arslan *et al.*, 2008).

As the fracture opens and deforms under conditions of continuous deformation, the layering or foliation in the surrounding lithology remains approximately sub-perpendicular to the fracture walls. The resulting structure shows an inward bending of the layering into the fracture centre. These structures are known as lozenge-type symmetrical foliation boudinage structures, and where the void closes completely, they are known as fishmouth foliation boudinage structures. These structures have been modelled by Platt and Vissers (1980), Lacassin (1988), Mandal and Karmakar (1989), Druguet and Carreras (2006), and Arslan *et al.* (2008).
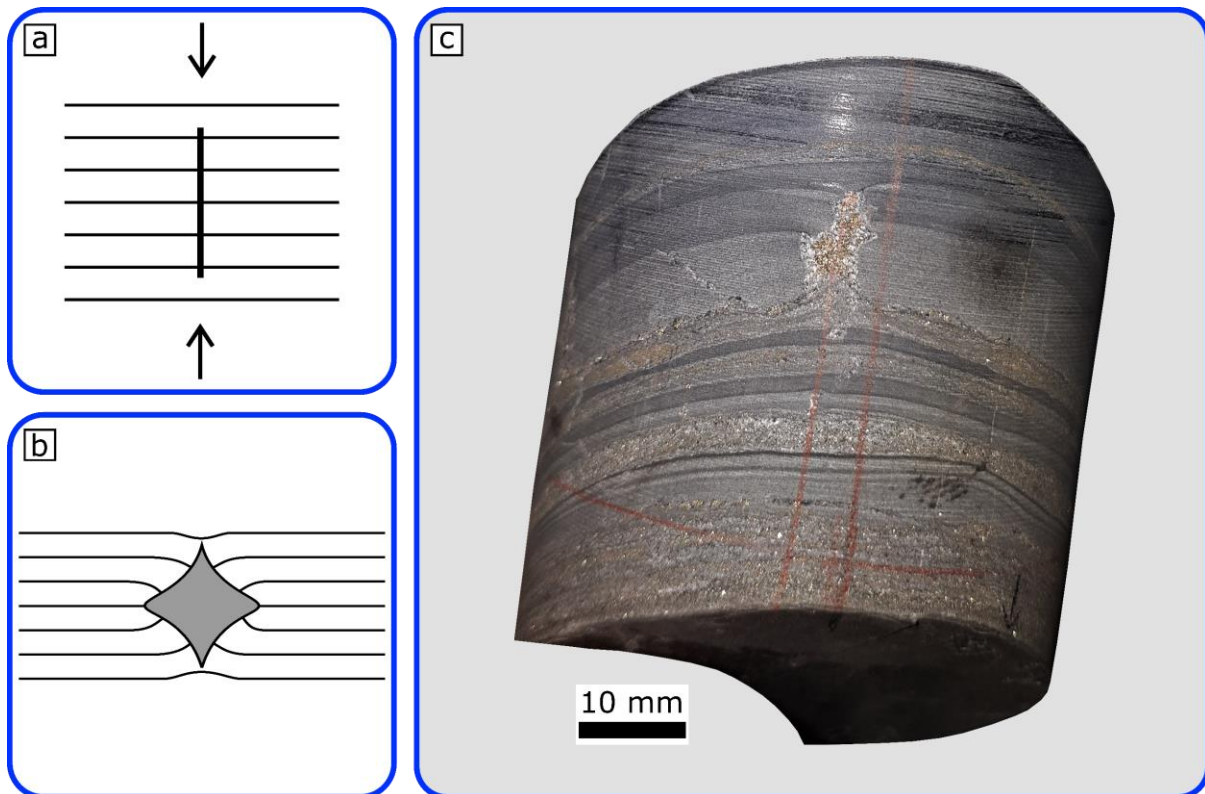
Figure A.3: Development of symmetrical foliation boudinage structures by layer-normal shortening of anisotropic and homogeneous layering. The presence of a layer-normal extension fracture induces the symmetrical opening of the fracture into a fluid filled void. **a)** Initial state; **B)** After the symmetrical foliation boudinage structure has developed; **c)** An example of symmetrical foliation boudinage structures from drill core at Mount Isa Mines.

A.4 Asymmetric Foliation Boudinage Structures (Non-Coaxial – Normal/Antithetic Fracture): Figure 2.9f + Figure 2.9h

A fracture which is deformed during non-coaxial flow such as in **Figure A.4i** and **Figure A.4i**, and where the fluid pressure is significantly high, may result in an open void which is asymmetric. The mineral fill in the interior of the void has a distinctive 'x' shape, known as x-type asymmetrical foliation boudinage structures (Arslan *et al.*, 2008). The layering or foliation in these structures bend into the centre of the fracture, with the final angle between the layering and the fracture wall approximating the initial angle of the fracture. As the bending layers on either side of the vein have no line of symmetry, this initial angle between the fracture wall and the layering will have a range of values, varying with distance up the

structure (Arslan *et al.*, 2008). Asymmetrical foliation boudinage structures have been modelled by Lacassin (1988), Arslan *et al.* (2008) and in Model III of Mandal and Karmakar (1989).

It is noticeable that the volume of infill is less in those structures where the fracture has rotated by a smaller amount. This can be seen in two examples from Mount Isa, where the angle between the initial fracture orientation and final angle of the foliation boudinage structure in **Figure A.4i** is greater than the angle between the fracture and foliation boudinage structure in **Figure A.4ii**.
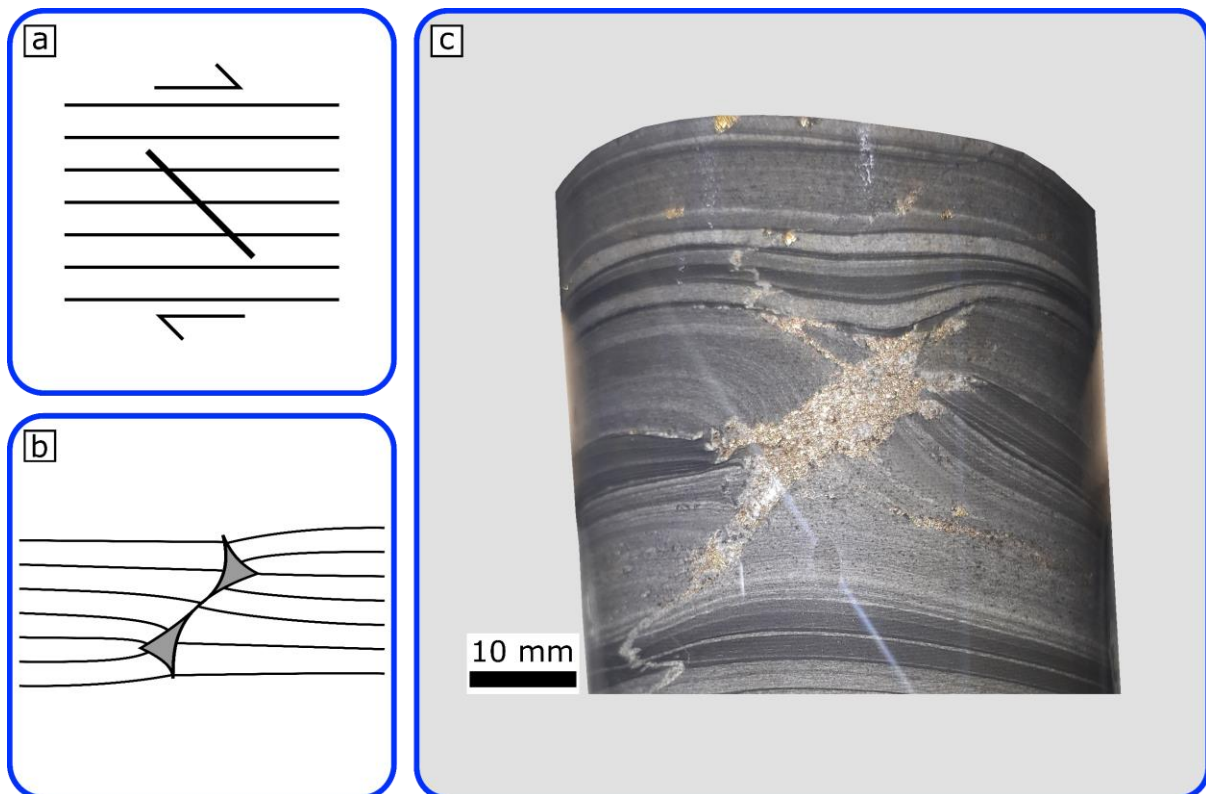
Figure A.4i: Development of asymmetric foliation boudinage structures from an initially oblique fracture during non-coaxial flow. The volume of infill is noticeably greater than that in **Figure A.4ii**. **a)** Initial fracture orientation; **b)** Asymmetric foliation boudinage structure; **c)** An example image of the final asymmetric foliation boudinage structure as seen in drill core at Mount Isa Mines.
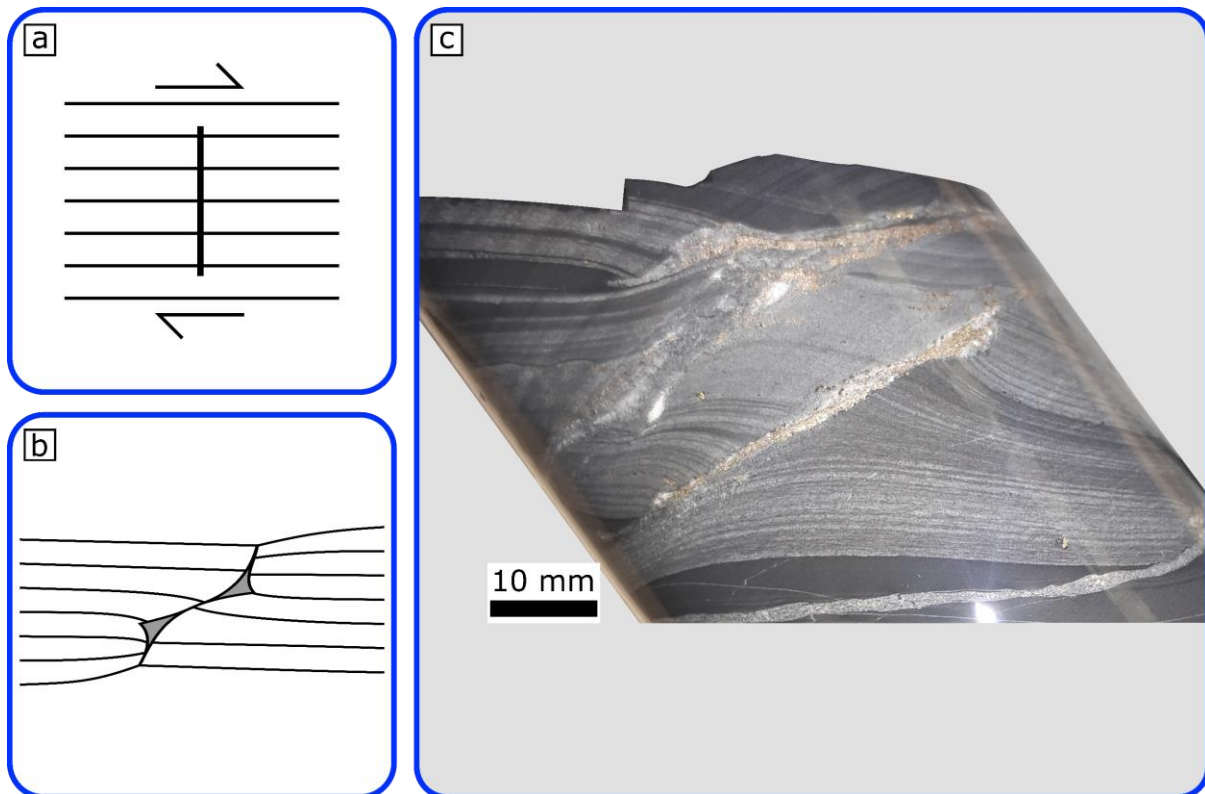
Figure A.4ii: Development of asymmetric foliation boudinage structures from an initial layer-normal fracture during non-coaxial flow. The volume of infill is noticeably less than that in **Figure A.4i**. **a)** Initial fracture orientation; **b)** Asymmetric foliation boudinage structure; **c)** An example image of the final asymmetric foliation boudinage structure as seen in drill core at Mount Isa Mines.

A.5 Flanking Structure – Vein prior to deformation: Figure 2.9c (+Figure 2.9d)

Flanking structures are distinguishable by the deformation surrounding an existing discontinuity, either a fracture, fault, vein, or dyke **[Figure A.5i; Figure A.5ii]** (Grasemann and Stüwe, 2001; Passchier, 2001; Grasemann *et al.*, 2003). If a vein forms in an anisotropic, homogeneous rock prior to shortening, deformation is observed as bending in the surrounding layers. The vein becomes integral to the deformation due to the competency difference between the vein and the surrounding lithology. Flanking structures form as the deformation flow is focused outside the vein in the surrounding layers. Deformation of the vein may also occur by shortening or shear, indicating the relative timing of deformation and vein development. An early vein with significant observable deformation could therefore be

a key observation in distinguishing flanking structures from foliation boudinage structures.

Flanking structures are observed in Mount Isa drill core surrounding early deformed veins

[Figure A.5i].
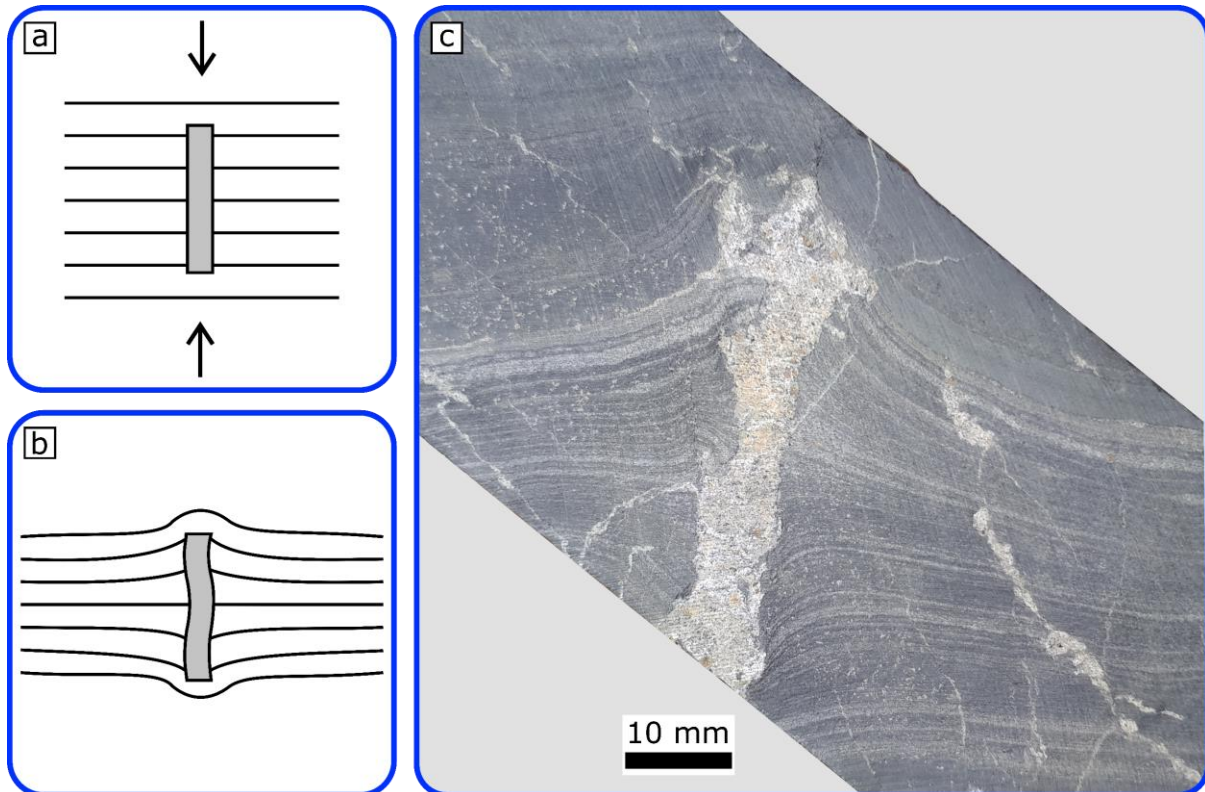
Figure A.5i: Development of a symmetrical flanking structure around an existing vein. Layer-normal shortening results in continuous deformation of the layering and vein. **a)** Vein and layering prior to shortening; **b)** The resulting flanking structure; **c)** An example of a flanking structure around a deformed vein in drill core at Mount Isa Mines.
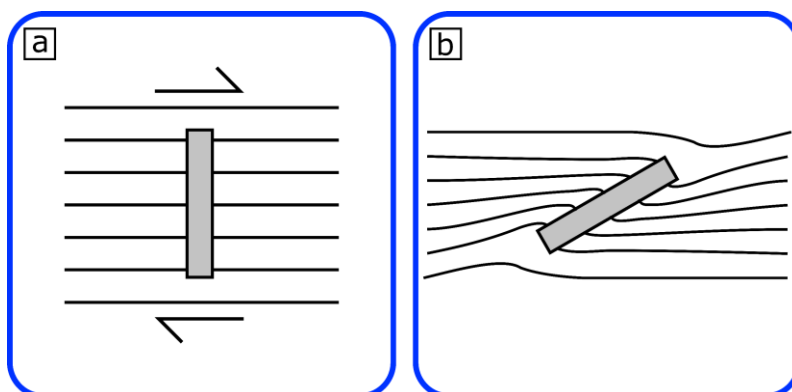
Figure A.5ii: Development of an asymmetrical flanking structure around an existing vein during non-coaxial deformation. **a)** Vein and layering prior to shortening; **b)** The resulting flanking structure.

A.6 Asymmetric Foliation Boudinage Structure – no fill (Coaxial – Oblique Fracture): Figure 2.9g and Figure 2.9i

Asymmetrical foliation boudinage structures can form by the deformation of discontinuities that are not conducive to opening under layer-normal shortening **[Figure A.6]**. A fracture or discontinuity in such an orientation is unlikely to form under these shortening conditions and may be pre-existing, remaining unfilled. The fracture is likely to remain closed, unless a significantly high fluid pressure is present. Continuous deformation surrounding the fracture will lead to the development of a structure similar to flanking structures. Movement along the fracture may occur as the structure extends parallel to the layering. These structures have been modelled in plasticine by Platt and Vissers (1980) and in Model II of Mandal and Karmakar (1989), where it has been termed asymmetric shear-fracture boudinage.
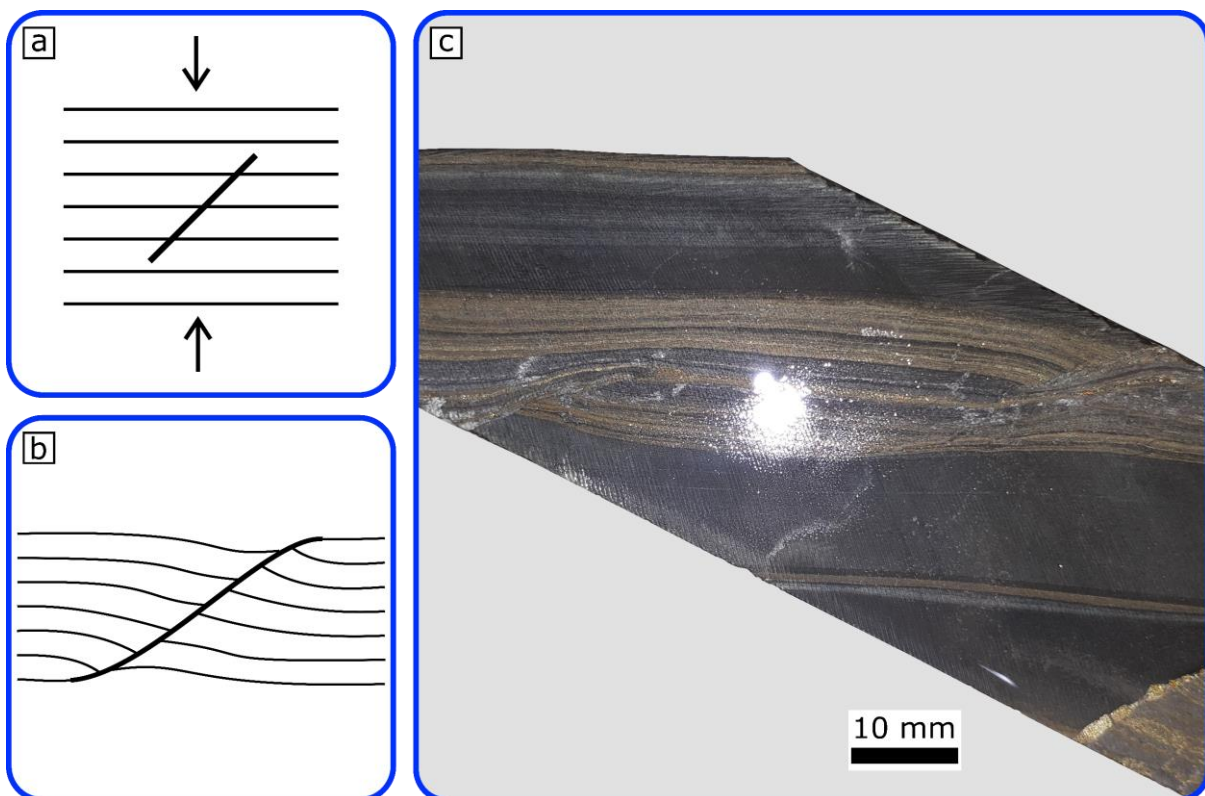
Figure A.6: Development of a flanking structure from an initially oblique fracture during coaxial flow. **a)** Initial fracture orientation; **b)** The resulting asymmetric, non-opening foliation boudinage structure; **c)** An example image of the final foliation boudinage structure as seen in drill core.

4.7. Asymmetric Foliation Boudinage Structure – no fill (Non-Coaxial – Synthetic Fracture): Figure 2.9j

When fractures that are synthetic to the shear direction undergo non-coaxial deformation, the result may be the formation of asymmetrical foliation boudinage structures that do not open **[Figure A.7]**. The fracture lies in a plane which inhibits the opening of the fracture under non-coaxial deformation. Instead, deformation is by slip along the fracture. These structures are similar to the reverse drag a-type flanking structures of Grasemann and Stüwe (2001), Passchier (2001) and Grasemann *et al.* (2003).
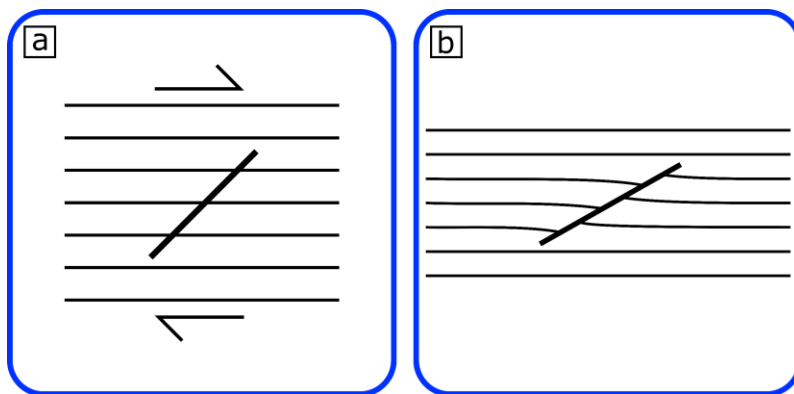
Figure A.7: Development of a flanking structure from an initially oblique fracture during non-coaxial flow. Owing to the initial orientation of the fracture, no opening occurs, unless a significantly high fluid pressure. **a)** Initial fracture orientation; **b)** The resulting asymmetric, non-opening, foliation boudinage structure.

APPENDIX B

Structures and Sulphides at Mount Isa: Additional Examples and Illustrations

This appendix constitutes a presentation of structures related to sulphide mineralisation at Mount Isa. The presentation was given at a workshop for Mount Isa Geologists in March 2019.

Slide 1

Slide 2

Slide 3

Foliation Boudinage

- Boudinage occurring in foliated rocks independent of lithology contrasts
  - No need for different lithologies (no competency differences) = homogeneous
  - Need some form of layering (foliation) = anisotropy
  - An initial fracture
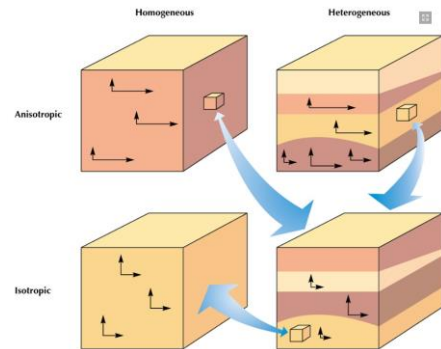
Slide 4

- Four main types:
  - Lozenge
  - Crescent
  - X-type
  - Double Crescent
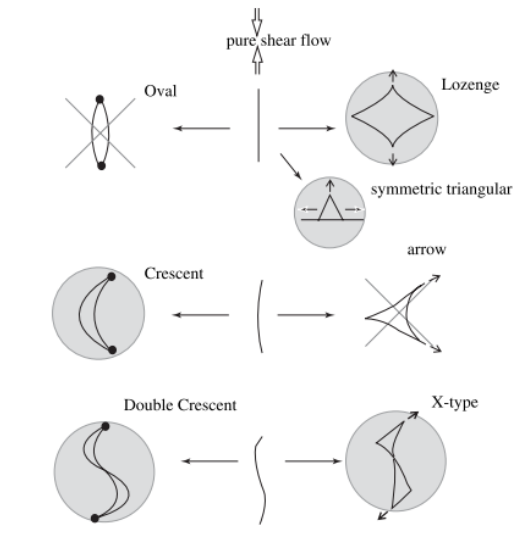
Slide 5
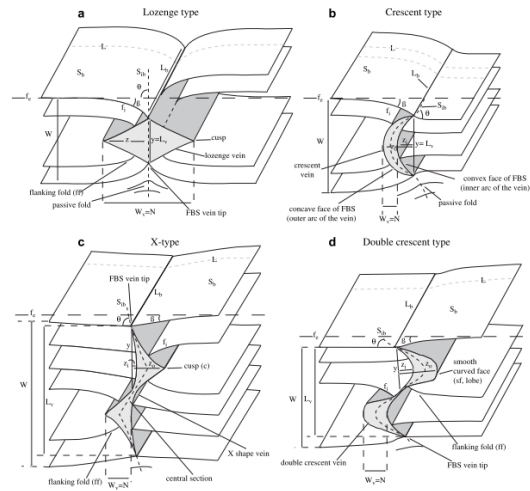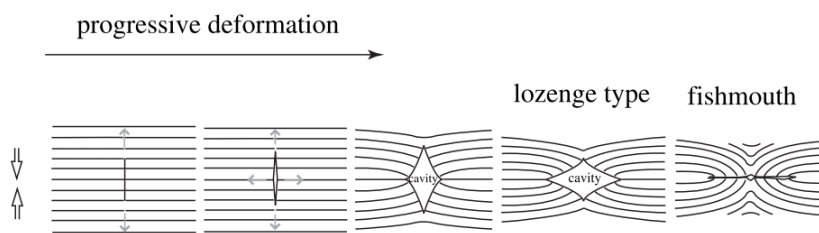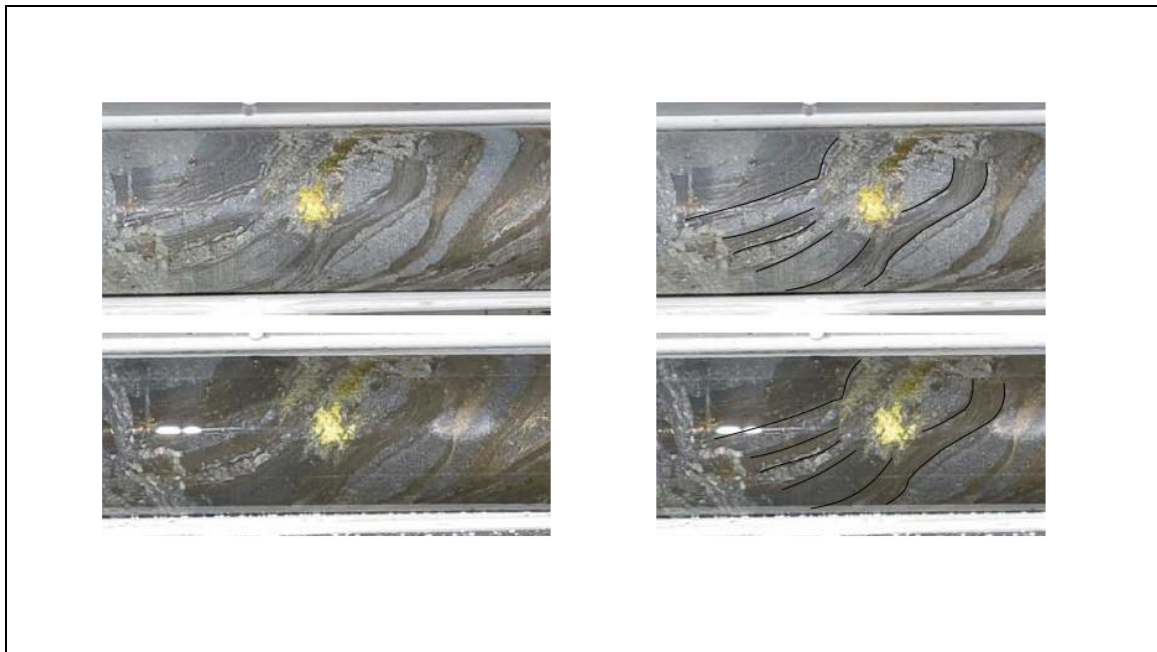
Slide 6
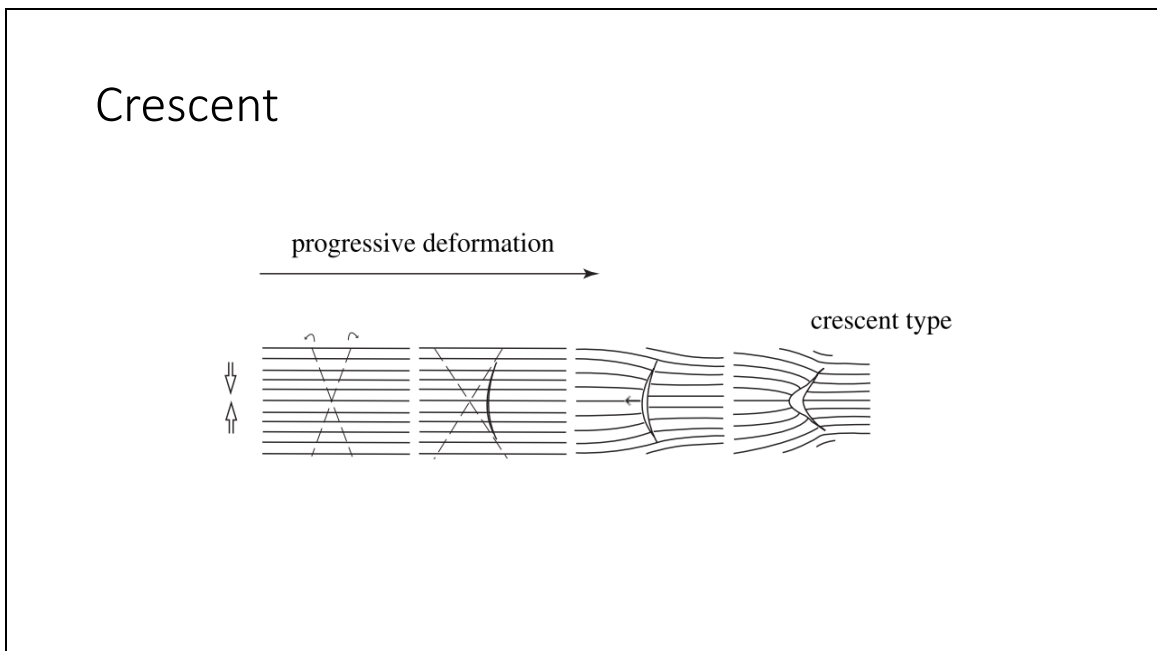
Slide 7
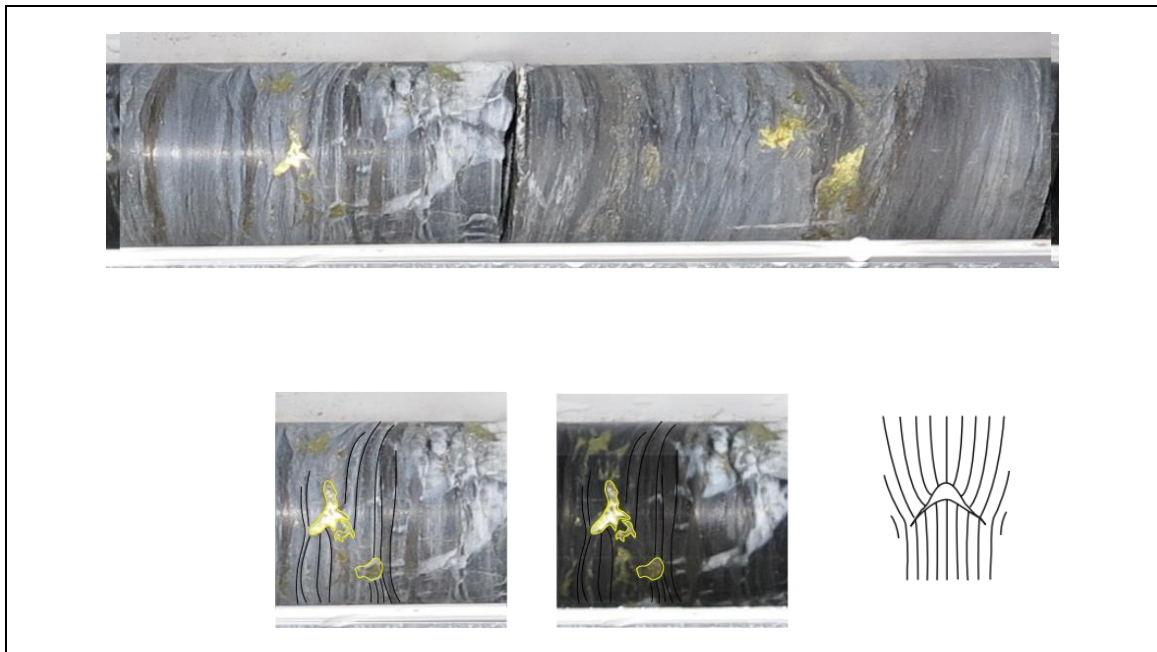
Slide 8

Slide 9

Slide 10
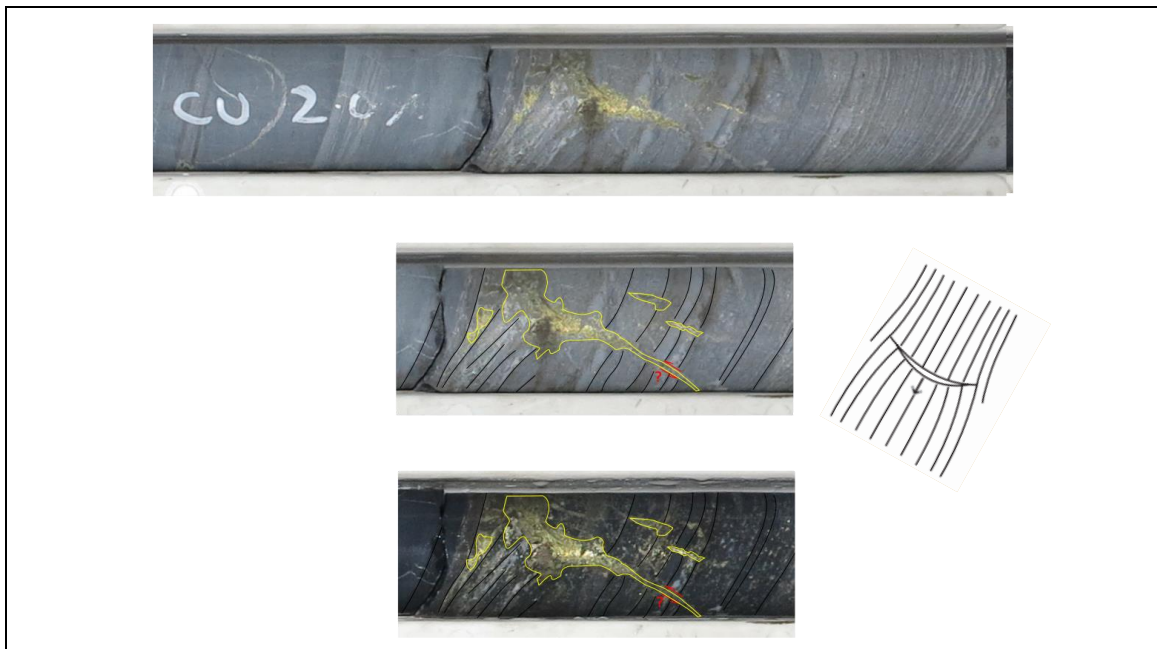
Slide 11
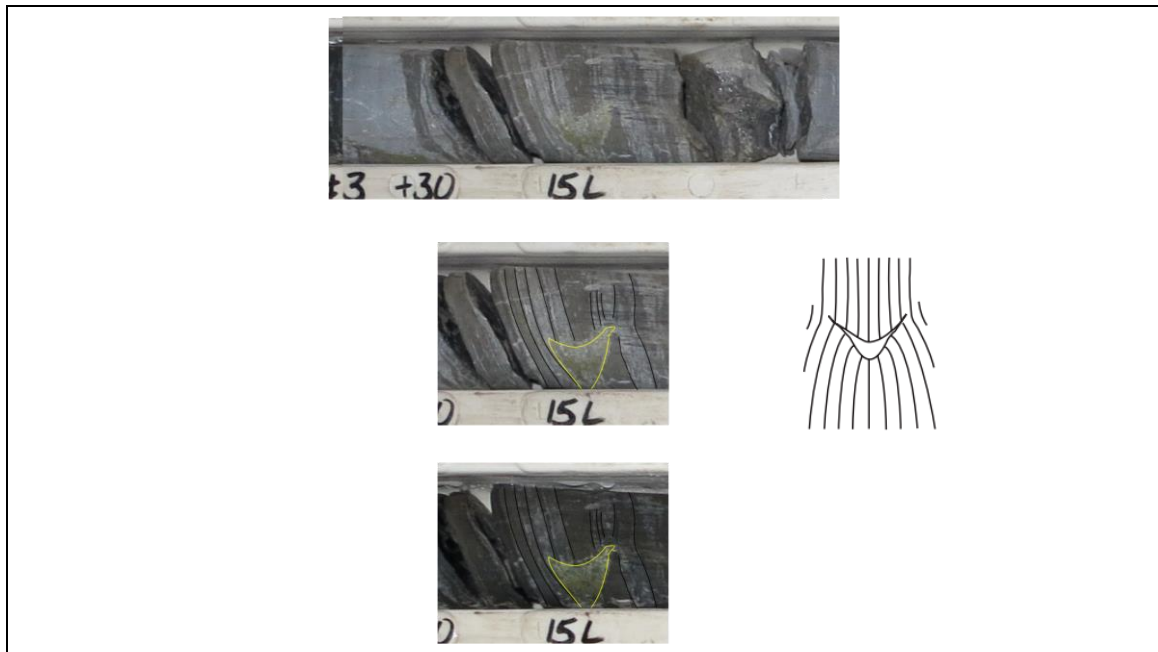
Slide 12
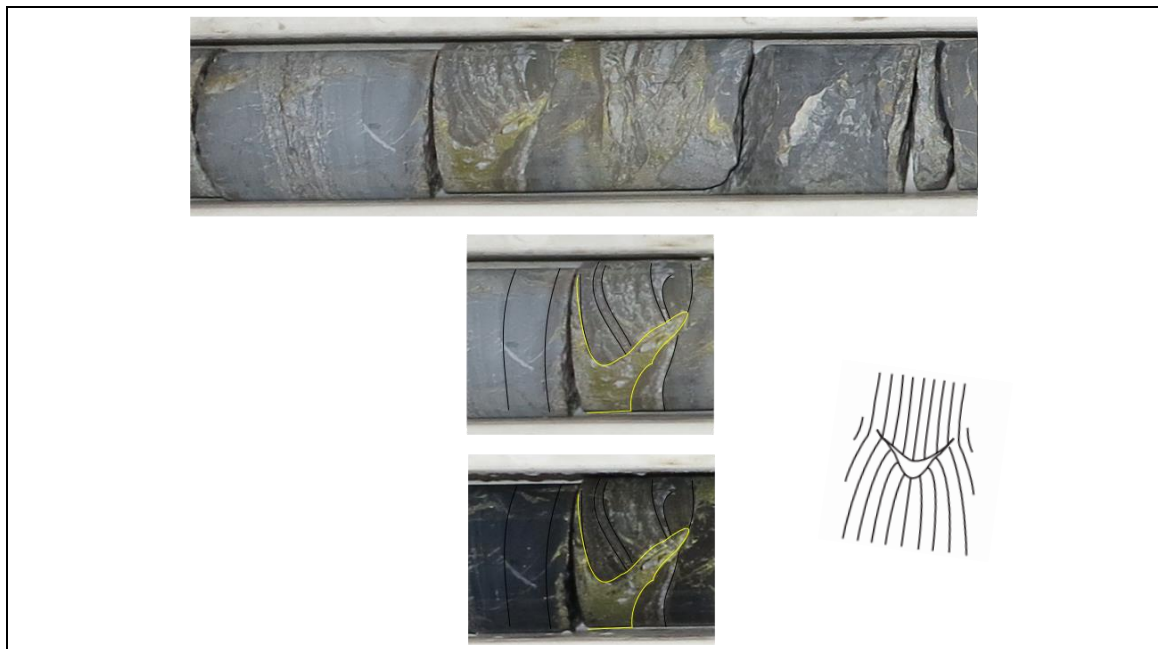
Slide 13
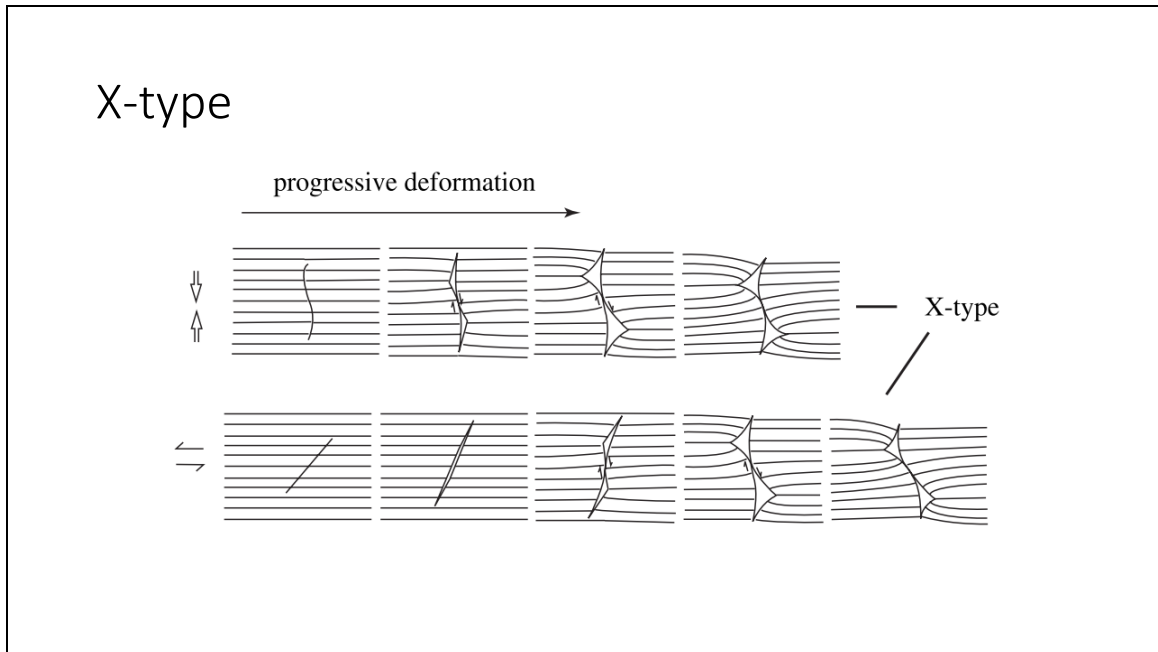
Slide 14
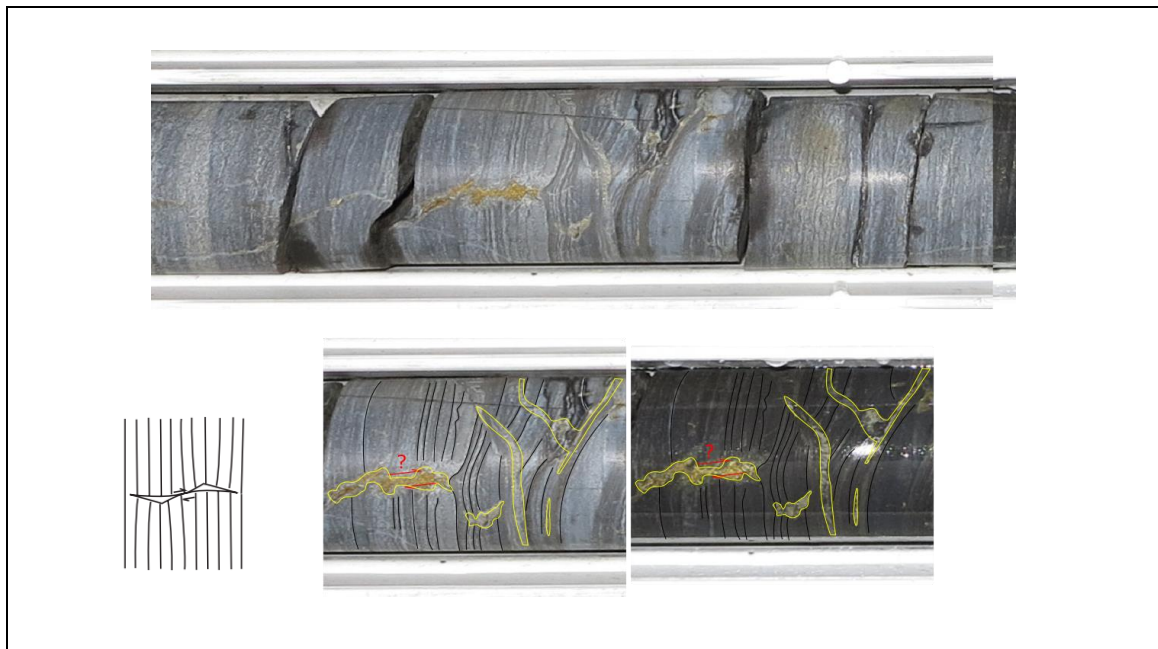
Slide 15
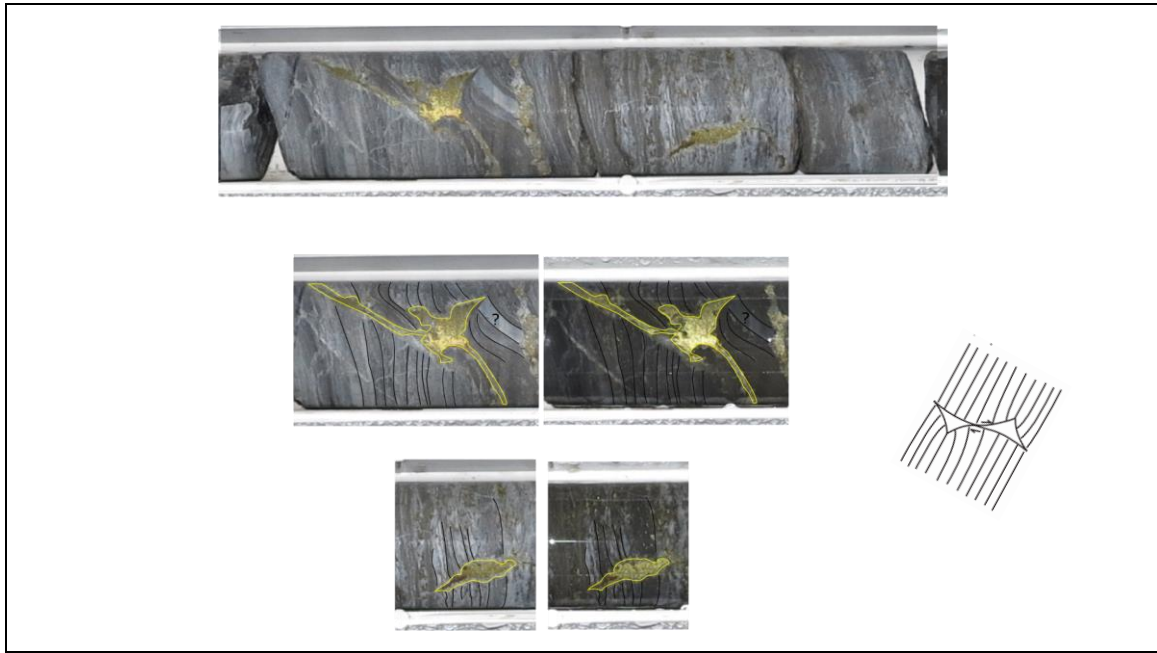
Slide 16

Slide 17

Slide 18

Slide 19

Not yet observed at Mount Isa

Slide 20

Rosebery Mine

- A current example of foliation boudinage control on mineralisation

Aerden (1991) JSG

Slide 21

Rosebery Mine

MAP

CROSS-SECTION

Aerden – J. Metamorphic Geol. 1994 FIGURE 2
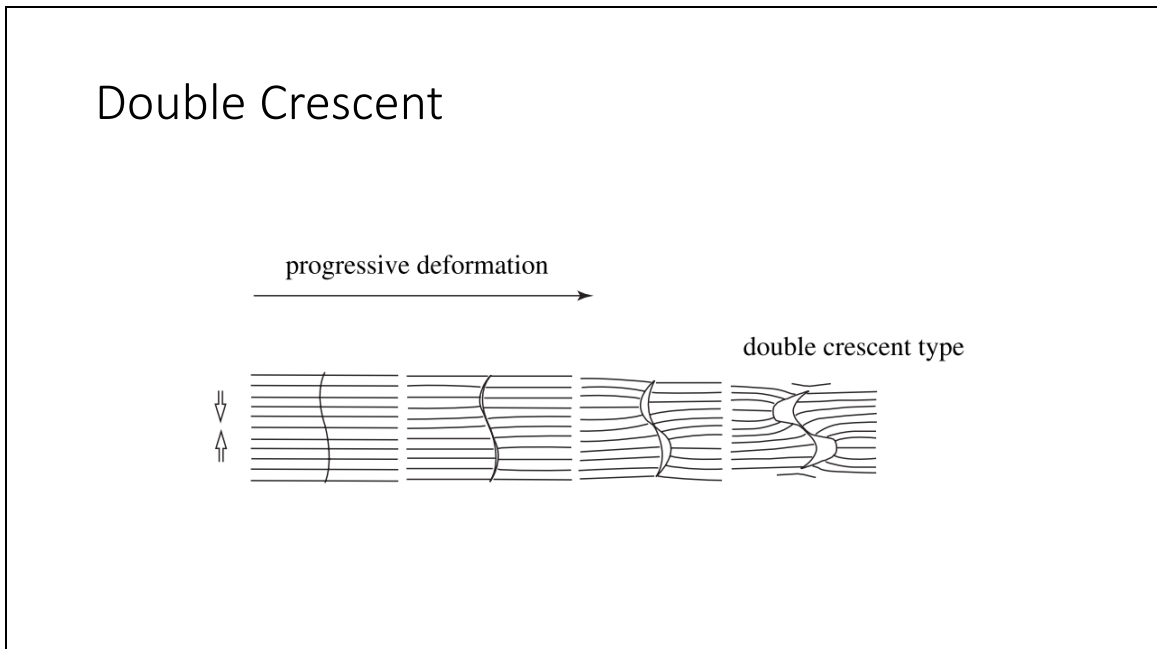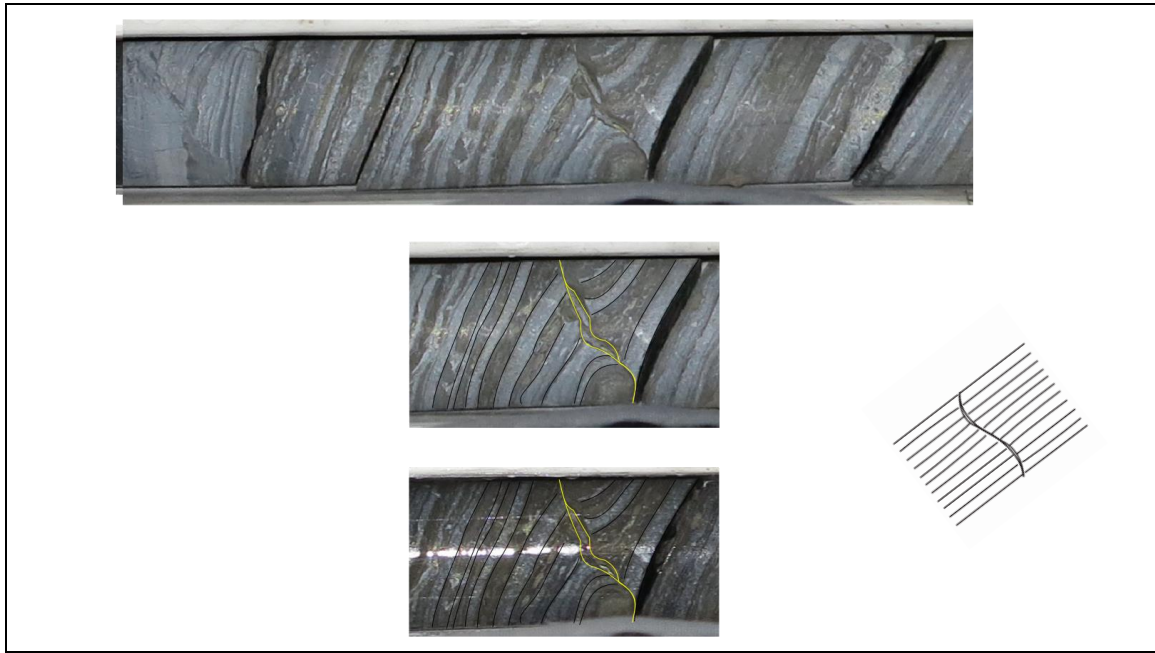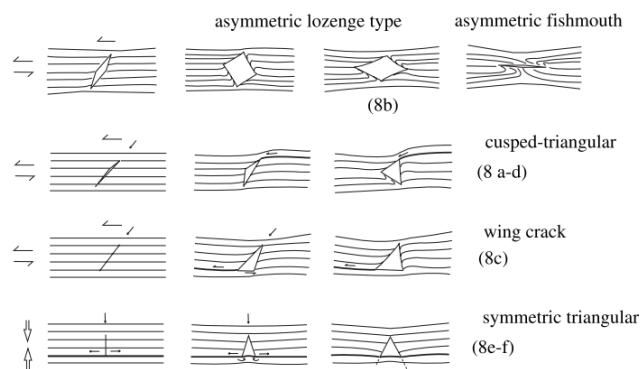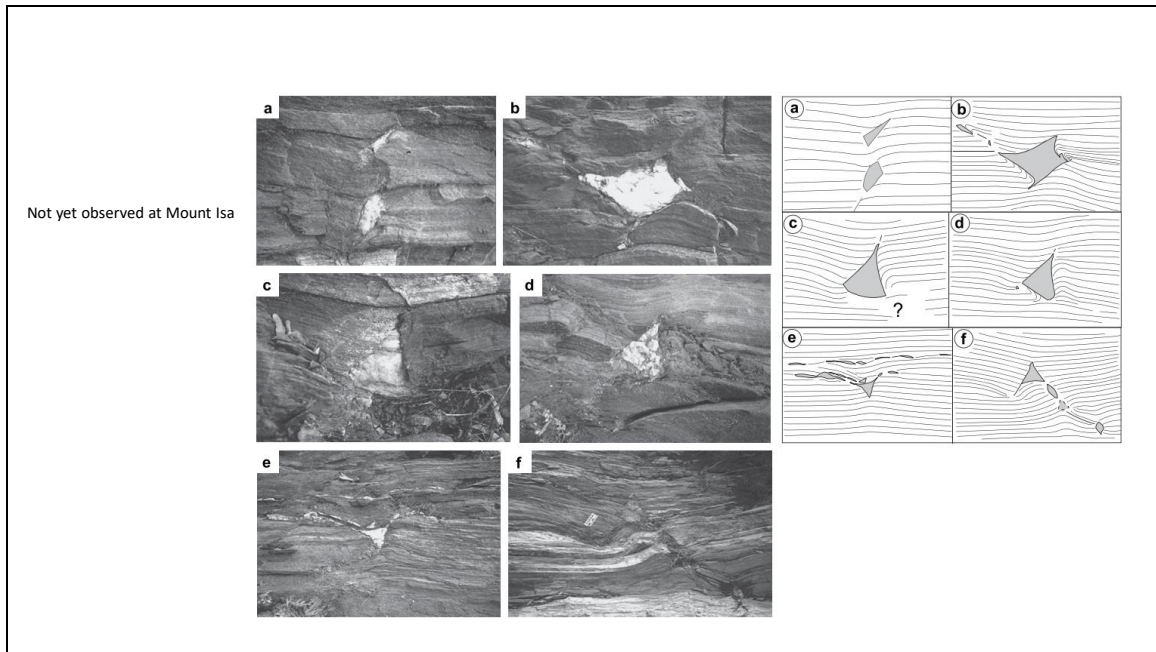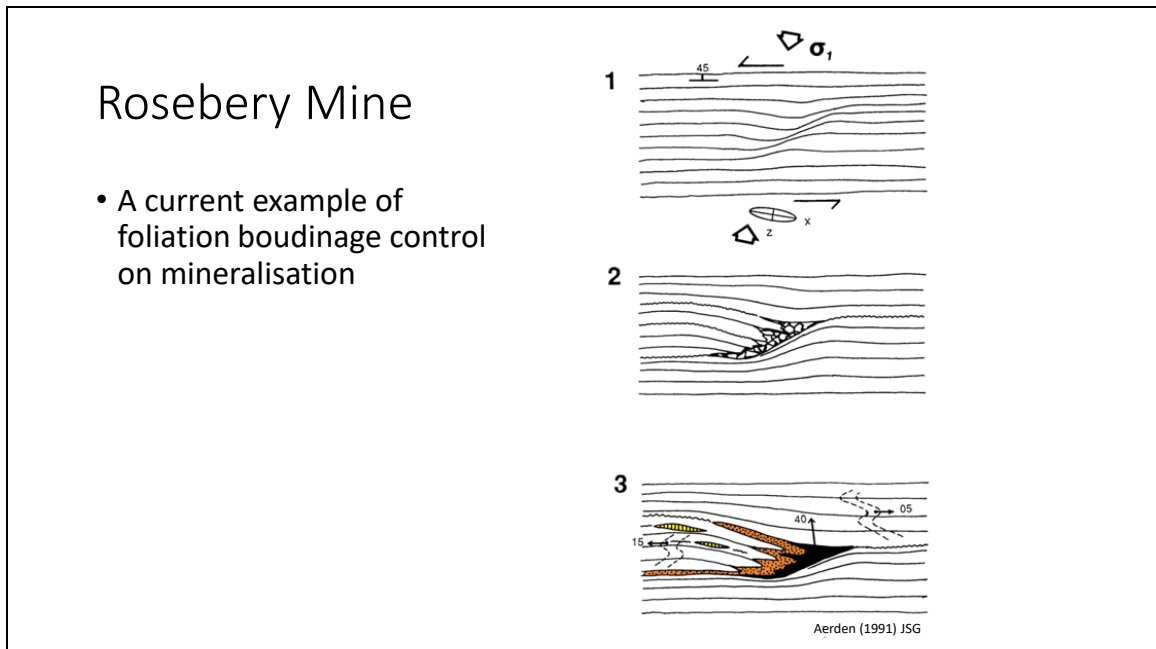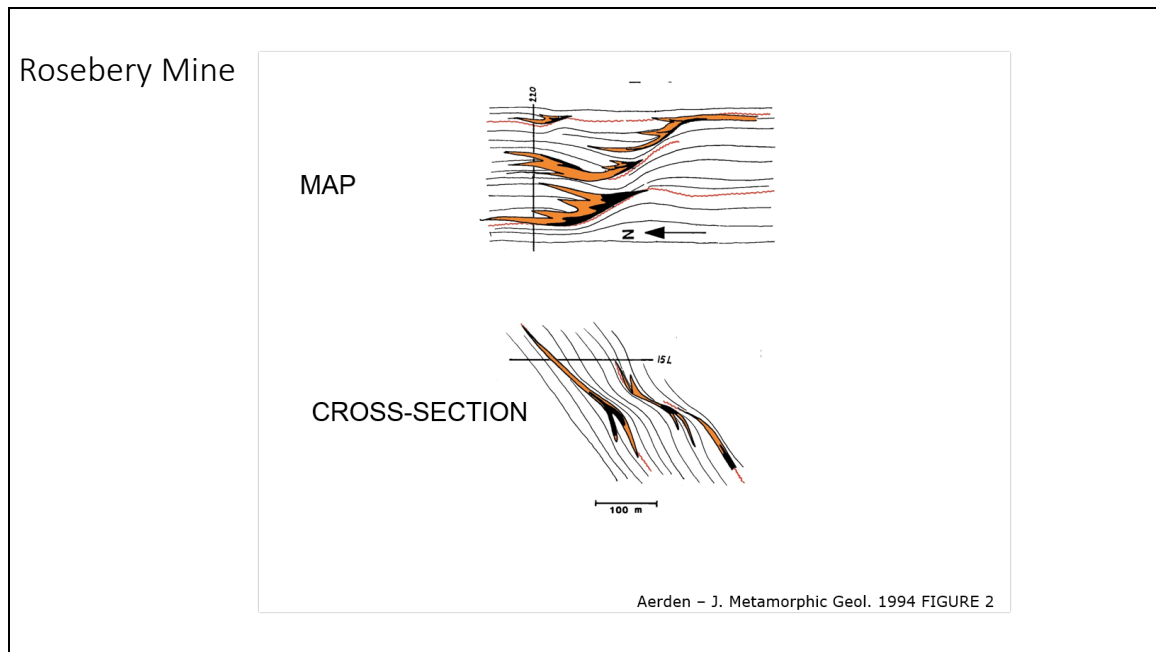
Slide 22

Current observations at MIM
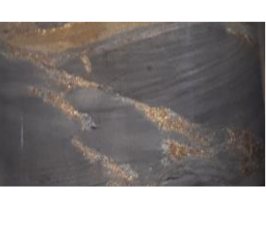
- Potential increase in foliation boudinage structures near the 2% Cu shell
  - Could be used as a targeting/localisation method for high grade Cu ore bodies
- Classification scheme for mineralisation
- Foliation boudinage occurring on all scales at Mount Isa:
  - Core scale
  - Micro scale
  - Mine scale

Slide 23

Classification Scheme

- Foliation Boudinage
- S_0 Parallel
- Extension veins at high angles to S_0
- Oblique to S_0
- Breccia hosted
- Fold hinge
- Boudin necks

Slide 24

Foliation Boudinage	S_0 Parallel	Extension veins at high angle to S_0	Oblique to S_0
Breccia Hosted	Fold Hinge	Boudin Necks	Others?????

Slide 25

Core scale foliation boudinage at MIM

Slide 26

Slide 27
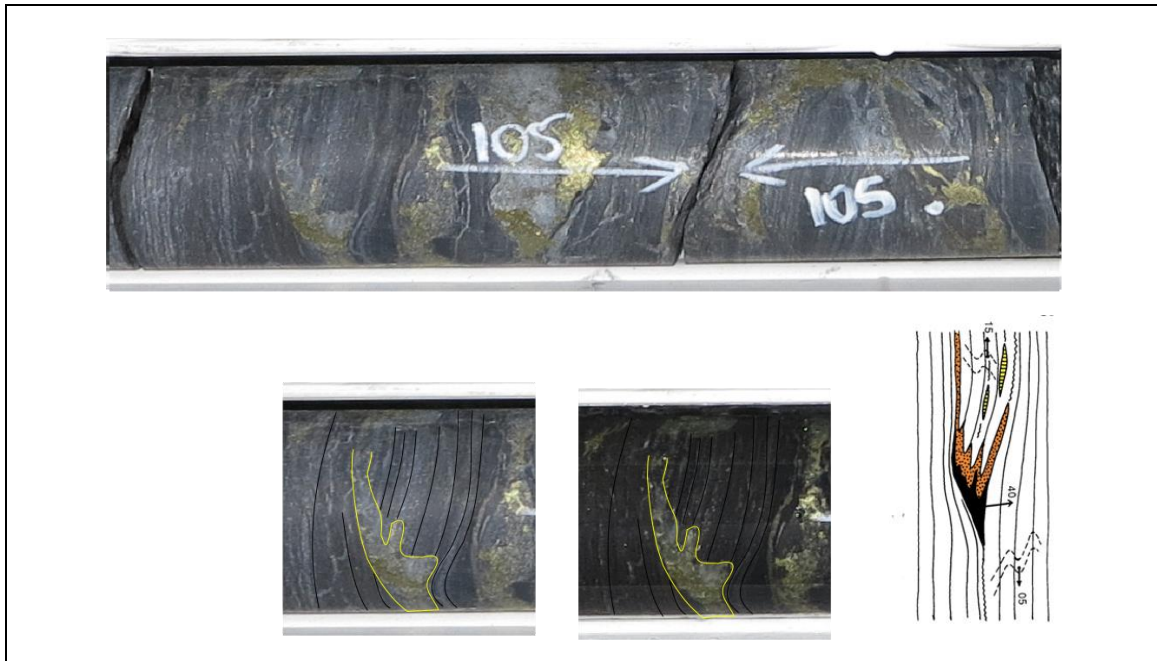
Slide 28

Slide 29

Slide 30
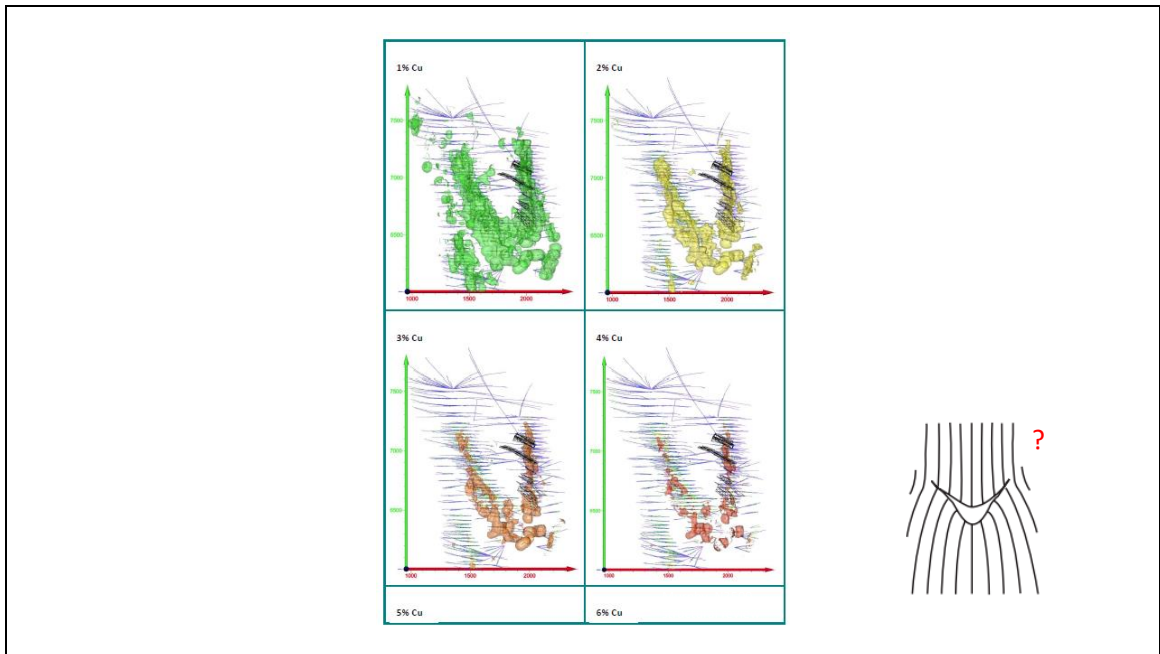
Slide 31
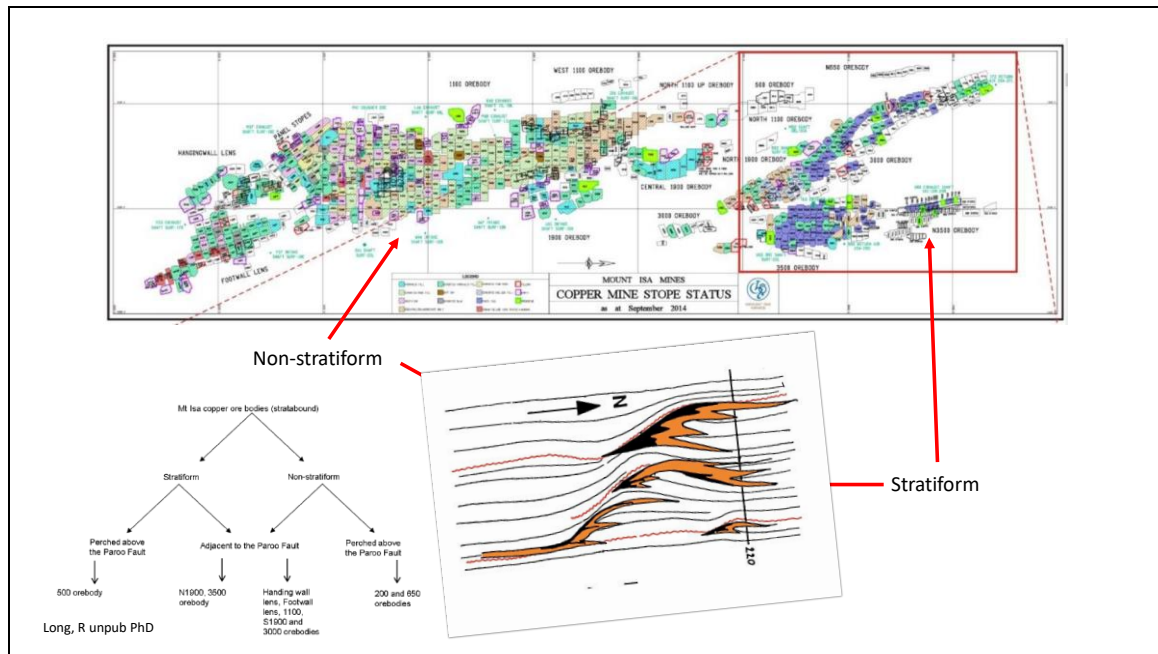
Slide 32

Slide 33

Slide 34
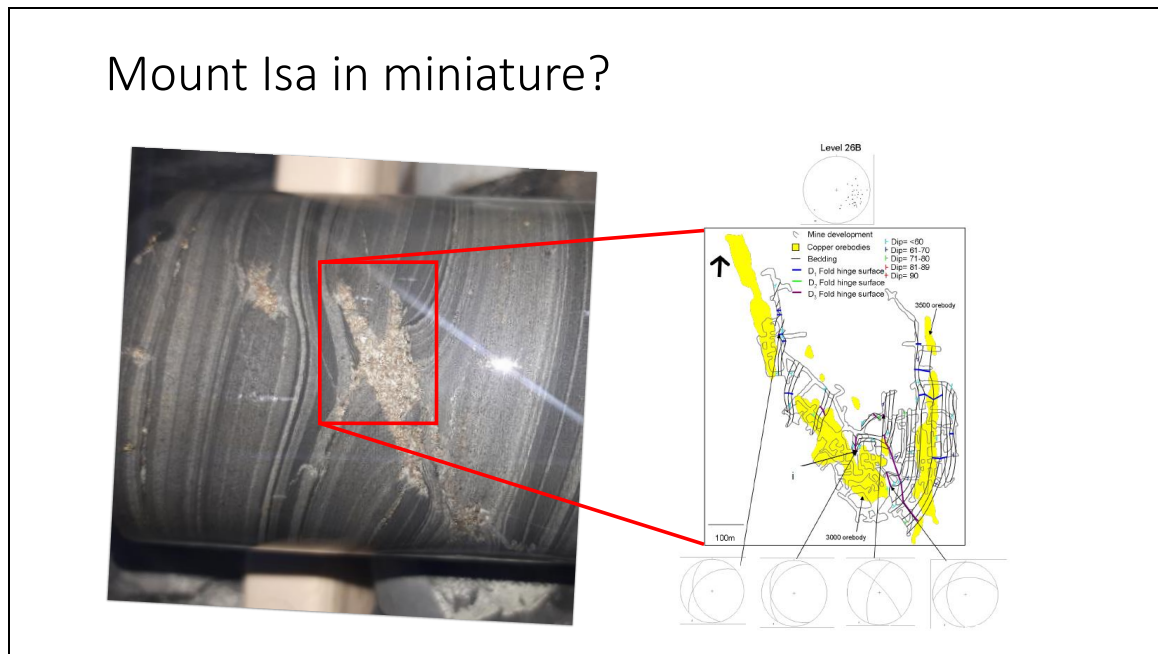
Slide 35

Foliation Boudinage nearby

Slide 36

More core examples

Slide 37

Slide 38

Slide 39

Slide 40

Slide 41

Slide 42

Slide 43

Slide 44

Slide 45

Slide 46

Slide 47

Acknowledgments

- Tom Blenkinsop – Supervisor
- Richard Lilly – Second Supervisor
- Michael Thompson – Identifying the scope for the project
- Dan Taylor – Getting the project going
- Pat Ila'Ava – Current help along the way
- National Earth Research Council – Funding
- MICO – Part funding

APPENDIX C

Foliation Boudinage Structures in the Mount Isa Cu System: Additional Material

Appendix C.1: Table of sampled drillhole coordinates, lengths, and collar orientations (negative plunges are below the horizontal).

Hole ID	East (m)	North (m)	RL (m)	Drillhole Length (m)	Collar Azimuth (°)	Collar Plunge (°)
201601132	1979.193	3465.884	2581.735	226.5	258	28
201602082	1957.491	3642.716	2574.835	122.8	90	25
201902142	2021.51	3854.92	2618.915	130	270	0
201903082	2047.047	3880.225	2649.895	519.8	85	2
201904022	2046.866	3880.292	2649.783	582.2	85	-18
201903122	1449.908	5742.455	2954.588	177.8	90	-46
201903112	1610.99	5817.437	2730.234	350	295	-36
201902182	2101.624	6583.68	2302.093	230	90	-65
201903052	2102.379	6583.731	2303.612	200	90	-10
201903092	2102.056	6583.736	2304.594	200	90	10
201902012	2118.286	6644.328	2304.735	200	90	-15
201605182	1986.02	6975.82	2045.8	132.8	90	0
201904012	1917.201	7334.105	1947.732	283	49	-65
T190ED1	1530	3214	3425	1050	87	-85
T667ED1	1580	7980	3470.9	1205.1	87	-75

Appendix C.2: Table of logged drillhole lithologies, foliation boudinage structure (FBS) occurrences and ore-grade Cu (>3% Cu).

Lithology	Total Length Logged (m)	Number of FBS	FBS as % of Total	Total Length >3% Cu (m)	Normalised Value >3% Cu (%)
Shale	1776.6	184	72%	3.7	0.2%
Pyritic Shale (5-20%)	515.4	41	16%	7.6	1.5%
Pyritic Shale (>20%)	110.4	0	0%	0	0.0%
Recrystallised Shale	210.4	12	5%	5.8	2.8%
Irregularly Brecciated Recrystallised Shale	458.7	2	1%	6.8	1.5%
Siliceous Shale	203.1	10	4%	4.9	2.4%
Brecciated and Fractured Siliceous Shale	164.9	6	2%	18.9	11.5%
Carbonaceous Mylonite	13.9	0	0%	0	0.0%
Buck Quartz	42.8	0	0%	0	0.0%
Greenschist	198.5	0	0%	0	0.0%
Total	3694.7	255	100%	47.7	

Appendix C.3: Stereographic projections showing all foliation boudinage structures with bedding measurements from the oriented RD drill core T667ED1.
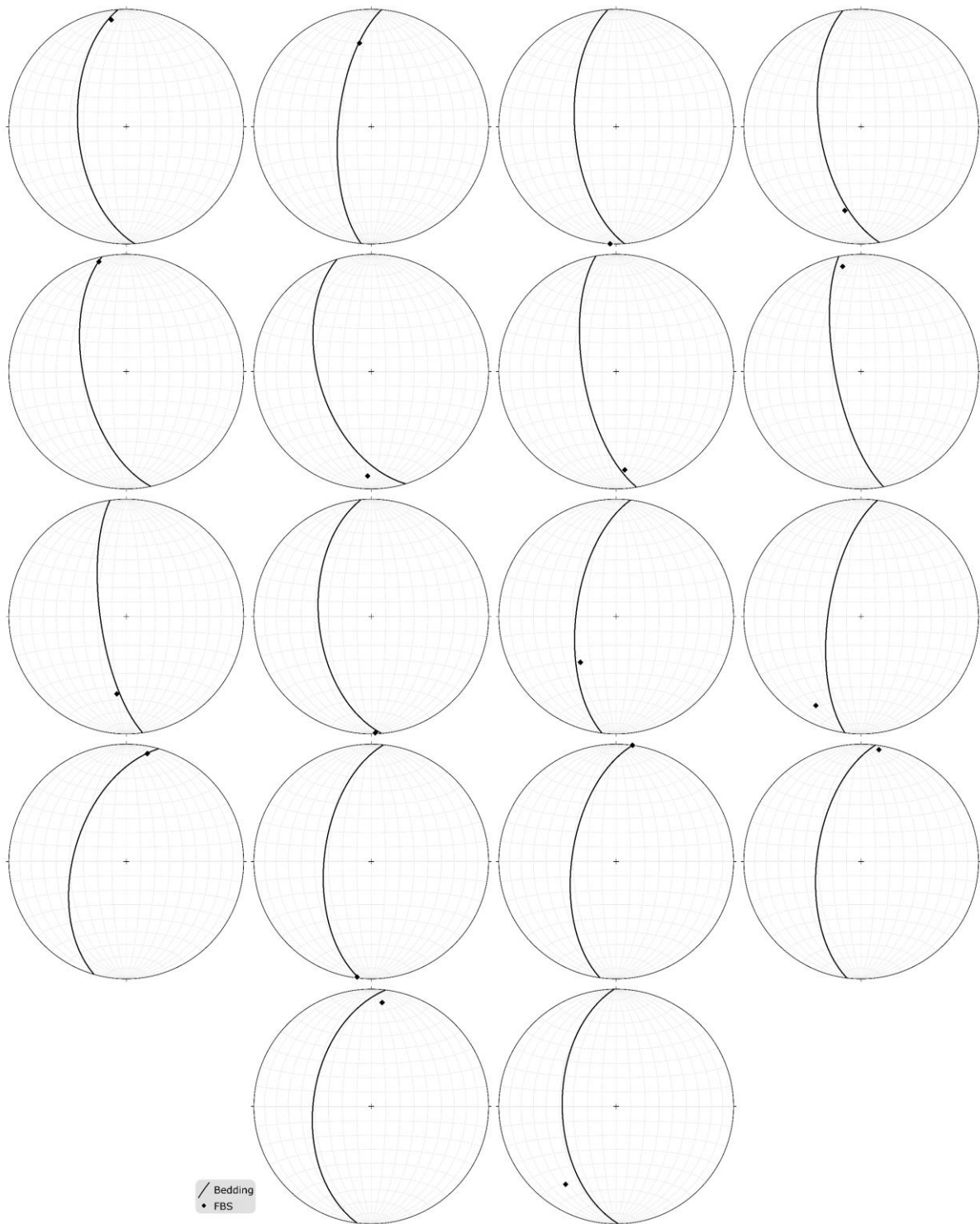
Appendix C.4: Downhole plots of Cu % for all drillholes analysed in this study.
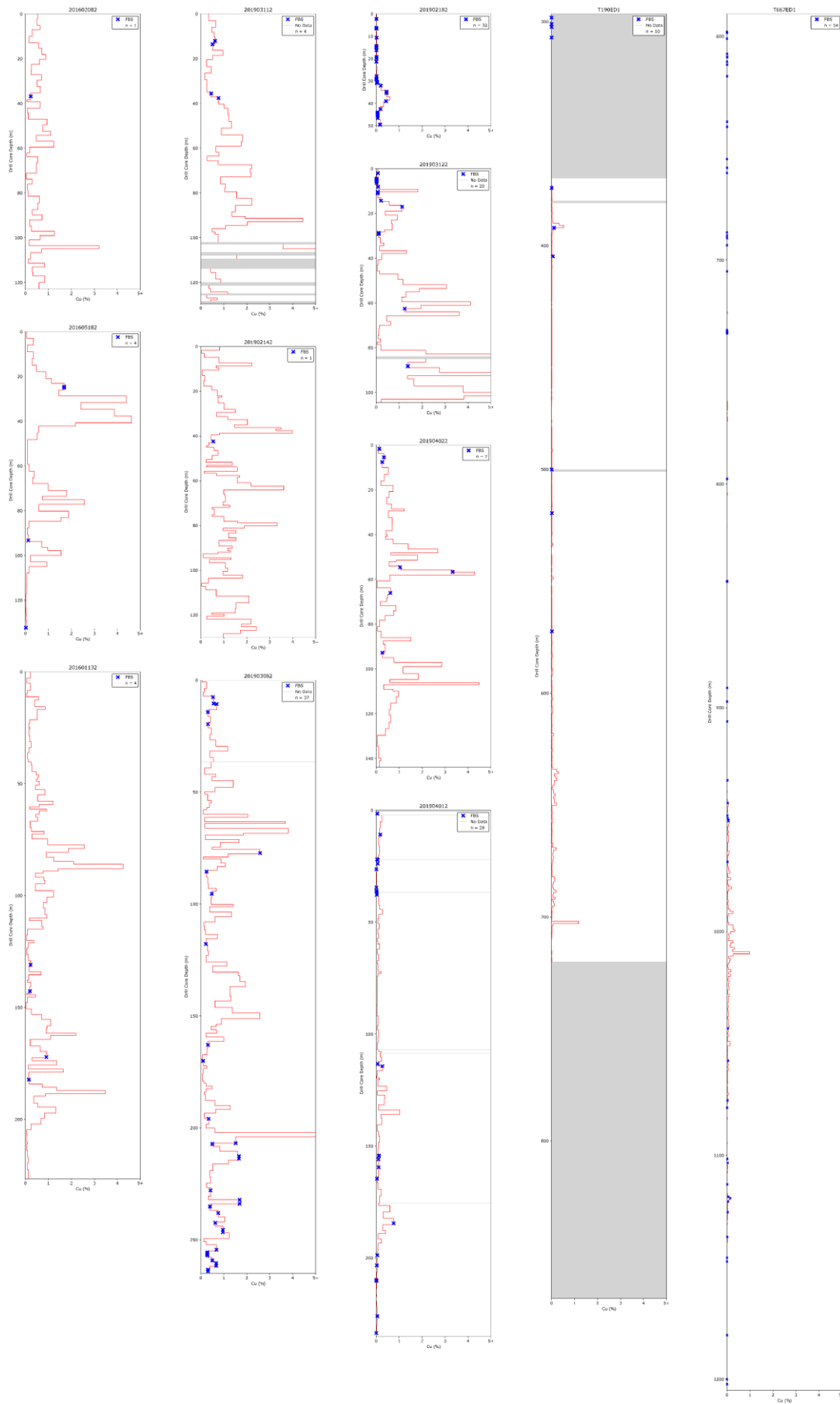
APPENDIX D

Sample Descriptions

In this appendix, photographs of hand samples, whole thin section scans, and petrographic descriptions are given for each sampled thin section. Samples are grouped based on the main geological structures present.

Foliation Boudinage Structure Samples

SAMPLE NUMBER: B,C,D,E,F,G,H,I   **Drillhole (Depth):**   201903092 (32.1m)

FIELD DESCRIPTION: FBS + pinch and swell + boudinage

MOUNT ISA MINE GEOLOGIST MAPPED LITHOLOGY: Shale (Urquhart Shale)

HAND SPECIMEN

Main FBS in sample - Sulphide filled foliation boudinage structure with shale layering bending into structure. Sulphide fill predominantly weakly magnetic pyrrhotite. Also observed on reverse of core. Boudin observed adjacent to the foliation boudinage structure, in a lighter coloured shale layer (dolomitisation?).

Diameter of drill core: ~50 mm
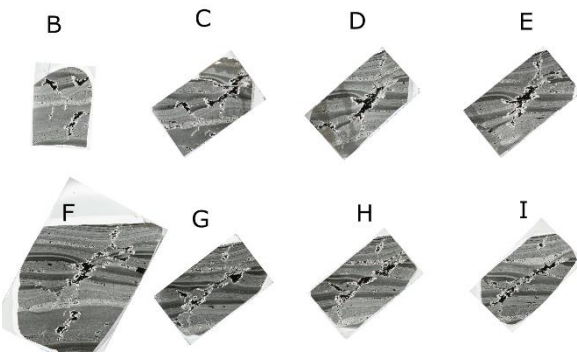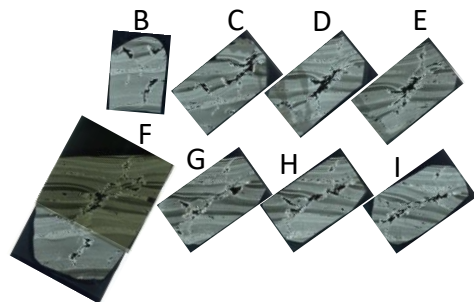
THIN SECTION

PPL

XPL

ORIGINAL ORIENTATION – view looked ~North

View of chip from above (map view)

F/R

NOT F/R

340° Azimuth - FBS lineation direction based on chip I orientation from above

-10°→091°

CLASSIFICATION

Pyrrhotite Mineralised Foliation Boudinage Structure

Rotation of FBS (with 20° azimuth difference between section and drill core)

OR

Orientations of extension and shortening based on conjugate angle

Sample I

Orientation of the bedding would only work in the direction of F/R
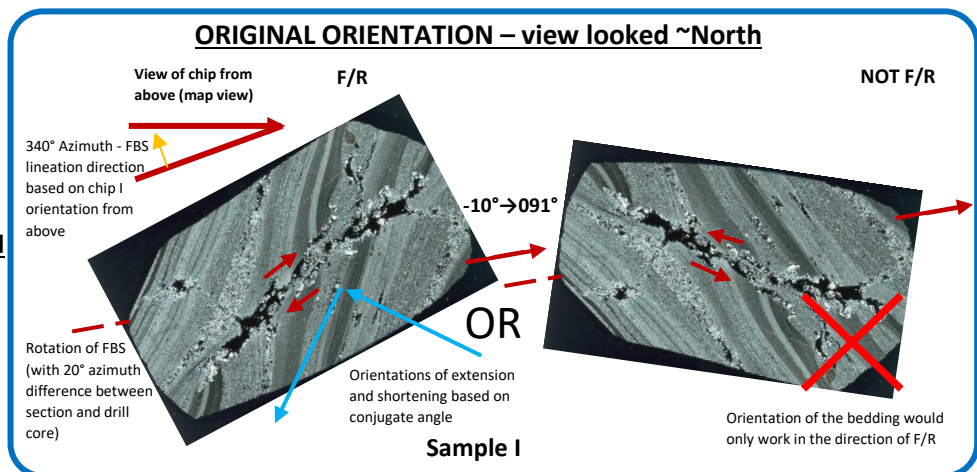
SAMPLE NUMBER: BW207   **Drillhole (Depth):**   T667 ED1 (598m)

FIELD DESCRIPTION: Possible FBS, doesn't look mineralised with sulphides. Measurement taken of orientations:

S0 = 56°->266°   FBS = 09°->352°   FBS Plane = 70°->165°

MIM GEOLOGIST MAPPED LITHOLOGY: 80% Pyritic Shale (5-20% pyrite); 20% Shale (Urquhart Shale)

'Partly moderately fractured weakly brecciated sheeted carbonate veined thin to thick bedded brown pyritic shale and thin to banded graphitic carbonaceous black and grey shales. Weakly disseminated MG pyrite. Vein minerals are carbonate silica chlorite sericite and pyrite.'

HAND SPECIMEN

Small-scale foliation boudinage structure with silica-dolomite infill. Minor bending of shale into the structure, showing characteristic antithetic drag displacement. Sample is half-core and structure is observed on cut face.

Diameter of drill core: 60 mm

THIN SECTION

PPL

XPL

10 mm

10 mm

ORIGINAL ORIENTATION – view looked ~North

NOT F/R   68°→100°   68°→100°   F/R

OR

Orientation of the bedding would only work in the direction of NOT F/R

This sample is oriented (T667ED1) – Bedding 56°->266°

Sample BW207
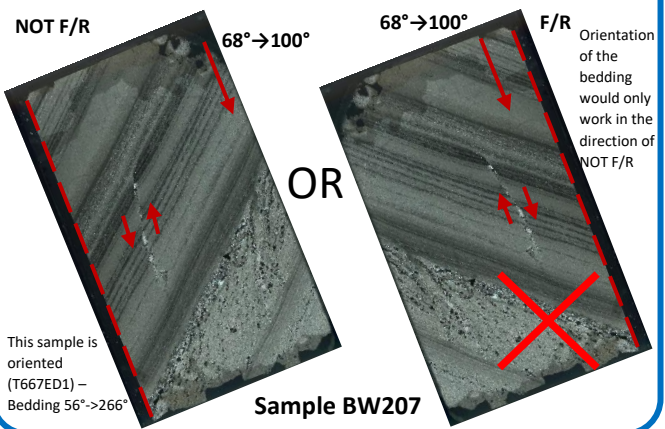
CLASSIFICATION

Unmineralised Foliation Boudinage Structure

SAMPLE NUMBER: BW208   **Drillhole (Depth):**   T667 ED1 (1180.3m)

FIELD DESCRIPTION: Possible unmineralised FBS – unoriented

MIM GEOLOGIST MAPPED LITHOLOGY: 55% Pyritic Shale (5-20% pyrite); 45% Shale (Urquhart Shale)

'Partly strongly fractured weakly brecciated moderately sheeted and stock-worked carbonate veined thin to thick bedded brown pyritic shale and thin to banded graphitic carbonaceous black and grey shales. Weakly disseminated MG pyrite. Vein minerals are carbonate silica chlorite sericite and pyrite. Locally clayey (about 30cm).'

HAND SPECIMEN

Silica-dolomite filled foliation boudinage structure. Seemingly no sulphides in the structure. Fewer 'obvious' shale layers adjacent to the structure mean the displacement and bending is more difficult to observe. Sample is half-core and structure is observed on cut face.

Diameter of drill core : 60 mm

THIN SECTION

PPL   *XPL*

10 mm   10 mm

ORIGINAL ORIENTATION – view looked ~North

F/R
59°→108°

NOT F/R

Orientation of the bedding would only work in the direction of NOT F/R

59°→108°

OR

This sample is close to an oriented measurement (4 metres away in T667ED1) – Bedding 51°->286°

Sample BW208
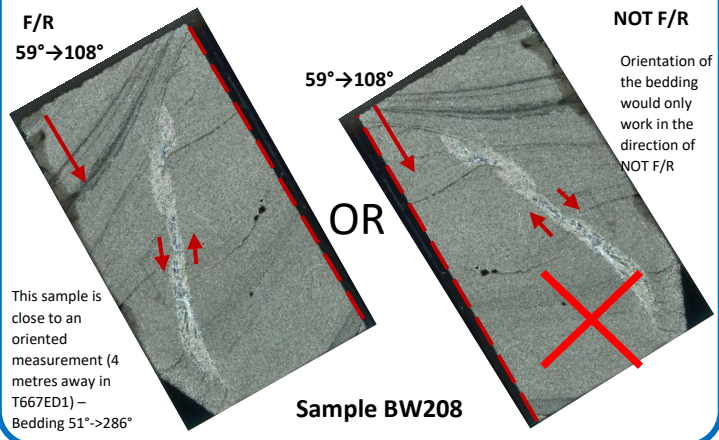
CLASSIFICATION

Unmineralised Foliation Boudinage Structure

SAMPLE NUMBER: BW302   **Drillhole (Depth):**   201903092 (8.0m)

FIELD DESCRIPTION: FBS; FBS prevalent throughout 7-8.7m. Measurement taken of orientation
(unoriented):

S0 = 68°->255°   FBS = 40°->328°   FBS Plane = 26°->201°

MIM GEOLOGIST MAPPED LITHOLOGY: Shale (Urquhart Shale)

HAND SPECIMEN

Mostly pyrrhotite filled foliation boudinage structure with silica-dolomite rim. Structure looks more symmetrical compared to most of the others. Shale layers, including fine-grained pyrite, bend into structure. Observed on reverse side of core. Sample contains many foliation boudin-like structures.

Diameter of drill core: ~50 mm

THIN SECTION

Perpendicular to BW601.

PPL
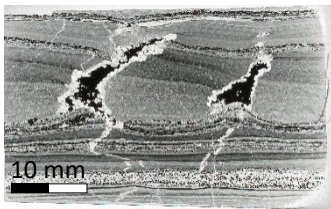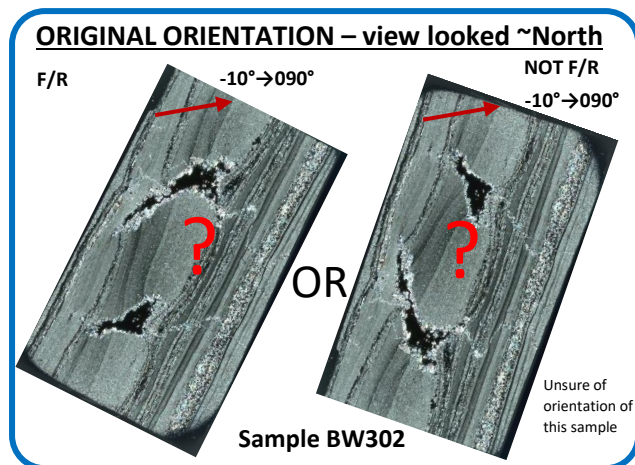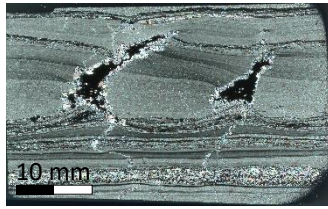
10 mm

XPL

10 mm

ORIGINAL ORIENTATION – view looked ~North

F/R   -10°→090°

NOT F/R
-10°→090°

?   OR   ?

Sample BW302

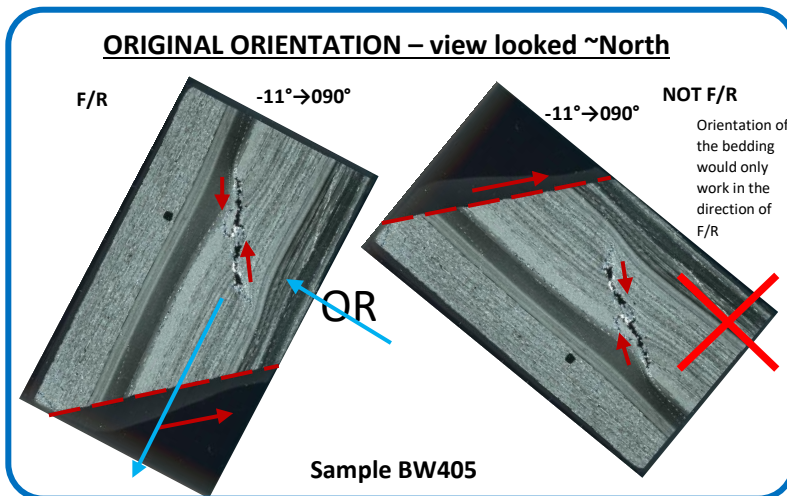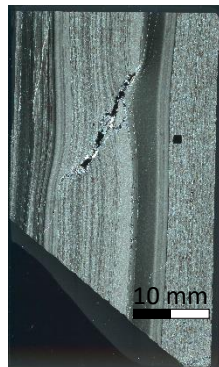Unsure of orientation of this sample

CLASSIFICATION

Pyrrhotite Mineralised Foliation Boudinage Structure

SAMPLE NUMBER: BW303   **Drillhole (Depth):**   201904012 (159.3m)

FIELD DESCRIPTION: FBS, pyrrhotite (+chalcopyrite)

MIM GEOLOGIST MAPPED LITHOLOGY: Shale (Urquhart Shale)

HAND SPECIMEN

Mostly pyrrhotite and chalcopyrite filled foliation boudinage structure. Sample has a higher proportion of chalcopyrite compared to other structures. Sample has broken along a plane of weakness (dark clay-rich shale layer) adjacent to the structure. Bending of shale into structure meets fracture wall at ~90°.

Diameter of drill core: ~50 mm

THIN SECTION

Perpendicular to BW602 and BW603.

PPL

XPL
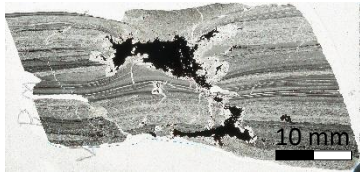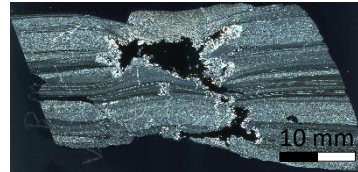
ORIGINAL ORIENTATION – view looked ~North

F/R   59°→056°   Not F/R 59°→056°

OR

Sample BW303

Orientation of the chip would only work in the direction of F/R

A-Dip

CLASSIFICATION

Pyrrhotite and Chalcopyrite Mineralised Foliation Boudinage Structure

SAMPLE NUMBER: BW309   **Drillhole (Depth):**   201903052 (30.3m)

FIELD DESCRIPTION: FBS

MIM GEOLOGIST MAPPED LITHOLOGY: Shale (Urquhart Shale)

HAND SPECIMEN

No image

Diameter of drill core: ~50 mm
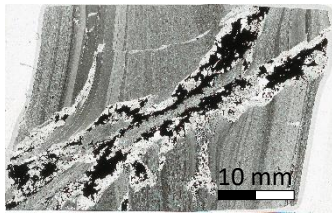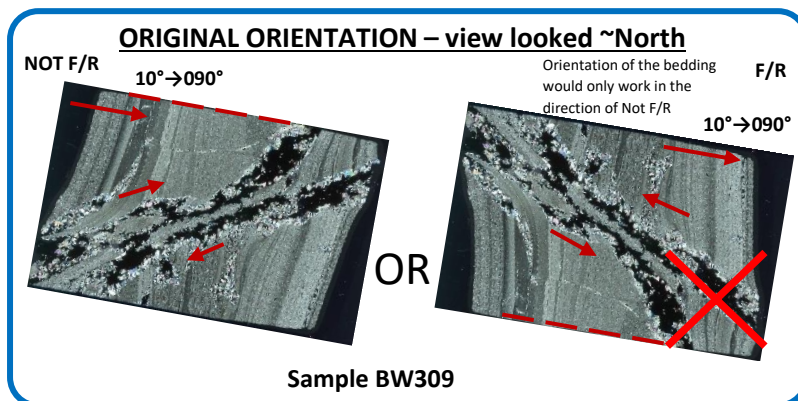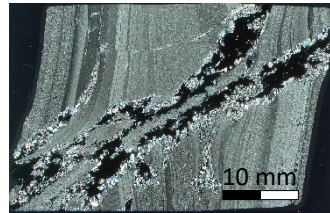
THIN SECTION

PPL   *XPL*

ORIGINAL ORIENTATION – view looked ~North

NOT F/R   F/R

$10°\rightarrow090°$ Orientation of the bedding would only work in the direction of Not F/R

$10°\rightarrow090°$

OR

Sample BW309

CLASSIFICATION

Pyrrhotite Mineralised Foliation Boudinage Structure

SAMPLE NUMBER:　　　　BW310　　　　　　　**Drillhole (Depth):**　　　201602082 (37.3m)

FIELD DESCRIPTION:　　　Possible non opening FBS

MIM GEOLOGIST MAPPED LITHOLOGY:　　　Pyritic Shale (5-20% pyrite)

HAND SPECIMEN

Shear displacement of fine-grained pyrite and shale layers. Appears to resemble a non-void opening foliation boudinage structure. Little to no mineral infill.

Diameter of drill core: ~36 mm

THIN SECTION
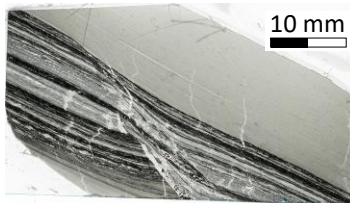
PPL　　　　　　　　　　*XPL*

CLASSIFICATION

Non-Opening Asymmetrical Foliation Boudinage Structure

SAMPLE NUMBER: BW403 **Drillhole (Depth):** 201903092 (32.1m)

FIELD DESCRIPTION: FBS + pinch and swell + boudinage

MIM GEOLOGIST MAPPED LITHOLOGY: Shale (Urquhart Shale)

HAND SPECIMEN

Top of sample - small-scale foliation boudinage structures with mainly pyrrhotite mineralisation and minor bending of shale layers. Coarse-grained pyrite grains observed.

Diameter of drill core ~50 mm
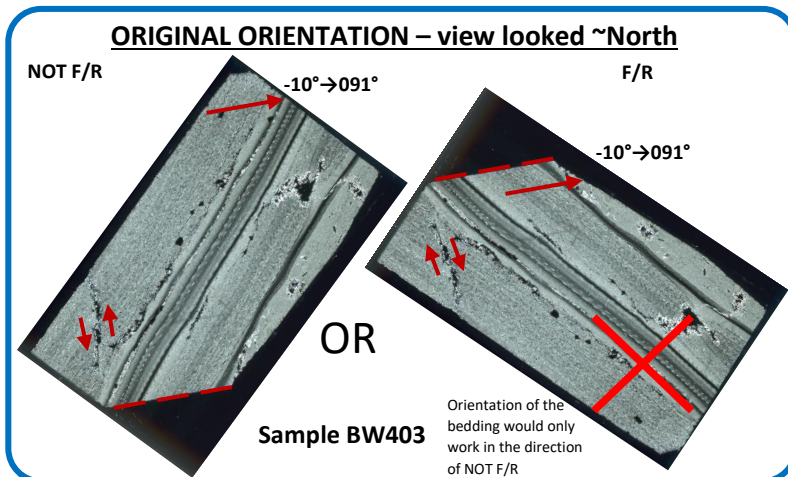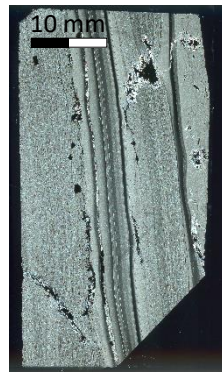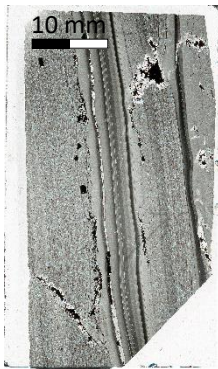
THIN SECTION

PPL

XPL

ORIGINAL ORIENTATION – view looked ~North

NOT F/R

-10°→091°

F/R

-10°→091°

OR

Sample BW403

Orientation of the bedding would only work in the direction of NOT F/R

CLASSIFICATION

Pyrrhotite Mineralised Foliation Boudinage Structure

SAMPLE NUMBER: BW405   **Drillhole (Depth):**   201903092 (15.45m)

FIELD DESCRIPTION: FBS (pyrrhotite). Measurements taken of orientation (unoriented):

S0 = 69°->254°   FBS = 45°->315°

MIM GEOLOGIST MAPPED LITHOLOGY: Shale (Urquhart Shale)

HAND SPECIMEN

Pyrrhotite filled foliation boudinage structures. Top FBS has less fill than other structures, with coarse-grained pyrite proximal to the structure. Other FBS seen throughout core sample. FBS at bottom of image shows significant initial silica-dolomite infill, with later sulphides.

Diameter of drill core: ~50 mm

THIN SECTION

PPL   *XPL*

ORIGINAL ORIENTATION – view looked ~North

F/R   -11°→090°   -11°→090°   NOT F/R

Orientation of the bedding would only work in the direction of F/R

OR

Sample BW405

CLASSIFICATION

Pyrrhotite Mineralised Foliation Boudinage Structure

SAMPLE NUMBER: BW406A   **Drillhole (Depth):**   201903092 (2.35m)

FIELD DESCRIPTION: FBS (pyrrhotite); zone of FBS from 1.4-2.7m; with zone of high angle veins too; Coarse pyrite in S0 parallel veins; Pyrrhotite in oblique veins and FBS; 2-2.5m strong planar anisotropy (S0) allowing zone of FBS to form. Measurement taken of orientation (unoriented):

S0 = 75°->253°   FBS Plane = 83°->197°   OR   27°->292°

(Measurements of FBS Plane probably not correct owing to beta measurement to side of FBS, not the ellipse of the plane)

MIM GEOLOGIST MAPPED LITHOLOGY: Shale (Urquhart Shale)

HAND SPECIMEN

Pyrrhotite foliation boudinage structure with silica-dolomite rim, with minor bending of shale layering into structure. Coarse-grained pyrite occurring throughout sample. Small veinlets (quartz/dolomite?) across sample.

Diameter of drill core: ~50 mm

THIN SECTION

Perpendicular to BW406B

PPL   *XPL*
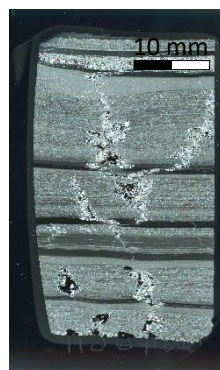
ORIGINAL ORIENTATION – view looked ~West

F/R
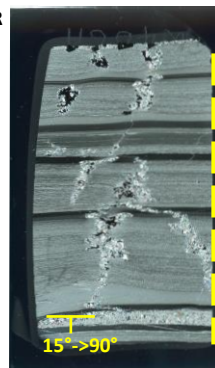
Viewed looking West and down 75° (out of plane of BW406B)

15°->90°   **Sample BW406A**

CLASSIFICATION

Pyrrhotite Mineralised Foliation Boudinage Structure

SAMPLE NUMBER: BW406B   **Drillhole (Depth):**   201903092 (2.35m)

FIELD DESCRIPTION: FBS (pyrrhotite); zone of FBS from 1.4-2.7m; with zone of high angle veins too; Coarse pyrite in S0 parallel veins; Pyrrhotite in oblique veins and FBS; 2-2.5m strong planar anisotropy (S0) allowing zone of FBS to form. Measurement taken of orientation (unoriented):

S0 = 75°->253°   FBS Plane = 83°->197°   OR   27°->292°

(Measurements of FBS Plane probably not correct owing to beta measurement to side of FBS, not the ellipse of the plane)

MIM GEOLOGIST MAPPED LITHOLOGY: Shale (Urquhart Shale)

HAND SPECIMEN

Pyrrhotite foliation boudinage structure with silica-dolomite rim, with minor bending of shale layering into structure. Coarse-grained pyrite occurring throughout sample. Small veinlets (quartz/dolomite?) across sample.
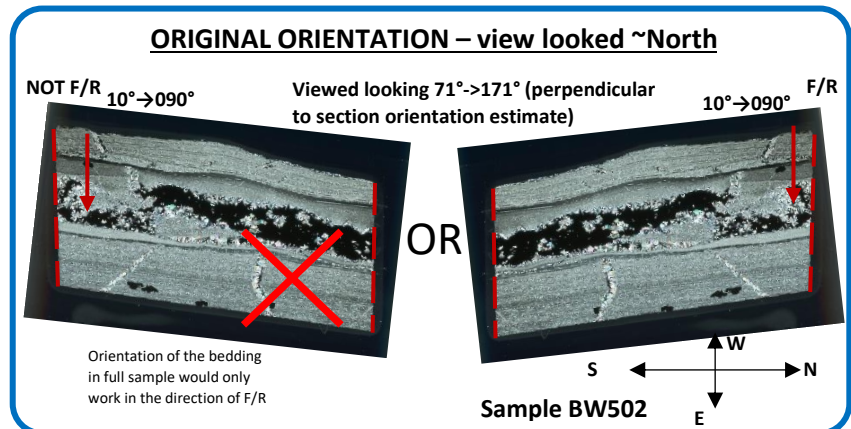
Diameter of drill core: ~50 mm

THIN SECTION

Perpendicular to BW406A.

PPL   *XPL*
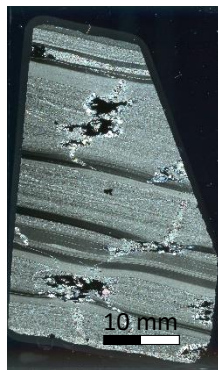
CLASSIFICATION

Pyrrhotite Mineralised Foliation Boudinage Structure

ORIGINAL ORIENTATION – view looked ~North

NOT F/R   15°   -10°→090°   -10°→090°   F/R

OR

Orientation of the bedding would only work in the direction of NOT F/R

Sample BW406B
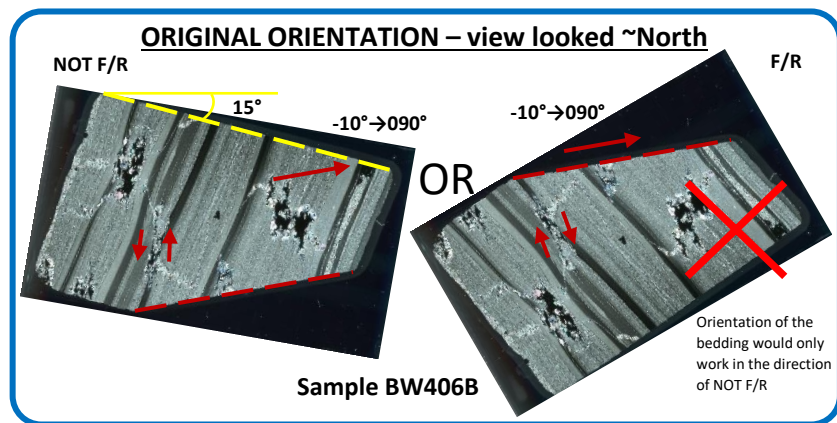
SAMPLE NUMBER: BW501 **Drillhole (Depth):** T667 ED1 (1202.2m)

FIELD DESCRIPTION: FBS (unoriented)

MIM GEOLOGIST MAPPED LITHOLOGY: 95% Shale (Urquhart Shale); 5% Pyrite (5-20% pyrite)

'Variably sheared zone. Partly strongly sheared moderately brecciated sheeted stock work carbonate veined (multi-phase cross cutting) laminated to banded graphitic carbonaceous black and grey shales and locally medium bedded brown pyritic shale. Moderately disseminated MG to CG pyrites. Vein minerals are carbonate silica chlorite sericite and pyrite. EOH.'

HAND SPECIMEN

Pyrrhotite filled foliation boudinage structure with silica-dolomite rim, in vein(?) with displacement. Obvious shale layering bending into structure. Coarse-grained pyrite with white mineral (quartz/talc?) pressure shadows. Late veins cut the bending shale layers and coarse-grained pyrite.
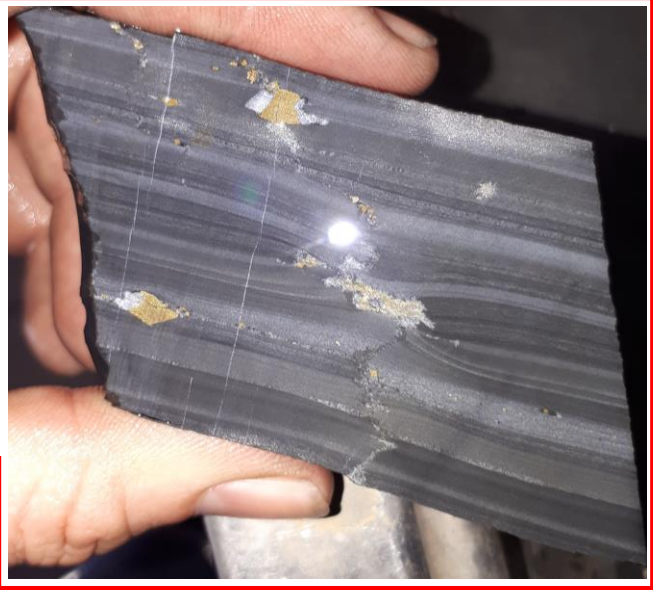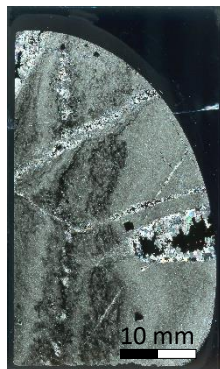
Diameter of drill core: 60 mm

THIN SECTION

Cut face is down-side of core, meaning upside of polished section is up core.

PPL *XPL*
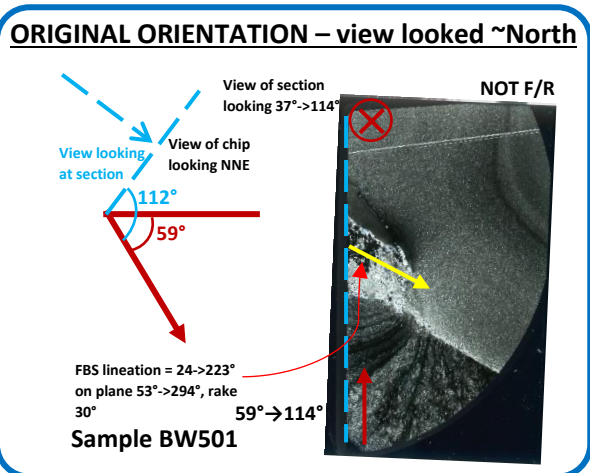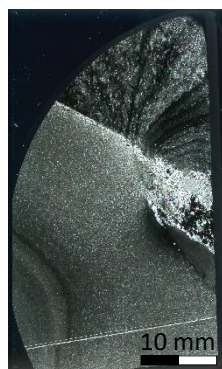
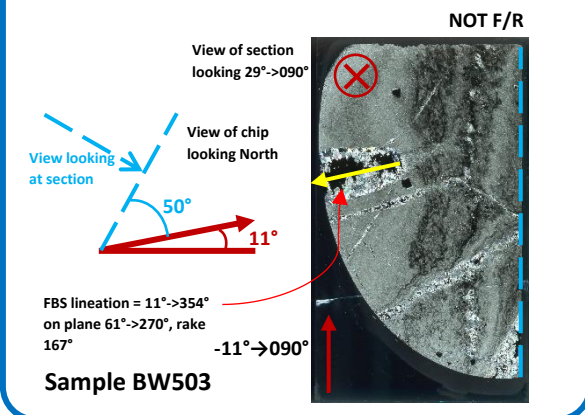**ORIGINAL ORIENTATION – view looked ~North**

View of section looking 37°->114°

NOT F/R

View looking at section

View of chip looking NNE

112°

59°

FBS lineation = 24->223° on plane 53°->294°, rake 30°

59°->114°

Sample BW501

CLASSIFICATION

Pyrrhotite Mineralised Foliation Boudinage Structure

SAMPLE NUMBER: BW502   **Drillhole (Depth):**   201903052 (1.0m)

FIELD DESCRIPTION: FBS progressing into ~oblique vein (possible cleavage?); is FBS using an existing cleavage as a fracture/nucleation plane?

MIM GEOLOGIST MAPPED LITHOLOGY: Shale (Urquhart Shale)

HAND SPECIMEN

Pyrrhotite filled foliation boudinage structures, with silica-dolomite rim. Bending apparent in adjacent shale layers. Silica-dolomite veins cut the sample, with one vein at top of sample potentially exploited by pyrrhotite mineralisation. Coarse-grained pyrite throughout sample. Sample has broken through plane of weakness (possibly as a result of coarse-grained pyrite rich layer. Sample observed on reverse of sample.

Diameter of drill core: ~50 mm

## THIN SECTION

Perpendicular to BW604 and BW605.

PPL   *XPL*
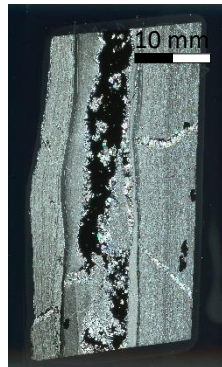
CLASSIFICATION

Pyrrhotite Mineralised Foliation Boudinage Structure

ORIGINAL ORIENTATION – view looked ~North

NOT F/R 10°→090°   Viewed looking 71°->171° (perpendicular to section orientation estimate)   F/R 10°→090°

OR

Orientation of the bedding in full sample would only work in the direction of F/R

Sample BW502

SAMPLE NUMBER: BW503   **Drillhole (Depth):**   201903092 (15.45m)

FIELD DESCRIPTION: FBS (pyrrhotite). Measurements taken of orientation (unoriented):

S0 = 69°->254°   FBS = 45°->315°

MIM GEOLOGIST MAPPED LITHOLOGY: Shale (Urquhart Shale)

HAND SPECIMEN

Pyrrhotite filled foliation boudinage structures. Top FBS has less fill than other structures, with coarse-grained pyrite proximal to the structure. Other FBS seen throughout core sample. FBS at bottom of image shows significant initial silica-dolomite infill, with later sulphides.

Diameter of drill core: ~50 mm

THIN SECTION

Cut face is down-side of core, meaning upside of polished section will be up core.

PPL   *XPL*
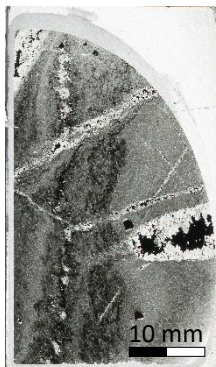
ORIGINAL ORIENTATION – view looked ~North

NOT F/R

View of section looking 29°->090°

View of chip looking North

View looking at section

50°

11°

FBS lineation = 11°->354° on plane 61°->270°, rake 167°

-11°→090°

Sample BW503

CLASSIFICATION

Pyrrhotite Mineralised Foliation Boudinage Structure

SAMPLE NUMBER: BW601   **Drillhole (Depth):** 201903092 (8.0m)

FIELD DESCRIPTION: FBS; FBS prevalent throughout 7-8.7m. Measurement taken of orientation
(unoriented):

S0 = 68°->255°   FBS = 40°->328°   FBS Plane = 26°->201°

MIM GEOLOGIST MAPPED LITHOLOGY: Shale (Urquhart Shale)

HAND SPECIMEN

Mostly pyrrhotite filled foliation boudinage structure with silica-dolomite rim. Structure looks more symmetrical compared to most of the others. Shale layers, including fine-grained pyrite, bend into structure. Observed on reverse side of core. Sample contains many foliation boudin-like structures.

Diameter of drill core: ~50 mm

THIN SECTION

Perpendicular to BW302.

PPL   *XPL*
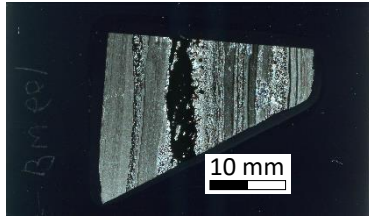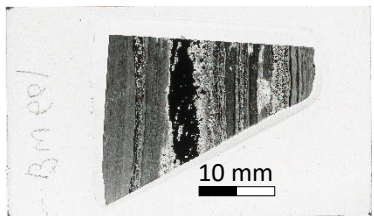
10 mm

10 mm

CLASSIFICATION

Pyrrhotite Mineralised Foliation Boudinage Structure

SAMPLE NUMBER: BW602 **Drillhole (Depth):** 201904012 (159.3m)

FIELD DESCRIPTION: FBS, pyrrhotite (+chalcopyrite)

MIM GEOLOGIST MAPPED LITHOLOGY: Shale (Urquhart Shale)

HAND SPECIMEN

Mostly pyrrhotite and chalcopyrite filled foliation boudinage structure. Sample has a higher proportion of chalcopyrite compared to other structures. Sample has broken along a plane of weakness (dark clay-rich shale layer) adjacent to the structure. Bending of shale into structure meets fracture wall at ~90°.

Diameter of drill core: ~50 mm

THIN SECTION

Perpendicular to BW603 and BW303.

PPL
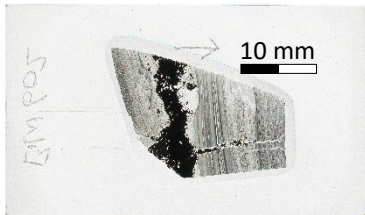
XPL
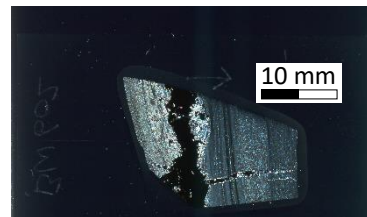
CLASSIFICATION

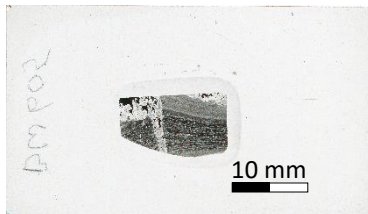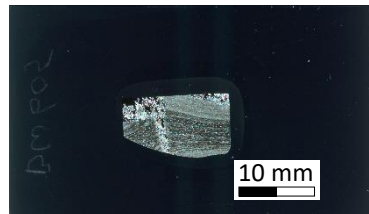*Pyrrhotite Mineralised Foliation Boudinage Structure*

SAMPLE NUMBER: BW603   **Drillhole (Depth):**   201904012 (159.3m)

FIELD DESCRIPTION: FBS, pyrrhotite (+chalcopyrite)

MIM GEOLOGIST MAPPED LITHOLOGY: Shale (Urquhart Shale)

HAND SPECIMEN

Mostly pyrrhotite and chalcopyrite filled foliation boudinage structure. Sample has a higher proportion of chalcopyrite compared to other structures. Sample has broken along a plane of weakness (dark clay-rich shale layer) adjacent to the structure. Bending of shale into structure meets fracture wall at ~90°.

Diameter of drill core: ~50 mm

THIN SECTION

Cut face is up-side of core, meaning polished section is looking uphole. Perpendicular to BW602 and BW303.

PPL
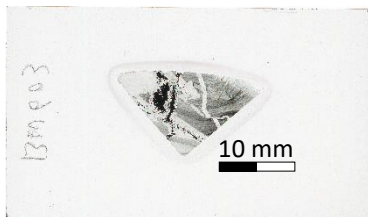
XPL
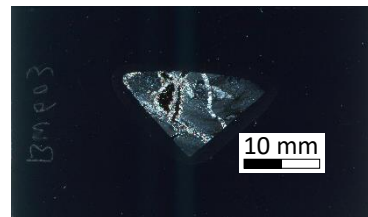
CLASSIFICATION

Pyrrhotite Mineralised Foliation Boudinage Structure

SAMPLE NUMBER: BW604   **Drillhole (Depth):**   201903052 (1.0m)

FIELD DESCRIPTION: FBS progressing into ~oblique vein (possible cleavage?); is FBS using an existing cleavage as a fracture/nucleation plane?

MIM GEOLOGIST MAPPED LITHOLOGY: Shale (Urquhart Shale)

HAND SPECIMEN

Pyrrhotite filled foliation boudinage structures, with silica-dolomite rim. Bending apparent in adjacent shale layers. Silica-dolomite veins cut the sample, with one vein at top of sample potentially exploited by pyrrhotite mineralisation. Coarse-grained pyrite throughout sample. Sample has broken through plane of weakness (possibly as a result of coarse-grained pyrite rich layer. Sample observed on reverse of sample.

Diameter of drill core: ~50 mm

THIN SECTION

Perpendicular to BW605 and BW502.

PPL   *XPL*
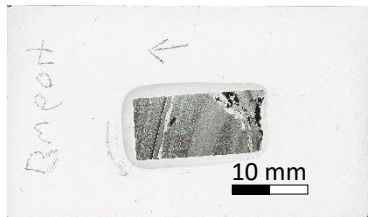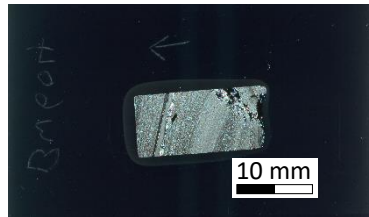
CLASSIFICATION

Pyrrhotite Mineralised Foliation Boudinage Structure

SAMPLE NUMBER: BW605   **Drillhole (Depth):** 201903052 (1.0m)

FIELD DESCRIPTION: FBS progressing into ~oblique vein (possible cleavage?); is FBS using an existing cleavage as a fracture/nucleation plane?

MIM GEOLOGIST MAPPED LITHOLOGY: Shale (Urquhart Shale)

HAND SPECIMEN

Pyrrhotite filled foliation boudinage structures, with silica-dolomite rim. Bending apparent in adjacent shale layers. Silica-dolomite veins cut the sample, with one vein at top of sample potentially exploited by pyrrhotite mineralisation. Coarse-grained pyrite throughout sample. Sample has broken through plane of weakness (possibly as a result of coarse-grained pyrite rich layer. Sample observed on reverse of sample.

Diameter of drill core: ~50 mm

THIN SECTION

Cut face is up-side of core, meaning polished section is looking uphole. Perpendicular to BW604 and BW502.

PL   *XPL*

10 mm   10 mm

CLASSIFICATION

Pyrrhotite Mineralised Foliation Boudinage Structure

Boudin Samples

SAMPLE NUMBER: A   **Drillhole (Depth):**   201605182 (113.7m)

FIELD DESCRIPTION: Boudinage of pyrite

MIM GEOLOGIST MAPPED LITHOLOGY: Pyritic Shale (5-20% pyrite)

HAND SPECIMEN

Pyrite dominated layers interlayered with shale. Pyrite is fractured and boudinage parallel to the layering. Possible both fine- and coarse-grained pyrite in sample.

Diameter of drill core: ~36 mm

THIN SECTION

PPL

XPL
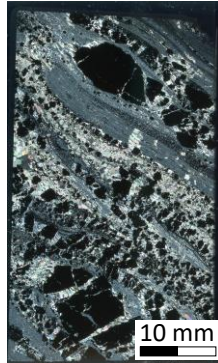
CLASSIFICATION

Boudinage of Pyrite

SAMPLE NUMBER:	B2	**Drillhole (Depth):**	201605182 (113.7m)

FIELD DESCRIPTION: Boudinage of pyrite

MIM GEOLOGIST MAPPED LITHOLOGY: Pyritic Shale (5-20% pyrite)

HAND SPECIMEN

Pyrite dominated layers interlayered with shale. Pyrite is fractured and boudinage parallel to the layering. Possible both fine- and coarse-grained pyrite in sample.

Diameter of drill core: ~36 mm

THIN SECTION

PPL

XPL
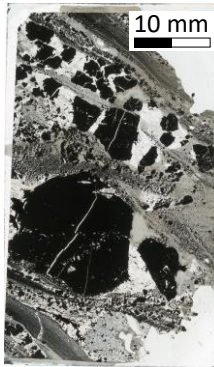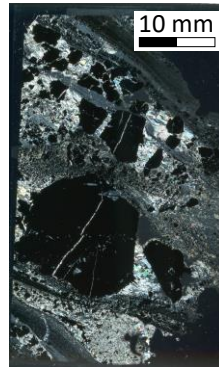
CLASSIFICATION

Boudinage of Pyrite

SAMPLE NUMBER: BW201A   **Drillhole (Depth):**   201904012 (175.5m)

FIELD DESCRIPTION: Possible FBS; not within normal shale; found within anastomosing fine-grained pyrite(?)

MIM GEOLOGIST MAPPED LITHOLOGY: Shale (Urquhart Shale)

HAND SPECIMEN

Anastomosing layers of fine-grained pyrite leading to competency contrast enabling boudinage of the layers. Shale appears to have undergone some alteration by silica-dolomite. Boudin necks filled with pyrrhotite and chalcopyrite.

Diameter of drill core: ~50 mm

THIN SECTION

PPL

XPL

10 mm

10 mm
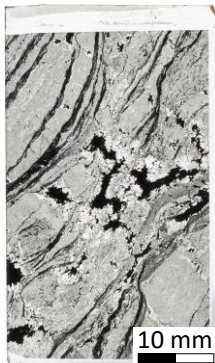
CLASSIFICATION

Pyrrhotite and Chalcopyrite Mineralised Boudin

SAMPLE NUMBER: BW201B **Drillhole (Depth):** 201904012 (175.5m)

FIELD DESCRIPTION: Possible FBS; not within normal shale; found within anastomosing fine-grained pyrite(?)

MIM GEOLOGIST MAPPED LITHOLOGY: Shale (Urquhart Shale)

HAND SPECIMEN

Anastomosing layers of fine-grained pyrite leading to competency contrast enabling boudinage of the layers. Shale appears to have undergone significant alteration by silica-dolomite. Boudin necks filled with pyrrhotite and chalcopyrite.

Diameter of drill core: ~50 mm

THIN SECTION

PPL

XPL
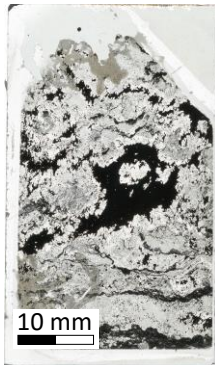
CLASSIFICATION

Pyrrhotite and Chalcopyrite Mineralised Boudin

SAMPLE NUMBER: BW203   **Drillhole (Depth):** 201904012 (22.0m)

FIELD DESCRIPTION: Possible FBS (pyrrhotite + chalcopyrite?)

MIM GEOLOGIST MAPPED LITHOLOGY: Shale (Urquhart Shale)

HAND SPECIMEN

Altered shale with chalcopyrite, pyrrhotite and silica-dolomite filled boudin. Chalcopyrite and pyrrhotite appear coeval in boudin neck.

Diameter of drill core: ~50 mm

THIN SECTION

PPL   *XPL*
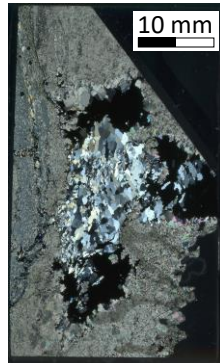
CLASSIFICATION

Silica-Dolomite, Pyrrhotite and Chalcopyrite Mineralised Boudin

SAMPLE NUMBER: BW209A   **Drillhole (Depth):**   201903052 (8.5m)

FIELD DESCRIPTION: Boudinage necks – some mineralisation in the neck region. Dolomite(?) fabric in stretching direction in neck – mutual growth of dolomite during boudinage.

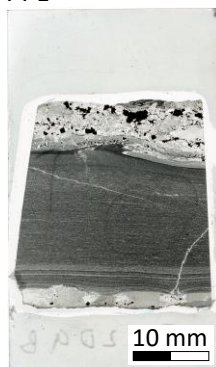**MIM GEOLOGIST MAPPED LITHOLOGY:**   Shale (Urquhart Shale)

HAND SPECIMEN

Boudinage of possible carbonate (dolomite) rich shale layer, which adds the competency difference needed for boudinage. Some sulphide mineralisation in boudin necks.

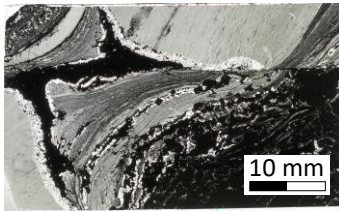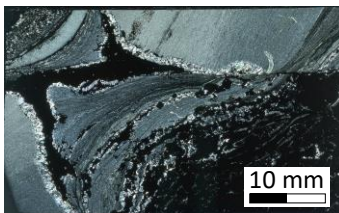Diameter of drill core: ~50 mm

THIN SECTION

PPL

10 mm

XPL

10 mm
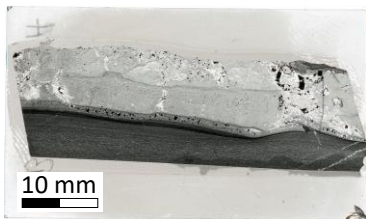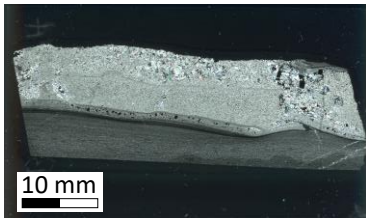
CLASSIFICATION

Minor Sulphide Mineralised Boudin

SAMPLE NUMBER: BW209B   **Drillhole (Depth):**   201903052 (8.5m)

FIELD DESCRIPTION: Boudinage necks – some mineralisation in the neck region. Dolomite fabric in stretching direction in neck – mutual growth of dolomite during boudinage.

MIM GEOLOGIST MAPPED LITHOLOGY: Shale (Urquhart Shale)

HAND SPECIMEN

Boudinage of possible carbonate (dolomite) rich shale layer, which adds the competency difference needed for boudinage. Some sulphide mineralisation in boudin necks.

Diameter of drill core: ~50 mm

THIN SECTION

PPL   *XPL*

10 mm   10 mm

CLASSIFICATION

Minor Sulphide Mineralised Boudin

SAMPLE NUMBER: BW304A   **Drillhole (Depth):**   201904012 (36.65m)

FIELD DESCRIPTION: Possible FBS (pyrite + pyrrhotite)

MIM GEOLOGIST MAPPED LITHOLOGY: Pyritic Shale (5-20% pyrite)

HAND SPECIMEN

Competency contrast caused by layers of shale, fine-grained pyrite, and coarse-grained pyrite. Boudin has well-defined fracture edge, possibly exploiting earlier discontinuities, similar to foliation boudinage. Boudin neck filled with pyrrhotite, with large deflection of fine-grained pyrite layers into neck region. Boudinage of fine-grained pyrite layers.

Diameter of drill core: ~50 mm

THIN SECTION

PPL

XPL

CLASSIFICATION

Pyrrhotite Mineralised Boudin

SAMPLE NUMBER: BW304B **Drillhole (Depth):** 201904012 (36.65m)

FIELD DESCRIPTION: Possible FBS (pyrite + pyrrhotite); boudinaged fine-grained pyrite

MIM GEOLOGIST MAPPED LITHOLOGY: Pyritic Shale (5-20% pyrite)

HAND SPECIMEN

Competency contrast caused by layers of shale, fine-grained pyrite, and coarse-grained pyrite. Boudin has well-defined fracture edge, possibly exploiting earlier discontinuities, similar to foliation boudinage. Boudin neck filled with pyrrhotite, with large deflection of fine-grained pyrite layers into neck region. Boudinage of fine-grained pyrite layers.

Diameter of drill core: ~50 mm

THIN SECTION

PPL

10 mm

XPL

10 mm
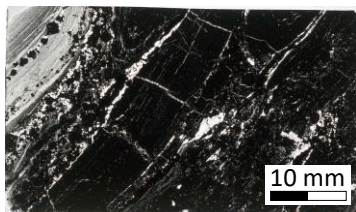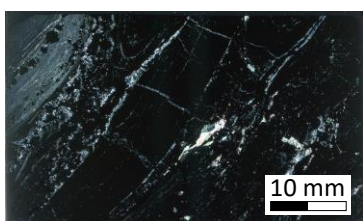
CLASSIFICATION

Boudinage of Pyrite

SAMPLE NUMBER: BW306   **Drillhole (Depth):**   201903092 (54.8m)

FIELD DESCRIPTION: Possible FBS (or boudin?). Measurements taken of orientations:

S0 = 56°->257°   Boudin neck lineation = 30°->179°

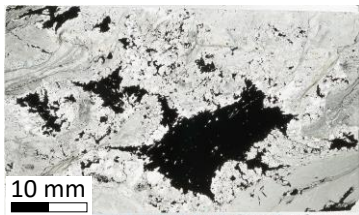**MIM GEOLOGIST MAPPED LITHOLOGY:**   Shale (Urquhart Shale)

HAND SPECIMEN

Chalcopyrite filled foliation boudinage structure or boudin geometry. Competency differences between layers in the shale (shale and altered shale) would imply that this is a regular boudin. Unusual for the quantity of mineralisation in the boudin neck.

Diameter of drill core: ~50 mm

THIN SECTION

PPL   *XPL*

10 mm   10 mm
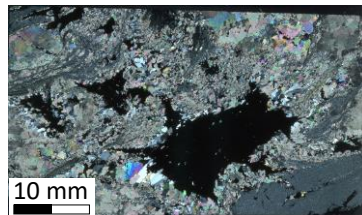
CLASSIFICATION

Chalcopyrite Mineralised Boudin

Shear Samples

SAMPLE NUMBER: 109.8-109.9   **Drillhole (Depth):**   201605182 (109.8m)

FIELD DESCRIPTION: Unusual feature in fine-grained pyrite bands

MIM GEOLOGIST MAPPED LITHOLOGY: Pyritic Shale (5-20% pyrite)

HAND SPECIMEN

Fine-grained pyrite layers, with apparent shear at ~30° angle. Some pinch and swell of layers.

Diameter of drill core: ~36 mm

THIN SECTION

PPL

10 mm

XPL

10 mm

CLASSIFICATION

Shear of Pyritic Shale

Breccia, Alteration and Replacement Samples

SAMPLE NUMBER:	BW202	**Drillhole (Depth):**	201904012 (2.1m)

FIELD DESCRIPTION: Point in drill core where it changes from bedding to irregularly recrystallised/breccia.

MIM GEOLOGIST MAPPED LITHOLOGY: Shale (Urquhart Shale) -into- Irregularly Brecciated and Recrystallised Shale

HAND SPECIMEN

The sample contains the 'contact' between relatively unaltered shale layers and the irregularly brecciated and recrystallised shale downhole. Appears to be a vein of silica-dolomite near contact.

Diameter of drill core: ~50 mm

THIN SECTION

PPL

XPL

10 mm

10 mm
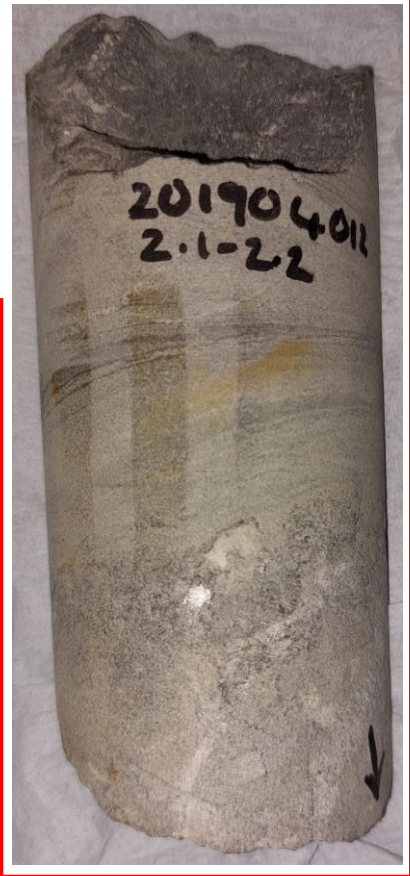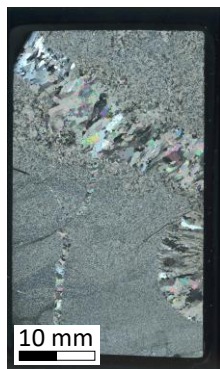
CLASSIFICATION

Altered and Recrystallised Shale

SAMPLE NUMBER: BW204   **Drillhole (Depth):** 201903092 (185.55m)

FIELD DESCRIPTION: Breccia (recrystallisation?) + high angle veins (chalcopyrite + pyrrhotite)

MIM GEOLOGIST MAPPED LITHOLOGY: Irregularly Brecciated and Recrystallised Shale

HAND SPECIMEN

Silica-dolomite breccia and replacement throughout sample. Post-breccia veins of dolomite(?) and subsequent chalcopyrite and pyrrhotite vein.
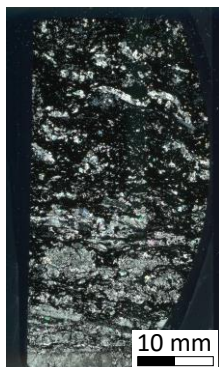
Diameter of drill core: ~50 mm

THIN SECTION

PPL   *XPL*

CLASSIFICATION

Altered and Recrystallised Shale – High Angle Veins

SAMPLE NUMBER: BW205   **Drillhole (Depth):**   201903092 (152.8m)

FIELD DESCRIPTION: S0 parallel pyrrhotite into total replacement by pyrrhotite; folds present in S0 parallel pyrrhotite.

MIM GEOLOGIST MAPPED LITHOLOGY: Shale (Urquhart Shale)

HAND SPECIMEN

Folded shale layers which have undergone replacement by dolomite and subsequent replacement by pyrrhotite. Folds likely pre-pyrrhotite in age.

Diameter of drill core: ~50 mm

THIN SECTION

PPL   *XPL*

10 mm

10 mm

CLASSIFICATION

Altered and Recrystallised Shale - Pyrrhotite Replaced Dolomitised Shale

SAMPLE NUMBER: BW206   **Drillhole (Depth):**   201605182 (99.25m)

FIELD DESCRIPTION: Pyrite strain shadow(?)

MIM GEOLOGIST MAPPED LITHOLOGY: Siliceous Shale
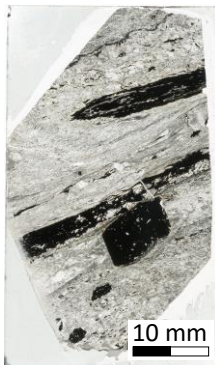

HAND SPECIMEN

Evidence of shale alteration. Coarse-grained pyrite (>5mm) with evidence of strain shadows parallel to shale layers. Strain shadow soft mineral, possibly talc. Isoclinal fold in fine-grained pyrite(?) layer also present.
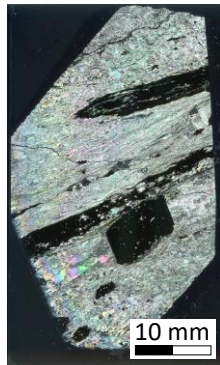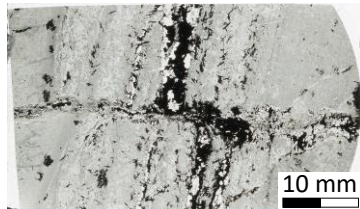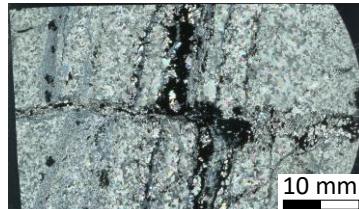
Diameter of drill core: ~36 mm

THIN SECTION

PPL   *XPL*

CLASSIFICATION

Altered and Recrystallised Shale - Pyrite Pressure Shadows

SAMPLE NUMBER: BW307   **Drillhole (Depth):**   201903092 (153.1m)

FIELD DESCRIPTION: S0 parallel veins (pyrrhotite)

MIM GEOLOGIST MAPPED LITHOLOGY: Shale (Urquhart Shale)

HAND SPECIMEN

Folded shale layers which have undergone replacement by dolomite and subsequent replacement by pyrrhotite. Folds likely pre-pyrrhotite in age. Pyrrhotite vein in hand sample is at high angle to layers.

Diameter of drill core: ~50 mm

THIN SECTION

PPL

XPL

10 mm

10 mm

CLASSIFICATION

Altered and Recrystallised Shale - Pyrrhotite Replaced Dolomitised Shale

SAMPLE NUMBER: BW308   **Location:** Underground Sample of 'typical chalcopyrite breccia' collected proximal to high-grade Cu workings

FIELD DESCRIPTION: Sample of typical Cu breccia collected from underground close to current orebody.
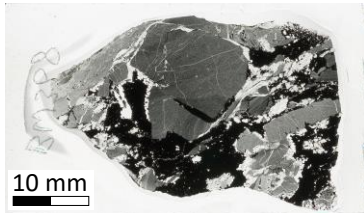
MIM GEOLOGIST MAPPED LITHOLOGY: NA (Cu breccia)
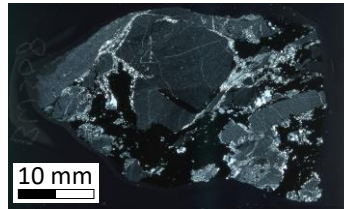
HAND SPECIMEN

No image

THIN SECTION

PPL

XPL

CLASSIFICATION

Cu Breccias

Other Samples

SAMPLE NUMBER:	BW301	**Drillhole (Depth):**	201904012 (108.5m)

FIELD DESCRIPTION: Possible FBS (pyrrhotite)

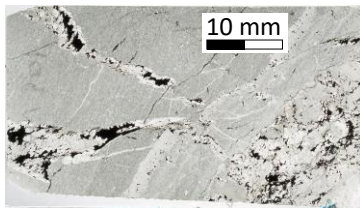**MIM GEOLOGIST MAPPED LITHOLOGY:**   Shale (Urquhart Shale)

HAND SPECIMEN

Possible pyrrhotite filled foliation boudinage structure. Absence of any obvious shale layers makes determination difficult. Silica-dolomite veins throughout. Breccia and recrystallised shale observed downhole in sample.
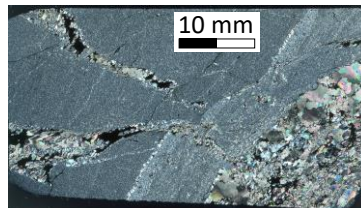
Diameter of drill core: ~50 mm

THIN SECTION

PPL

XPL

CLASSIFICATION

Silica-Dolomite Breccia Veins

SAMPLE NUMBER: BW305A   **Drillhole (Depth):**   201903052 (172.8m)
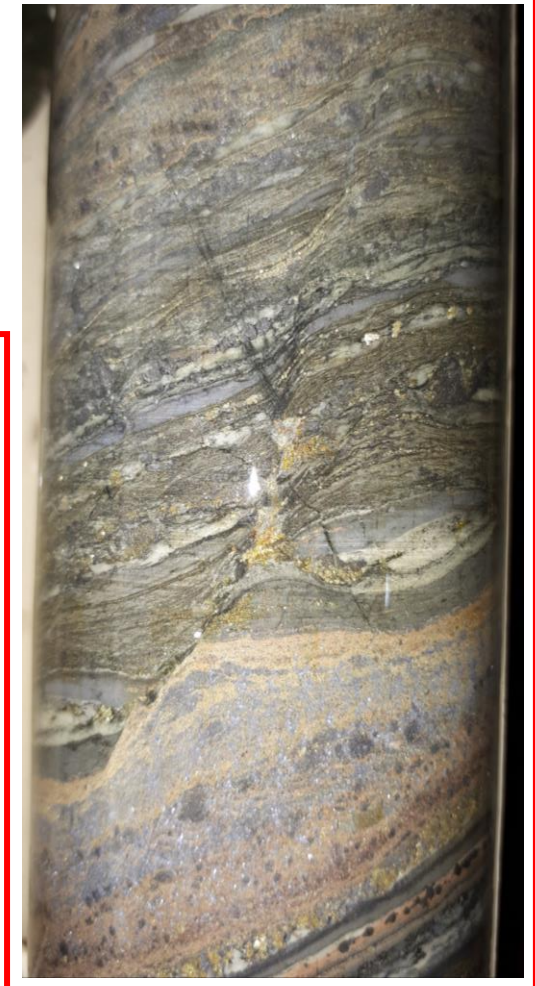
FIELD DESCRIPTION: Possible FBS in Pb-Zn zone? Or possible shear?

MIM GEOLOGIST MAPPED LITHOLOGY: Pyritic Shale (5-20% pyrite)

HAND SPECIMEN

Shear and possible foliation boudinage structure in the zone of high Pb-Zn content. Infill of shear or foliation boudinage structure appears to be chalcopyrite. Difficult to determine relative ages from sample.
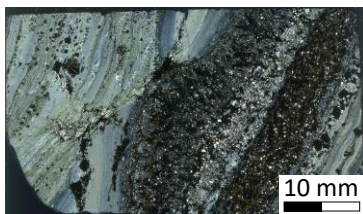
Diameter of drill core: ~50 mm

THIN SECTION

PPL

10 mm

XPL

10 mm

CLASSIFICATION

Possible Foliation Boudinage Structure in Pb-Zn Mineralisation

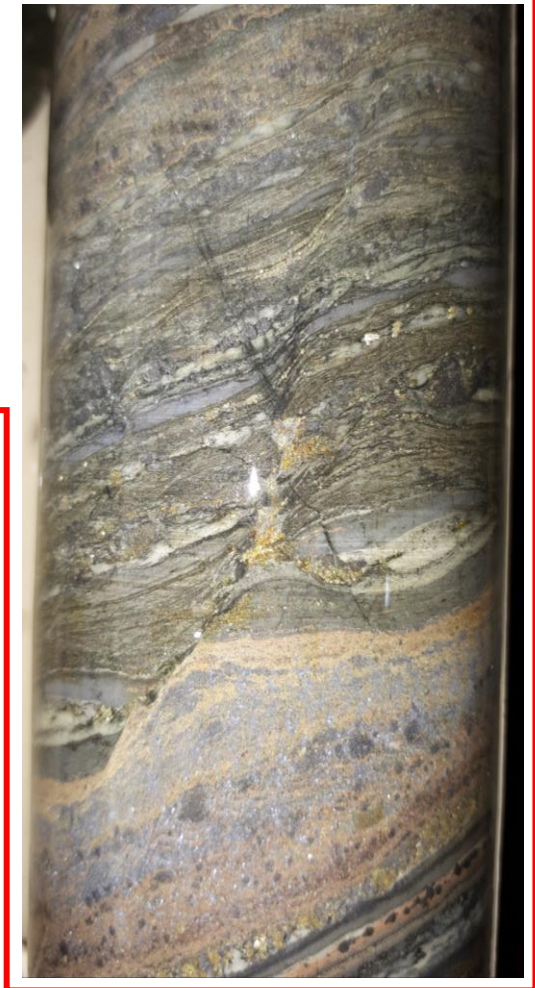**SAMPLE NUMBER:**   BW305B   **Drillhole (Depth):**   201903052 (172.8m)

FIELD DESCRIPTION: Possible FBS in Pb-Zn zone? Or possible shear?

MIM GEOLOGIST MAPPED LITHOLOGY: Pyritic Shale (5-20% pyrite)

HAND SPECIMEN

Shear and possible foliation boudinage structure in the zone of high Pb-Zn content. Infill of shear or foliation boudinage structure appears to be chalcopyrite. Difficult to determine relative ages from sample. Extensional crenulation cleavage within more well-layered areas of the drill core.

Diameter of drill core: ~50 mm
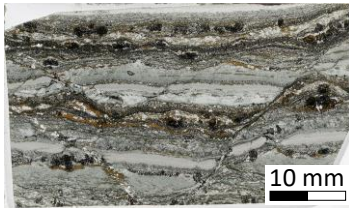
THIN SECTION

PPL

10 mm

XPL

10 mm

CLASSIFICATION

Possible Extensional Crenulation Cleavage in Pb-Zn Mineralisation

SAMPLE NUMBER: BW401A   **Drillhole (Depth):**   201903052 (172.6m)

FIELD DESCRIPTION: Possible FBS within Pb-Zn zone? (Pyrrhotite + chalcopyrite)

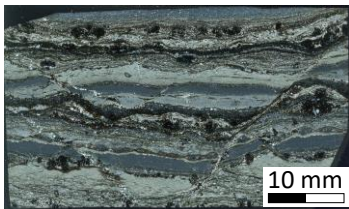**MIM GEOLOGIST MAPPED LITHOLOGY:**   Pyritic Shale (5-20% pyrite)

HAND SPECIMEN

Appears similar to a mineralised shear with pyrrhotite and some chalcopyrite. Pb-Zn mineralisation in layers, which have undergone significant replacement by silica-dolomite. Chalcopyrite and pyrrhotite paragenetically later than Pb-Zn. Extensional crenulation cleavage also evident in sample.

Diameter of drill core: ~50 mm

THIN SECTION

PPL

10 mm

XPL

10 mm

CLASSIFICATION

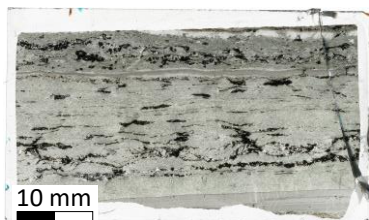*Possible Foliation Boudinage Structure in Pb-Zn Mineralisation*

SAMPLE NUMBER: BW401B   **Drillhole (Depth):**   201903052 (172.6m)

FIELD DESCRIPTION: Possible FBS within Pb-Zn zone? (Pyrrhotite + chalcopyrite)

MIM GEOLOGIST MAPPED LITHOLOGY: Pyritic Shale (5-20% pyrite)

HAND SPECIMEN

Appears similar to a mineralised shear with pyrrhotite and some chalcopyrite. Pb-Zn mineralisation in layers, which have undergone significant replacement by silica-dolomite. Chalcopyrite and pyrrhotite paragenetically later than Pb-Zn. Extensional crenulation cleavage also evident in sample.
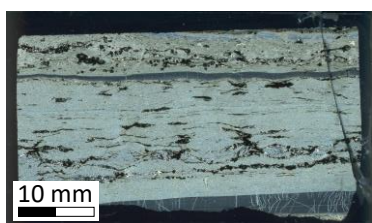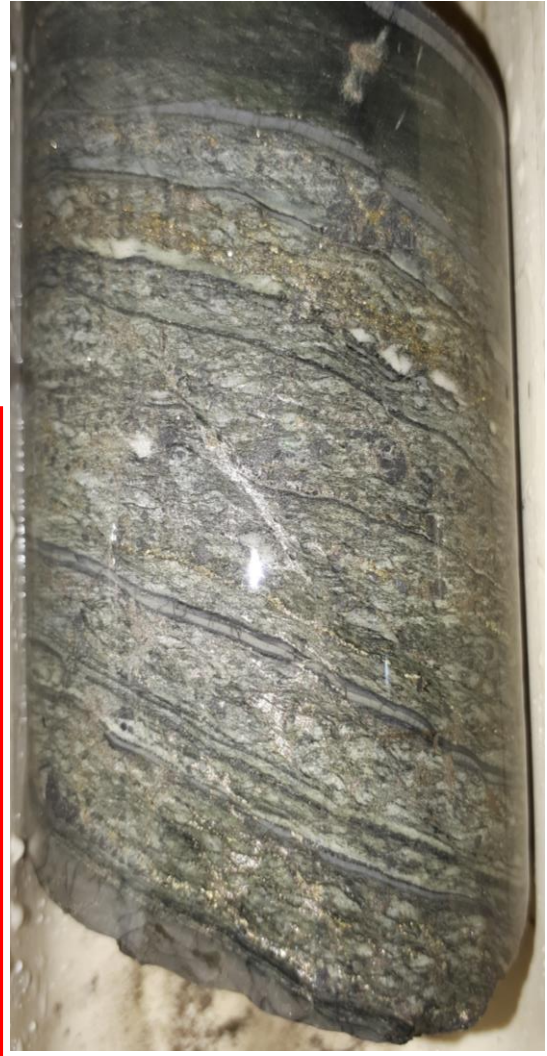
Diameter of drill core: ~50 mm

THIN SECTION

PPL

XPL

CLASSIFICATION

Possible Extensional Crenulation Cleavage in Pb-Zn Mineralisation

SAMPLE NUMBER: BW402   **Drillhole (Depth):**   201903092 (168.0m)

FIELD DESCRIPTION: Possible FBS (chalcopyrite with possible dolomite or talc)

MIM GEOLOGIST MAPPED LITHOLOGY: Shale (Urquhart Shale) -into- Irregularly Brecciated and Recrystallised Shale

HAND SPECIMEN

Possible chalcopyrite filled foliation boudinage structures. Bending of layers into structures is apparent in the sample. Unusual in that they seem to be only filled with chalcopyrite, unlike many other foliation boudinage structures observed which are filled with predominantly pyrrhotite. All fabrics in sample have a roughly consistent orientation.

Diameter of drill core: ~50 mm

THIN SECTION

PPL   *XPL*

10 mm   10 mm
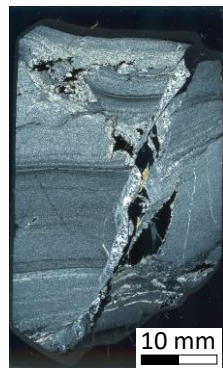
CLASSIFICATION

Possible Cu Mineralised Foliation Boudinage Structure

SAMPLE NUMBER: BW404   **Drillhole (Depth):** 201904012 (107.0m)

FIELD DESCRIPTION: Possible FBS (pyrrhotite)

MIM GEOLOGIST MAPPED LITHOLOGY: Shale (Urquhart Shale)

HAND SPECIMEN

Sample appears to have similar geometries to foliation boudinage structures, although bending into the structure is difficult to determine as layering is not obvious at the structures. The structures may be veins.

Diameter of drill core: ~50 mm

THIN SECTION

PPL

10 mm

XPL

10 mm

CLASSIFICATION

Silica-Dolomite and Pyrrhotite Veins

SAMPLE NUMBER: BW407   **Location:**   Underground Sample

FIELD DESCRIPTION: Sample collected underground with FBS-like structure.

MIM GEOLOGIST MAPPED LITHOLOGY: NA (shale)

HAND SPECIMEN

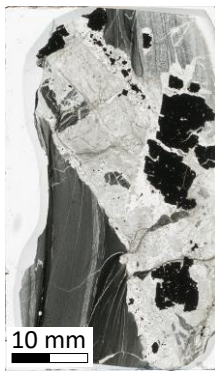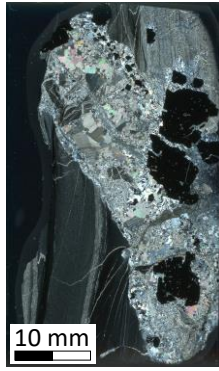Sample of shale with silica-dolomite and coarse-grained pyrite. On the scale of the hand sample, the structure resembles a foliation boudinage structure, but is likely a vein.

THIN SECTION

PPL   *XPL*

CLASSIFICATION

Silica-Dolomite Vein

APPENDIX E

Geological Map of the Mount Isa Area: Measurements from Road Cutting Mapping

This appendix contains an adapted version of the 2020 geological map published by the Geological Survey of Queensland (Spatial and Graphic Services Statewide Operations Department of Natural Resources Mines and Energy, 2020). All measurement symbols were transposed from those on the Geological Survey of Queensland map.

Measurements were collected from three road cutting locations as part of this study, termed the 'Airport', 'Shed 7', and 'Lookout' outcrops. All measurements at these localities were collected using the 'Fieldmove Clino' application. Bedding measurements were the primary focus of data collection, in order to strengthen the justification for the bedding orientations assumed in reorienting the foliation boudinage structures in unoriented core (Chapter 7).
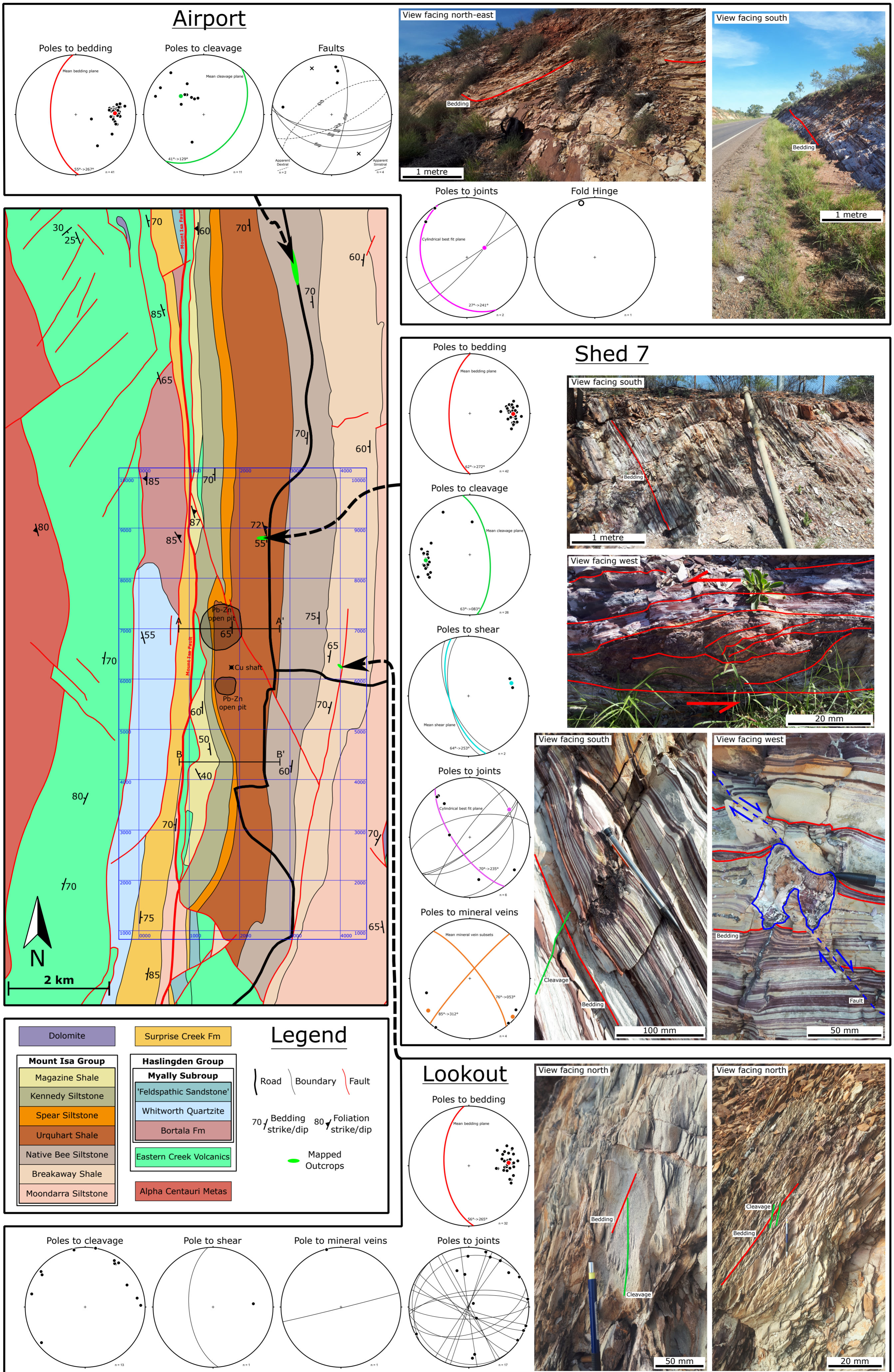
Shed 7

- Outcrop located in the Urquhart Shale; in an east-west road cutting.
- Bedding orientations consistent with those throughout the mine, and with their location on the western limb of a D2 anticline.
- Cleavage consistent with that produced in the D2 event.
- Pre-deformation veins present, with flanking structures **[Figure 3.9; Appendix A]**.
- Apparent dextral displacement – with vein continuation after restoration. Vein is pre-movement.
- Sinistral shear sub-parallel to bedding observed in west facing section.

Airport

- Outcrop located in the Native Bee; in a north-south road cutting.
- Bedding consistent with those throughout the mine, and with their location on the western limb of a D2 anticline.
- Some low-frequency, low-amplitude folds observed across the outcrop.
- Cleavage present, less well defined in this ~north-south road cutting.
- Cleavage possibly as a result of a later deformation event.

Lookout

- Outcrop located in the Breakaway Shale; in a NW-SE road cutting.
- Bedding orientations consistent with those throughout the mine, and with their location on the western limb of a D2 anticline.
- Cleavage well developed throughout the outcrop, possibly separated into two cleavage subsets.
- The outcrop crumbles easily with the combined effects of bedding and strong cleavage.
- Measurements at this locality may have been impacted by their proximity to the mapped fault.

Airport

Poles to bedding

Poles to cleavage

Faults

View facing north-east

View facing south

Poles to joints

Fold Hinge

Shed 7

Poles to bedding

Poles to cleavage

Poles to shear

Poles to joints

Poles to mineral veins

View facing south

View facing west

View facing south

View facing west

Legend

Dolomite	Surprise Creek Fm

Mount Isa Group

Magazine Shale

Kennedy Siltstone

Spear Siltstone

Urquhart Shale

Native Bee Siltstone

Breakaway Shale

Moondarra Siltstone

Haslingden Group
Myally Subroup

'Feldspathic Sandstone'

Whitworth Quartzite

Bortala Fm

Eastern Creek Volcanics

Alpha Centauri Metas

Road | Boundary | Fault

70 Bedding strike/dip | 80 Foliation strike/dip

Mapped Outcrops

Lookout

Poles to bedding

View facing north

View facing north

Poles to cleavage

Pole to shear

Pole to mineral veins

Poles to joints

APPENDIX F

Desurveying Codes and 3-Dimensional Model Material (Electronic Appendix)

Appendix F.1: Desurveying computer codes (Python).

- Basic Tangent
- Balanced Tangent
- Average Angle
- Minimum Curvature

Appendix F.2: Desurveying computer codes (R).

- Basic Tangent
- Balanced Tangent
- Average Angle
- Minimum Curvature

Appendix F.3: Formation of a symmetrical foliation boudinage structure over time (GIF).

Appendix F.4: Formation of an asymmetrical foliation boudinage structure over time (GIF).

Appendix F.5: A 3D PDF of the foliation boudinage structure modelled in the MOVE software.

Appendix F.6: MOVE model fly around video.

Appendix F.7: CT model fly around video.

Appendix F.8: The 3-dimensional displacement surface of the modelled foliation boudinage structure (GIF).

APPENDIX G

Reorientation Methods and Additional Material for Strain Analysis

Appendix G.1: Table of mineral phases indexed in this study.

Mineral	Formula	Crystal System	Space Group	Laue Group	EBSD Samples	Reference
Pyrrhotite	FeS	Hexagonal	190(P -62c)	9(6/mmm)	EBSD_1,2,3 ,4,5,6,7,8,9, 10,11,12	(NIST Structural Database – Journal of Solid State Chemistry, (1990), vol.84, pages 211-225)
Chalcopyrite	$CuFeS_2$	Tetragonal	122(I -4 2 d)	5(4/mmm)	EBSD_1,2,3 ,4,5,6,7,8,9, 10,11,12	(Inorganic Crystal Structural Database – Z.Kristallogr. [ZEKRDZ], (1989), vol.186, [AGES167-169]
Galena	PbS	Cubic	225(F m-3m)	11(m-3m)	EBSD_3,4,5 ,6,7,8,9,10, 11,12	HKL phases – Nippon Kinzoku Gakkaishi, (J. Jpn. Inst. Met.)
Arsenopyrite	FeAsS	Triclinic	2(P-1)	1(-1)	EBSD_3,4,5 ,6,7,8,9,10, 11,12	American Mineralogist, (1961), vol. 46, pages 1448-1469
Quartz	SiO_2	Trigonal	152(P 3_1 2 1)	7(-3m)	EBSD_1,2,3 ,4,5,6,7,8,9, 10,11,12	HKL phases – Sands (1969) [Quartz-new]
Pyrite	FeS_2	Cubic	205(P a-3)	10(m-3)	EBSD_1,2,3 ,4,5,6,7,8,9, 10,11,12	HKL phases – ActaChemSca, 23, 2186-88
Calcite	$CaCO_3$	Trigonal	-	7(-3m)	EBSD_1,2,3 ,4,5,6,7,8,9, 10,11,12	HKL phases – Calcite.cry
Dolomite	$CaMg(CO_3)_2$	Trigonal	-	6(-3)	EBSD_1,2,3 ,4,5,6,7,8,9, 10,11,12	HKL phases – Dolomite.cry

Appendix G.2: X-Ray Diffraction graphs of pyrrhotite in samples from Mount Isa.
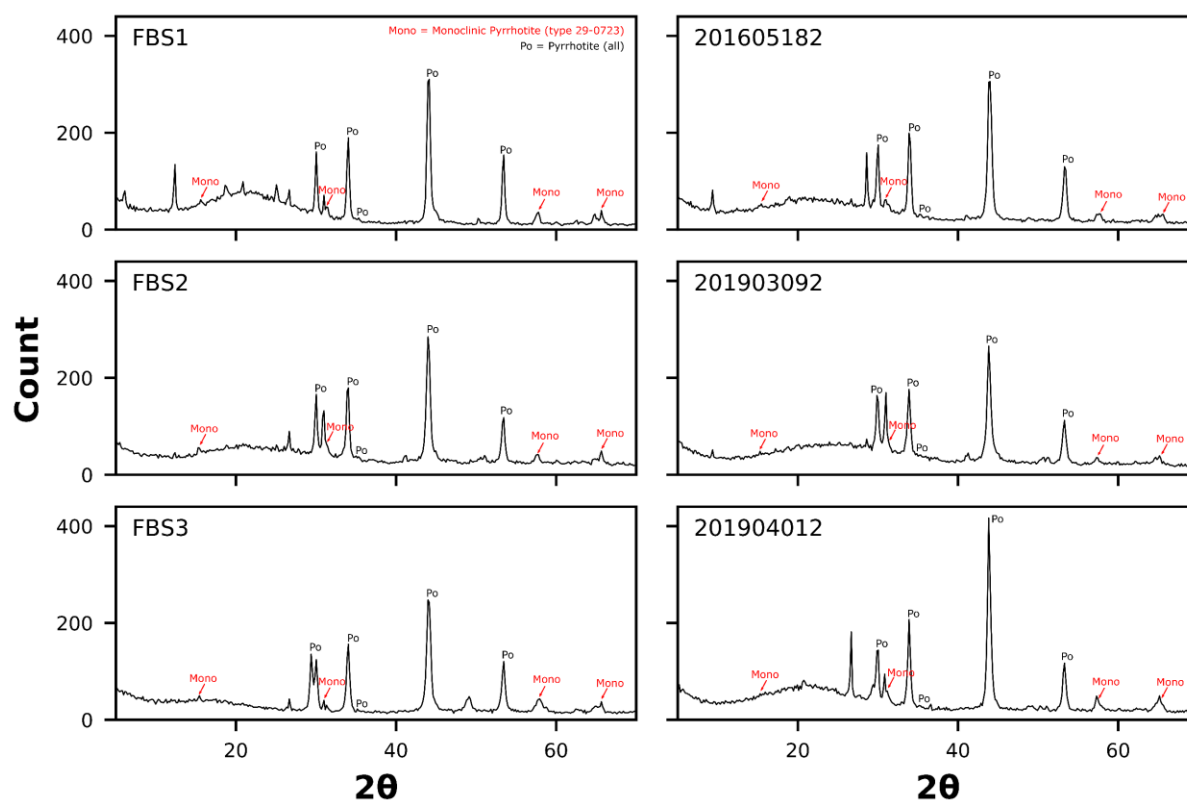
Appendix G.3: The set-up of EBSD analysis maps in this study.

FBS	FBS Plane	Carbon Coat (nm)	Step Size (μm)	Pixel Size (μm)	Fields	Magnification	Working Distance (mm)	Acquisition Time (hours)	Exposure Time (μs)	Detector Insertion (mm)
FBS1	XZ	~5.4	8	1.8	-	x150	20	~76	49.2	190
FBS1	YZ	7.3	8	2.01	23	x134	17	-	53.5	191
FBS1	XY	5.3	8	4.81	1	x56	17	~5	91.8	191
FBS2	XZ	7.3	6	3.59	1	x75	17	~4	52.4	191.1
FBS2	YZ	~5	6	1.5	23	x150	20	~15	48	190
FBS2	XY	5.9	6	3.59	1	x75	17	~4	52.9	191
FBS3/4	XZ	7.1	14.1	1.75	-	x154	22	~19	37.1	195.3
FBS3/4	YZ	5.9	14.1	3.55	14	x76	20	~11	54.9	191

**Appendix G.4:** Method for reorienting unoriented drill core.

1. Drillhole Plunge and Azimuth plotted as plunge and trend.

2. Plane to pole plotted and represents the plane perpendicular to the drillhole direction.

3. Small circle plotted for the drillhole (90° - Alpha angle of the S0 (bedding) plane).

4. Dip direction plotted for the drillhole as a plane passing through the drillhole.

5. Plot assumed S0 (bedding) orientation.

6. Plot pole to S0 (bedding).

7. Plot known bedding dip direction (vertical plane passing through the pole to the known S0 orientation; this is calculated from oriented core or underground bedding measurements proximal to the drillhole.

8. The previously plotted plane intersects the small circle in two locations, these are the poles to the S0.

9. Choose the pole that best represents the assumed S0 (bedding) orientation and plot great circle.

10. Plot great circle which passes through both the drillhole pole and pole of bedding (above).

11. The angle between the above great circle and the vertical plane through the drillhole, measured clockwise along the great circle of the drillhole, is the Beta angle between the bottom of core and the actual S0.

Appendix G.5: Method of reorienting polished thin sections using stereonets.

1. Assume XZ-, YZ- and XY-planes of foliation boudinage structure face north, west, and down, respectively.

2. Plot these planes of foliation boudinage structure on stereonet.

3. Plot the direction of grain long-axes as rakes on these planes.

4. Plot the known drillhole direction at the sample location as a linear measurement on the stereonet.

5. Plot the straight drill core edge as a linear rake measurement in the correct section plane.

6. Find the plane that passes through both the known drillhole direction and the drillhole edge in the section.

7. Rotate the stereonet by the angle between the two linear measurements.

8. The actual orientation of the polished thin section must now be some rotation about the known drillhole direction.

9. In the samples of foliation boudinage structures the bedding is parallel to the XY-plane and normal to the intersection of the XZ- and YZ-planes.

10. Plot this bedding plane on the stereonet.

11. Rotate the stereonet about the known drillhole direction to get bedding plane into approximate dip and dip direction of known bedding measurements proximal to the drill core location, or reoriented drill core orientation from section 7.3.7.

12. Lineation of foliation boudinage structure long-axis is the intersection of the XY- and YZ-planes.

13. The plane through the XZ- and YZ- long-axis linear directions of grains from step 3 is the 3-dimensional plane of shortening within the foliation boudinage structure mineral infill.
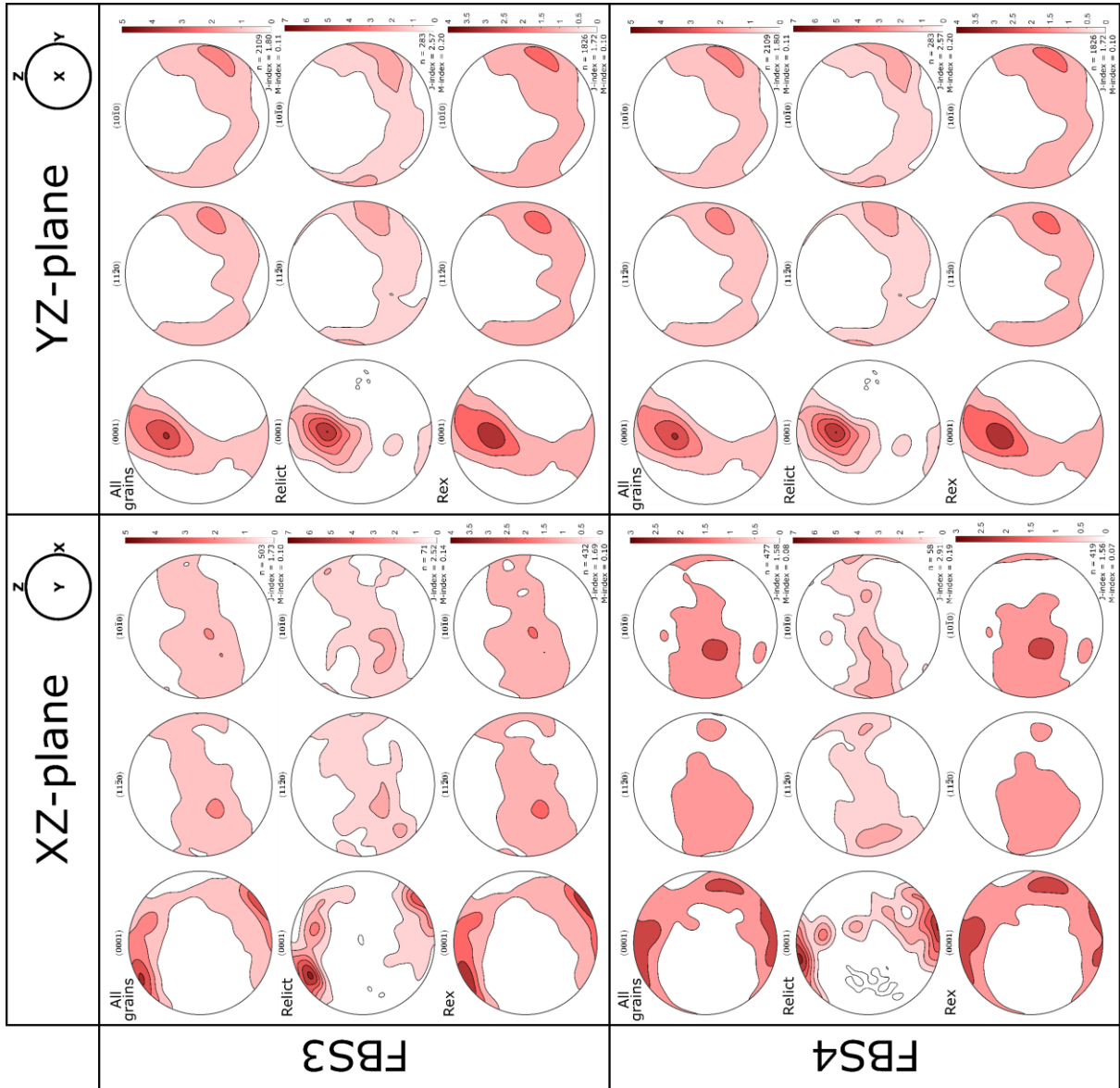
14. The normal to this plane approximates the direction of shortening (if shortening only through coaxial deformation).
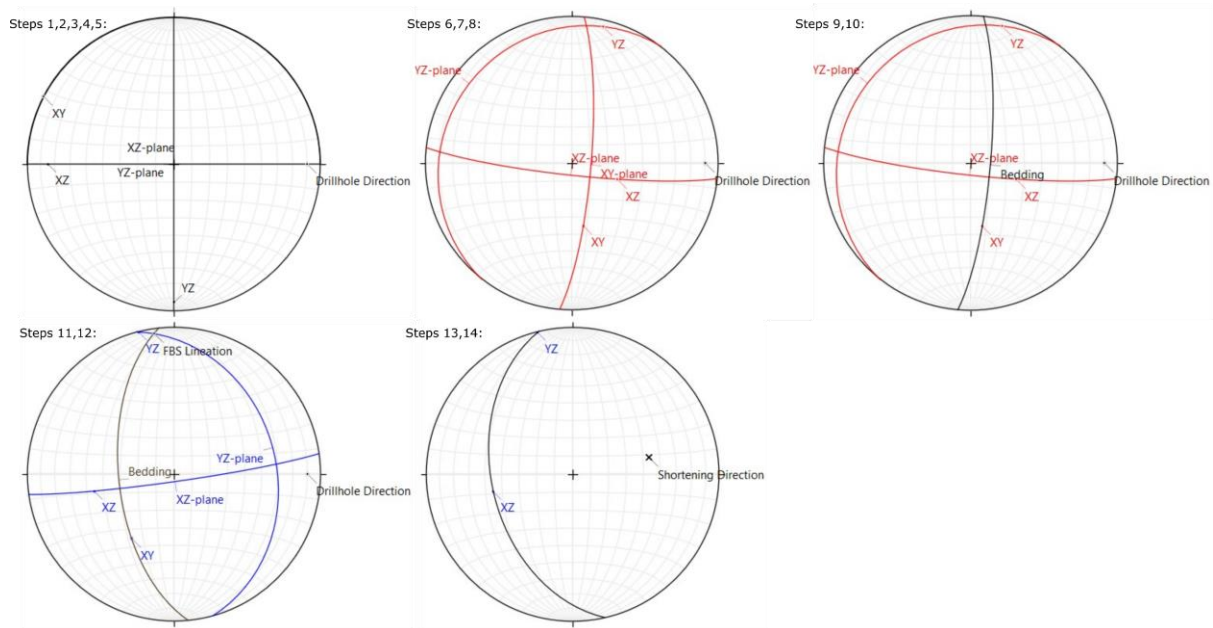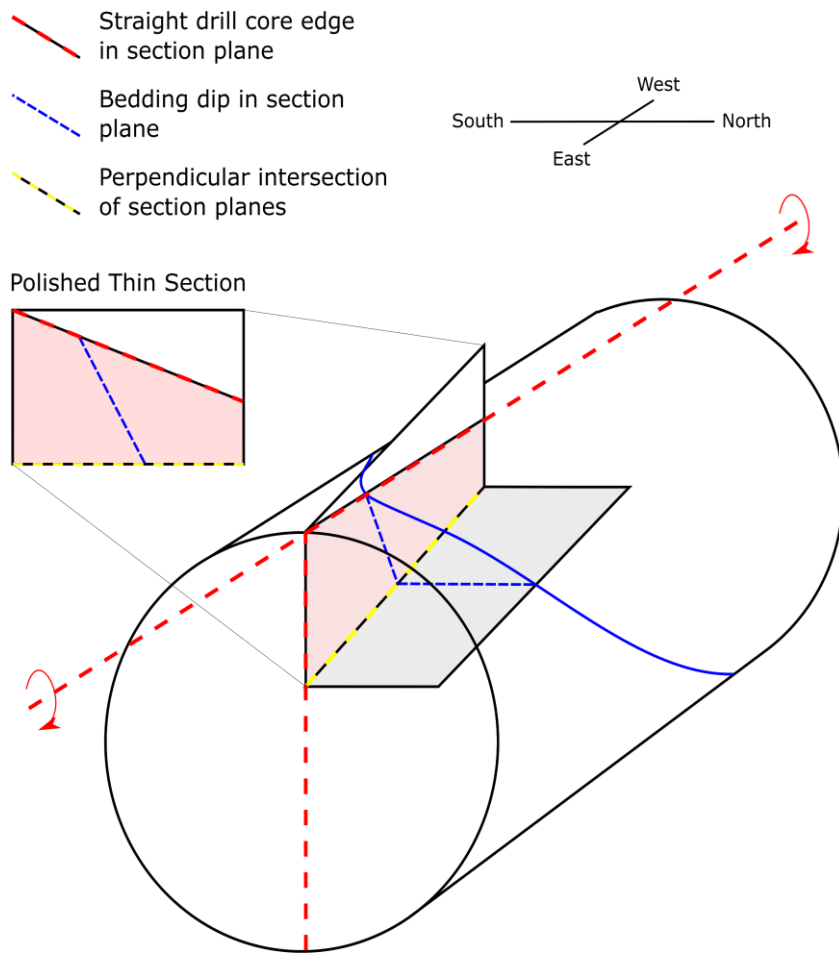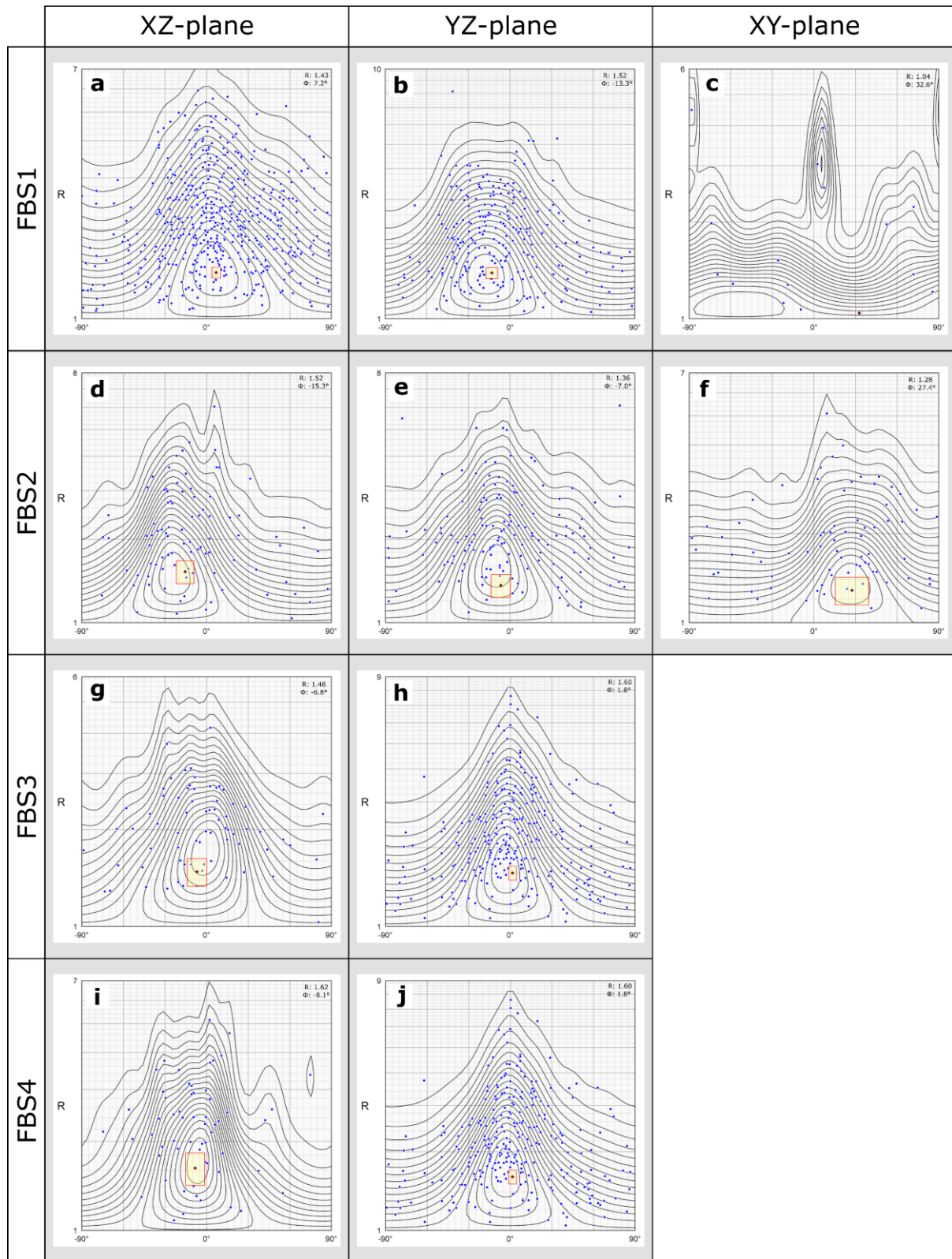
Appendix G.6: Pole figures for all foliation boudinage structures in this study. Pole figures show all grains (one point per grain), relict grains and recrystallised grains.
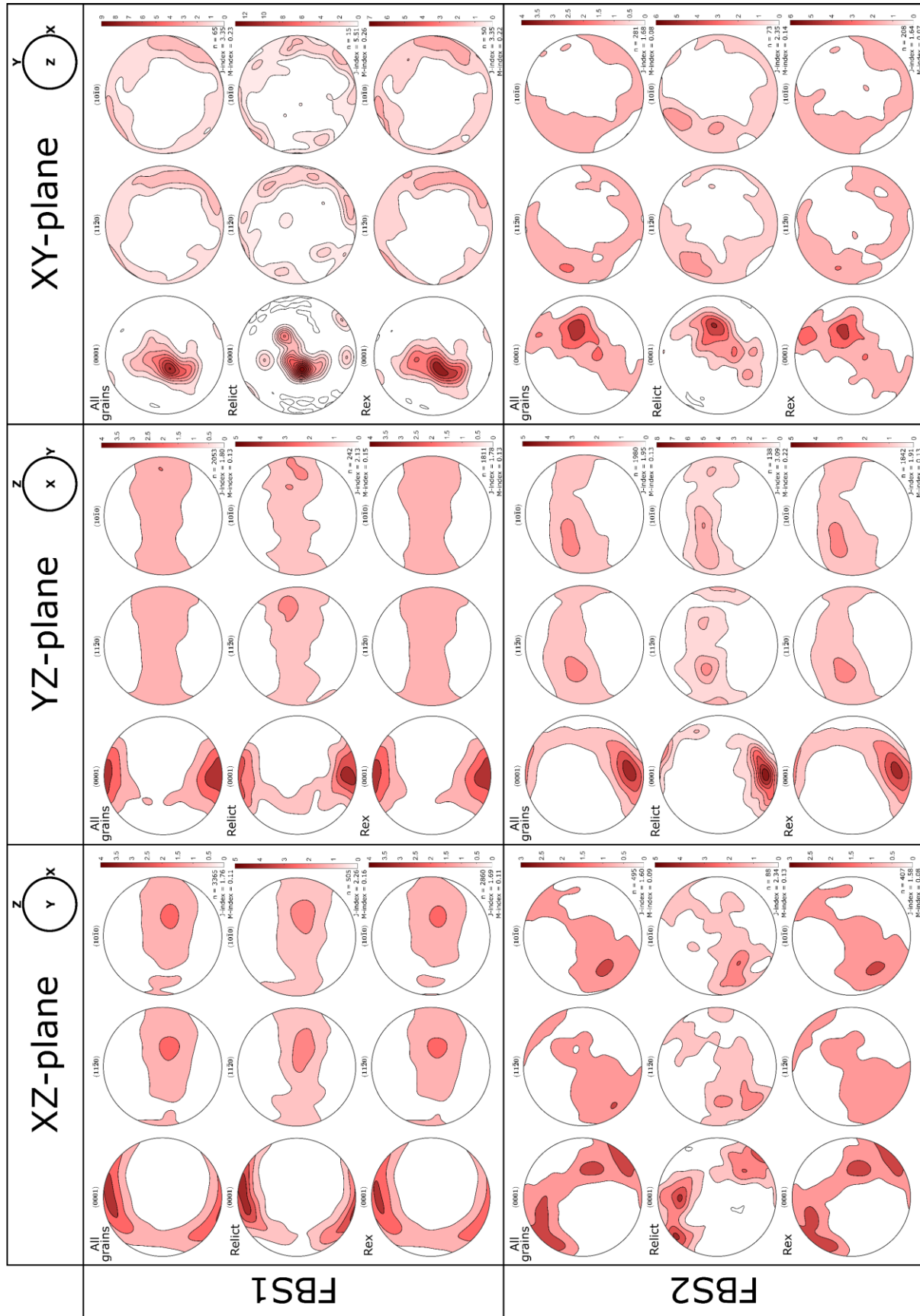
Appendix G.7: All Rf/phi plots for all orientations of FBS.

Appendix G.8: Error analysis in the shortening directions of foliation boudinage structure infills using the polished thin section reorientation method shown in **Appendix G.5**.

Error analysis:

- Error is negligible for the planes cut through the foliation boudinage structure.

- Error is negligible for the drillhole edge in the thin section.

- Error is negligible for the known drillhole edge direction.

- Error is negligible for the bedding plane parallel to the XY-plane/normal to XZ- and YZ-planes intersection.

- Some error involved in the rotation of the data about the drillhole direction and is assumed to be approximately ±5°. The rotation relies partly on assumed bedding dips and oriented measurements proximal to the sample location.

- Error in drillhole edge direction in FBS1 is greater than for the other calculations as the drill core straight edge is not within the section plane. The angle between the section plane and the drill core edge has been measured with a ±5° error in both the azimuth and plunge and a ±10° error in the rotation angle around the known drillhole direction.

Appendix G.9: Errors in the shortening direction using the reorientation of polished thin sections method.

FBS	Plunge (°)	Azimuth (°)
FBS1	±9	+12/-9
FBS2	±1	±4
FBS3	±1	±3
FBS4	±1	±3

APPENDIX H

3-Dimensional Modelling of Foliation Boudinage Structures: Additional Material

Appendix H.1: All cross-sections through the modelled foliation boudinage structure, displaying the areas, displacements, and displacement vectors. All images to the same scale.